Delft University of Technology

Modelling and Optimization of Medium Voltage High Power Medium Frequency Transformers

Luo, T.

DOI
10.4233/uuid:0ceccfce-30e0-49f8-ab72-44dcc016dbf5

Publication date
2025

Document Version
Final published version

Important note
To cite this publication, please use the final published version (if applicable).
Please check the document version above.

MODELLING AND OPTIMIZATION OF MEDIUM VOLTAGE HIGH POWER MEDIUM FREQUENCY TRANSFORMERS

Modelling and Optimization of Medium Voltage High Power Medium Frequency Transformers

Dissertation

for the purpose of obtaining the degree of doctor
at Delft University of Technology,
by the authority of the Rector Magnificus prof. dr. ir. T.H.J.J. van der Hagen,
chair of the board for Doctorates,
to be defended publicly on
Wednesday, 15 January 2025 at 10:00 o'clock

by

Tianming Luo

Master of Science in Electrical Engineering,
China Electric Power Research Institute, China,
born in Jinan, China.

This dissertation has been approved by the promotors.

Composition of the doctoral committee:

Rector Magnificus,   chairperson
Prof. ir. P.T.M. Vaessen   Delft University of Technology, promotor
Prof. dr. ir. P. Bauer   Delft University of Technology, promotor
Dr. ir. M. Ghaffarian Niasar   Delft University of Technology, co-promotor

Independent members:

Prof. dr. ir. M. Popov   Delft University of Technology
Prof. dr. E. Lomonova   Eindhoven University of Technology
Prof. dr. ir. R.V. Sabariego   KU Leuven
Dr. ir. F. van Overbeeke   EM force
Prof. dr. ir. O. Isabella   Delft University of Technology, reserve member

To my parents

CONTENTS

LIST OF ABBREVIATION

Abbreviation	Full Words
AC	Alternating Current
BEM	Boundary Element Method
CFD	Computational Fluid Dynamics
DAB	Dual Active Bridge
DC	Direct Current
DoF	Degree of Freedom
EMI	Electromagnetic Interference
FDM	Finite Difference Method
FEM	Finite Element Method
GSE	Generalized Steinmetz Equation
IGSE	Improved Generalized Steinmetz Equation
i2GSE	Improved-Improved Generalized Steinmetz Equation
MF	Medium Frequency
MMF	Magneto-Motive Force
MoM	Method of Moments
MSE	Modified Steinmetz Equation
MV	Medium Voltage
PET	Power Electronic Transformer
SE	Steinmetz Equation
SRC	Series Resonant Converter
SST	Solid State Transformer
ZCS	Zero Current Switching
ZVS	Zero Voltage Switching

LIST OF SYMBOLS

A	Magnetic vector potential
A_c	Cross-sectional area of the magnetic core
A_w	Cross-sectional area of the windings
A_L	Inductance factor
a	Radius
a_c, b_c	Side lengths of rectangular cross section of magnetic core
B	Flux density
B_s	Saturation flux density
B_m	Amplitude of flux density
C	Capacitance
C_h	Thermal capacitance
C_l	Approximately universal function of Prandtl number for laminar flow
C_t	Function of Prandtl number for turbulent flow
C_{tt}	Turn-to-turn capacitance
C_{tc}	Turn-to-core capacitance
D	Duty cycle
d	Thickness of winding layers
d_{air}	Distance between windings
E	Electric field strength
f	Frequency
$F(E)$	Cumulative probability of breakdown
F_f	Fringing factor
k_i	Image coefficient
k_{SE}, α_{SE} and β_{SE}	Steinmetz equation coefficients
K_w	Rogowski factor
G	Winding length
Gr	Grashof number
G_p	Proximity effect coefficient
g	Gravity
H	Magnetic field strength
H_c	Coercivity
h_w	Height of layer in windings
h_c	Height of core windows
h_t	Heat transfer coefficient
I	Current
I_p	Current of transformer primary side
I_s	Current of transformer secondary side

J_{rms}	Current density, RMS value
k_w	Window utilization factor
k_t	Thermal conductivity
L	Inductance
L_e	Lifetime
L_m	Magnetizing inductance
L_{leak}	Leakage inductance
l_c	Effective magnetic path length
l_g	Length of air gap
l_t	Length of conductors
l_h	Characteristic length in thermal convection
m_t	Weight
n	Harmonic order
N_p	Number of turns of transformer primary side
N_s	Number of turns of transformer secondary side
Nu	Nusselt number
P_c	Core loss
P_w	Winding loss
P_s	Winding loss due to skin effect
P_p	Winding loss due to proximity effect
P_h	Heat source
Pr	Prandtl number
Q_h	Heat transfer rate
R_{dc}	DC Resistance
Ra	Rayleigh number
Re	Reynold number
R_s	Resistance with skin effect
R_t	Thermal resistance
S	Apparent power
t_i	Thickness of insulation
T	Temperature
T_s	Period
T_c	Curie temperature
U_p	Voltage of transformer primary side
U_s	Voltage of transformer secondary side
u_∞	Oncoming fluid velocity
V	Voltage
V_t	Volume
w_c	Width of core windows
W_m	Magnetic energy
Z	Impedance
α_t	Thermal diffusivity
β_t	Thermal expansion coefficient
Φ	Magnetic flux
η_p	Porosity factor

η	Efficiency
μ	Permeability
μ_r	Relative Permeability
μ_0	Vacuum permeability
δ	Skin depth
Δ	Penetration ratio
ΔB	Peak-to-peak flux density
σ_c	Conductivity
σ	Stefan-Boltzmann constant
ω	Angular frequency
κ	Frequency related factor, equal to $\sqrt{-j\omega\mu\sigma}$
ϵ	Permittivity
ϵ_0	Permittivity of free space
ϵ_e	Emittance
ν	Kinematic viscosity
$\mathbf{A}$	Magnetic vector potential, vector
$\mathbf{B}$	Flux density, vector
$\mathbf{E}$	Electric field strength, vector
$\mathbf{n}$	Norm vector
$\mathbf{q}_h$	Heat flux, vector
$\mathbf{S}$	Poynting vector
$\mathbf{Z}$	Impedance matrix
$\mathscr{R}$	Reluctance
$\mathscr{R}_c$	Reluctance of core
$\mathscr{R}_g$	Reluctance of air gaps
$\mathscr{R}_f$	Reluctance of fringing flux
$\mathscr{F}$	Magneto-motive force
$\mathscr{F}_b$	Fourier transform of boundary condition f_b

LIST OF FIGURES

LIST OF TABLES

SUMMARY

AC power transformers are one of the most sophisticated technologies in electrical engineering. However, they have some drawbacks facing volume-sensitive or weight-sensitive applications and energy conversion situations. The solid-state transformer is a promising power electronic technology that can solve the requirements of these applications. It utilizes power electronics and medium frequency (MF) transformers to achieve high power density and multiple functions in energy conversion. With the development of semiconductor switches, it is possible to handle medium voltage in the MF range (1kHz to 1MHz). Therefore, as an essential part of solid-state transformers, medium voltage high power medium frequency transformers require validated tools to model and optimize their design, which is the goal of this thesis. There are several challenges in designing such transformers. They include multiphysics models, Litz wire models, insulation design and design optimization, which are addressed in the thesis.

Multiphysics Models

Modelling MF transformers involves multiple physics, which are coupled to varying degrees. It is difficult and time-consuming to solve the full-coupled fields. Therefore, it is necessary to simplify the problem. This thesis focuses on the magnetic, electric and thermal fields, and decoupled models are utilized. Several commonly used models are summarized and compared. A 2D winding loss model is proposed based on analysing eddy currents in round conductors. This model considers the interaction between eddy currents and improves the accuracy of winding loss calculation. Besides, a two-dimensional circle boundary element & analytical coupled method is developed for linear media. The suitable shape of the boundary element and the analytical solution for the inside domain leads to a significantly smaller number of elements and faster computational speed compared to 2D FEM. This model can be applied to the quasi-static magnetic, static electric field and heat conduction, which shows good potential for modelling the MF transformers.

Litz Wire

In MF applications, eddy current is an important source of loss. Litz wires are widely used to reduce the impact of eddy currents. Through twisting, Litz wires can dramatically reduce the proximity effect losses and average the current distribution in a certain frequency range. However, it is difficult to achieve perfect twisting in practice, which makes the current distribution become an unknown variable. Due to the complex structures, accurate fast modelling of Litz wires is a challenge. This thesis proposes two Litz wire models that are able to calculate the current distribution. Both models show good accuracy and fast computational speed compared to 3D finite element models (FEMs). The method coupling the Litz wires and the winding models is

also investigated. The key idea of the homogenization technique is adopted, and the method is validated through measurements.

Insulation Design

In solid state transformers, the stresses applied to the insulation are generated by the semiconductor switches. It has several features, including kHz frequency, non-sinusoidal waveform, and high steepness. These features can degrade the behaviour of the insulation compared to AC stress, and the impacts are not quantitatively concluded. It makes the insulation design a problem. In this thesis, typical insulation failures in air-solid insulation are tested at various frequencies. The insulation coordination requirements in related standards are summarized. Based on the standards and literature, an insulation structure and a design field selection method for the medium voltage (MV) MF transformers are provided, along with several key points in the design process.

Design Optimization

Design optimization can help improve the performance of MF transformers. Transformer design is a non-linear and non-convex problem comprising continuous and discrete variables. There are various optimization function formats and optimization techniques. However, no specific combination shows clearly superior performance. In the thesis, the combination of particle swarm optimization and the linear objective function is used to optimize the efficiency and power density of MF transformers. A MF transformer design is selected from obtained possible designs based on the efficiency, power density and safety margin for thermal stability. The estimated parameters based on the final design are given and validated through 3D FEM.

This thesis studies the modelling and optimization of medium voltage high power medium frequency transformers. The thesis proposes and validates several new models and methods to achieve accurate and fast modelling. An effective design optimization procedure is built and validated. Several recommendations for future work are suggested.

SAMENVATTING

AC-voedingstransformatoren zijn een van de meest geavanceerde technologieën in de elektrotechniek. Ze hebben echter een aantal nadelen bij volume- of gewichtsgevoelige toepassingen en energieomzettingssituaties. De solid-state transformator is een veelbelovende vermogenselektronische technologie die de vereisten van deze toepassingen kan oplossen. Het maakt gebruik van vermogenselektronica en middenfrequentietransformatoren (MF) om een hoge vermogensdichtheid en meerdere functies in energieomzetting te bereiken. Met de ontwikkeling van halfgeleiderschakelaars is het mogelijk om middenspanning te verwerken in het MF-bereik (1kHz tot 1MHz). Daarom hebben middenspanning hoogvermogen middenfrequentietransformatoren, als een essentieel onderdeel van solid-state transformatoren, hulpmiddelen nodig om hun ontwerp te modelleren en te optimaliseren, wat het doel is van dit proefschrift. Er zijn verschillende uitdagingen bij het ontwerpen van dergelijke transformatoren. Deze omvatten multifysische modellen, Litz-draadmodellen, isolatieontwerp en ontwerpoptimalisatie, die in dit proefschrift worden behandeld.

Multifysische modellen

Bij het modelleren van MF transformatoren komen meerdere fysische aspecten kijken, die in verschillende mate gekoppeld zijn. Het is moeilijk en tijdrovend om de volledig gekoppelde velden op te lossen. Daarom moet het probleem vereenvoudigd worden. Deze dissertatie richt zich op de magnetische, elektrische en thermische velden en er worden ontkoppelde modellen gebruikt. Verschillende veelgebruikte modellen worden samengevat en vergeleken. Er wordt een 2D wikkelverliesmodel voorgesteld op basis van de analyse van wervelstromen in ronde geleiders. Dit model houdt rekening met de interactie tussen wervelstromen en verbetert de nauwkeurigheid van de berekening van het wikkelverlies. Daarnaast is een tweedimensionale cirkelrandelement- en analytische gekoppelde methode ontwikkeld voor lineaire media. De geschikte vorm van het randelement en de analytische oplossing voor het binnenste domein resulteren in aanzienlijk minder elementen en een snellere berekeningssnelheid vergeleken met tweedimensionale eindige-elementenmethoden (FEM). Dit model kan worden toegepast op quasi-statische magnetische velden, statische elektrische velden en warmtegeleiding, wat goede potentie biedt voor het modelleren van middenfrequentie transformatoren.

Litzedraad

In MF-toepassingen is wervelstroom een belangrijke bron van verlies. Litzedraden worden veel gebruikt om de invloed van wervelstromen te verminderen. Door te twisten kunnen Litz draden de nabijheidseffectverliezen drastisch verminderen en de stroomverdeling in een bepaald frequentiebereik gemiddeld maken. In de praktijk is het echter moeilijk om een perfecte verdraaiing te bereiken, waardoor de

stroomverdeling een onbekende variabele wordt. Vanwege de complexe structuren is het nauwkeurig en snel modelleren van litze draden een uitdaging. In dit proefschrift worden twee Litz-draadmodellen voorgesteld die de stroomverdeling kunnen berekenen. Beide modellen hebben een goede nauwkeurigheid en een snelle rekensnelheid in vergelijking met 3D eindige elementen modellen (FEMs). De methode om het Litz-draadmodel in het wikkelmodel op te nemen wordt ook onderzocht. Het sleutelidee van de homogenisatietechniek wordt toegepast, en de methode wordt gevalideerd door metingen.

Isolatieontwerp

In halfgeleidertransformatoren wordt de spanning op de isolatie opgewekt door de halfgeleiderschakelaars. Deze heeft verschillende kenmerken, waaronder een kHz-frequentie, een niet-sinusvormige golfvorm en een hoge steilheid. Deze eigenschappen kunnen het gedrag van de isolatie verslechteren in vergelijking met wisselstroomspanning en de gevolgen zijn niet kwantitatief vastgesteld. Dit maakt het isolatieontwerp tot een probleem. In dit proefschrift worden typische isolatiefouten in luchtvaste isolatie getest bij verschillende frequenties. De eisen voor isolatiecoördinatie in gerelateerde normen worden samengevat. Op basis van de normen en literatuur worden een isolatiestructuur en een selectiemethode voor ontwerpvelden voor middenspanningstransformatoren (MV) MF gegeven.

Optimalisatie van het ontwerp

Ontwerpoptimalisatie kan de prestaties van MF-transformatoren helpen verbeteren. Transformatorontwerp is een niet-lineair en niet-convex probleem dat bestaat uit continue en discrete variabelen. Er bestaan verschillende optimalisatiefunctieformaten en optimalisatietechnieken. Er is echter geen specifieke combinatie die duidelijk betere prestaties levert. In dit proefschrift wordt de combinatie van deeltjeszwermoptimalisatie en de lineaire objectiefunctie gebruikt om het rendement en de vermogensdichtheid van MF transformatoren te optimaliseren. Een MF transformatorontwerp wordt geselecteerd uit verkregen mogelijke ontwerpen op basis van het rendement, de vermogensdichtheid en de veiligheidsmarge voor thermische stabiliteit. De geschatte parameters op basis van het uiteindelijke ontwerp worden gegeven en gevalideerd met behulp van 3D FEM.

Deze dissertatie bestudeert de modellering en optimalisatie van middenspanning hoogvermogen middenfrequent transformatoren. In dit proefschrift worden verschillende nieuwe modellen en methoden voorgesteld en gevalideerd om nauwkeurige en snelle modellering te bereiken. Er wordt een effectieve optimalisatieprocedure voor het ontwerp ontwikkeld en gevalideerd. Verschillende aanbevelingen voor toekomstig werk worden voorgesteld.

1

INTRODUCTION

The first step is always the hardest.

1.1. BACKGROUND

MICHAEL Faraday discovered electromagnetic induction in 1831 [1] and paved the way for the development of modern electrical power systems. After discovering electromagnetic induction, it took half a century to invent the modern transformer. In 1884, Zipernowsky, Bláthy and Déri designed the first closed-core transformer, which was 3.4 times more efficient than the open-core design. This is known as the ZBD transformer, as shown in Figure 1.1 [2]. In 1885, William Stanley perfected the design of transformers and made transformers cheap to produce and easy to adjust for final use [3]. Transformers can regulate the voltage level, which gives AC power systems a decisive advantage. Stanley demonstrated the first practical system using alternating current with transformers to adjust the voltage level of the distribution system in 1886 [4]. With the help of transformers, AC power systems can step up the voltage level to achieve high efficiency in long-distance transmission and step down the voltage level to suit user needs. Finally, AC power systems won the war of currents in the nineteenth century [5].
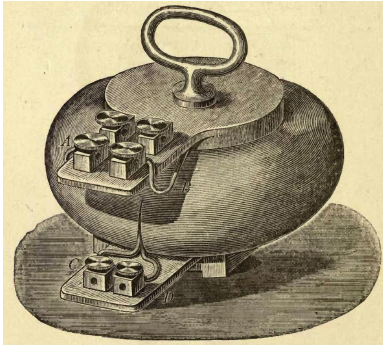
(a) ZBD transformer in 1885   (b) Stanley's transformer in 1886

Figure 1.1: Early stage of transformers

With massive AC power systems built worldwide, AC power transformers have become one of the most sophisticated technologies in electrical engineering. There are many standards and guidelines covering every aspect of transformers, from voltage level to rating, from connection to test. It results in high efficiency and reliable commercial transformers at relatively low cost ($40 to $100/kVA for distribution transformers [6]).

However, the weight and volume of transformers can become a challenge in volume-sensitive or weight-sensitive applications like transportation and offshore wind farms. For an oil-type distribution transformer (between 250kVA and 2000kVA), its power density is about $0.24 - 0.45$kVA/kg [7]. Delivering 100kW, which is close to the power of passenger cars, already requires using transformers that weigh several hundreds of kilograms. To clearly understand the relationship between the size of transformers and their properties, a single-phase AC transformer is considered under a sinusoidal waveform. Based on the area product method in transformers, the relations in (1.1) are derived [8]. Where A_c is the cross-sectional area of the magnetic core, A_w is

the cross-sectional area of windings. S is the apparent power of the transformer, U_p, I_p and N_p are primary side voltage, current and turn number, respectively. B_s is the saturation flux density of the core material, f is the operation frequency, J_{rms} is the current density in windings, and k_w is the window utilization factor limited by geometrical limits and insulation requirements.

$$A_c = \frac{U_p}{\sqrt{2}\pi B_s N_p f}$$
$$A_w = \frac{2N_p I_p}{k_w J_{rms}}$$
$$A_c A_w = \frac{\sqrt{2}S}{\pi k_w J_{rms} B_s f}$$

(1.1)

If B_s, J_{rms} and k_w are fixed by the material property, insulation and other requirements, the volume V_t and weight m_t of transformers are roughly scaled following (1.2). It implies that frequency f is the only way to reduce the volume and weight under given power if there is no breakthrough in relative materials, cooling, and other technologies.

$$V_t^{4/3} \text{ and } m_t^{4/3} \propto \frac{S}{f}$$

(1.2)

However, increasing the operation frequency of transformers requires other components in the same system to operate at the same frequency, or there is a frequency converter to adjust the frequency. The first way is impractical because the AC is set at 50 or 60 Hz based on characteristics of other devices, e.g. generators, motors and transmission lines. The second way is the only choice. In the early years, mercury arc rectifiers or vacuum tubes were used to achieve frequency change. During this time, applications like rectifiers, inverters, and isolated DC-DC converters emerged [9], [10]. However, due to the limitation of switch performance, the high power density of transformers at increased frequency cannot be exploited. With the development of power electronics, the semiconductor switches gradually push the switching frequency to higher values, and their power density is comparable with AC transformers [11], [12]. With the emergence of wide band-gap semiconductor devices, like SiC Mosfets, their higher withstand voltage and switching frequency show the potential to achieve higher efficiency and power density in high power applications [13].

1.2. MEDIUM FREQUENCY POWER TRANSFORMER APPLICATIONS

MEDIUM frequency power transformers usually work with power electronics. In isolated DC-DC converters, as shown in Figure 1.2, they achieve electrical isolation and voltage conversion. These converters are also the main part of solid-state transformers (SSTs) [6], [14], and power electronic transformers (PETs)[15], [16]. In this thesis, the voltage range from 1kV to 36kV is defined as medium voltage (MV), and the frequency range from 1kHz to 1MHz is defined as medium frequency (MF). The application of these converters involves the following categories:

1
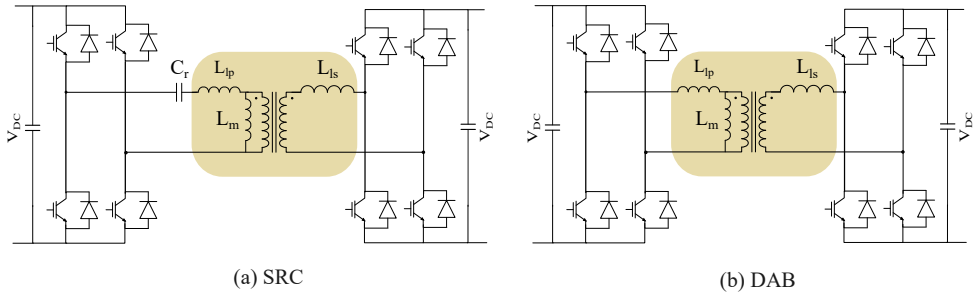
Figure 1.2: Topology of DAB and SRC isolated DC-DC converter for SST.

1. Distribution transformers

   This application is not sensitive to volume and weight, but other functional requirements give SST the possibility to replace AC transformers. With more distributed energy sources and energy storage systems integrated into the electric power system, the power system will face more frequent fluctuation and more complex control problems. It challenges the stability and safety of the power system. Therefore, besides the voltage regulation, new functions are needed at the interface between low and medium voltage, e.g. low voltage DC-link, reactive power compensation and active filtering, fault isolation and limitation. If you want to realize the additional functions with traditional AC transformers, many additional devices are needed. SSTs with MV MF transformers are a possible solution to achieve these functions [17].

2. Renewable Energy

   With the increasing share of renewable energy in the power system, efficiently delivering the energy from these large distributed wind farms and photovoltaic plants to the power system is essential. DC collection systems have gained much interest, especially in photovoltaic plants and off-shore wind farms. Photovoltaic plants generate DC voltage and traditionally use inverters and AC transformers to connect to the system. SSTs can replace the combination of inverters and transformers with higher power density and higher efficiency [18]. For off-shore wind farms, DC collection systems can be free from reactive power in cable and compensating devices. Besides, DC-DC converters can also eliminate the large AC transformers [19].

3. Transportation electrification

   The transport sector contributes the third largest CO2 emissions in 2022 [20]. Therefore, it is important to reduce emissions from this sector to achieve climate neutrality in the EU by 2050 [21]. Transportation electrification is a good solution to reduce emissions. In general, SSTs are a good option if there are both AC and DC loads or if they are sensitive to volume or weight. Aircraft perfectly matches these. More electric aircraft and all electric aircraft use electric power to supply part or all of their propulsion system [22], which requires a high-power converter.

At the same time, weight is critical to their design. Therefore, SSTs are a promising choice. Trains use a combination of step-down AC transformers and rectifiers to supply power to motors. SSTs can replace this combination and provide considerable volume and weight reduction [16], which can provide efficiency improvement at the system level. All-electric ships are also an opportunity to use SSTs because of the coexistence of different loads [23].

1.3. STATE OF ART AND CHALLENGE

WITH the fast development of high-power SSTs in the last 20 years, high-power MF transformers also attract much attention from academia and industry. Table 1.1 summarises several MF transformer prototypes.

The table shows that variables like power, frequency, and voltage can change from case to case based on different power electronic designs. To achieve high efficiency in practice, MV MF power transformers must be designed and optimized based on conditions of each case, leading to a large amount of design work. Therefore, suitable

Reference	[24]	[25]	[26]	[27]	[28]	[29]	[30]
Year	2022	2019	2013	2017	2017	2022	2020
Construction type	Shell	Shell	Shell	Shell	Shell	Core	Core
Power kW	166	25	166	240	100	1000	150
Frequency kHz	40	48	20	10	10	5	20
Voltage kV	7:7	7:0.4	1:0.4	0.9:0.6	0.75:0.75	5:2.5	0.9:0.9
Core material	ferrite	ferrite	nano	nano	ferrite	nano	nano
Conductor	Litz wire	Litz wire	Litz wire	Litz wire	Litz wire	Cu tube	Litz wire
Cooling	air	air	water	air	air	water & air	air
Insulation	solid	solid	solid	solid	solid	oil	solid
Gravimetric power density kW/kg	6.7	4	-	-	4.5	2.17	-
Volumetric power density kW/dm^3	5.4	7.4	32.7	-	-	1.59	50
Efficiency %	99.7	99.6	99.4	99.2	99.3	-	99.6

Table 1.1: Parameters of several MF transformer prototypes from the literature

1

transformer models and design optimization tools are necessary. Compared to AC transformers, there is no extensive experience in MV MF transformer designs. There are several challenges arising from operating conditions of SSTs.

- Eddy current modeling

  An accurate winding loss model considering eddy current is needed [31], [32]. The transformers work in the MF range, and the skin depth would be one to two orders of magnitude smaller than under AC, which limits the effective cross-section area of the conductors, while the higher power demands the input current to be hundreds of amperes. Besides, Litz wires are a widely used choice to suppress the eddy current and keep enough cross-section area. However, its complex structure makes it a challenge to build a model with reasonable accuracy and computational speed [33], [34].

- Equivalent circuit parameters determination

  MF transformers usually work with power electronics, and their circuit model is essential in converter analysis. Parameters generally include turn ratio, stray capacitance, leakage and magnetizing inductance. The leakage inductance plays an important role in topologies like DAB [35] and SRC [36]. The magnetizing inductance is often used for achieving soft switching (ZVS or ZCS) [37], [38]. Besides, stray capacitance can cause resonant, over-voltage, and EMI issues [39], [40]. All the circuit parameters need to be carefully controlled. Therefore, models that can accurately obtain these parameters are necessary.

- Insulation behaviour

  Insulation is an essential part of electrical equipment, which prevents undesired current flow. The studied transformers work under MV stress, where the insulation problem is inevitable. The insulation behaviour in MF transformers is also different from that in AC transformers. Firstly, the voltage is in the MF range. Additionally, its waveform is controlled by power electronics and is not sinusoidal. As shown in the literature, higher frequency and rectangular waveform are easier to lead to partial discharges and ageing, which presents a more challenging situation for insulation [41], [42]. At the same time, compared to the widely studied insulation behaviour under AC stress, the impact of voltage waveform and frequency on insulation degradation are not quantitatively concluded. This makes the insulation design challenging because the allowed E_{max} under the operation conditions is unknown.

- Thermal behaviour

  Thermal management is critical for devices, as high temperatures can change material properties and accelerate material degradation. Bad thermal condition threatens performance and longevity of transformers. Due to the excellent volume reduction, MF transformers have worse heat dissipation conditions [43], [44]. From (1.1), it is assumed that cooling surface area is approximately proportional to $f^{-1/2}$. Suppose MF and AC transformers with the same rate are

regarded as solid blocks with the same heat source and heat transfer coefficients on the surface. In that case, the temperature difference between environment and surface is proportional to $f^{1/2}$. If an MF transformer works at 5kHz, the temperature difference on the surface can be 10 times that for an AC transformer. Therefore, thermal stability in MF transformers is an important issue and needs reasonable designs.

- Optimization procedures

  Building models is to obtain an optimization procedure for MF transformers [28], [30]. MF transformer design optimization is to achieve the best design parameters based on certain objectives. In MF transformer design, the objective can be varied, and many factors can be part of it, like efficiency, volumetric power density, gravimetric power density and cost [45]. It results in a multi-objective optimization problem. Additionally, various methods exist to solve multi-objective optimization problems, such as brute-force [28], gradient descent [46], particle swarm optimization [47], and genetic algorithm [48]. Therefore, a fast, reliable optimization process is important.

1.4. OBJECTIVE AND RESEARCH QUESTIONS

As previously described, designing a high power MV MF transformer is a complex procedure. This thesis focuses on developing models in electromagnetic and thermal fields and an optimization process for MV MF transformers. The goal of this thesis is to:

> *"Provide validated tools to model and optimize the design of medium voltage high power medium frequency transformers."*

To achieve the goal of this thesis, several research questions are formulated.

1. What models are able to estimate the electric and thermal properties of MF transformers accurately and fast? (Chapter 2 - 3)

   - Review the existing models regarding magnetic, electric and thermal aspects.
   - Investigate the potential to enhance model performance by considering features from MF transformers.
   - Propose suitable models, validate and compare their performance with others across various aspects, like accuracy and computational speed.

2. How to model Litz wires and incorporate its results into the model for windings? (Chapter 4)

   - Summarize the existing Litz wire models.
   - Identify the critical points in modelling Litz wires and propose suitable models.
   - Verify the proposed models and compare them with existing models.
   - Explore the method to combine the Litz wire model and the windings model.

3. What are the considerations when designing an air-solid insulation for MV MF transformers? (Chapter 5)

   • Test and measure breakdown and partial discharge performances under MF stress on experimental samples.

   • Identify the major insulation and check the requirements in related standards.

   • Identify the worst-case scenario for insulation and develop a reasonable insulation design to address it.

4. How to optimize the design of MV MF transformers? (Chapter 6)

   • Identify the specifications and design variables.

   • Formulate a cost function as the criterion of optimization.

   • Build a design optimization algorithm based on developed models.

1.5. OUTLINE OF THE THESIS

THIS thesis aims to achieve the goal by addressing four research questions related to various aspects of modelling and design optimization for MV MF transformers. Figure 1.3 presents the thesis outline and connections between chapters.

Chapter 2 summarizes the multiphysical models for MF transformers. Besides, several refined methods have been proposed and validated. Chapter 3 introduces the proposed 2D round boundary element method. Its applications for different targets are given and validated. Chapter 4 introduces the existing and validated proposed models for Litz wires and the method to couple the model with the winding model. Chapter 5 presents the consideration of the air-solid insulation system design and the results of insulation tests. Chapter 6 introduces the optimization space, algorithm, and obtained results. Chapter 7 summarizes the conclusions and presents the perspective of future works.
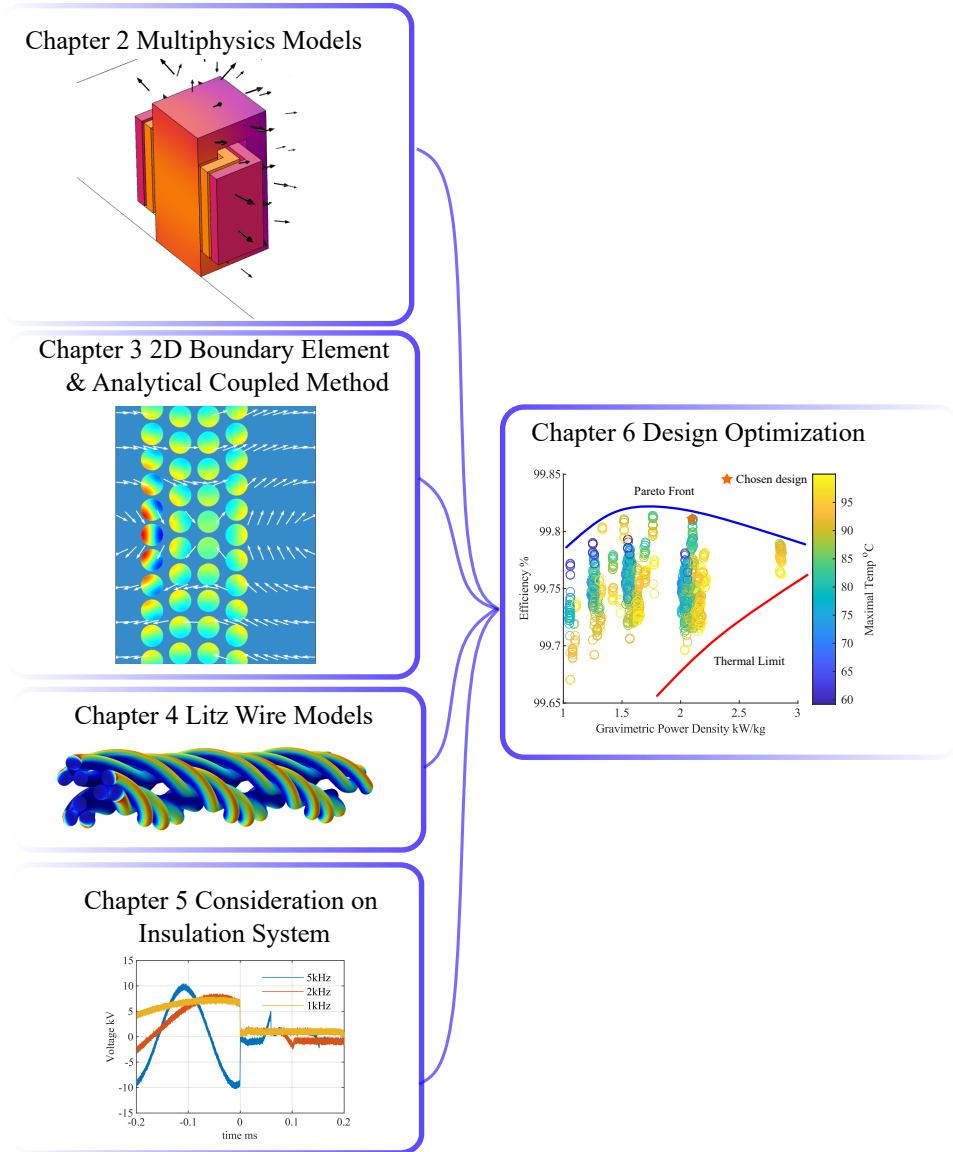
Figure 1.3: Outline of the thesis

2

MULTIPHYSICAL MODELS FOR MF TRANSFORMERS

The models for MF transformers involve multiple physics, and they are coupled together in different degrees. This chapter introduces the models related to magnetic, electric and thermal fields for MF transformers. The models involve magnetizing inductance, core losses, winding loss, parasitic parameters and thermal conditions. Several different existing models are summarized and compared. New winding loss models are proposed based on the analysis of magnetic field distribution for round conductors, which can take the interaction between conductors into account. The models used for magnetizing inductance, core loss, and thermal condition are chosen based on some comparison and analysis.

Parts of this chapter have been published in:

- 2-D Winding Losses Calculation for Round Conductor Coil, IEEE Transactions on Power Electronics, vol. 38, no. 4, pp. 5107–5117, Apr. 2023.
- Improved Winding Losses Calculation Based on Bessel Functions, IEEE Transactions on Magnetics, vol. 59, no. 6, pp. 1–10, Jun. 2023.

2.1. INTRODUCTION

T RANSFORMERS are passive devices that transfer electrical energy from one AC electrical circuit to another or multiple AC circuits. An ideal transformer should have a perfect magnetic core, i.e., infinite high permeability and lossless windings. An ideal two-winding transformer follows (2.1), where U_p, U_s are terminal voltages, N_p, N_s the number of turns, I_p, I_s are terminal currents, Φ is the magnetic flux. Therefore, there is no stored energy, and all the power from one side is transferred to another without loss.
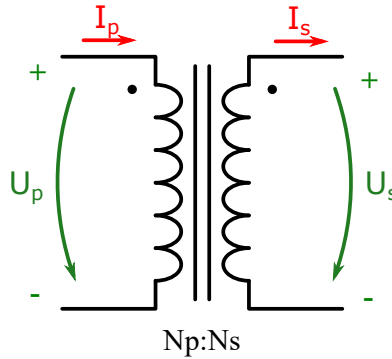
Figure 2.1: Ideal transformer

$$\frac{U_p}{N_p} = -\frac{d\Phi}{dt} = \frac{U_s}{N_s}$$

$$I_p N_p = I_s N_s$$

(2.1)

However, it is impossible to have the ideal transformer in practice. There is a complex coupled field as shown in Figure 2.2. Once an AC voltage is applied on one side of a transformer, an electric field distribution is built. Then, a current flows along the winding, generating ohmic heat, and a displacement current generates the dielectric loss in the insulation. The current generates a magnetic field, and most of the flux flows in the magnetic core and links with another winding. The flux induces a voltage in another winding and then delivers the energy to the other side. At the same time, due to the imperfection of the core, a small amount of current is needed to generate the flux and some energy is stored or dissipated. Some of the flux leaks from the shared path, forming an isolated loop. So, there is no perfect coupling. Besides, the magnetic field also induces voltage in conductors and generates eddy current loss. All the losses result in the rise of temperature. The increasing temperature feedbacks on the material properties. The electromagnetic and thermal fields also impact the mechanical field and, subsequently, the acoustic field.

The transformer model is not a new topic. However, due to the different excitation, several aspects need more attention when designing MF transformers. This chapter first introduces the model for the magnetic core, which involves the magnetizing inductance and core losses. The second part summarizes the winding model and introduces the proposed models for winding loss. This part also covers the winding loss and parasitic
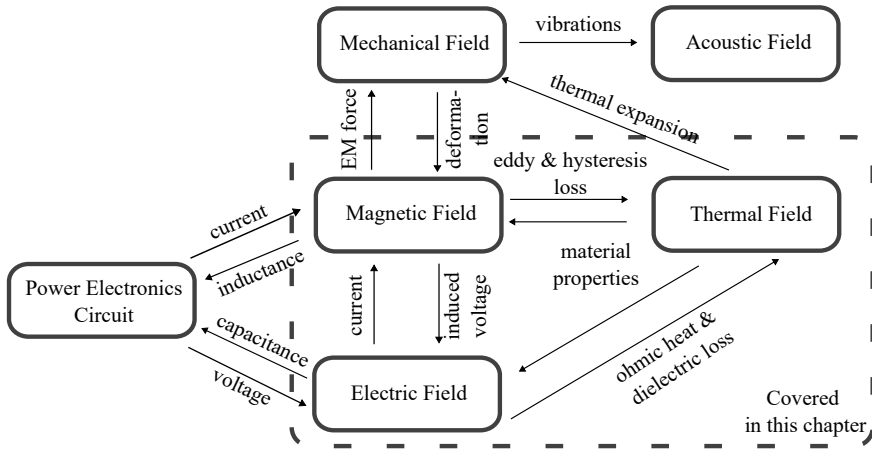
Figure 2.2: Coupled field in MF transformers

parameters, like leakage inductance and stray capacitance. The third part introduces models for the thermal condition of transformers.

2.2. MAGNETIC CORE

MAGNETIC materials have high permeability, which can increase flux density and guide the flux path. Magnetic cores composed of magnetic materials increase the inductance and magnetic coupling in transformers. For MF transformers, a suitable core material should satisfy several requirements [8]:

- High permeability μ.

- High saturation magnetic flux density B_s.

- High upper operating frequency f.

- High Curie temperature T_c.

- Low Coercivity H_c.

- Low loss P_c.

Based on material properties, ferrites, amorphous alloys, and nano-crystalline materials are often choices for MF transformers.

2.2.1. MAGNETIZING INDUCTANCE

Magnetizing inductance relates to the mutual flux, which generally represents the flux inside the magnetic core. It characterizes the relation between the nonzero net magneto-motive force (MMF) and the mutual flux, which is important for estimating the core losses and the saturation current. The magnetizing current can also be used for the converter operation, typically for achieving ZVS [38].

Magnetizing inductance L_m can be estimated by many methods [8], like FEM, reluctance method, and analytical method [49]. The reluctance method determines the inductance based on magnetic circuit theory as given in (2.2). Reluctance $\mathscr{R}$ describes the relation between the flux and the MMF in a given medium, which is analogous to the resistance in electric circuits. Figure 2.3 shows the magnetic flux in a gapped core, the blue arrow is the flux in the core, and the red arrow is the flux in the air.

$$L_m = \frac{N_p^2}{\mathscr{R}} \tag{2.2}$$
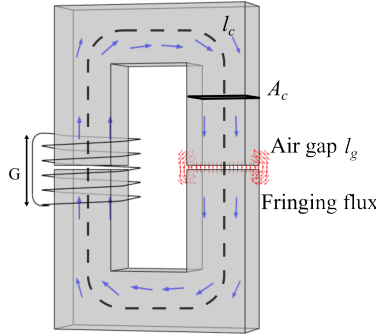
Figure 2.3: Magnetic flux path in a gapped core.

A basic reluctance calculation for a gapped core is listed in (2.3) [8]. $\mathscr{R}_c$ is the reluctance of the core, $\mathscr{R}_g$ is the reluctance of the possible air gaps, $\mathscr{R}_f$ is the reluctance of the fringing flux when there are air gaps. l_c is effective magnetic path length, A_c is effective magnetic cross section, l_g is air gap path length, a_c and b_c are the two side lengths of the rectangular cross-section.

$$\begin{aligned}
\mathscr{R}_c &= \frac{l_c}{\mu_c A_c} \\
\mathscr{R}_g &= \frac{l_g}{\mu_0 A_c} \\
\mathscr{R}_f &= \frac{1}{\mu_0 (a_c + b_c + 2l_g)} \\
\mathscr{R} &= \mathscr{R}_c + \frac{\mathscr{R}_g \mathscr{R}_f}{\mathscr{R}_g + \mathscr{R}_f}
\end{aligned} \tag{2.3}$$

In [50], a fringing factor is provided, and the reluctance can also be calculated with (2.4), where G is the winding length.

$$\begin{aligned}
F_f &= 1 + \frac{l_g}{\sqrt{A_c}} \ln\left(\frac{2G}{l_g}\right) \\
\mathscr{R} &= \frac{1}{F_f}(\mathscr{R}_g + \mathscr{R}_c)
\end{aligned} \tag{2.4}$$

Figure 2.4 shows the inductance factor A_L calculated from 3D FEM and reluctance calculation for a core with various gaps. Inductance factor represents the specific inductance (with 1 turn) characteristic of a given magnetic core. Geometry and parameters are from the UU 93/152/30 N87 ferrite core. By comparing with 3D FEM, (2.4) and (2.3) have similar results considering the impact of the fringing flux. Besides, the differences between 3D FEM and the reluctance method can be considerable, even without an air gap. However, considering the about 20% tolerance in A_L shown in the datasheet [51] and the assembly error in manufacturing transformers, an accurate but complex method like 3D FEM is not necessary. Therefore, the reluctance method (2.4) is used for the design.
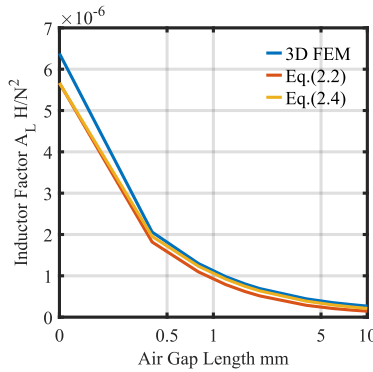
Figure 2.4: Calculated inductance factor with various air gaps for UU 93/152/30, which uses three methods, 3D FEM, equations (2.2) and (2.4).

2.2.2. CORE LOSS MODELS

Core loss is one of the most important losses in transformers, which is still not fully understood theoretically. It is a function of many conditions, like the magnetic material, geometry of the core, magnetic flux density $B(t)$ and operating temperature T, etc. According to the literature, the methods for core loss estimation can be categorized into three kinds: loss separation method, Steinmetz equation based method, and data-driven method.

1. Loss separation method [52]–[55]

The loss separation method is based on the sources of the core losses, which consists of three parts, i.e., the hysteresis loss P_h, the eddy current loss P_e and the excess loss P_{ex} [52]. This method is used in both time domain [53], [54] and frequency domain [55], [56]. In the frequency domain, the relation between core losses and frequency, flux density amplitude is given in (2.5), where k_e, k_h, k_{ex} and β are relative coefficients.

$$P_c = P_h + P_e + P_{ex} = k_h f B_m^\beta + k_e (f B_m)^2 + k_{ex} (f B_m)^{1.5} \tag{2.5}$$

The hysteresis loss is the energy used to align and rotate magnetic moments of the core material. The area enclosed by the hysteresis loop is the hysteresis loss in one

cycle, as Figure 2.5 shows, and the larger the area is, the more hysteresis loss there is. In the frequency domain, the loss is calculated based on k_h and β, which is not obtainable for the non-sinusoidal waveform. In the time domain, there are several theory-based hysteresis models, like Vector play model [57], Jiles-Atherton model [58], [59], and Preisach model [60]. The Jiles-Atherton model is based on a macroscopic energy calculation, and the Preisach model describes the time and space distribution of domain-wall motion. However, these models need more information and are not very practical.
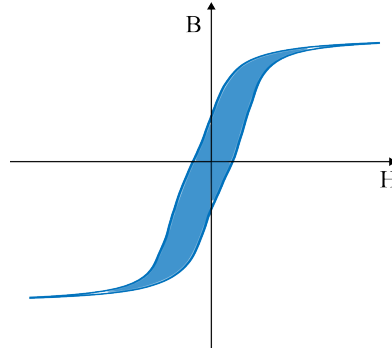
Figure 2.5: Hysteresis loop.

The eddy current loss is the loss caused by the induced eddy current in the conductive core. When there is a magnetic field change, a voltage is induced in the core, and the eddy current occurs. Magnetic materials with high conductivity require more attention to eddy current problems. Skin depths for typical materials at different frequencies are listed in Table 2.1, which explains the use of laminations.

Core materials	Relative permeability	Conductivity S/m	Skin depth at Frequencies		
			1kHz	10kHz	100kHz
Mn-Zn(N87)	2.2E3	0.1	1.07m	339mm	107mm
Amorphous alloy (2605SA1)	3E4	7.7E5	105μm	33μm	10μm
Nano-crystalline (VITROPERM 500F)	2E4	8.7E5	120μm	38μm	12μm

Table 2.1: Skin depth for typical core materials at varied frequency

A round cross-section core with radius a is under a sinusoidal magnetic field H_{ext}, the average magnetic field $\bar{H}$ considering the eddy current is given in (2.6). Figure 2.6 show the complex permeability $\mu_r = \mu_r' - j\mu_r''$ versus penetration ratio a/δ, where δ is the skin depth. It represents the frequency response of eddy current. When the a/δ reaches 0.64, the imaginary part of normalized permeability is 0.1, which means about 10% of magnetic energy is lost due to eddy current [8]. Therefore, the cross-section of

cores should not be comparable with skin depth.

$$\bar{H} = \frac{2J_1(\kappa a)}{\kappa a J_0(\kappa a)} H_{\text{ext}}$$
$$\kappa = \sqrt{-j\omega\mu\sigma_c}$$

(2.6)

2
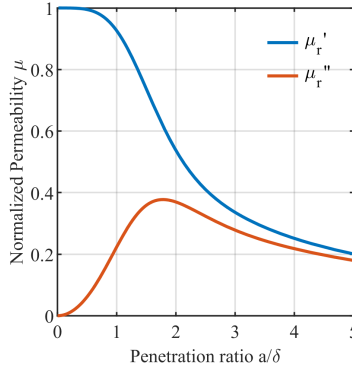
Figure 2.6: Equivalent complex permeability with eddy current

There are two main hypothesis for excess loss. One explanation is the excess loss represents all other loss mechanisms, like the motion of randomly distributed domain walls [52]. The other is it is an eddy current loss due to nonlinear electromagnetic field diffusion [61].

Whether the estimation is done in the frequency domain or time domain, the information about hysteresis and excess loss is not easy to obtain. Therefore, the loss separation method is not very suited for the non-sinusoidal situation.

2. Steinmetz equation based method [62]–[66]

Steinmetz equation (SE) (2.7) provides a method to calculate the total time-averaged core losses density under sinusoidal waveforms [62], where k_{SE}, α_{SE} and β_{SE} are the coefficients of SE. Due to its simplicity and accumulated data, it is widely used in the design of magnetic power devices like transformers, inductors, and electric machines.

$$P_c = k_{SE} f^{\alpha_{SE}} B_m^{\beta_{SE}}$$

(2.7)

Due to the advancements in power electronics, core loss estimation under arbitrary waveforms is required. One way is to deal with waveform, like the method introduced in [8]. The periodic non-sinusoidal magnetic flux density is expanded into a Fourier series. Then the loss is the summation of each term, as given in (2.8), where n is the harmonic order.

$$P_c = \sum_{n=1}^{\infty} k_{SE\_n}(nf)^{\alpha_{SE\_n}} B_{m\_n}^{\beta_{SE\_n}}$$

(2.8)

Another way is to modify the SE. The MSE [63] replaces the frequency term by dB/dt based on the fact that core losses caused by magnetic domain wall motions depend on the rate of change of magnetic flux. The GSE [64] improves MSE and eliminates the mismatch between the SE and the MSE for sinusoidal waveforms. The IGSE [65] further improves the approach by considering minor hysteresis loops. The equations are shown in (2.9), where ΔB is peak-to-peak flux density, coefficients k_{SE}, α_{SE} and β_{SE} are the same coefficients as used in the SE (2.7).

$$P_{c\_igse} = \frac{1}{T_s} \int_0^{T_s} k_i \left| \frac{dB}{dt} \right|^{\alpha_{SE}} (\Delta B)^{\beta_{SE} - \alpha_{SE}} dt$$

$$k_i = \frac{k}{(2\pi)^{\alpha_{SE}-1} \int_0^{2\pi} |\cos\theta|^{\alpha_{SE}} 2^{\beta_{SE} - \alpha_{SE}} d\theta} \tag{2.9}$$

The i2GSE [66] adds a term representing magnetic relaxation to the IGSE. The equation of i2GSE is given in (2.10), where τ is the relaxation time of materials, coefficients k_r, α_r, β_r and q_r are coefficients related to relaxation process and are determined empirically.

$$P_{c\_i2gse} = P_{c\_igse} + \sum_{l=1}^{n} Q_{rl} P_{rl}$$

$$P_{rl} = \frac{1}{T_s} k_r \left| \frac{dB(t\_)}{dt} \right|^{\alpha_r} (\Delta B)^{\beta_r} \left(1 - e^{-\frac{t_1}{\tau}} \right)$$

$$Q_{rl} = e^{-q_r \left| \frac{dB(t_+)/dt}{dB(t\_)/dt} \right|} \tag{2.10}$$

IGSE does not require any extra parameters and can cope with any flux waveform. Therefore, it is widely applied [24], [28]. However, all coefficients are only valid in a limited range set by parameters like flux amplitude B, frequency f, and temperature T. The limited coefficient effective range is a general problem of the Steinmetz approach.

3. Data-driven method

Recent breakthroughs in data-driven approaches, particularly neural networks and other machine learning methods, have demonstrated remarkable efficiency in addressing complex non-linear problems involving multi-variable classification and regression [67], [68]. In practice, core loss is a typical non-linear problem and is determined by many conditions, which suits the data-driven approaches. Compared to a few parameters used in SE, a data-driven model can have thousands of parameters, which can capture the information behind core losses. Three different approaches, as shown in Figure 2.7, for modelling core loss with neural networks are studied in [69], and their results show the absolute average of relative errors are less than 3%.

Data-driven models are very powerful and convenient for the user. However, if there is no data from the desired operation conditions, the accuracy of the results is suspicious. Therefore, a database with good data quality is critical for developing good data-driven
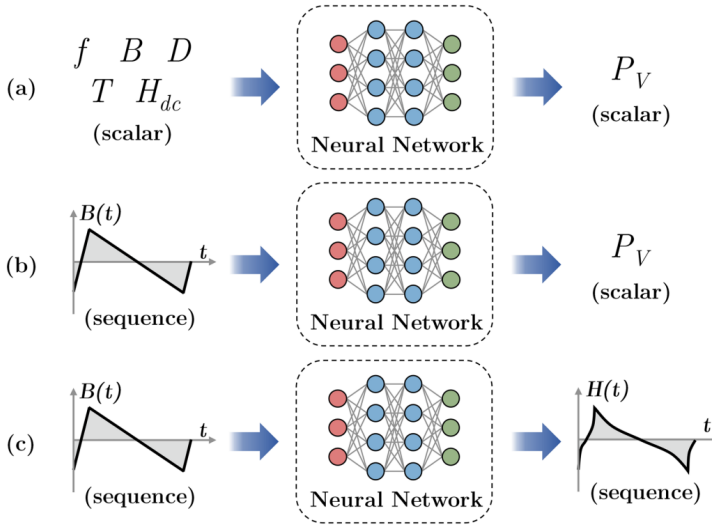
Figure 2.7: Three approaches for modelling magnetic material properties using neural networks: (a) Scalar values to scalar values, (b) Time series signals to scalar values, (c) Time series signals to time series signals [69].

models. An AI-based platform and an open-source core loss database with 10 materials and a total of 575009 test data are provided [69]–[71]. It can be a convenient tool for magnetic component designers and researchers.

2.2.3. APPLICATION IN A THREE-LEVEL VOLTAGE WAVEFORM

The targeted MF transformers are used in isolated DC-DC converters. DAB and SRC are the most common topologies, and both of them follow the three-level voltage waveform. Corresponding flux density waveform is given in (2.11) and is shown in Figure 2.8. D is the duty-cycle in the range 0-1, T_s is the period, B_m is the amplitude of flux density.

$$
B(t) = \begin{cases}
\dfrac{4B_m}{DT_s}t - B_m & 0 < t < DT_s/2 \\
B_m & DT_s/2 < t < T_s/2 \\
\left(1 + \dfrac{2}{D}\right)B_m - \dfrac{4B_m}{DT}t & T_s/2 < t < (1+D)T_s/2 \\
-B_m & (1+D)T_s/2 < t < T_s
\end{cases}
\tag{2.11}
$$

Therefore, the methods introduced in 2.2.2 can be simplified for a three-level voltage waveform. The Fourier expansion of the flux density is given in (2.12), which can be used in the summation of the SE of each harmonic.

$$
\begin{aligned}
A_n &= \frac{4B_m(\cos(\pi D n) - 1)}{Dn^2\pi^2}, & n = 1,3,5... \\
B_n &= \frac{4B_m\sin(\pi D n)}{Dn^2\pi^2}, & n = 1,3,5...
\end{aligned}
\tag{2.12}
$$
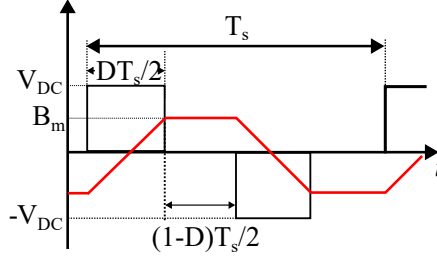
Figure 2.8: Typical three-level converter voltage waveform and corresponding flux waveform

The IGSE and i2GSE are also simplified based on the given waveform, as given in (2.13) and (2.14).

$$P_{c\_igse} = 2^{\alpha_{SE}+\beta_{SE}} k_i f^{\alpha_{SE}} B_m^{\beta_{SE}} D^{1-\alpha_{SE}}$$

$$\approx \left(\frac{2}{\pi D}\right)^{\alpha_{SE}-1} \frac{4}{0.2761 + \dfrac{1.7061}{\alpha_{SE}+1.354}} k_{SE} f^{\alpha_{SE}} B_m^{\beta_{SE}} \quad (2.13)$$

$$P_{rl} = 2^{2\alpha_r+\beta_r+1} k_r f^{\alpha_r+1} D^{-\alpha_r} (B_m)^{\alpha_r+\beta_r} (1 - e^{\frac{D-1}{2\tau f}})$$

$$Q_{rl} = \begin{cases} e^{-q_r} & D = 1 \\ 0 & \text{else} \end{cases} \quad (2.14)$$

Figure 2.9 compares the measurement losses from [72] with SE, harmonic SE, IGSE, i2GSE and AI [69]. The harmonic SE method uses the first three harmonic magnitudes. The measurements are done on the N87 toroid core under trapezoidal voltage with $D = 0.6$ and 1, AC flux magnitude 0.18T and 50 °C. The SE coefficients are obtained from the TDK datasheet, which is fitted for 50kHz, 0.2T and 50 °C sinusoidal waveform. AI have good results in both cases. Among SE methods, results from i2GSE are better than those of other methods when $D = 0.6$. The i2GSE is the same as IGSE when $D = 1$, and results are also close to measurements. With increasing frequency, the relative error of i2GSE gradually increases, which can be attributed to the limited validation range of relaxation-related coefficients. Harmonic SE is closer to IGSE when $D = 0.6$. However, its error is quite large when $D = 1$. The IGSE is only better than SE when $D = 0.6$, but it performs more stably in two cases. Because the minimal frequency of the database is 50kHz in [69], and the estimation for lower frequency is based on extrapolation, the results are questionable. Besides, it is hard to obtain valid parameters for i2GSE in different materials and in a wide frequency and flux density range. Therefore, the IGSE is still chosen in this thesis.

2.3. WINDINGS

IN spite of the magnetic core, windings are the other essential part of magnetic components. They consist of single or multi-turn of wires wound around the magnetic core and connect to the external electric circuits. Their arrangements decide
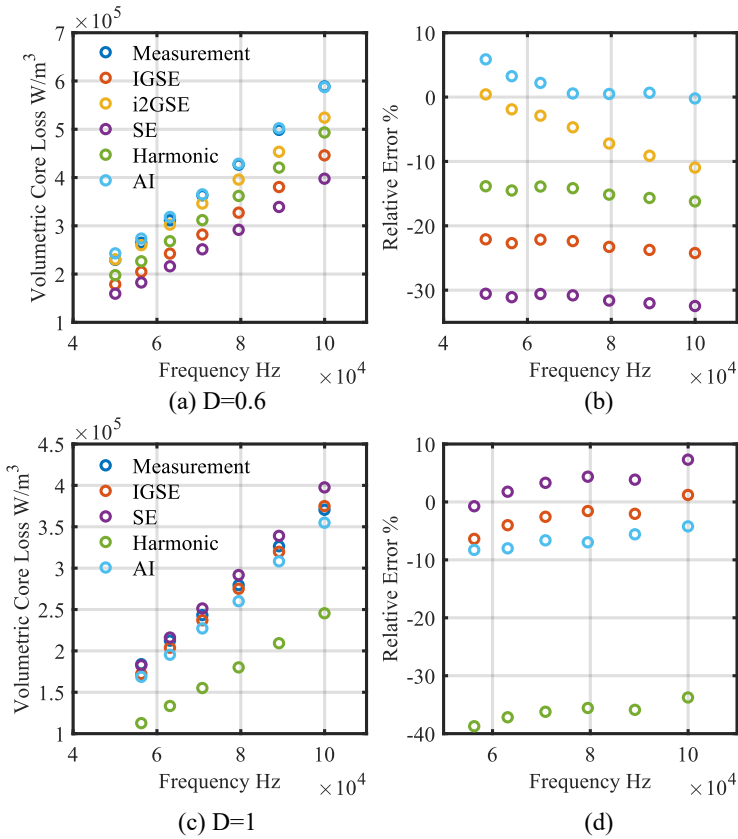
Figure 2.9: Comparison of core losses between measurement and various methods under various frequencies, (a) volumetric core loss with $D = 0.6$, (b) relative error with $D = 0.6$, (c) volumetric core loss with $D = 1$, (d) relative error with $D = 1$.

the winding losses and parasitic parameters, like leakage inductance and stray capacitance. For MF frequency applications, several different conductors and winding arrangements are developed to achieve different purposes [73], [74].

2.3.1. CLASSIC WINDING LOSS MODELS

Winding losses are essential losses in magnetic components. Due to eddy current, winding losses winding losses increase dramatically with increasing frequency. As mentioned in 1.3, high power rates require a relatively high cross-section area for conductors. Therefore, the windings used in MF transformers need to be carefully analysed for eddy current effects. In general, the loss calculation methods include analytical, empirical and numerical methods. Because conductors are normally linear materials, the winding loss is solved under the frequency domain. Finite element methods (FEM) is a versatile method that can calculate the winding loss under arbitrary winding arrangements. However, to guarantee the accuracy of computation, the
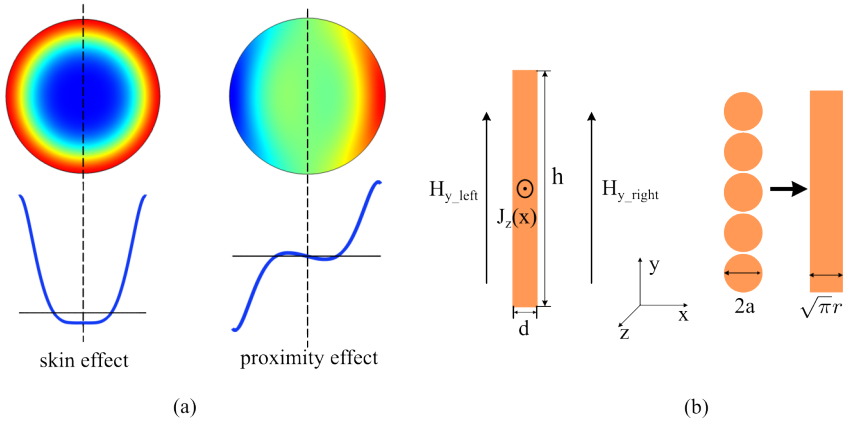
Figure 2.10: Current distribution under skin and proximity effect (a), illustration for Dowell's method (b).

smallest size of an element inside conductors should be smaller than one-third of skin depth based on analysis in [75].   It requires a large number of elements and computational resources. In contrast, analytical and empirical methods are time-saving and are widely adopted in winding loss calculation.

1. Analytical methods [76], [77]

The analytical methods are generally based on Dowell's model and Ferreira's formula, which are briefly introduced here. One important idea is the orthogonality between the skin and proximity effect, which enables the independent calculation for loss from each effect. It is shown in (2.15), where I is the current, H is the external magnetic field caused by external sources, R_s is the resistance considering skin effect, G_p is the proximity effect coefficient. It is necessary to note that the values in the frequency domain represent peak values without specific notation. The total eddy current loss can simply sum them up.

$$P_s = \frac{1}{2} R_s I^2$$
$$P_p = \frac{1}{2} G_p H^2$$
(2.15)

The simple explanation is, as shown in Figure 2.10 (a), the current distribution of the skin effect is an even function, and the current distribution of the proximity effect is an odd function. Therefore, the integral of the production of two currents is zero.

• Dowell's model [76]

Dowell's model solves one-dimensional Maxwell equations for windings, which is based on the following assumption:

• Foil conductors fully fill the whole window height assuring a one-dimensional field along the window.

- The magnetic core is ideal, i.e., it has an infinite permeability, thus considering only the field strength in the window.

Joule loss per unit length in a conduction layer is given in (2.16), where $\Delta = d/\delta$ represents the penetration ratio, d is the layer thickness, h_w is the layer height, σ_c is the conductivity of the layer, H is the magnetic field on the two sides of the layer, as shown in Figure 2.10 (b).

$$P_w = \frac{h_w}{4\delta\sigma_c}\left((H_{\text{right}} - H_{\text{left}})^2 \frac{\sinh(2\Delta) + \sin(2\Delta)}{\cosh(2\Delta) - \cos(2\Delta)}\right.$$
$$\left. + 2H_{\text{right}}H_{\text{left}}\frac{\sinh(\Delta) - \sin(\Delta)}{\cosh(\Delta) + \cos(\Delta)}\right) \quad (2.16)$$

Combining the orthogonality, the R_s and G_p of Dowell's model can be rewritten as (2.17).

$$R_{s\_D} = \frac{1}{2h_w\delta\sigma_c}\frac{\sinh(\Delta) + \sin(\Delta)}{\cosh(\Delta) - \cos(\Delta)}$$
$$G_{p\_D} = \frac{2h_w}{\delta\sigma_c}\frac{\sinh(\Delta) - \sin(\Delta)}{\cosh(\Delta) + \cos(\Delta)} \quad (2.17)$$

Therefore, the xth layer in a winding, the magnetic field strength H is $(2x-1)I/2h_w$, the losses is given in (2.18).

$$P_{x^{th}} = R_{dc}\frac{I^2\Delta}{4}\left(\frac{\sinh(\Delta) + \sin(\Delta)}{\cosh(\Delta) - \cos(\Delta)} + (2x-1)^2\frac{\sinh(\Delta) - \sin(\Delta)}{\cosh(\Delta) + \cos(\Delta)}\right) \quad (2.18)$$

Different shape conductors are transformed into foil conductors with equal DC conductance with the help of the porosity factor. For example, a layer composed of n_t round conductors with radius a is replaced by a foil with thickness $d = \sqrt{\pi}a$, as shown in Figure 2.10 (b). The foil has a conductivity σ_c', which is equal to $\eta_p\sigma_c$. η_p is known as the porosity factor, and its value is $\eta_p = n_t d/h_w$.

Dowell's model is accurate for compacted windings. However, if the field along another direction is not ignorable, the problem becomes a two-dimensional problem, and Dowell's method is no longer suitable.

- Ferreira's formula [77]

The formulas give the analytical solution of skin effect and proximity effect for round conductors, as shown in (2.19). $\Re$ is real part, and $\Im$ is imaginary part.

$$R_{s\_F} = \frac{1}{\pi a^2\sigma_c}\Re\left(\frac{J_0(\kappa a)}{J_0(\kappa a) + J_2(\kappa a)}\right)$$
$$G_{p\_F} = -2\pi\mu a^2\omega\Im\left(\frac{J_2(\kappa a)}{J_0(\kappa a)}\right) \quad (2.19)$$

However, the proximity effect formulus is derived under a uniform external field, which does not consider the interaction of eddy current. G_{p_F} is overestimated when the interaction is considerable, especially for a compact winding with considerable

eddy current. Based on this feature, Mühlethaler [78] proposed a method to calculate the winding losses under a relatively low penetration ratio. The method calculates the static magnetic field on each conductor and obtains the losses based on Ferreira's formula. Researchers try to reduce the error by introducing new factors [79]. However, it does not totally solve the interaction between eddy currents.

2. Empirical methods

Empirical equations are also used in winding loss estimation. Their validation ranges depend on the scenario under which data are collected. They can be fast and accurate for specific cases. Several empirical equations are proposed with the help of FEM. Nan proposed a semi-empirical equation to improve proximity effect estimation [80], [81]. Dimitrakakis [82] proposed a semi-empirical model for winding with arbitrary conductors distribution. Bahmani [83] proposed a pseudo-empirical model for foil and round winding losses. Ahmed provided an air-core winding loss calculation model based on fitted field strength [84].

2.3.2. PROPOSED WINDING LOSS MODELS

The round conductors are often used in windings, and there is still some problem in using Ferreira's formula in general situations. Based on the analysis of round conductors under an external magnetic field, new methods are proposed.

- Revised 1D equations

A revised 1D equation is derived for layers composed of round conductors, as shown in Figure 2.11 (a). First, the proximity effect coefficient G_p in the 1D situation is analyzed. In Dowell's model, the magnetic field H_{ext} is calculated by (2.20), where $\mathscr{F}$ is magneto-motive force. The value is not true for round conductors.

$$H_{\text{ext}} = \frac{\mathscr{F}_r + \mathscr{F}_l}{2h_w} \tag{2.20}$$

According to [85], for a round conductor under a H_{ext} is along the y direction like Figure 2.11 (a), the magnetic field strength outside the conductor can be easily derived as (2.21).

$$H_y = H_{\text{ext}} - \frac{a^2 H_{\text{ext\_y}} J_2(\kappa a)}{J_0(\kappa a)} \frac{x^2 - y^2}{(x^2 + y^2)^2}$$
$$H_x = \frac{a^2 H_{\text{ext}} J_2(\kappa a)}{J_0(\kappa a)} \frac{2xy}{(x^2 + y^2)^2} \tag{2.21}$$

It can be seen from (2.21) that the induced eddy current influences the magnetic field strength near the conductors, and only when the point is infinite far from the conductor the field strength can be regarded as H_{ext}. Therefore, it is unreasonable to obtain H_{ext} from the same method used in Dowell's method. Because the MMFs are constant values at each side of a conductor layer, they cannot be regarded as being infinitely far.

Next, the correct relation between MMFs and H_{ext} needs to be found. Under the 1D model's assumption, conductors in a layer can be regarded as infinite repeated cells, like
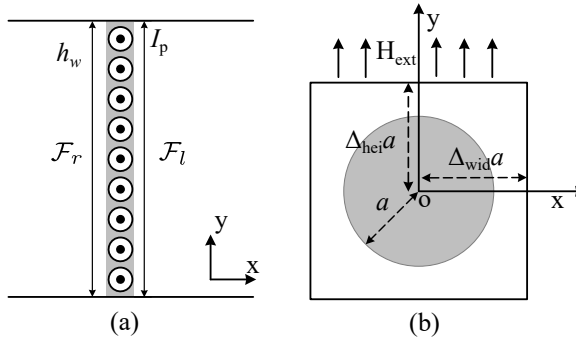
Figure 2.11: 1D winding model composed of round conductors (a), a conductor cell under a uniform external field (b).

Figure 2.11 (b). Because the y-axis is the even symmetry axis, the relation between MMF and H_{ext} can be obtained by integrating H_y over one of the vertical edges of the cell, which is equal to the MMF.

$$
\begin{aligned}
\frac{MMF}{n} &= 2a\Delta_{hei}H_{ave} & = \int_{-\Delta_{hei}a}^{\Delta_{hei}a} H_y \mathrm{d}y \\
&= 2a\Delta_{hei}H_{ext}\left(1 - \frac{J_2(\kappa a)}{J_0(\kappa a)(\Delta_{hei}^2 + \Delta_{wid}^2)}\right)
\end{aligned}
\tag{2.22}
$$

The Δ_{hei} can be easily determined by the core window height l and the number of turns n in this layer. The Δ_{wid} is just set as 1 to make sure the distorted magnetic field is mainly caused by the eddy current in the nearest conductor. To mark the different physical meanings of field strength from (2.20), H_{ave} is obtained from (2.20) instead of H_{ext}. According to the relation between H_{ave} and H_{ext}, proximity effect coefficient in 1D becomes (2.23).

$$
G_{p\_rF} = -2\pi\mu a^2\omega\Im\left(\frac{J_2(\kappa a)}{J_0(\kappa a) - \dfrac{J_2(\kappa a)}{1 + \Delta_{hei}^2}}\right)
\tag{2.23}
$$

Figure 2.12 shows the relative error of different equations of the second layer compared to 2D FEM with two different layer settings. Revised G_p improves the accuracy significantly compared to the original one. From (a), the revised formula would overestimate the losses by 10% to 20% when a/δ is higher than 1.5. Because it does not fully solve the interaction between different conductors' eddy currents, which has more impact when Δ_{hei} is small. The Dowell model would overestimate the losses when Δ_{hei} is large, i.e., sparse windings.

The revised proximity effect coefficient (2.23) considers the mismatch between the external magnetic field and the magnetic field parallel to the layers and significantly improves the accuracy compared to the original one.

2
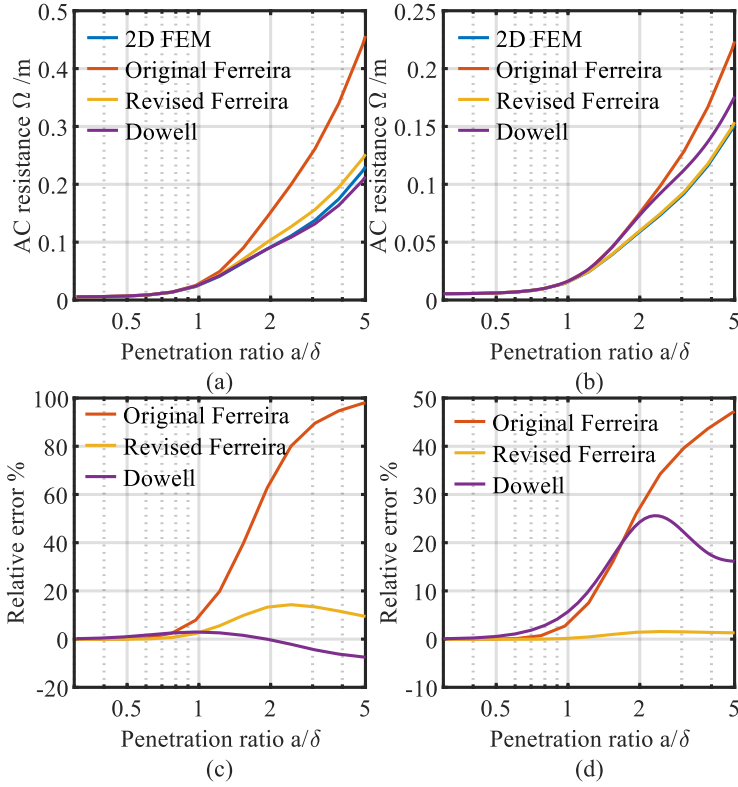
Figure 2.12: AC resistance per unit length and relative difference between different equations and 2D FEM with varying layouts of layer, (a) and (c) the 2nd layer with $\Delta_{hei} = \Delta_{wid} = 1.1$; (b) and (d) the 2nd layer with $\Delta_{hei} = \Delta_{wid} = 1.6$.

Based on the FEM assistant method, the revised 1D proximity effect coefficient can be further improved. A geometric factor λ_p is introduced and $\lambda \Delta_{hei}^2$ replaces the $1 + \Delta_{hei}^2$ in (2.23). The geometric factor λ is obtained by fitting 2D FEM data. The data involve 25 sets of 2D rectangular arrangements, which cover cases with $\Delta_{wid}, \Delta_{hei} = 1.1 - 2.1$, and penetration ratio $a/\delta = 0.2 - 20$, which could cover most cases in 1D layer. A one-parameter exponential growth function with the variable $k = \Delta_{hei}/\Delta_{wid}$ is chosen to fit the result. The result is shown in (2.24).

$$G_{p\_rF} = -2\pi\mu a^2 \omega \Im \left(\frac{J_2(\kappa a)}{J_0(\kappa a) - J_2(\kappa a)/(\lambda \Delta_{hei}^2)} \right)$$

$$\lambda_p = 1.2695 + 5.46 \times 10^{-5} e^{k/0.15}$$

(2.24)

Figure 2.13 shows the relative error of proximity effect coefficient G_p of different methods in rectangular and hexagonal arrangements. The fitted geometric factor improves the accuracy compared to the G_p in (2.23). Compared to the results for rectangular arrangement, the fitted proximity effect coefficient has relatively larger

errors. It overestimates the losses by around 5% when the penetration ratio is 1. However, compared to other methods, it still performs more stable.
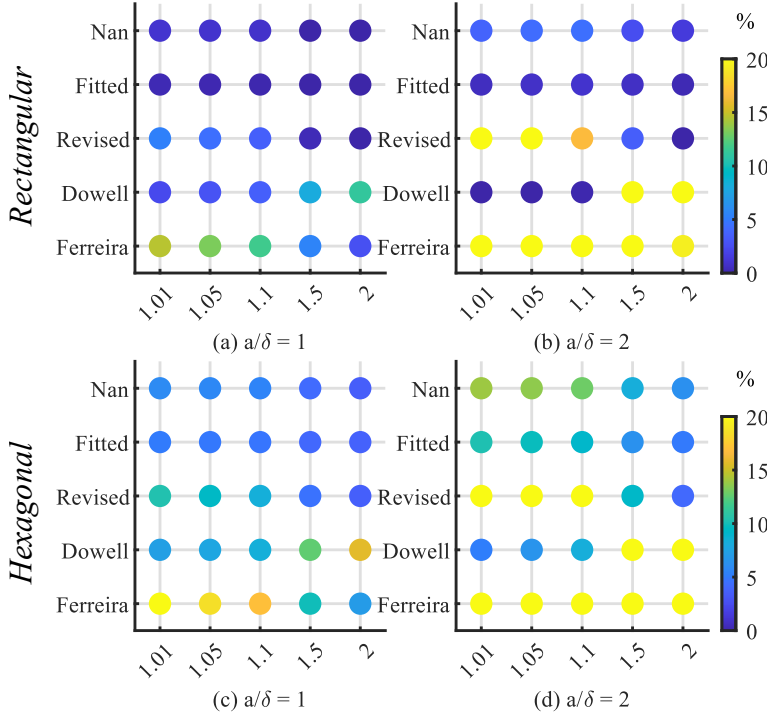
Figure 2.13: Relative error% of proximity effect coefficients from different methods compared to FEM in the rectangular (a) (b) and hexagonal arrangements (c) (d). The penetration ratios a/δ used are 1 (a) (c) and 2 (b) (d), respectively. For a value larger than 20%, the colour is the same as the 20%.

Besides, the losses inside the layer of round conductors are also different from those of an isolated round conductor. As illustrated in Figure 2.14, through analogy to AC resistance in isolated 2D squre conductor R_{s_squre} and Dowell's model R_{s_D}, a complementary term R_{comp} is added to R_{s_F} with another geometric factor λ_s as (2.26).

$$R_{s\_squre} = R_{dc} \left(\frac{1}{2} + \frac{\Delta}{4} \frac{\sinh(\Delta) + \sin(\Delta)}{\cosh(\Delta) - \cos(\Delta)} \right)$$

$$R_{s\_D} = R_{dc} \left(\frac{\Delta}{2} \frac{\sinh(\Delta) + \sin(\Delta)}{\cosh(\Delta) - \cos(\Delta)} \right) \tag{2.25}$$

$$R_{s\_F} = R_{dc} \left(\frac{1}{2} + \frac{1}{2} \Re \left(\frac{J_0(\kappa a) - J_2(\kappa a)}{J_0(\kappa a) + J_2(\kappa a)} \right) \right)$$

$$R_{comp} = R_{dc} \left(\frac{1}{2} \Re \left(\frac{J_0(\kappa a) - J_2(\kappa a)}{J_0(\kappa a) + J_2(\kappa a)} \right) - \frac{1}{2} \right)$$
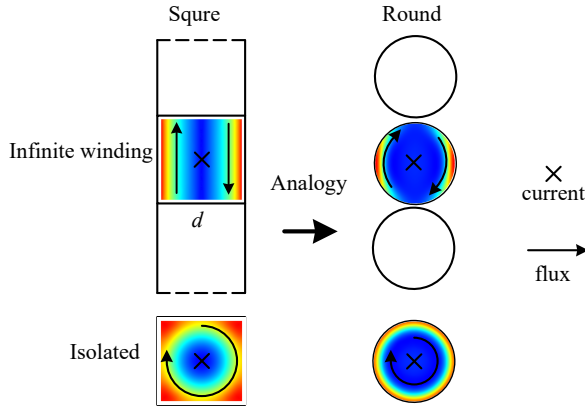
Figure 2.14: Analogy between square conductors and round conductors and colour represents current density

$$R_{ac} = R_{s\_F} + \lambda_s R_{comp} \quad \lambda_s = \frac{0.9223}{\Delta_{hei}^{3.424}} \tag{2.26}$$

Figure 2.15 shows the relative difference between several different situations. (a) and (b) shows R_{s_F} in (2.19) is accurate for an isolated conductor but not accurate for a conductor in a layer. It is obvious that the smaller Δ_{hei}, the higher the difference there is. (c) and (d) compare the fitted equation (2.26), Dowell's model R_{s_D} in (2.17) and FEM results for a layer composed of round conductor, when the penetration ratio is 2. In general, the fitted equation shows a minor error compared to others. It gives a slightly larger error when turns are close because the geometric factor λ_s is used to take the eddy current into account, which is also related to frequency.

The revised 1D method proves the interaction between conductors is the major error source for Ferreira's formula. New equations for layers composed of round conductors are obtained based on revising the proximity effect factor G_p and FEM assistant fitting. The equations can suit most 1D situations.

- A 2D recursive method

In actual situations, the 1D models only can be applied to limited winding layouts. There are a large number of winding configurations that do not comply with the 1D assumption. For example, there could be air gaps in magnetic cores, or winding layers do not fill the entire core window. In such cases, the one-direction magnetic field assumption in the 1D model cannot be fulfilled. Therefore, a 2D recursive method is proposed based on the analysis in the preceding part and the method of image.

The equivalent external field is calculated for each conductor. Based on the preceding analysis, it is known that the eddy current impacts field strength in both directions. The changes due to an external field along the y-axis are given in (2.21), and the field distribution due to an external field along the x-axis is given in (2.27).
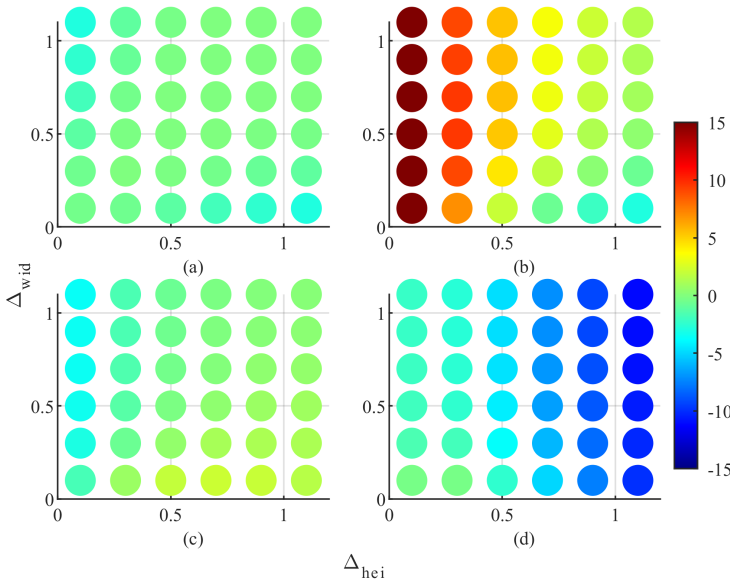
Figure 2.15: Relative difference% between (a) Ferreira's formula and FEM for an isolated conductor, (b) FEM for a winding layer and an isolated conductor, (c) fitted equation and FEM for a winding layer, and (d) Dowell's model and FEM for a winding layer, penetration ratio a/δ used is 2

$$H_y = \frac{a^2 H_{\text{ext\_x}} J_2(\kappa a)}{J_0(\kappa a)} \frac{2xy}{(x^2 + y^2)^2}$$
$$H_x = H_{\text{ext\_x}} + \frac{a^2 H_{\text{ext\_x}} J_2(\kappa a)}{J_0(\kappa a)} \frac{x^2 - y^2}{(x^2 + y^2)^2} \tag{2.27}$$

For each conductor, the field distribution along the cell edge approximates the combination of (2.21) and (2.27), when Δ_{hei} and Δ_{wid} are 1. Compared to calculating the detail of distribution, the average field strength on the cell edges is much easier to calculate, and their value can represent the distribution. The procedure to determine the equivalent uniform external fields is shown in Figure 2.16. The method of images is used to replace the effect of a magnetic boundary as [78].

The method of images is a technique that solves partial differential equations. It satisfies boundary conditions by combining solutions of the mirror images. The basic idea is shown in Figure 2.17 (a), which is clear and simple. However, when the boundary conditions enclose the boundary, it is not straightforward to know how to get mirror images. As Figure 2.17 (b) shows, there are two ways to obtain mirror images. One way is forming surrounding layers of mirror images, and the number of layers is used to count the images. Another way is counting the images by counting how many mirror actions are needed to build the images. In (b), the number in a circle marks the required mirror action number to form these images. For example, it needs to mirror the real windings once to form the images marked by ①. The difference between the two ways will be compared in the following part.
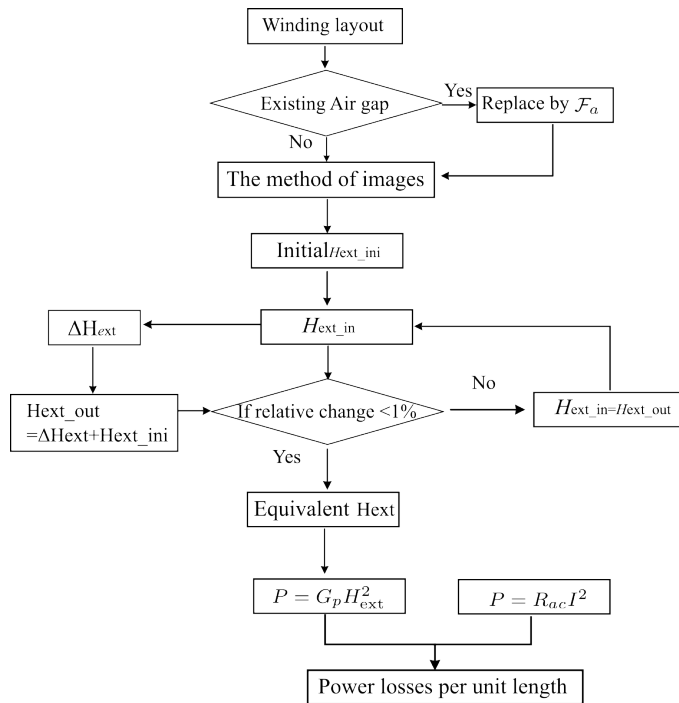
Figure 2.16: Flowchart for 2D recursive method

(a)

(b)
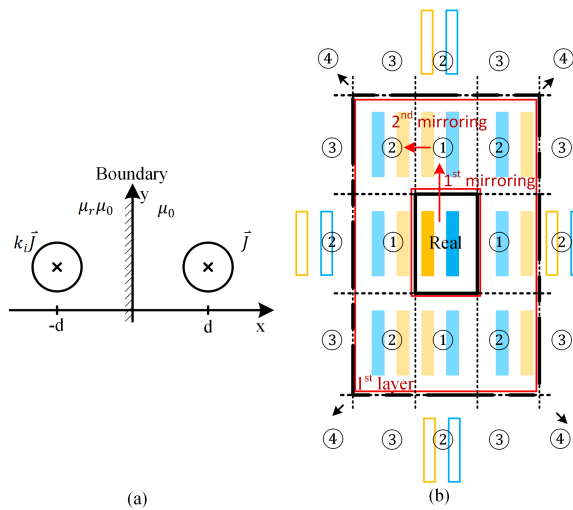
Figure 2.17: Illustration of the method of images, (a) basic idea, (b) the method applied to a core window, the number in a circle marks the required times of mirroring.

If there is an air gap, the fringe flux can cause a huge proximity effect loss in the nearby conductors. Therefore, it is necessary to consider the impact of fringe flux on winding loss. In [86], [87], the impact of air gaps is analyzed based on solving PDE and boundary conditions. However, it is complex and difficult to be incorporated into the method. Roshen [88] derived fringing field formulas due to an air gap, which can be used to calculate the field. Another way to consider fringe flux impact is adding an anti-MMF source and having a core without gap, used in [78], [89]. The anti-MMF source is assumed to be not influenced by the frequency and the location of conductors. The anti-MMF source is represented by a surface current J determined by (2.28), l_g is the total length of air gaps.

$$J = \mathscr{F}_a / l_g \tag{2.28}$$

Through analyzing the magnetic circuit in Figure 2.18, the relation between the MMF of all conductors $\mathscr{F}$ and the anti-MMF source $\mathscr{F}_a$ can be obtained based on equating the flux through $\mathscr{R}_{\text{fringe}}$ in two circuits.

$$\mathscr{F}_a = -\frac{\mathscr{F}/\mathscr{R}_m}{1/\mathscr{R}_m + 1/\mathscr{R}_{\text{gap}} + 1/\mathscr{R}_{\text{fringe}}} \tag{2.29}$$
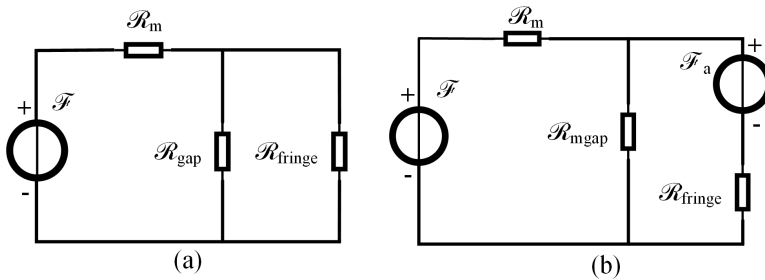
Figure 2.18: Magnetic circuit of a gaped core (a), and equivalent magnetic circuit with the anti-MMF (b)

Where $\mathscr{R}_m$ is the reluctance of core, $\mathscr{R}_{\text{gap}}$ is the reluctance of air gap, $\mathscr{R}_{\text{fringe}}$ is the reluctance of path for fringe flux, $\mathscr{R}_{\text{mgap}}$ is the reluctance of the magnetic material filling the air gap and $\mathscr{R}_{\text{mgap}} \ll \mathscr{R}_m$.

Figure 2.19 shows the accuracy of the field strength calculation with a surface current as anti MMF source. Figure (a) shows the magnitude of the relative difference between an air gap and a surface current. In most of the region, the value is lower than -2, i.e. 1% differences. Only in a few areas the relative difference can reach -1. There is a small region in the middle having considerable relative differences. However, it is known that the absolute difference is very small according to (b). Only in the region adjacent to the air gap, both the relative difference and absolute difference are significant. However, in practice, the winding should not be located in this area. Therefore, a surface current as an anti-MMF source can satisfy the accuracy in calculating fringe flux.

After replacing the air gaps and generating mirror images, the magnetic field under the DC situation is calculated and is set as the initial equivalent external magnetic field

(a) Relative difference in magnetic field

(b) Absolute difference in magnetic field
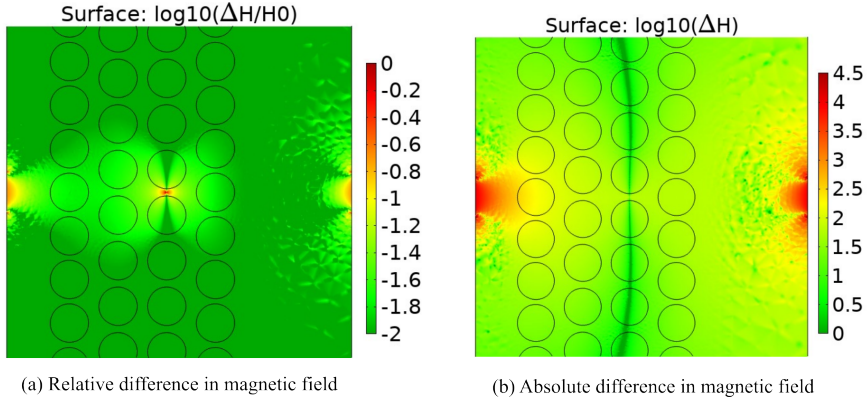
Figure 2.19: Effect of an anti-MMF source

in iteration. Then, the changes ΔH_{ext} due to eddy current are calculated by the second terms in (2.21) and (2.27). The output value ΔH_{ext_out} is obtained by summing the initial value ΔH_{ext_ini} and changing part ΔH_{ext}. The output value becomes the input value for the next loop. Repeat this loop until the relative change between the summation of squared input and output equivalent field of all cells is smaller than a threshold value, and 1% is used. The reason for using the summation of field squared as the index is that proximity loss is proportional to field squared.

Finally, the iteration results are used to calculate the proximity effect losses. Sum all losses of real conductors to obtain the winding losses per unit length and scale the losses to get an estimated value.

To verify the method, three different arrangements are calculated as shown in Figure 2.20. Black parts are possible air gaps, and conductors with the same colour are of the same winding. Details about the configurations are given in Table 2.2. The semicolon in the row 'Number of turns' of Table 2.2 separates the information of two windings.

First, the two ways of generating the mirror images are compared. Case (3) has a different height of the winding. Top and bottom turns of each layer have much higher eddy current losses due to the high field strength. Therefore, the initial field value is important, and the comparison is done on the top turn in each layer. Figure 2.21 shows the relative error of the square of the magnetic field of two top turns with different image generation ways compared to the FEM result. In both ways, when the image value increases, the results converge. If the net MMF is zero, i.e., transformer mode, the relative error is smaller than 10% after converging. However, the results are quite different when the net MMF is not zero, i.e., inductor mode,. The second way has significant errors, which has more than 20% error even when the image value is equal to 6. Therefore, it is better to use the number of mirror actions to count images.

Then, the resistance per unit length for the core window without air gap cores is calculated.

Figure 2.22 (a), (b) and (c) show the resistances per unit length and relative error compared to 2D FEM in net zero MMF mode, like transformer. The results show the 2D

2

(1)   (2)   (3)

(4) inside core window   (5) outside core window
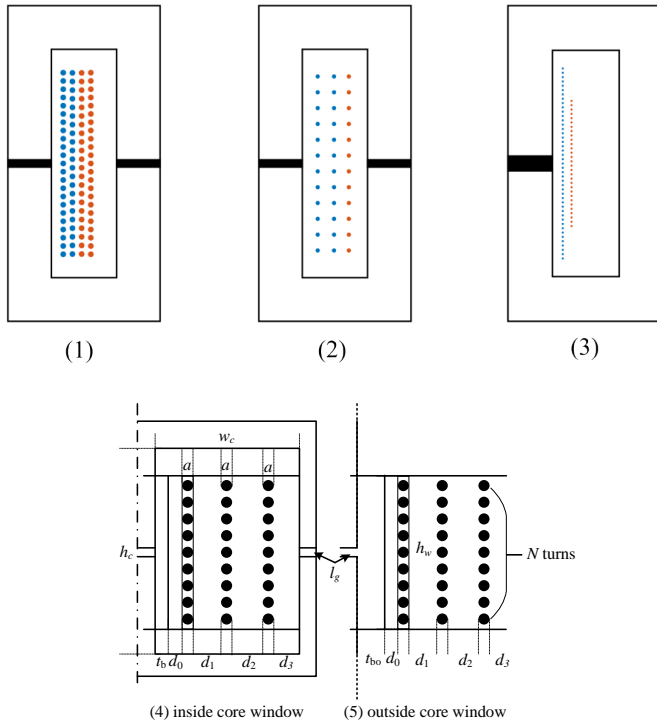
Figure 2.20: Illustration of multilayer winding configurations, (1) (2) equal layer heights with different number of turns per layer, (3) different layer heights. Notation of a winding inside the core window (4) and outside the core window (5).
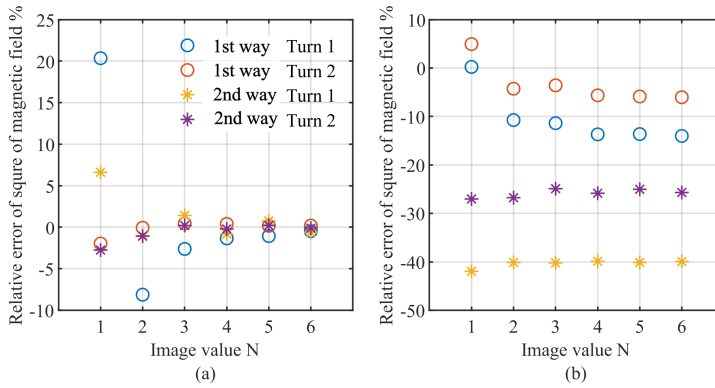
Figure 2.21: Relative error of square of magnetic field compared to FEM results, (a) is for transformer mode, (b) is for inductor mode. Method 1 uses the times of mirroring. Method 2 uses the number of layers to count images. Turn 1 represents the top turn in 1st layer, and turn 2 represents the top turn in 2nd layer

No.	Case (1)	Case (2)	Case (3)
Conductor radius a [mm]	0.5	0.4	0.25
Conductivity σ_c		$5.96 \times 10^7 \mathrm{S/m}$	
Number of turns N_*	23,22;22,23	12,12;12	45;30
Height of winding h_w [mm]	26.1	26.1	26.1;17.4
Parameter d_* [mm]	0.04,0.27 ×3,3.05	0.63,1.45 ×2,1.98	0.04,0.68, 6.18
Thickness of bobbin $t_\mathrm{b}/t_\mathrm{bo}$ [mm]	1.1/1.75	1.1/1.75	1.1/1.1
Air gap l_g [mm] for inductor	1	1	2 (only left leg)
Height of core window h_c [mm]	$30.4+g_i$	$30.4+g_i$	30.4
Width of core window w_c [mm]	9	9	9

Table 2.2: Detail information about winding configurations

approach and Mühlethaler's approach can achieve less than 10% error results when
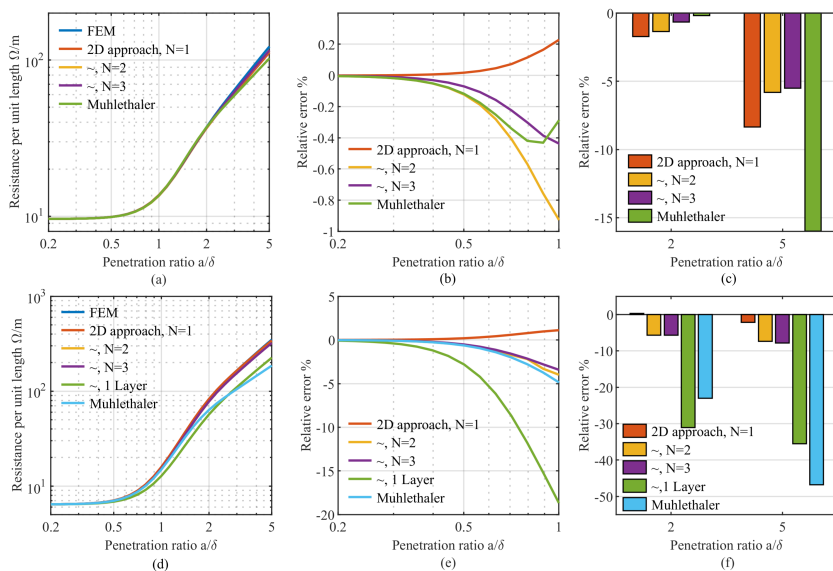
Figure 2.22: Resistances per unit length and relative error compared to 2D FEM in cases (3) without air gap. Zero MMF, (a), (b), (c), respectively. Equal current, (d), (e), (f), respectively.

$a/\delta \leq 1$. However, the error of Mühlethaler's approach increases significantly when the frequency is high. Besides, results with different image setting values are compared. When value N changes from 1 to 2, the relative error slightly decreases, and the change is not obvious when N increases again. Figure 2.22 (d), (e) and (f) show the results of equal current mode, like an inductor. Mühlethaler's approach has a similar performance as the 2D approach when $a/\delta \leq 1$. However, it underestimates the resistance considerably with higher frequency. Results from different ways of counting images show huge differences in this case. The result with one layer of images has poor accuracy. On the contrary, results using the times of mirroring have less than 10% error. Because the difference in the initial field value is shown in Figure 2.21. According to the changes due to various N values, the default value of N is set as 2. The higher N leads to longer computational time and little improved accuracy.

Figure 2.23(a), (b) and (d) show the result of case (1). All approaches or equations provide less than 10% error results when $a/\delta \leq 1$. It indicates that 15% shorter windings do not reduce the effectiveness of 1D methods much. The 2D approach and Mühlethaler's approach have less error than Dowell's model. However, Mühlethaler's approach has significant errors when the frequency is high, as shown in (c). For case (2), which has a larger Δ_{hei}, the 2D approach and Mühlethaler's approach have better results. Dowell's method overestimates significantly at high frequency.
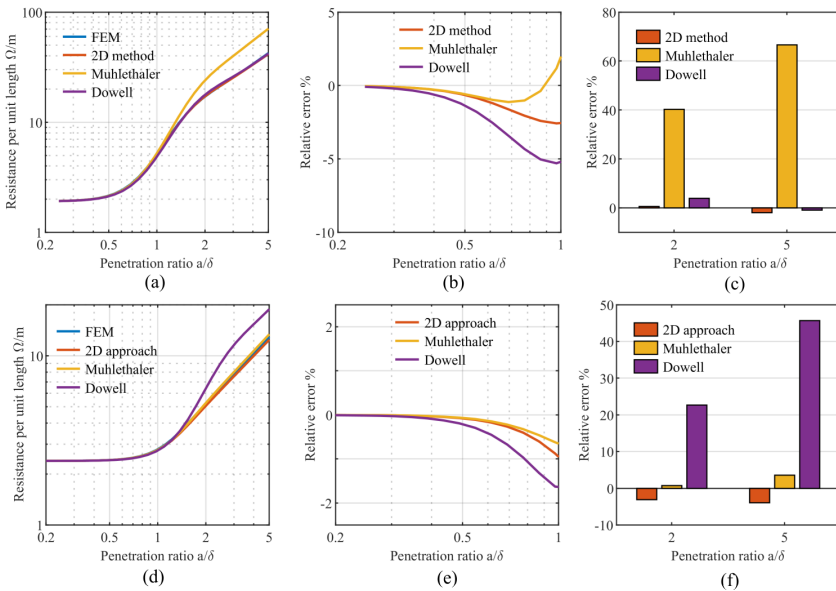
Figure 2.23: Resistances per unit length and relative error compared to 2D FEM in transformer mode without air gap, case (1), (a), (b), (c), respectively. case (2), (d), (e), (f), respectively.

Then, the resistance per unit length for the core window with air gap is calculated. Besides the resistances per unit length inside the core window, resistances outside the core window are also calculated for the double 2D method [78], [90]. It needs to be mentioned that the air gap in 2D FEM outside the core window is replaced by a

magnetic core with a surface current density. The reason for making this substitution is that the flux density in the air gap is much smaller than inside the core window if the air domain is assigned to the air gap. This substitution leads to less than 10% overestimation for losses inside the core window. It is assumed that the substitution does not lead to a worse estimation for losses outside the core window.

Figure 2.24 shows resistances per unit length and relative losses inside and outside the core window. For cases (1) and (2), the resistances per unit length inside and outside the core window significantly differ. Therefore, the double 2D method is preferred. The estimations from the proposed 2D approach are close to 2D FEM results. Mühlethaler's approach performs better in case (2) than in case (1) because it does not consider the interactions between eddy currents, and the distance between conductors is larger in case (2). In case (3), resistances per unit length inside and outside the core window do not show much difference because there is only one air gap. The proposed approach behaves better, with roughly 5% less highest error than Mühlethaler's approach for $a/\delta \leq$ 2.
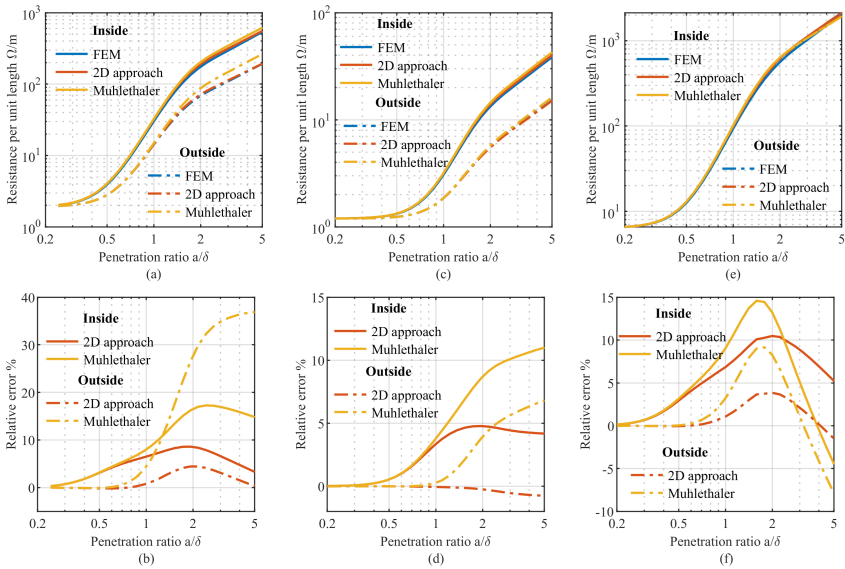
Figure 2.24: Resistances per unit length and relative error compared to 2D FEM in equal current mode, case (1), (a) (b); case (2), (c), (d); case (3), (e), (f), respectively

2.3.3. Leakage inductance models

Leakage inductance is an inductive component in imperfectly coupled transformers. Magnetic flux that doesn't link the primary windings and secondary windings acts as inductive impedance, i.e. leakage inductance. Accurate leakage inductance estimation and design are important for the converter level design. For SRC, integrated transformers are widely adopted [36], [91], which utilize the leakage inductance as part of converter tanks. For DAB with phase shift control, the leakage inductance decides the power the

converter can deliver [35].

The transformer leakage inductance can be calculated using numerical methods, reluctance networks, and analytical methods. Numerical methods like FEM have good accuracy but high computational time. Reluctance network [92] converts the domain into a network of lump elements, which is faster also less accurate than FEM. Although analytical models are restricted by their assumptions, they are still the first choice in the design because of their fast computational speed. Several analytical models are introduced in the following.

1. Frequency dependant model

With considerable eddy current, the magnetic field inside and around the winding is impacted. Consequently, the leakage inductance also changes with frequency.

 • Dowell's method [93]

Dowell's method can also predict the leakage inductance in 1D, which considers the impact of eddy current. The leakage inductance is calculated based on time average magnetic energy (2.30).

$$W_m = \frac{1}{4} L I^2 = \frac{1}{4} \mu \int H^2 \mathrm{d}S \tag{2.30}$$

Due to the orthogonality between skin and proximity effects, the time average magnetic energy stored in conductors can also be calculated independently. The time average magnetic energy caused by each effect stored in one layer is given in (2.31).

$$
\begin{aligned}
W_{ms} &= I^2 \frac{\mu \delta}{16 h_w} \frac{\sinh(\Delta) - \sin(\Delta)}{\cosh(\Delta) - \cos(\Delta)} \\
W_{mp} &= H^2 \frac{\mu \delta h_w}{4} \frac{\sinh(\Delta) + \sin(\Delta)}{\cosh(\Delta) + \cos(\Delta)}
\end{aligned}
\tag{2.31}
$$

The time average magnetic energy stored in the other core window area can be calculated through MMF plot and (2.32), where d_{air} is the distance between windings, and H_{air} is the magnetic field in the air gap.

$$W_{mair} = \frac{1}{4} \mu H_{air}^2 h d_{air} \tag{2.32}$$

Then the leakage inductance can be obtained from the total time average magnetic energy stored in the core windows, as (2.33).

$$\frac{1}{4} L_{leak} I^2 = \sum W_{ms} + \sum W_{mp} + \sum W_{mair} \tag{2.33}$$

2. Static models

Several models focus on low-frequency inductance [94]–[97] and do not consider the impact of eddy current in windings. Wilcox derived mutual inductance and self-inductance formulas for a coil on magnetic cores of circular cross-section [49], [98].

2

- Single Fourier series model (Rogowski) [96]

The single Fourier series model, also known as Rogowski model, mirrors the original windings in the x direction. A single Fourier series is used to describe the spatial current distribution. With the current distribution, the magnetic field is derived. The leakage inductance is also obtained from time average magnetic energy (2.30).

Rogowski model considers the flux at the winding ends by correcting the equivalent length (winding height) of the magnetic flux path through the air. This method is generally used in leakage inductance calculation for LF power transformers.

The leakage inductance L_{leak} is given in (2.34), where N is the number of turns, h is the height of windings, d_p, d_{air} and d_s are the width of the primary winding, total width between windings and the width of the secondary winding, respectively. Mogorovic [99] introduced the Rogowski factor K_w to Dowell's model.

$$
L_{leak} = \frac{\mu_0 N^2}{h_{equ}} \mu_0 N^2 \left(d_{ps} + \frac{d_p + d_s}{3} \right)
$$

$$
h_{equ} = \frac{h}{K_w} \qquad K_w = 1 - \frac{1 - e^{-\lambda}}{\lambda} \tag{2.34}
$$

$$
\lambda = \pi h / (d_p + d_{air} + d_s)
$$

- Double Fourier series model (Roth) [97], [100]

The double Fourier series model is also known as Roth model. It uses a double Fourier series to describe current density distribution in a two-dimensional geometry. The magnetic field distribution is calculated by superimposing the field generated by each winding. The leakage inductance is also obtained from time average magnetic energy (2.30). The basic theory is given in (2.35), where w_c, h_c are the dimension of core window, h_k, w_k are the dimension of the kth winding. A comprehensive mathematical detail can be found in [100].

$$
J_z(x, y) = \sum_{m=0}^{\infty} \sum_{n=0}^{\infty} J_{k,mn} cos \left(m\frac{2\pi}{w_c}x \right) cos \left(n\frac{2\pi}{h_c}y \right)
$$

$$
A_{z,k}(x, y) = \sum_{m=0}^{\infty} \sum_{n=0}^{\infty} A_{k,mn} cos \left(m\frac{2\pi}{w_k}x \right) cos \left(n\frac{2\pi}{h_k}y \right) \tag{2.35}
$$

$$
W_m = \frac{1}{4} \iint A_z J_z dS
$$

- Margueron's model [94], [95]

Compared to the double Fourier series, Margueron's model uses the magnetic vector potentials of a single winding. The method of images is used to mirror these windings and consider the impact of the finite permeability of the magnetic core. The summation of all original windings and mirror images is used to calculate the leakage inductance following (2.30). The magnetic vector potential of a rectangular winding is obtained by assuming a uniform current distribution.

Figure 2.25 shows the estimated leakage inductance per unit length and the relative error compared to 2D FEM in 3 cases. In case (1), the leakage inductance for low

frequencies has close results except for Dowell's model. This implies that the Rogowski factor K_w can improve the accuracy of Dowell's model when the windings have equal heights and compact turn alignments. Two static methods deviate from FEM results for increasing frequencies. For case (2), the relative error is much larger than in case (1) because of the large distance between turns in the same layer. Two static methods could reduce the error by using turns as the basic element, which can accurately calculate the magnetic energy between turns. However, it increases the complexity of calculations. For case (3), 1D methods have considerable errors because the windings do not comply with their assumptions, and the 2D static method has a good accuracy at low frequency, which is similar to the case (1).
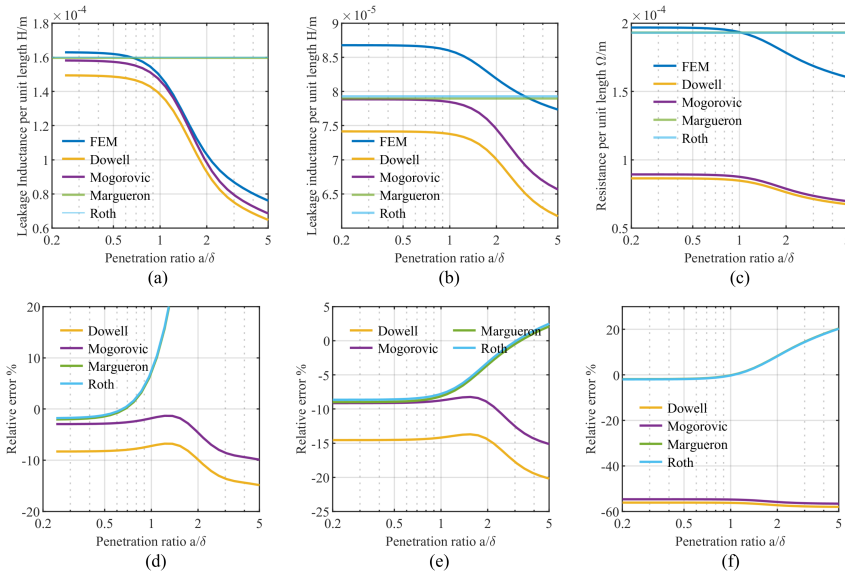
Figure 2.25: Leakage inductance per unit length and relative error compared to 2D FEM for cases in Figure 2.20, case (1), (a) and (d); case (2), (b) and (e); case (3), (c) and (f).

2.3.4. STRAY CAPACITANCE MODELS

Capacitances play an important role in high $\mathrm{d}v/\mathrm{d}t$ situations. With the widespread adoption of wide band-gap semiconductors, higher switching frequency and voltage highlight the significance of stray capacitance. It can lead to larger current and overvoltage in the transient and cause EMI issues [101], [102]. In general, the capacitance models can be divided into two types, analytical models and numerical models.

The analytical model usually has two steps. The step one is calculating the capacitance of typical structures. Based on an assumed electric field flux, each part of capacitance is calculated. The capacitance of the typical structure is the equivalent capacitance of the formed network, as shown in Figure 2.26 (a). With different assumed field fluxes, the results can be different, as shown in [103], [104]. A turn-to-turn
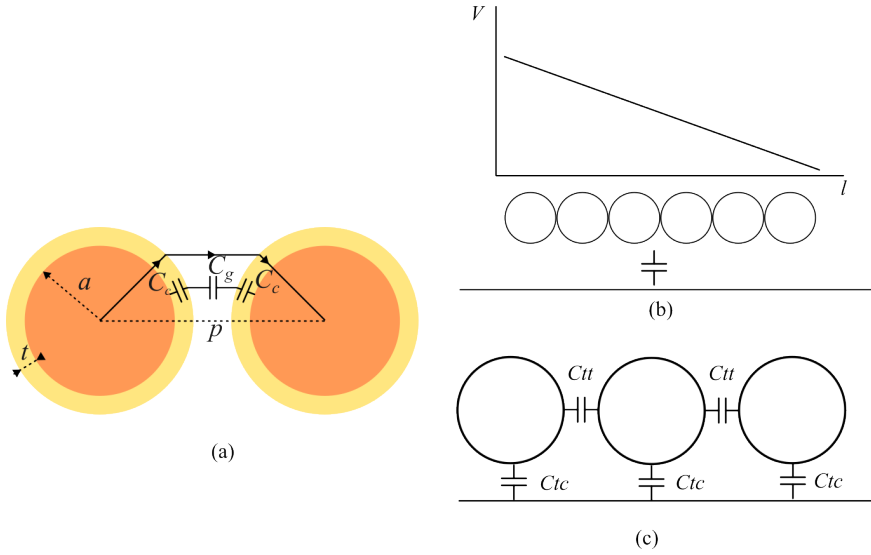
Figure 2.26: Illustration of an analytical model, the capacitance of between turns (a), energy conservation (b), capacitor network (c).

capacitance C_{tt} is given as an example [8]. The capacitances C_c and C_g representing the capacitance of the insulation layer and the gap are calculated by (2.36), t_i is the insulation layer thickness, a is the radius of conductors, p is the distance between two centre points of conductors, l_t is the length of conductors, ϵ_c and ϵ_g are the permittivity of the insulation layer and the gap. Then the C_{tt} is the series of two C_c and a C_g. The turn-to-core capacitance C_{tc} doubles the value of the C_{tt} when the distance between the turn centre point and core is $p/2$.

$$
C_c = \frac{2\pi\epsilon_c l_t}{\ln\left(1 + \dfrac{t_i}{a}\right)} \qquad C_g = \frac{\pi\epsilon_g l_t}{\cosh^{-1}\left(\dfrac{p}{2(a + t_i)}\right)}
$$

$$
C_{tt} = \frac{0.5C_c C_g}{0.5C_c + C_g} = \frac{\pi\epsilon_g\epsilon_c l_t}{\epsilon_g \ln\left(1 + \dfrac{t_i}{a}\right) + \epsilon_c \cosh^{-1}\left(\dfrac{p}{2(a + t_i)}\right)}
$$

$$
C_{tc} = 2C_{tt}
$$

(2.36)

For step two, two different methods can be used. One is based on energy conservation [105]–[107]. It calculates the stored electric energy and equates to the energy stored in an equivalent layer capacitance based on an assumed voltage distribution, as illustrated in Figure 2.26 (b). For example, if there is only one layer with N turns, and the core is grounded, then the capacitance is given in (2.37). Another method is based on a capacitor network [103], [104]. The network is composed of several capacitors representing the typical structures, as Figure 2.26 (c). The capacitance is the equivalent capacitance of the network. However, this method ignores the existence of inductance and suits the frequency above the first resonant point [102].

$$\frac{1}{2}C_{equ}V^2 = \frac{N-1}{2}C_{tt}\left(\frac{V}{N-1}\right)^2 + \sum_{n=1}^{N}\frac{1}{2}C_{tc}\left(\frac{(n-1)V}{N-1}\right)^2$$

$$C_{equ} = \frac{1}{N-1}C_{tt} + \frac{N}{2}C_{tc}$$

(2.37)

The numerical models are more versatile and can handle complex geometry. The common numerical methods include FEM [108], the method of moments (MoM) [109], [110], charge simulation method [111] and finite difference method [112]. The FEM is based on approximating the solution in elements dividing the domain of interest. Compared to FEM, the MoM only needs a discretization of the boundary instead of the whole domain, which significantly reduces the matrix size. At the same time, the matrix is dense matrix in MoM compared to sparse matrix in FEM. In [109], [113], MoM using Fourier harmonic as basis function is used to calculate the capacitance per unit length of cables composed of round conductors with an insulation layer.

2.4. THEMAL MODEL

THEMAL management is one of the most important tasks in MF transformer design. As described in 1.3, increasing the frequency worsens the cooling conditions due to the reduced surface area. Therefore, an accurate thermal model is essential for properly designing MF transformers and avoiding overheating. It is also important for tuning loss models since losses are impacted by temperature.

2.4.1. HEAT TRANSFER MECHANISM

There are three basic heat transfer modes, i.e., thermal conduction, convection and radiation.

1. Thermal conduction

Thermal conduction occurs when there is a temperature difference between two regions. The heat flux, $\mathbf{q}_h$, resulting from thermal conduction is proportional to the magnitude of the temperature gradient and opposite to its sign, (2.38), which is known as Fourier's law [114]. The constant, k_t, is called the thermal conductivity with unit W/m·K. The heat transfer rate Q_h is the product of the heat flux and the area A_s. Table 2.3 lists typical values of some regular materials used in MF transformers.

$$\mathbf{q}_h = -k_t \nabla T$$

$$Q_h = A_s \mathbf{q}_s$$

(2.38)

2. Thermal convection

Thermal convection is the transfer of heat between a body's surface and a flowing fluid. The fluid adjacent to the surface forms a thin slowed-down region called a boundary layer. Heat is conducted into this layer and moves away with the flowing fluid. The steady-state form of thermal convection flux $\mathbf{q}$ is expressed by (2.39), known as Newton's law of cooling.

Material	Thermal conductivity W/m·K	Density kg/m^3	Specific heat capacity J/kg·K
Air	[115]	1.2 @ 293.15K	[116]
Copper	400 @ 273.15K	8940	385
Aluminium	236 @ 273.15K	2700	900
MnZn	3.5-5	4800	700-800
Epoxy	0.65-0.75	1800-1900	1100

Table 2.3: Typical thermal parameters of some materials

$$\mathbf{q} = \bar{h}_t(T_{surf} - T_\infty) \tag{2.39}$$

The constant h_t is the heat transfer coefficient with unit W/m^2·K, T_{surf} is the absolute temperature of the surface, T_∞ is the absolute temperature of the oncoming fluid. The bar over h_t indicates that it is an average over the surface. The determination of coefficient h_t is a complicated problem that is impacted by temperature differences, the geometry of the body, the flow pattern near the surface, and fluid properties.

A set of dimensionless numbers is used to help understand and analyse heat transfer in various convection situations.

- Nusselt number Nu relates convection heat transfer to conduction heat transfer, given in (2.40). h_t is the heat transfer coefficient, k_{tf} is fluid thermal conductivity, l_h is characteristic length.

$$Nu = \frac{h_t l_h}{k_{tf}} \tag{2.40}$$

- Reynolds number Re characterize the relative influence of inertial and viscous force, given in (2.41). Constant v is the kinematic viscosity, the ratio of dynamic viscosity to density, and u_∞ is oncoming fluid velocity.

$$Re = \frac{u_\infty l_h}{v} \tag{2.41}$$

- Prandtl number Pr represents the ratio of kinematic viscosity to thermal diffusivity, given in (2.42). Constant α_t is thermal diffusivity.

$$Pr = \frac{v}{\alpha_t} \tag{2.42}$$

- Grashof number Gr compares buoyant forces to viscous forces, given in (2.43). Constant g is gravity, and β_t is the thermal expansion coefficient, L_v is the vertical length. It equals to reciprocal of absolute temperature for ideal gas.

$$Gr = \frac{g\beta_t \Delta T L_v^3}{v^2} \tag{2.43}$$

- Rayleigh number Ra compares buoyancy forces to viscous forces in natural convection, given in (2.44).

$$Ra = Gr \cdot Pr \tag{2.44}$$

In the dimensionless numbers, the Nusselt number directly relates to the heat transfer coefficient for convection. The following empirical formulas are given to estimate the Nusselt number under various conditions [117], [118].

- Natural convection

  1. Vertical flat plate with uniform T.

     Nusselt number is calculated by (2.45), and the characteristic length is the height of the plate. C_l is an approximately universal function of Prandtl number for laminar flow, Nu_l is the fully laminar Nusselt number, C_t^V is a function of Prandtl number for turbulent flow, Nu_t is the turbulent Nusselt number.

$$C_l = \frac{0.671}{(1 + (0.492/Pr)^{9/16})^{4/9}}$$
$$Nu_l = \frac{2}{\ln\left(1 + 2/(C_l Ra^{1/4})\right)}$$
$$C_t^V = \frac{0.13 Pr^{0.22}}{(1 + 0.61 Pr^{0.81})^{0.42}} \tag{2.45}$$
$$Nu_t = C_t^V Ra^{1/3}/(1 + 1.4 \times 10^9 Pr/Ra)$$
$$Nu = (Nu_l^6 + (Nu_t)^6)^{1/6}$$

  2. Horizontal heated upward-facing plate with uniform T.

     Nusselt number is calculated by (2.46), and the characteristic length is the ratio of area to perimeter. C_t^U is a function of Prandtl number for turbulent flow.

$$Nu_l = \frac{1.4}{\ln\left(1 + 1.4/(0.835 C_l Ra^{1/4})\right)}$$
$$C_t^U = 0.14\left(\frac{1 + 0.0107 Pr}{1 + 0.01 Pr}\right) \tag{2.46}$$
$$Nu_t = C_t^U Ra^{1/3}$$
$$Nu = (Nu_l^{10} + (Nu_t)^{10})^{1/10}$$

  3. Horizontal heated downward-facing plate Nusselt number is calculated by (2.47), and the characteristic length is the ratio of area to perimeter. Nu^T is the laminar thin-layer Nusselt number.

$$Nu^T = \frac{0.527}{\ln\left(1 + (1.9/Pr)^{9/10})^{2/9}\right)} Ra^{1/5}$$
$$Nu_l = \frac{2.5}{\ln\left(1 + 2.5/Nu^T\right)} \tag{2.47}$$

4. Parallel isothermal plates Nusselt number is calculated by (2.48), and the characteristic length is the ratio of gap length to total surface area. Nu_{fd} is the Nusselt number in the fully developed regime.

$$Nu_{fd} = Ra/24$$
$$Nu_l = 1.32C_l Ra^{1/4} \tag{2.48}$$
$$Nu = (Nu_l^{-1.9} + (Nu_f d)^{-1.9})^{-1/1.9}$$

- Force convection

The forced convection happening on a flat plate follows the two-dimensional laminar boundary layer analysis. In this thesis, turbulence is not considered. Then, the Nusselt number is calculated by (2.49), and the characteristic length is the length along the fluid movement.

$$Nu = 0.664 Re^{1/2} Pr^{1/3} \tag{2.49}$$

3. Radiation

Any object at a raised temperature compared to its surroundings emits energy in the form of electromagnetic waves. The emitted energy for a non-black body is described by Stefan-Boltzmann law (2.50), where σ is the Stefan-Boltzmann constant 5.669×10^{-8} W/(m$^2 \cdot$K^4), ϵ_e is the emittance, also called emissivity, in the range from 0 to 1, T is the absolute temperature.

$$e_b(T) = \epsilon_e \sigma T^4 \tag{2.50}$$

The net radiant heat transfer from object 1 to object 2 is given in (2.51), where A_1 is the surface area of object 1, F_{1-2} is the view factor. Equation (2.52) gives the F_{1-2} under two situations [114]. One is that the surface area of object 2 is much larger than that of object 1. The view factor is equal to emittance ϵ. Another is that objects are two parallel sheets with width w and distance d.

$$Q_{net} = A_1 F_{1-2} \sigma (T_1^4 - T_2^4) \tag{2.51}$$

$$F_{1-2} = \epsilon_{e1} \qquad \text{if } A_1 << A_2$$
$$F_{1-2} = \sqrt{1 + \left(\frac{d}{w}\right)^2} - \frac{d}{w} \quad \text{Parallel sheet} \tag{2.52}$$

Surface emittance is a property that depends on several factors like surface finish, type of paint applied on the surface, etc. Some typical values are listed in Table 2.4.

Material	Emittance ϵ_e
Copper	0.02
Aluminium(oxidized)	0.2-0.3
Paint (including white)	0.9
Enamel	0.8-0.95
Ceramic	0.9-0.95

Table 2.4: Typical emittance of some materials

2.4.2. EQUIVALENT THERMAL CIRCUIT

Generally, to avoid calculating computational fluid dynamics (CFD) with the finite volume method or the finite difference method, a common method is to calculate the thermal behaviour through an equivalent thermal circuit [24], [28].

Equivalent thermal circuit models heat flow by analogue to electrical circuits, like Figure 2.27. The heat transfer rate Q_h is represented by current, temperature T is represented by voltage, heat source P_h is represented by constant current source, absolute thermal resistances R_t are represented by resistors and thermal capacitances C_h are represented by capacitors. Each node follows the relation in (2.53). If only the steady-state is interested, the right side of the equation equals 0, and the thermal circuit becomes a thermal resistor network.

$$C_{hj}\frac{\mathrm{d}T_j}{\mathrm{d}t} = \sum_{i=1,i\neq j}^{n} \frac{1}{R_{ti,j}}(T_i - T_j) + P_{hj}, \, C_{hj}\frac{\mathrm{d}T_j}{\mathrm{d}t} = 0 \tag{2.53}$$
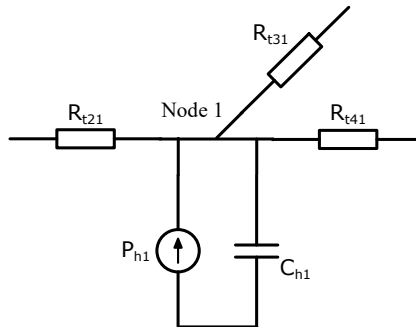
Figure 2.27: Illustration for equivalent thermal circuit

The node selection depends on the geometries of transformers. Figure 2.28 (a) and (b) show the node selection for shell and core type transformers, respectively. Because of the symmetry, the node is only selected in half of the geometries. Then, the thermal resistance considering all three kinds of heat transfer modes is calculated. After calculating the thermal resistance between nodes, a thermal resistor network like 2.28 (c) is obtained. Solve the network, and the temperatures of nodes are obtained.

2
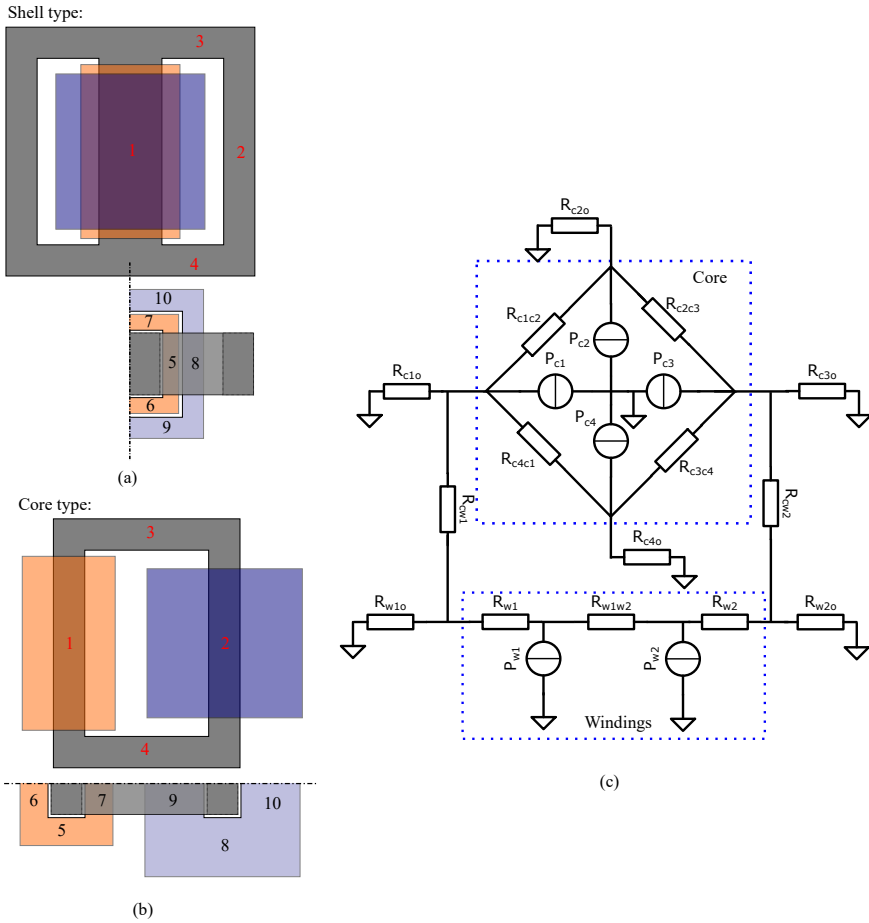
Figure 2.28: Node selection of shell and core type of MF transformers (a),(b), and thermal resistor network illustration (c).

To verify the effectiveness of the thermal circuit model, a 3D CFD simulation is done for a typical shell-type structure. The heat sources in the core and windings are set with volumetric average value. As Figure 2.29 shows, temperature rising of nodes for core (Node 1 and 2) and for two windings (Node 5 and 8) from thermal network is close to the 3D CFD results. Therefore, the thermal circuit is used in the design process.

2.5. CONCLUSION

I N this chapter, the models, especially analytical models, in electrical, magnetic and thermal aspects are summarized. Based on the analysis of magnetic field distribution in round conductors, new 1D and 2D winding loss models are proposed, which take the interaction between eddy currents into account. The impact of the air gap on the field distribution is analyzed, and anti-MMF sources are used to replace gaps for the field
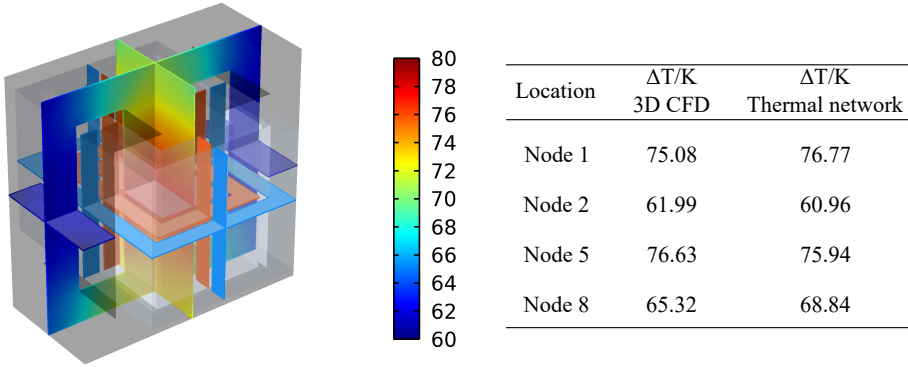
Figure 2.29: 3D temperature distribution in a shell type structure.

Location	ΔT/K 3D CFD	ΔT/K Thermal network
Node 1	75.08	76.77
Node 2	61.99	60.96
Node 5	76.63	75.94
Node 8	65.32	68.84

calculation. The new models are validated by 2D FEMs. Based on some comparison and analysis, the reluctance method (2.4) is used to calculate magnetizing inductance. IGSE is used to estimate the core loss, and thermal circuits are chosen to calculate thermal conditions.

3

A TWO-DIMENSIONAL BOUNDARY ELEMENT & ANALYTICAL COUPLED METHOD

Mathematics compares the most diverse phenomena and discovers the secret analogies that unite them.

Joseph Fourier

A proper method to solve the partial differential equations is the key to achieving reasonable accuracy and computational speed in the modelling. In this chapter, a two-dimensional circle boundary element & analytical coupled method is developed for windings. The circle elements are used in discretization, which complies with the geometry of round conductors. The element shape and the analytical solution for the inside domain lead to significantly smaller element numbers compared to 2D FEM. This method is used to model windings in quasi-static magnetic, static electric fields and heat conduction, which show good accurate and fast computation speeds.

3.1. Introduction

Partial differential equations (PDEs) are fundamental to describing physics. The transformer models are based on the solution of PDEs in different situations. This thesis focuses on magnetic, electric and heat transfer in MF transformers. The proper estimation of steady state is the basis of the design optimization. There are several common PDEs used in stationary situations, like Poisson's equation, Helmholtz's equation and Laplace's equations. A proper method for solving the PDEs is beneficial for design optimization, which should combine reasonable accuracy and computational speed.

$$\text{Poisson's equation: } \nabla^2 \phi = f_d \tag{3.1}$$

$$\text{Helmholtz's equation: } \nabla^2 \phi + \kappa^2 \phi = f_d \tag{3.2}$$

$$\text{Laplace's equation: } \nabla^2 \phi = 0 \tag{3.3}$$

The most straightforward method is obtaining analytical solutions. Many analytical models are used in traditional design. However, these models are always based on some simple geometries and assumptions, and they would give considerable error in more complex geometries. At the same time, it is a challenge or even impossible to find an exact analytical solution in a complex domain. Therefore, several numerical methods are alternative approaches to solve PDEs, like finite element method (FEM), finite difference method (FDM), boundary element method (BEM), etc.

In this chapter, the objects of PDEs are the quasi-static magnetic field, static electric field and stationary thermal conduction. In general, the objects are composed of a background domain and some other domains. The background domain can be described by Laplace's equation, and other domains can be described by Poisson's or Helmholtz's equation. Two-dimensional models can provide more accurate results than 1D models and need much less computational resources than 3D models. BEM only looks at the solution on the boundary and has a small element number. The circle element is very suited to the round conductor used in MF transformers. Besides, the domain inside the circle element can be solved analytically based on the information from the circle element. Therefore, a 2D circle boundary element method is developed.

This chapter first introduces the mathematical derivation of the 2D circle boundary element. The couplings between the information on the circle element and the field inside it are presented. Based on the relation between different circle and line elements, a small filled-in matrix is built. Afterwards, the applications of the proposed method in three different physical fields are shown. All properties of domains are linear, constant and isotropic.

3.2. Circle boundary element v.s. other choices

Numerical methods play an important role in solving PDE, which can be attributed to the fast development and decreasing cost of computational technology. A basic method is to approximate the PDE solution by the summation of a set of trial function u_i, as (3.4).

$$\phi = \sum_{i=1}^{N} c_i u_i \tag{3.4}$$
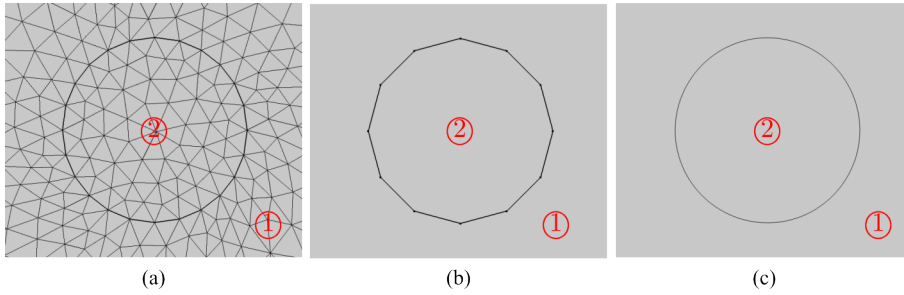
Figure 3.1: Different discretisation, FEM (a), BEM with line element (b), BEM with circle element (c)

The coefficient value c_i of each trial function can be found by a selected method of weighted residuals with test function w. The resulting coefficients are obtained by minimizing the error between the summation of test functions and the actual solution. $\mathscr{L}$ is an arbitrary linear differential operator with constant coefficients f_d, which is an arbitrary source distribution in Ω.

$$\int_{\Omega} (\mathscr{L}u - f_d)\, w \mathrm{d}\Omega = 0 \tag{3.5}$$

BEM and FEM are based on the weighted residual method. If the domain ① in Figure 3.1 follows Laplace's equation, i.e., operator $\mathscr{L}$ is ∇^2 and f_d is 0, the weighted residual statement for the domain ① becomes (3.6) [119], where $\partial_i u$ is the derivative of u with respect to i, $\bar{q}$ is the derivative of u with respect to normal direction on boundary Γ.

$$\begin{aligned}
\int_{\Omega} \partial_i u\, \partial_i w\, \mathrm{d}\Omega &= \int_{\Gamma} \bar{q}\, w\, \mathrm{d}\Gamma & \text{finite element methods} \\
\int_{\Omega} u\, \partial_{ii} w\, \mathrm{d}\Omega &= \int_{\Gamma} (u\, \partial_i w - \partial_i u\, w)\mathrm{d}\Gamma & \text{boundary element methods}
\end{aligned} \tag{3.6}$$

Different test functions are used to solve the coefficients of the trial function. FEM uses Bubnov-Galerkin method, i.e., the test function w is the same as the trial function u. BEM uses Petrov-Galerkin method, which chooses the fundamental solution as the test function, i.e., the solution for a Dirac source. Based on this, there are several differences existing between BEM and FEM, which are listed in Table 3.1 [119], [120].

Since the background domain follows Laplace's equation, the fundamental solution is not a problem, and the properties of domain can also be regarded as linear and isotropic. Hence, the drawbacks of BEM are not significant in the fields of interest. Meanwhile, BEM generates a small dense matrix, which is promising for achieving fast computational speeds.

Figure 3.1 shows the different discretisations. It is obvious that FEM needs more elements than BEM. The BEM generally use line elements, which can suit most situations. However, circle elements are more suitable for the situation in this thesis because their shape complies with round conductors. It can lead to two advantages. The first one is less element number. For example, Figure 3.1 (b) has 12 elements for one round, and (c) has only one element. If the trial function of line elements is a

BEM	FEM
discretization of boundary	discretization of whole domain
approximate u and $\partial_i u$	approximate u
small, dense matrix	large, sparse matrix
require fundamental solution	no prior knowledge required
difficult to solve inhomogeneous or nonlinear problem	solve most linear second-order PDE

Table 3.1: Comparison between BEM and FEM

constant, the trial function of circle elements can be up to fifth-order Fourier series and still have fewer unknown coefficients. The second is the solution for the domain ②, which is enclosed by the circle element and can be analytically derived based on the coefficients of trial functions of the circle element. With line elements, the field or parameter in the enclosed domain needs another BEM [121] or other technique [122], [123].

Therefore, a method combining circle boundary elements and analytical solutions is developed to model the situation in this thesis.

3.3. FORMULAS FOR BOUNDARY ELEMENT

THE targeted fields are generally described by Poisson's equation and Helmholtz's equation. Laplace's equation is a special case of Poisson's equation and Helmholtz's equation. When the source term or the eigenvalue term of the background domain has a trivial contribution, Laplace's equation is used to describe the background domain. This section introduces the general solution of Laplace's equation in 2D and the formulas connecting circle elements and line elements.

3.3.1. FUNDAMENTAL FUNCTION AND GENERAL SOLUTION

Using the fundamental function as a test function is an important feature of BEM, which accounts for the improved accuracy in the flux calculation and in the infinite or semi-infinite domain. Fundamental functions are prerequisites for BEM. The fundamental functions u^* and q^* for Laplace's equation are given in (3.7), $\mathbf{n}_i$ is the outward norm vector.

$$\nabla^2 \phi = -\delta(r)$$

$$u^* = -\frac{1}{2\pi} \ln(r) \quad q^* = \partial_i u^* \, \mathbf{n}_i = -\frac{1}{2\pi r} \partial_i r \, \mathbf{n}_i$$

(3.7)

Besides, the general solution of Laplace's equation helps to solve the relation between the domain inside the circle element and the background domain. Laplace's equation is solved in polar coordinates whose origin is at the center of a circle element, as shown in Figure 3.2 (a). The PDE becomes (3.8) and is solved by the separation of
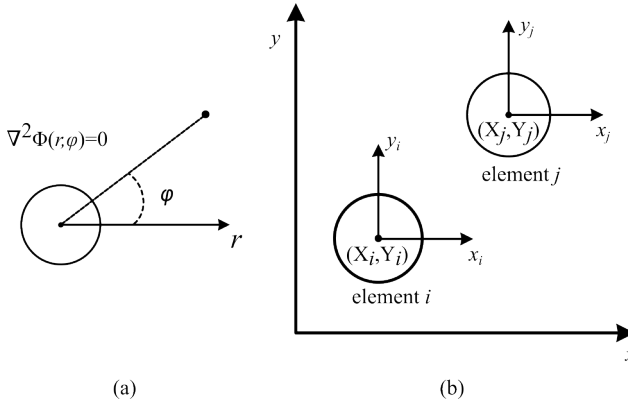
Figure 3.2: Illustration of coordinates

variables.

$$\frac{\partial^2 \phi(r,\varphi)}{\partial r^2} + \frac{1}{r}\frac{\partial \phi(r,\varphi)}{\partial r} + \frac{1}{r^2}\frac{\partial^2 \phi(r,\varphi)}{\partial \varphi^2} = 0 \tag{3.8}$$

Assume the general solution of (3.11) has the form $\phi(r,\varphi) = R(r)S(\varphi)$, and the PDE becomes (3.9).

$$r^2\frac{\partial^2 R(r)}{\partial r^2} + r\frac{\partial R(r)}{\partial r} - n^2 R = 0$$

$$\frac{\partial^2 S(\varphi)}{\partial \varphi^2} + n^2 S(\varphi) = 0 \tag{3.9}$$

Due to the periodical condition, n only can be a non-negative integer, and their general solutions are given in (3.10).

$$R(r) = \begin{cases} C_0 + D_0 \ln(r), & n = 0 \\ C_n r^n + \dfrac{D_n}{r^n}, & n >= 1 \end{cases}$$
$$S(\varphi) = A_n \cos(n\varphi) + B_n \sin(n\varphi) \tag{3.10}$$

Multiplying $R(r)$ and $S(\varphi)$, the final general solution of ϕ is given in (3.11). It describes the potential surrounding the circle element, and all coefficients are parameters of this circle element.

$$\phi(r,\varphi) = C + D\ln(r) + \sum_{n=1}^{+\infty} r^n (A_n' \cos(n\varphi) + B_n' \sin(n\varphi))$$

$$+ \sum_{n=1}^{+\infty} r^{-n}(A_n'' \cos(n\varphi) + B_n'' \sin(n\varphi)) \tag{3.11}$$

If r is set as a value r_0, the variable ϕ is contributed by sources on both sides of r. Based on natural boundary conditions, the contributions from inside are given in (3.12).

$$\phi_i = D\ln(r) + \sum_{n=1}^{+\infty} r^{-n}(A_n'' \cos(n\varphi) + B_n'' \sin(n\varphi)) \tag{3.12}$$

The contributions from outside are given in (3.13).

$$\phi_o = C + \sum_{n=1}^{+\infty} r^n(A_n' \cos(n\varphi) + B_n' \sin(n\varphi)) \tag{3.13}$$

3.3.2. CIRCLE BOUNDARY ELEMENT

Based on the boundary integral equation (3.14) in BEM, two integrations are needed. One is the integration of the product of the flux trial function q and potential fundamental function u^*, and another is the integration of the product of the potential trial function u and flux fundamental function q^*. The coefficient c is the free term coefficient and equals $1/2$ for circle boundaries.

$$c(\zeta)u(\zeta) + \int_\Gamma q^*(x,\zeta)u(x)\mathrm{d}\Gamma = \int_\Gamma u^*(x,\zeta)q(x)\mathrm{d}\Gamma$$

$$c(\zeta) = \begin{cases} 1 & \zeta \in \Omega \\ 0 & \zeta \notin \Omega \,\&\, \zeta \notin \Gamma \\ 1 - \dfrac{\alpha}{2\pi} & \zeta \in \Gamma \end{cases} \tag{3.14}$$

The first integral is given in (3.15) [124], [125], where (x_{ij}, y_{ij}) is the vector from circle element i to node j. $\Re|\Im$ represents that it is either $\Re$ or $\Im$. The other equations have the same sequence showing the corresponding notations.

$$
\begin{array}{ccc}
\text{trial function } q & \text{integral } \displaystyle\int_\Gamma u^* q\,\mathrm{d}\Gamma & \text{Cartesian} \\[2ex]
1 & -a_i \ln(r_i) & -\dfrac{a_i}{2}\ln\left(x_{ij}^2 + y_{ij}^2\right) \\[2ex]
\underbrace{\Re|\Im}\left(e^{In\varphi_i}\right) & \dfrac{a_i^{n+1}}{2n}\underbrace{\Re|\Im}\left(\dfrac{e^{In\varphi_i}}{r_i^n}\right) & \dfrac{a_i^{n+1}}{2n}\underbrace{\Re|\Im}\left(\dfrac{1}{(x_{ij} - Iy_{ij})^n}\right)
\end{array} \tag{3.15}
$$

Based on the (3.14), it is known that the second integral for a circle element i with radius a_i can be obtained by (3.12) and (3.15). The results are given in (3.16). If the node is on the same element as the trial function, the integral is zero for the harmonic term, but it is $1/2$ for the constant term.

$$
\begin{array}{ccc}
\text{trial function } u & \text{integral } \displaystyle\int_\Gamma q^* u\,\mathrm{d}\Gamma & \text{Cartesian} \\[2ex]
1 & 0 & 0 \\[2ex]
\underbrace{\Re|\Im}\left(e^{In\varphi_i}\right) & -\dfrac{a_i^n}{2}\underbrace{\Re|\Im}\left(\dfrac{e^{In\varphi_i}}{r_i^n}\right) & -\dfrac{a_i^n}{2}\underbrace{\Re|\Im}\left(\dfrac{1}{(x_{ij} - Iy_{ij})^n}\right)
\end{array} \tag{3.16}
$$

Based on (3.16) and (3.15), the connection from circle element to node potential is built.

To obtain the potential on element j generated by element i, the integral (3.16) and (3.15) in polar coordinates of element i is converted to the polar coordinates of element j. For the constant trial function, both integrals have a shared logarithm function term. After converting and Maclaurin expansion, the function becomes a series, as given in (3.17).

$$
\begin{aligned}
\ln(r_i) \quad &= \quad \frac{1}{2}\ln\left((x_{ij}+a_j\cos\varphi_j)^2+(y_{ij}+a_j\sin\varphi_j)^2\right) \\
&= \quad \frac{1}{2}\ln\left(x_{ij}^2+y_{ij}^2\right)+\sum_{m=1}^{\infty}\frac{(-1)^{m+1}}{m}\left(\Re\left(\frac{a_j^m\cos(m\varphi_j)}{(x_{ij}-Iy_{ij})^m}\right)+\Im\left(\frac{a_j^m\sin(m\varphi_j)}{(x_{ij}-Iy_{ij})^m}\right)\right)
\end{aligned}
$$
(3.17)

Similarly, the integrals of the harmonic trial function follow the same format. After converting coordinates and binomial expansion, it becomes a series of harmonics, as given in (3.18).

$$
\begin{aligned}
\Re|\Im\left(\frac{e^{In\varphi_i}}{r_i^n}\right) \quad &= \quad \Re|\Im\left(\left((x_{ij}+a_j\cos\varphi_j)-I(y_{ij}+a_j\sin\varphi_j)\right)^{-n}\right) \\
&= \quad \Re|\Im\left(\sum_{m=0}^{\infty}\frac{(n+m-1)!}{(n-1)!m!}(-1)^m\frac{a_j^m e^{-Im\varphi_j}}{(x_{ij}-Iy_{ij})^{m+n}}\right)
\end{aligned}
$$
(3.18)

The connection between circle elements can be established based on (3.17), (3.18).

3.3.3. LINE BOUNDARY ELEMENT

Compared to the circle boundary element, line elements are more generally used. The trial function of one element usually uses the collocation method, i.e., the trial potential or flux function on one element is described by the value on several points and shape function Φ_p, shown in (3.19). The points where the unknown values are considered are called nodes.

$$
u=\sum_{p=1}^{P}\Phi_p u_p
$$
(3.19)
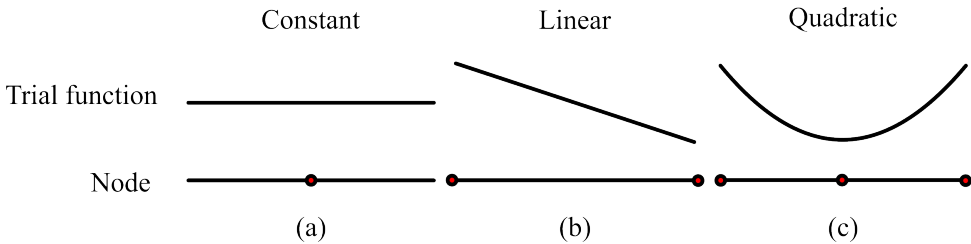
Figure 3.3: Different collocation method, constant (a), linear (b), quadratic (c)

Figure 3.3 shows three different collocation methods. The constant element (a) has a node in the middle of each element. The linear elements (b) have two nodes at the ends of each element, and the quadratic elements (c) have an extra middle node compared to the linear element. In order to incorporate the circle boundary element, the integrals from line boundary elements need to be transformed into a harmonic format. Due to the complexity of linear elements and higher-order polynomials, the constant element is used. Therefore, the trial function is a constant for each line element. Due to the node in the middle of the element, the free term coefficient c equals 0.5. Besides, the line elements are assumed to be parallel to either the x-axis or y-axis, which is generally true in the targeted geometries.

The integral of the constant potential trial function over an element paralleling to x-axis is given in (3.20), where b is the half length of the element. The integral for the element along the y-axis can be calculated in the same way.

$$\int_{\Gamma} q^* u d\Gamma = -\frac{1}{2\pi} \int_{-b}^{b} \frac{u_p y_{ij}}{(x_{ij} - \zeta)^2 + y_{ij}^2} d\zeta$$

$$= -\frac{u_p}{2\pi} \left(\arctan\left(\frac{x_{ij} + b}{y_{ij}}\right) - \arctan\left(\frac{x_{ij} - b}{y_{ij}}\right) \right) \quad (3.20)$$

If b is infinity, the result of the integral becomes (3.21). When the trial function and the node are at the same, the integral equals zero because $r_{,i}$ is perpendicular to n_i in (3.7).

$$\int_{\Gamma} q^* u d\Gamma = -\frac{1}{2} u_p \quad (3.21)$$

The integral of the constant flux trial function over an element parallel to the x-axis is given in (3.22). Similarly, the integral over an element along the y-axis can be obtained.

$$\int_{\Gamma_x} u^* q d\Gamma_x = -\frac{1}{4\pi} \int_{-b}^{b} q_p \ln\left((x_{ij} - \zeta)^2 + y_{ij}^2\right) d\zeta$$

$$= -\frac{q_p}{4\pi} \left(\ln\left((b + x_{ij})^2 + y_{ij}^2\right)(b + x_{ij}) + \ln\left((b - x_{ij})^2 + y_{ij}^2\right)(b - x_{ij}) - 4b \right.$$

$$\left. + 2y \left(\arctan\left(\frac{x_{ij} + b}{y_{ij}}\right) - \arctan\left(\frac{x_{ij} - b}{y_{ij}}\right) \right) \right) \quad (3.22)$$

If b is infinity, the result of the integral becomes (3.23).

$$\int_{\Gamma_x} u^* q d\Gamma_x = \frac{1}{2} q_p \text{abs}(y_{ij}) \quad (3.23)$$

Based on the preceding formulas, the connection between constant line elements can be established. Then, the two integrals over the line element need to be expanded into harmonics. Two situations are given. One is that b is infinity, and another b is a

finite value. The integral is shown in (3.24) when b is infinity.

$$
\begin{array}{ccc}
 & \text{Integral} & \text{After Converting} \\[6pt]
\displaystyle\int_{\Gamma} q^* u \mathrm{d}\Gamma & -\dfrac{1}{2}u_p & -\dfrac{1}{2}u_p \\[12pt]
\displaystyle\int_{\Gamma_x} u^* q \mathrm{d}\Gamma_x & \dfrac{1}{2}q_p\mathrm{abs}(y_{ij}) & \dfrac{1}{2}q_p\mathrm{abs}(y_{ij}+a_j\sin(\varphi_j)) \\[12pt]
\displaystyle\int_{\Gamma_y} u^* q \mathrm{d}\Gamma_y & \dfrac{1}{2}q_p\mathrm{abs}(x_{ij}) & \dfrac{1}{2}q_p\mathrm{abs}(x_{ij}+a_j\cos(\varphi_j))
\end{array}
\tag{3.24}
$$

The integral of the potential trial function follows the (3.20) when b is a finite value. After the expansion, the constant and harmonic terms are given in (3.25). If $y_{ij} < 0$, then each coefficient in (3.25) must be mupliplied by -1.

$$
\int_{\Gamma_x} q^* u \mathrm{d}\Gamma_x = \frac{Iu_p}{4\pi}
\begin{cases}
\ln\left(\dfrac{-b-x_{ij}+Iy_{ij}}{b+x_{ij}+Iy_{ij}}\right) - \ln\left(\dfrac{b-x_{ij}+Iy_{ij}}{-b+x_{ij}+Iy_{ij}}\right) \\[12pt]
\dfrac{1}{m}\left(-T_1(m)a_j^m e^{Im\varphi_j} + T_2(m)a_j^m e^{-Im\varphi_j}\right)
\end{cases}
$$

$$
T_1(m) = \frac{(-1)^{m+1}}{(b+x_{ij}+Iy_{ij})^m} + \frac{1}{(b-x_{ij}-Iy_{ij})^m}
$$

$$
T_2(m) = \frac{(-1)^{m+1}}{(b+x_{ij}-Iy_{ij})^m} + \frac{1}{(b-x_{ij}+Iy_{ij})^m}
\tag{3.25}
$$

The integral of the flux trial function follows the (3.22) when b is a finite value. After converting coordinates and expansion, the value on a circle element is given in (3.26).

$$
\int_{\Gamma_x} u^* q \mathrm{d}\Gamma_x = -\frac{q_p}{4\pi}
\begin{cases}
\Re\left(\begin{array}{c}-4\mathrm{b}+\mathscr{G}(x_{ij}+Iy_{ij}+b)+\mathscr{G}(x_{ij}-Iy_{ij}+b) \\ -\mathscr{G}(x_{ij}+Iy_{ij}-b)-\mathscr{G}(x_{ij}-Iy_{ij}-b)\end{array}\right) \\[14pt]
\left(\ln\left((x_{ij}+b)^2+y_{ij}^2\right)-\ln\left((x_{ij}-b)^2+y_{ij}^2\right)\right)a_j\cos\varphi_j \\[12pt]
-I\left(\ln\left(\dfrac{-b-x_{ij}+Iy_{ij}}{b+x_{ij}+Iy_{ij}}\right)-\ln\left(\dfrac{b-x_{ij}+Iy_{ij}}{-b+x_{ij}+Iy_{ij}}\right)\right)a_j\sin\varphi_j \\[12pt]
\dfrac{1}{m(m-1)}\left(T_1(m-1)a_j^m e^{Im\varphi_j}+T_2(m-1)a_j^m e^{-Im\varphi_j}\right) \quad m\geq 2
\end{cases}
$$

$$
\mathscr{G}(x) = x\ln(x)
\tag{3.26}
$$

For the elements along the y-axis, both integrals need to exchange the positions of x_{ij} and y_{ij}, and the harmonic term needs to follow the change shown in (3.27). Based on the (3.25), (3.26) and (3.27), the connection from line elements to circle elements is built.

$$
\begin{aligned}
e^{Im\varphi_j} &\rightarrow I^m e^{-Im\varphi_j} \\[6pt]
e^{-Im\varphi_j} &\rightarrow (-I)^m e^{Im\varphi_j} \\[6pt]
\cos\varphi &\leftrightarrow \sin\varphi
\end{aligned}
\tag{3.27}
$$

3.4. SIMPLIFICATION BASED ON THE METHOD OF IMAGES

THE targeted objects usually possess one or several boundaries, which can be regarded as symmetry axes. They can help to simplify the problem. Because the BEM matrix is a dense matrix, the reduction of the matrix size can improve the efficiency. The boundary conditions (BCs) in the targeted fields usually have two categories:

- Dirichlet BC: Specify the value of the function on a given boundary.

$$\phi = f_b$$

- Neumann BC: Define the normal derivative of the function on a boundary.

$$\frac{\partial \phi}{\partial n} = f_b$$

Assuming there is an infinite line along the x-axis at $y = 0$ and the condition is f_b, the PDE is solved by Fourier transform on x. The general solution is (3.28), where $\mathscr{F}_b$ is Fourier transform of f_b.

$$\Phi(\omega, y) = C_1(\omega)e^{|\omega|y} + C_2(\omega)e^{-|\omega|y} \tag{3.28}$$

Then, the boundary conditions become:

- Dirichlet BC: $C_1(\omega) + C_2(\omega) = \mathscr{F}_b$

- Neumann BC: $C_1(\omega) - C_2(\omega) = \mathscr{F}_b/|\omega|$

The above equations show both boundary conditions can be replaced by the contribution from the ϕ_2 and ϕ_3, as given in (3.29).

$$\phi(x, y) = \phi_1(x, y) + \phi_2(x, y) + \phi_3(x, y)$$

Frequency domain over x	ϕ_1	ϕ_2	ϕ_3	
Dirichlet BC	$C_1(\omega)e^{|\omega|y}$	$-C_1(\omega)e^{-|\omega|y}$	$\mathscr{F}_b e^{-|\omega|y}$	(3.29)
Neumann BC	$C_1(\omega)e^{|\omega|y}$	$C_1(\omega)e^{-|\omega|y}$	$-\dfrac{\mathscr{F}_b}{|\omega|}e^{-|\omega|y}$	

The ϕ_2 can be regarded as the contribution from the mirror images. In the Dirichlet boundary condition, it represents a perfectly absorbing boundary condition, i.e., the image coefficient $k_i = -1$. In the Neumann boundary condition, it represents a perfectly reflecting boundary condition, i.e., the image coefficient $k_i = 1$. In spite of the image coefficient, the vector (x_{ij}, y_{ij}) in section 3.3.2 and 3.3.3 is replaced by the vector from the mirror images to the targeted elements. Then, the impact of ϕ_3 is considered. If the f_b is a constant value or a rectangular function, the potential ϕ_3 is the double of the constant line element described in the section 3.3.3.

Sometimes, boundaries can still be handled using the method of images, even when the flux or potential is not specified. Continue using the boundary along the x direction as the example. If both sides of the boundary follow Laplace's equation and there is no source on the boundary, the boundary conditions can be generalized into (3.30), where δ_u and δ_b is a related material property in two domains.

$$\phi_u(x,0) = \phi_b(x,0)$$

$$\delta_u \frac{\partial \phi_u(x,y)}{\partial y}\Big|_{y=0} = \delta_b \frac{\partial \phi_b(x,y)}{\partial y}\Big|_{y=0} \tag{3.30}$$

$$\frac{\partial \phi_u(x,y)}{\partial x}\Big|_{y=0} = \frac{\partial \phi_b(x,y)}{\partial x}\Big|_{y=0}$$

The potential function is shown in (3.28), and the corresponding flux function is shown in (3.31).

$$q(x,y) = \frac{1}{2\pi} \int_{-\infty}^{+\infty} j\omega C_1(\omega) e^{|\omega|y} e^{j\omega x} + j\omega C_2(\omega) e^{-|\omega|y} e^{j\omega x} d\omega \, \vec{x}$$

$$+ \frac{1}{2\pi} \int_{-\infty}^{+\infty} |\omega| C_1(\omega) e^{|\omega|y} e^{j\omega x} - |\omega| C_2(\omega) e^{-|\omega|y} e^{j\omega x} d\omega \, \vec{y} \tag{3.31}$$

Then, the relations between coefficients of the two domains is shown as follows (3.32). If the domain without source can be regarded as a semi-infinity plane, i.e. C_{b2} or C_{u1} is zero, the relation between the C_1 and C_2 of the other domain can be obtained. If the domain without source has thickness, the method of multiple images can be considered [126].

$$2\delta_u C_{u1}(\omega) = (\delta_u + \delta_b) C_{b1}(\omega) + (\delta_u - \delta_b) C_{b2}(\omega)$$

$$2\delta_u C_{u2}(\omega) = (\delta_u - \delta_b) C_{b1}(\omega) + (\delta_u + \delta_b) C_{b2}(\omega) \tag{3.32}$$

Using the method of images can lead to a wrong potential when the net source in the model is not zero. The potential relates to the reference point and the mirrored images. It is not shown in the preceding sections because the default distance from the reference point is set as 1 and $\ln(1) = 0$. This problem sometimes does not impact the result of interested parameters.

3.5. ANALYSIS OF THE DOMAIN INSIDE CIRCLE ELEMENTS

T HE domain inside a circle element interacts with the background domain. Therefore, it is necessary to solve the field and flux in this domain. Compared to solving it with another BEM, analytical analysis has better efficiency.

When there are two different domains, several boundary conditions should be satisfied on the interface. In two-dimensional analysis, the normal and tangential terms of fluxes are listed as follows.

- Normal term of fluxes from scalar potentials: $\mathbf{n}_b \cdot \nabla \phi$

- Tangential term of fluxes from scalar potentials: $\mathbf{n}_b \times \nabla \phi$

- Normal term of fluxes from vector potentials: $\mathbf{n}_b \cdot (\nabla \times \boldsymbol{\phi})$

- Tangential term of fluxes from vector potentials: $\mathbf{n}_b \times (\nabla \times \boldsymbol{\phi})$

The vector potential only has z direction term in two-dimensional cases. Through some manipulation, it is known $\mathbf{n}_b \cdot \nabla \phi = -\mathbf{n}_b \times (\nabla \times (0,0,\boldsymbol{\phi}_z))$ and $\mathbf{n}_b \times \nabla \phi = \mathbf{n}_b \cdot (\nabla \times (0,0,\boldsymbol{\phi}_z))$.

Firstly, boundary conditions on circle elements are considered. The domain inside a circle element can follow Poisson's equation or Helmholtz's equation, depending on the problem. It is different from the background domain and leads to some BCs applied to the circle element. The general solutions of PDEs inside circle elements are given as follows, assuming f_d is a constant.

- Poisson's equation (3.1):

$$\phi_r(r,\varphi) = \frac{f_d r^2}{4} + C_r + \sum_{n=1}^{+\infty} r^n (\alpha_n \cos(n\varphi) + \beta_n \sin(n\varphi))$$

$$\frac{\partial \phi_r(r,\varphi)}{\partial r} = \frac{f_d r}{2} + \sum_{n=1}^{+\infty} n r^{n-1} (\alpha_n \cos(n\varphi) + \beta_n \sin(n\varphi)) \tag{3.33}$$

$$\frac{1}{r}\frac{\partial \phi_r(r,\varphi)}{\partial \varphi} = \sum_{n=1}^{+\infty} n r^{n-1} (-\alpha_n \sin(n\varphi) + \beta_n \cos(n\varphi))$$

- Helmholtz's equation (3.2):

$$\phi_r(r,\varphi) = \frac{f_d}{\kappa^2} + \sum_{n=0}^{+\infty} J_n(\kappa r)(\alpha_n \cos(n\varphi) + \beta_n \sin(n\varphi))$$

$$\frac{\partial \phi_r(r,\varphi)}{\partial r} = \sum_{n=0}^{+\infty} \frac{\kappa}{2}(J_{n-1}(\kappa r) - J_{n+1}(\kappa r))(\alpha_n \cos(n\varphi) + \beta_n \sin(n\varphi)) \tag{3.34}$$

$$\frac{1}{r}\frac{\partial \phi_r(r,\varphi)}{\partial \varphi} = \sum_{n=0}^{+\infty} \frac{\kappa}{2}(J_{n-1}(\kappa r) + J_{n+1}(\kappa r))(-\alpha_n \sin(n\varphi) + \beta_n \cos(n\varphi))$$

The general solution of Laplace's equation and its derivative in the background domain is shown in (3.35).

$$\phi_e(r,\varphi) = C_e + D\ln(r) + \sum_{n=1}^{+\infty} r^n (A'_n \cos(n\varphi) + B'_n \sin(n\varphi)) + r^{-n}(A''_n \cos(n\varphi) + B''_n \sin(n\varphi))$$

$$\frac{\partial \phi_e(r,\varphi)}{\partial r} = \frac{D}{r} + \sum_{n=1}^{+\infty} n r^{n-1}(A'_n \cos(n\varphi) + B'_n \sin(n\varphi)) - n r^{-n-1}(A''_n \cos(n\varphi) + B''_n \sin(n\varphi))$$

$$\frac{1}{r}\frac{\partial \phi_e(r,\varphi)}{\partial \varphi} = \sum_{n=1}^{+\infty} n r^{n-1}(-A'_n \sin(n\varphi) + B'_n \cos(n\varphi)) + n r^{-n-1}(-A''_n \sin(n\varphi) + B''_n \cos(n\varphi))$$

$$\tag{3.35}$$

Assume the source term on the circle boundary is described by (3.36).

$$\sigma_b(\varphi) = \sigma_0 + \sum_{n=1}^{+\infty} (\sigma_{cn} \cos(n\varphi) + \sigma_{sn} \sin(n\varphi)) \tag{3.36}$$

The BCs in targeted applications can be generalized into (3.37), a is the radius of the circle element.

$$\phi_e(a, \varphi) = \phi_r(a, \varphi)$$

$$\delta_e \frac{\partial \phi_e(r, \varphi)}{\partial r}\Big|_{r=a} - \delta_r \frac{\partial \phi_r(r, \varphi)}{\partial r}\Big|_{r=a} = \sigma_b(\varphi) \tag{3.37}$$

$$\frac{1}{r} \frac{\partial \phi_e(r, \varphi)}{\partial \varphi}\Big|_{r=a} = \frac{1}{r} \frac{\partial \phi_r(r, \varphi)}{\partial \varphi}\Big|_{r=a}$$

If the domain in the circle element follows Poisson's equation, the coefficients follow the relation in (3.38).

$$D = \frac{\delta_r}{\delta_e} \frac{f_d a^2}{2} + \frac{a\sigma_0}{\delta_e}$$

$$C_r = C_e + D\ln(a) - \frac{f_d a^2}{4}$$

$$2\delta_e A'_n|B'_n = (\delta_e + \delta_r)\alpha_n|\beta_n + \frac{\sigma_{cn}|\sigma_{sn}}{na^{n-1}} \tag{3.38}$$

$$2\delta_e a^{-2n} A''_n|B''_n = (\delta_e - \delta_r)\alpha_n|\beta_n - \frac{\sigma_{cn}|\sigma_{sn}}{na^{n-1}}$$

Similarly, for a domain following Helmholtz's equation, the coefficients follow the relation in (3.39).

$$D = -\frac{\delta_r}{\delta_e}\kappa a J_1(\kappa a)\alpha_0 + \frac{a\sigma_0}{\delta_e}$$

$$C_e + D\ln(a) = \frac{f_d}{\kappa^2} + J_0(\kappa a)\alpha_0$$

$$2\delta_e A'_n|B'_n = \left((\delta_e + \delta_r)J_{n-1}(\kappa a) + (\delta_e - \delta_r)J_{n+1}(\kappa a)\right)\frac{\kappa}{2na^{n-1}}\alpha_n|\beta_n + \frac{\sigma_{cn}|\sigma_{sn}}{na^{n-1}} \tag{3.39}$$

$$2\delta_e A''_n|B''_n = \left((\delta_e - \delta_r)J_{n-1}(\kappa a) + (\delta_e + \delta_r)J_{n+1}(\kappa a)\right)\frac{\kappa a^{n+1}}{2n}\alpha_n|\beta_n - \frac{\sigma_{cn}|\sigma_{sn}}{n}a^{n+1}$$

Sometimes, the domain inside a circle element is two or more concentric round domains. Assume the radius of two round domains from inside are a and b. The outer domain also follows Laplace's equation but has properties different from those of the background domain. Its solution is the same as (3.35). By solving the BCs, the relationship between the centre domains inside circle elements and the background domain can also be found. The BCs between two domains are shown in (3.40), assuming there is no boundary source term.

$$\phi_e(b, \varphi) = \phi_{r2}(b, \varphi)$$

$$\delta_e \frac{\partial \phi_e(r, \varphi)}{\partial r}\Big|_{r=b} = \delta_{r2} \frac{\partial \phi_{r2}(r, \varphi)}{\partial r}\Big|_{r=b} \tag{3.40}$$

$$\frac{1}{r} \frac{\partial \phi_e(r, \varphi)}{\partial \varphi}\Big|_{r=b} = \frac{1}{r} \frac{\partial \phi_{r2}(r, \varphi)}{\partial \varphi}\Big|_{r=b}$$

After equating the coefficients of harmonics, the relations between coefficients are given in (3.41).

$$\delta_e D_e = \delta_{r2} D_{r2}$$

$$C_e + D_e \ln(b) = C_{r2} + D_{r2} \ln(b)$$

$$2\delta_e b^{2n} A'_{en}|B'_{en} = (\delta_{r2} + \delta_e) b^{2n} A'_{r2}|B'_{r2} + (\delta_e - \delta_{r2}) A''_{r2}|B''_{r2}$$

$$2\delta_e A''_{en}|B''_{en} = (\delta_e - \delta_{r2}) b^{2n} A'_{r2}|B'_{r2} + (\delta_e + \delta_{r2}) A''_{r2}|B''_{r2}$$

(3.41)

Table 3.2 summarizes the relations between the coefficients of the circle element and the inside domain. The relations are given when either a PDE or a surface source is followed for the inside domain. Based on the relations, some parameters set in the inside domain can be transferred to the condition of the circle element, such as potential or flux.

Laplace	Poisson	Helmholtz
$\dfrac{A''}{A'}\Big\vert\dfrac{B''}{B'}$	$a^{2n}\dfrac{\delta_e - \delta_r}{\delta_e + \delta_r}$	$a^{2n}\dfrac{(\delta_e - \delta_r)J_{n-1}(\kappa a) + (\delta_e + \delta_r)J_{n+1}(\kappa a)}{(\delta_e + \delta_r)J_{n-1}(\kappa a) + (\delta_e - \delta_r)J_{n+1}(\kappa a)}$
$A''\vert B''$	$a^{2n}\dfrac{\delta_e - \delta_r}{2\delta_e}\alpha_n\vert\beta_n$	$\dfrac{\kappa a^{n+1}}{4n\delta_e}\left((\delta_e - \delta_r)J_{n-1}(\kappa a) + (\delta_e + \delta_r)J_{n+1}(\kappa a)\right)$
C	$C_r + \left(\dfrac{\delta_e}{2\delta_r} - \ln(a)\right)D$	$\dfrac{f_d}{\kappa^2} - \left(\ln(a) + \dfrac{\delta_e J_0(\kappa a)}{\delta_r \kappa a J_1(\kappa a)}\right)D$
D	$\dfrac{\delta_r f_d a^2}{2\delta_e}$	$-\dfrac{\delta_r}{\delta_e}\kappa a J_1(\kappa a)\alpha_0$

	Surface source	Laplace (outer layer)
$\dfrac{A''}{A'}\Big\vert\dfrac{B''}{B'}$	$-a^{2n}$	$b^{2n}\dfrac{(\delta_e - \delta_{r2})b^{2n} + (\delta_e + \delta_{r2})A''_{r2}/A'_{r2}}{(\delta_e + \delta_{r2})b^{2n} + (\delta_e - \delta_{r2})A''_{r2}/A'_{r2}}$
$A''\vert B''$	$-\dfrac{a^{n+1}}{2n\delta_e}\sigma_{cn}\vert\sigma_{sn}$	$\dfrac{(\delta_e - \delta_{r2})b^{2n}}{2\delta_e}A'_{r2}\vert B'_{r2} + \dfrac{\delta_e + \delta_{r2}}{2\delta_e}A''_{r2}\vert B''_{r2}$
C	-	$C_{r2} + \left(\dfrac{\delta_e}{\delta_{r2}} - 1\right)\ln(b)D$
D	$\dfrac{a\sigma_0}{\delta_e}$	$\dfrac{\delta_{r2}}{\delta_e}D_{r2}$

Table 3.2: Relations between coefficients of the circle element and the inside domain.

3.6. COUPLING AND MATRIX FORMING

THE formulas for BEM and domain inside circle elements are analytically analyzed separately in previous sections. In this section, the two parts are coupled together,

and a matrix describing the targeted field is generated. Based on the (3.14), a matrix, like (3.42), is formed, U and Q are the potential and flux on elements.

$$\begin{pmatrix} 0.5 & \cdots \\ \vdots & 0.5 \end{pmatrix} \begin{pmatrix} U_c \\ U_l \end{pmatrix} + \begin{pmatrix} uu_{cc} & uu_{lc} \\ uu_{cl} & uu_{ll} \end{pmatrix} \begin{pmatrix} U_c \\ U_l \end{pmatrix} = \begin{pmatrix} qu_{cc} & qu_{lc} \\ qu_{cl} & qu_{ll} \end{pmatrix} \begin{pmatrix} Q_c \\ Q_l \end{pmatrix} \tag{3.42}$$

For circle elements, there are some inherent properties that can simplify the matrix. The first is the relation between flux and potential is set, as shown in (3.35). With (3.15) and (3.16), the harmonic terms in potential and flux integral can be combined into one term, as shown in (3.43), when the trial function is not on the targeted element. Also, the constant term is only related to the coefficient D.

$$qu_{ccij}(-na_j^{n-1}A'_{jn}|B'_{jn}) - uu_{ccij}(a_j^n A'_{jn}|B'_{jn}) = 0$$

$$qu_{ccij}(\frac{n}{a_j^{n+1}}A''_{jn}|B''_{jn}) - uu_{ccij}(a_j^{-n}A''_{jn}|B''_{jn}) = \Re|\Im\left(\frac{e^{In\varphi_j}}{r_j^n}\right)A''_{jn}|B''_{jn} \tag{3.43}$$

$$-\frac{D_j}{a_j}qu_{ccij} = D_j\ln(r_j)$$

When the trial function is the same as the targeted element, the D_i, A''_{in} and B''_{in} cancel each other. Therefore, the unknown parameters are C_i, A'_{in} and B'_{in}.

$$C_i + \sum uu_{ij}U_j = \sum qu_{ij}Q_j$$

$$a_i^n A'_{in}|B'_{in} + \sum uu_{ij}U_j = \sum qu_{ij}Q_j \tag{3.44}$$

The relations between (3.12) and (3.13) (Section 3.5) should be followed. The analytical analysis is coupled with circle boundary elements, and no additional equations are needed to solve the domain inside the circle elements.

To solve the equations practically, the harmonics are truncated at N^{th} order. The relation between coefficients is listed in Table 3.3. To simplify some formulas, equations in (3.45) are used.

$$\eta_{nm} = \frac{(n+m-1)!}{(n-1)!m!} \qquad \xi_{nm} = \frac{(-1)^m}{(x_{ij} - Iy_{ij})^{n+m}}$$

$$S_x = \text{Sign}(x_{ij}) \qquad S_y = \text{Sign}(y_{ij})$$

$$G(\alpha,\beta) = H(\alpha,\beta,b) - H(\alpha,\beta,-b) \qquad H(\alpha,\beta,\gamma) = \ln\left(\frac{-\alpha-\gamma+I\beta}{\alpha+\gamma+I\beta}\right)$$

$$T_1(\alpha,\beta,\gamma) = \frac{1}{\gamma}\left(\frac{(-1)^{\gamma+1}}{(b+\alpha+I\beta)^\gamma} + \frac{1}{(b-\alpha-I\beta)^\gamma}\right) \tag{3.45}$$

$$T_2(\alpha,\beta,\gamma) = \frac{1}{\gamma}\left(\frac{(-1)^{\gamma+1}}{(b+\alpha-I\beta)^\gamma} + \frac{1}{(b-\alpha+I\beta)^\gamma}\right)$$

$$\mathcal{G}(\alpha,\beta) = \mathcal{H}(\alpha+b+I\beta) + \mathcal{H}(\alpha+b-I\beta) - \mathcal{H}(\alpha-b+I\beta) - \mathcal{H}(\alpha-b-I\beta)$$

$$\mathcal{H}(\alpha) = \alpha\ln(\alpha)$$

Source		Coef	Line element — Node value	Line element — C	Circle element — $a_j^m A'$	Circle element — $a_j^m B'$
Circle	Constant	D	$\frac{1}{2}\ln\left(x_{ij}^2+y_{ij}^2\right)$		$-\Re(\eta_{1m}\zeta_{0m})$	$-\Im(\eta_{1m}\zeta_{0m})$
	Harmonics	$A_i' \& B_i'$			$\Re(\eta_{nm}\zeta_{nm})A_i'$ $+\Im(\eta_{nm}\zeta_{nm})B_i'$	$\Im(\eta_{nm}\zeta_{nm})A_i'$ $-\Re(\eta_{nm}\zeta_{nm})B_i'$
ϕ_{2x}	Harmonics	$A_i'' \& B_i''$			$\Re(\eta_{nm}\zeta_{nm})A_i''$ $-\Im(\eta_{nm}\zeta_{nm})B_i''$	$\Im(\eta_{nm}\zeta_{nm})A_i''$ $+\Re(\eta_{nm}\zeta_{nm})B_i''$
ϕ_{2y}	Harmonics	$A_i'' \& B_i''$			$(-1)^n\Re(\eta_{nm}\zeta_{nm})A_i''$ $-(-1)^n\Im(\eta_{nm}\zeta_{nm})B_i''$	$(-1)^n\Im(\eta_{nm}\zeta_{nm})A_i''$ $+(-1)^n\Re(\eta_{nm}\zeta_{nm})B_i''$
Line	Potential	$\frac{u_x}{4\pi}$	$-IS_y$ $G(x_{ij},y_{ij},b)$	$-IS_y\left(\begin{matrix}-T_1(x_{ij},y_{ij},m)\\+T_2(x_{ij},y_{ij},m)\end{matrix}\right)$	$-S_y\left(\begin{matrix}T_1(x_{ij},y_{ij},m)+\\T_2(x_{ij},y_{ij},m)\end{matrix}\right)$	
	Potential	$\frac{u_y}{4\pi}$	$-IS_x$ $G(y_{ij},x_{ij},b)$	$-I^{m+1}S_x\left(\begin{matrix}-T_1(y_{ij},x_{ij},m)\\+(-1)^m T_2(y_{ij},x_{ij},m)\end{matrix}\right)$	$-I^m S_x\left(\begin{matrix}T_1(y_{ij},x_{ij},m)+\\(-1)^m T_2(y_{ij},x_{ij},m)\end{matrix}\right)$	
	Flux	$\frac{q_x}{4\pi}$	$\Re(\mathcal{G}(x_{ij},y_{ij}))-4b)$	$\ln\dfrac{(x_{ij}+b)^2+y_{ij}^2}{(x_{ij}-b)^2+y_{ij}^2},\ m=1$ $\dfrac{1}{m}\left(\begin{matrix}T_1(x_{ij},y_{ij},m-1)\\+T_2(x_{ij},y_{ij},m-1)\end{matrix}\right)$	$-IG(x_{ij},y_{ij},b),\ m=1$ $\dfrac{I}{m}\left(\begin{matrix}T_1(x_{ij},y_{ij},m-1)\\-T_2(x_{ij},y_{ij},m-1)\end{matrix}\right)$	
	Flux	$\frac{q_y}{4\pi}$	$\Re(\mathcal{G}(y_{ij},x_{ij}))-4b)$	$\dfrac{I^m}{m}\left(\begin{matrix}T_1(y_{ij},x_{ij},m-1)\\+(-1)^m T_2(y_{ij},x_{ij},m-1)\end{matrix}\right)$	$\ln\dfrac{(y_{ij}+b)^2+x_{ij}^2}{(y_{ij}-b)^2+x_{ij}^2},\ m=1$ $\dfrac{I^{m+1}}{m}\left(\begin{matrix}-T_1(y_{ij},x_{ij},m-1)\\+(-1)^m T_2(y_{ij},x_{ij},m-1)\end{matrix}\right)$	

Table 3.3: Relation between coefficients

The matrix can be solved with either direct or iterative methods. After solving the built matrix, factors of all circle elements and line elements are obtained. Based on these factors, more information can be inferred.

3.7. APPLICATIONS IN MF TRANSFORMER DESIGN

IN previous sections, the circle boundary element method is introduced in a general form, and the relations between physical quantities and factors are not clear. In this section, the physical meaning of some factors is introduced for targeted fields. Some useful relations are also introduced.

3.7.1. QUASI-STATIC MAGNETIC FIELD

In a quasi-static magnetic field, magnetic vector potentials $\mathbf{A}$ obey the following PDE in the frequency domain, which belongs to Helmholtz's equation.

$$\nabla^2 \mathbf{A} - j\omega\sigma_c\mu_c\mathbf{A} = \mu_c\sigma_c\nabla\Phi \tag{3.46}$$

The magnetic vector potential $\mathbf{A}$ is defined in such a way that its curl is equal to the magnetic flux density $\mathbf{B}$. It can also specify the electric field $\mathbf{E}$, together with the electric potential Φ, as shown in (3.47). Because adding curl-free components to $\mathbf{A}$ does not change the observed magnetic field, a gauge is needed. Coulomb gauge is adopted in this thesis.

$$\mathbf{B} = \nabla \times \mathbf{A} \text{ and } \mathbf{E} = -\nabla\Phi - j\omega\mathbf{A} \tag{3.47}$$

Through comparing (3.46) and (3.2), it is known what the factors in the circle element method represent in the quasi-static magnetic field. The relations between factors and physical parameters are shown in (3.48), where κ is the eigenvalue in Helmholtz's equation, f_d is the source term, δ is the coefficient in flux terms in 3.3.2 and σ_b is the boundary source term. The subscript c represents domains inside circle elements, and the subscript e represents the background domain. The ω is the angular frequency, μ is the permeability, σ_c is the conductivity, Φ is the electrical potential, I is the current, J_b is the surface current density.

$$\begin{aligned}
\kappa^2 &= -j\omega\sigma_c\mu, \quad f_d = \mu_c\sigma_c\nabla\Phi \\
\delta &= 1/\mu_c, \qquad D_r = -\frac{\mu_e I}{2\pi} \\
f_{b\_\text{Neumann}} &= \sigma_b = -\mu J_b
\end{aligned} \tag{3.48}$$

The domain inside a circle element generally represents a round conductor. Based on $\mathbf{J} = \sigma\mathbf{E}$ and a constant Φ over the cross-section, the relation between $-\nabla\Phi$ and I is obtained by averaging the $\mathbf{E}$ over the cross-section of the conductor, and (3.49) is obtained.

$$\frac{1}{\sigma_c S_c} \oiint \mathbf{J}\, ds = \frac{I}{\sigma_c S_c} = -\nabla\Phi - \frac{1}{S_c}\oiint j\omega\mathbf{A}\, ds \tag{3.49}$$

The AC impedance per unit length Z_ac can be derived from (3.49), as given in (3.50). $\bar{A}$ is the average magnetic vector potential over the cross-section, R_dc is the DC resistance per unit length.

$$Z_\text{ac} = R_\text{dc} + \frac{j\omega\bar{A}}{I} \tag{3.50}$$

The $\bar{A}$ is obtained by integrating (3.34). Combining (3.39), the result based on parameters of the circle element is as shown in (3.51).

$$\bar{A} = C + D\ln(a) - \frac{\mu_c}{\mu_e}\frac{DJ_2(\kappa a)}{\kappa a J_1(\kappa a)} \tag{3.51}$$

Combining (3.51) and (3.50), the relation between Z_{ac} and the parameters of the circle element is given.

$$Z_{ac} = R_{dc} - \frac{j\omega\mu}{2\pi}\left(\frac{C}{D} + \ln(a) - \frac{\mu_c}{\mu_e}\frac{J_2(\kappa a)}{\kappa a J_1(\kappa a)}\right) \tag{3.52}$$

The preceding part describes the relation between the electrical circuit element and the parameters of the corresponding circle element. Then, the energy flow in or out of circle elements is calculated by Poynting vector **S**. The active power P and reactive power Q per unit length is shown in (3.53), where * represents conjugate, T_n is part of relation between A'_n and A''_n without boundary source term σ_b obtained from (3.39).

$$\begin{aligned} S = P + jQ = \oint \mathbf{S}_{r=a}d\varphi &= \frac{I^2}{\sigma_c\pi a^2} + j\omega\frac{\mu_c I^2}{2\pi}\frac{J_2(\kappa a)}{\kappa a J_1(\kappa a)} \\ &+ \frac{j\omega}{\mu_e}\sum_{n=1}\left(\pi n a^{2n}\left(1+T_n\right)\left(1-T_n^*\right)(A'_n A'^*_n + B'_n B'^*_n)\right) \end{aligned} \tag{3.53}$$

$$T_n = \frac{(\mu_c - \mu_e)J_{n-1}(\kappa a) + (\mu_c + \mu_e)J_{n+1}(\kappa a)}{(\mu_c + \mu_e)J_{n-1}(\kappa a) + (\mu_c - \mu_e)J_{n+1}(\kappa a)}$$

- Settings of the method

To compare with other methods on accuracy and computational speed, the winding configurations in 2.3.2 are reused here. Before the computation, parameters like harmonic term order N and the maximal mirrored image for cases inside the core window need to be set. The number of mirror cations N_r are used. Figure 3.4 (a) and (b) show the resistance and leakage inductance per unit length with varying N and certain
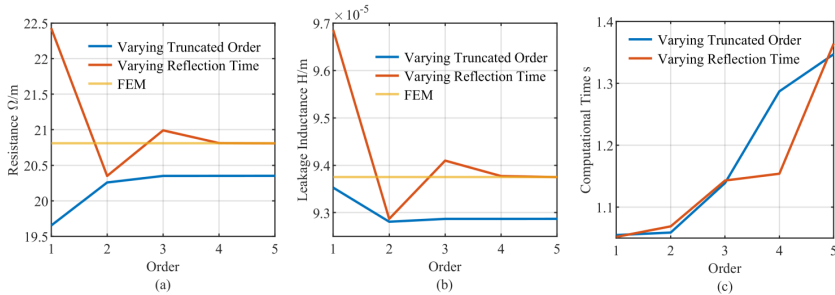
Figure 3.4: Resistance (a), leakage inductance (b) per unit length and computation time (c) of Case 1 at 100kHz with varying truncated order or reflection time.

$N_r = 2$, or varying N_r and certain $N = 3$. When N is larger than 2, the values converge, and therefore the order N is set as 2. Compared to different N, different N_r show more influence on the result inside the core window. When N_r is larger than 4, the difference is negligible. However, as (c) shows, the higher N_r, the longer the computation time is. Therefore, N_r is set to 2.

- AC resistance

Because several 1D and 2D methods for winding AC resistance are already compared in Section 2.3.2, only 2D FEM, the proposed method and the 2D methods [127] are compared. Figure 3.5 shows the results for all three cases with net zero MMF. For case (1) and (2), the proposed BEM method has similar accuracy as the 2D method, both provide results with less than 5% error compared to 2D FEM. In case (3), the proposed BEM method is more stable than the other 2D method. Based on the results, it is known that the proposed BEM method gives less than 3% error in all situations and can suit various winding configurations.
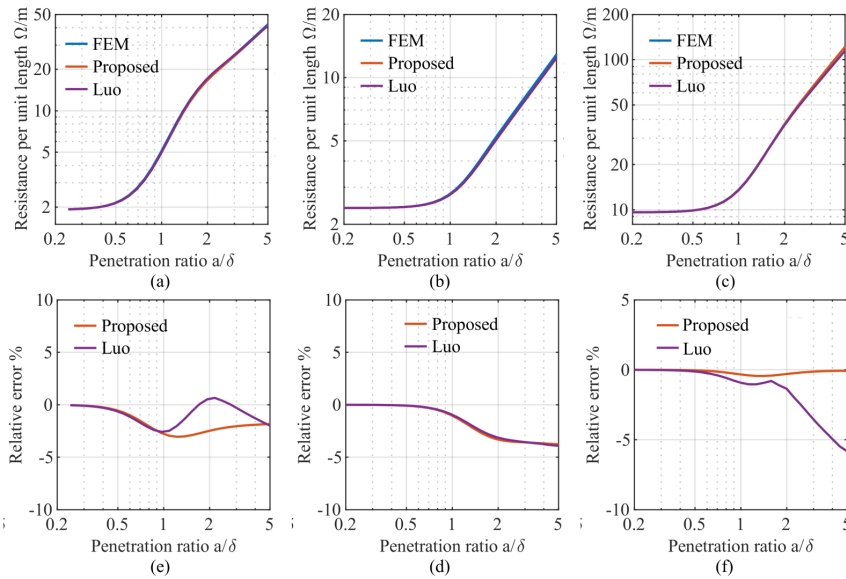
Figure 3.5: Resistances per unit length and relative error compared to 2D FEM in transformer mode without air gap, case (1), (a), (d); case (2), (b), (e); case (3), (c), (f), respectively

Then, each turn carries the same current, i.e., connect in series, and air gaps are applied. Similarly, only the proposed method and the 2D method in Section 2.3.2 are compared with 2D FEM. Due to the possible considerable difference between the situation inside and outside the core window, the AC resistance is calculated under both situations. In case (1) and (2), there are two gaps on different core legs. Therefore, the AC resistance per unit length is estimated in two situations, i.e., winding inside and outside core windows. Figure 3.6 shows the results for all cases. All methods provide less than 10% error results when $a/\delta \leq 1$. The proposed method shows more accurate

results compared to the other 2D methods, and the relative differences compared to FEM are quite small, less than 1%.
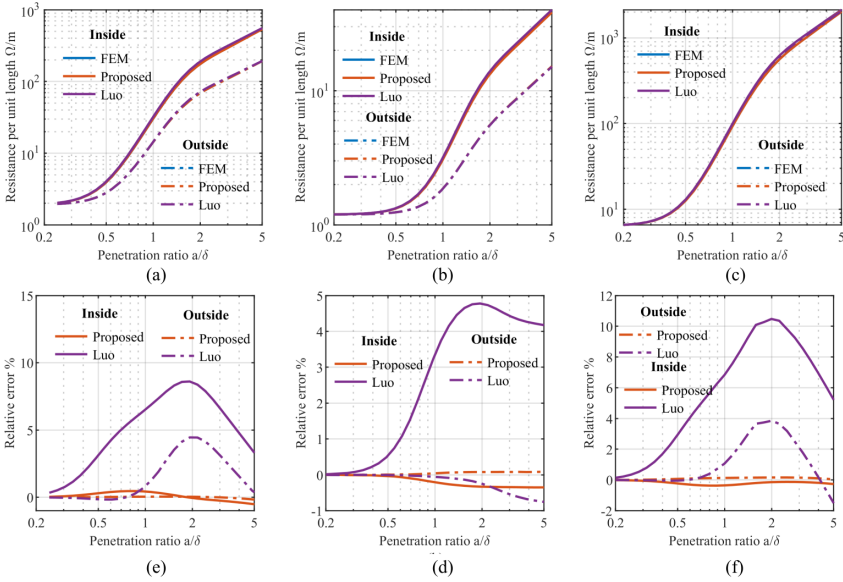
Figure 3.6: Resistances per unit length and relative error compared to 2D FEM in inductor mode with air gap, case (1), (a), (b); case (2), (c), (d); case (3), (e), (f), respectively

- Leakage inductance

Leakage inductance can also be calculated by setting the net MMF as zero. Figure 3.7 shows the estimated leakage inductance per unit length inside the core window for all cases. It is shown that the static method gradually deviates from FEM results with increasing frequencies, and the 1D method is restricted by its assumption. The proposed BEM method takes the impact of eddy current into account and can handle various winding configurations. It has less than 3% error for the entire frequency range and all cases, which is better than other methods.

- Validation by 3D FEM and measurement

In order to further validate the method in real situations, 3D FEM and measurement are done. 3D FEMs for case (1) and case (2) in both transformer and inductor modes were simulated. To guarantee the accuracy of computation, the boundary layer mesh is used, and the smallest size of an element is smaller than one-third of skin depth based on analysis in [75]. Two corresponding samples were built, and their details are listed in Table 3.4. Using different connections, two samples can become transformers or inductors. The measurements are done by the impedance analyzer Agilent 4294A.

The short circuit method was used to measure transformer leakage inductance and winding losses. The core losses are assumed to be negligible. The resonant frequency is
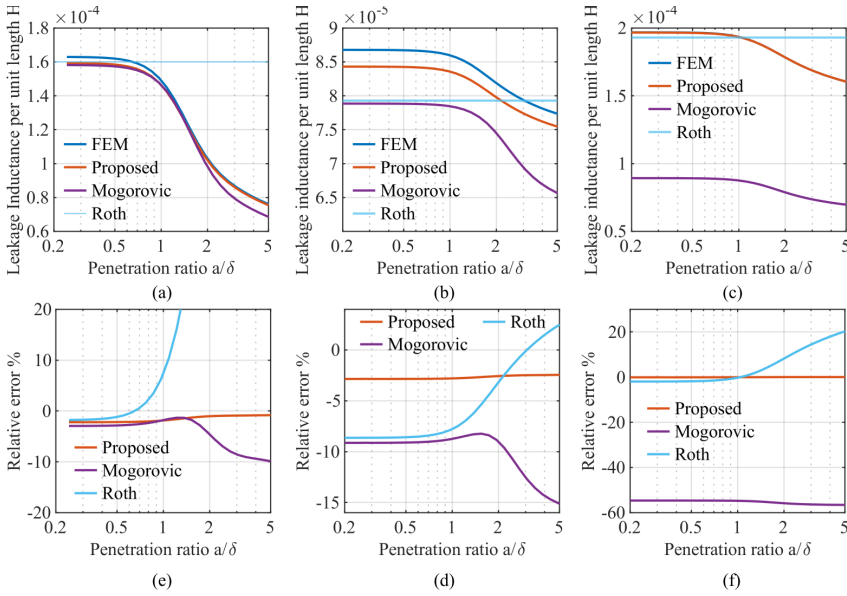
Figure 3.7: Leakage inductance per unit length and relative error compared to 2D FEM of the case (1), (a), (b); case (2), (c), (d); case (3), (e), (f), respectively

in the region $a/\delta > 15$, far from the interested region $a/\delta \leq 5$, and the measured AC resistance does not need correction. However, core loss is considerable for inductors. Due to the potential error from inaccurate complex permeability, an auxiliary transformer based on [128] is used to estimate the core loss. Besides, the impact of parasitic capacitance C_p is compensated based on an equivalent circuit of inductors, as shown in Figure 3.9. After compensation, the summation of winding resistance R_w and core resistance R_c is obtained.

Table 3.4: Basic information for samples

Sample	Case (1)	Case (2)
Core size	EE42/21/20	
Core material	N87	
Effective magnetic length l_e [mm]	97	
Effective magnetic cross-section $S_c [mm^2]$	234	
Mean turn length l_m [mm]	90.76	95.97
Partial length inside core window l_{in} [mm]	40	40
Partial length outside core window l_{out} [mm]	50.76	55.97

Estimated 2D values need scaling before comparing with 3D FEM and
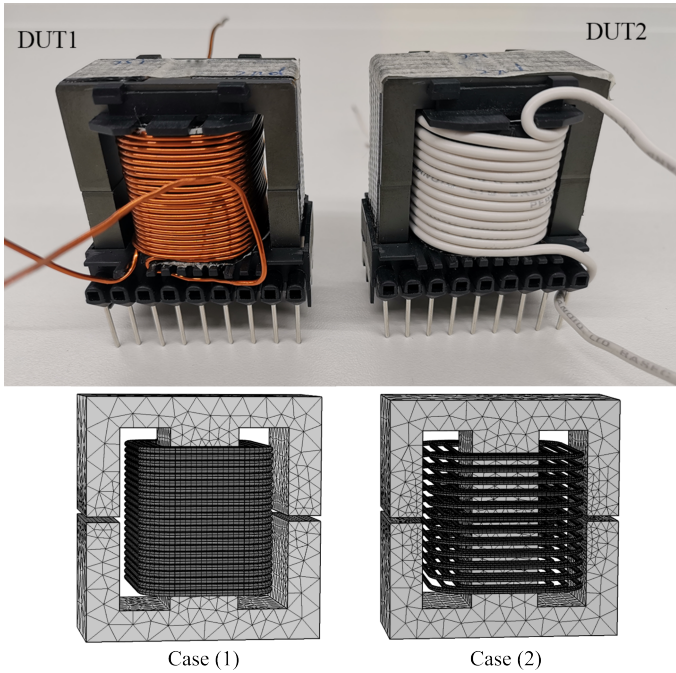
Figure 3.8: Picture and 3D FEM mesh of test samples, right is the case (1) and left is the case(2)
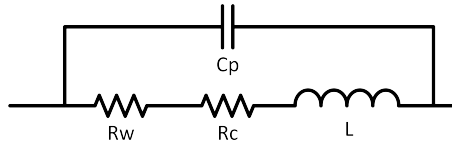
Figure 3.9: Equivalent circuit of inductors

measurement. Generally, the value is scaled by the mean turn length (MTL) l_m. However, the values inside and outside the core window can be significantly different. Then, the scaling can use a double 2D method [78], [90], [100]. Based on 2D FEM results, transformers resistances use normal MTL, leakage inductances, and inductors resistances use the double 2D method. The relevant parameters for scaling are listed in Table 3.4.

Figure 3.10 and Figure 3.11 show the AC resistance and leakage inductance for cases (1) and (2), respectively. For AC resistance in transformer mode, the scaled results are close to the results from measurement and 3D FEM in both cases. The error stays below 10% for the whole frequency range. Compared to another 2D approach, the proposed method does not perform much better. However, it can estimate the leakage inductance at the same time. For AC resistance in inductor mode, scaled resistances and 3D FEM have obviously larger differences from measurements compared to transformer mode. In both cases, 3D FEM results match 2D estimations better than
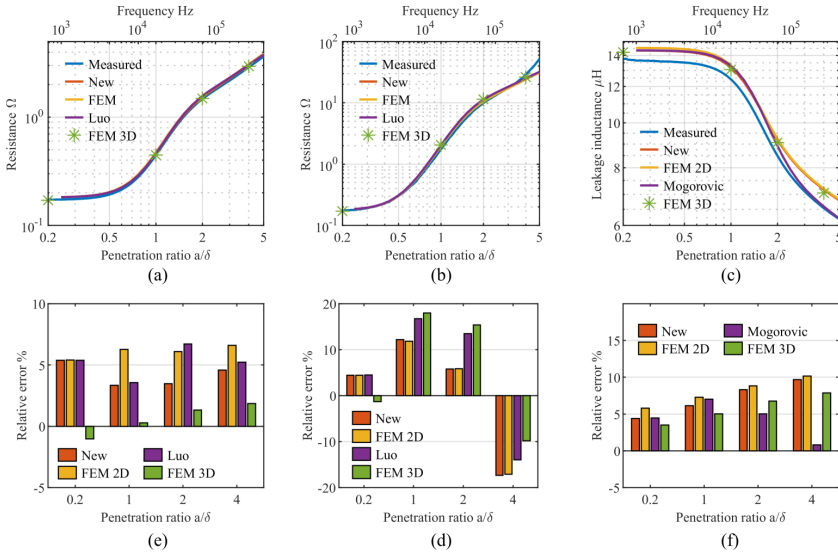
Figure 3.10: Scaled values and relative error for case (1), AC resistance in transformer mode (a),(d), AC resistance in inductor mode, (b), (e), leakage inductance, (c), (f), respectively.
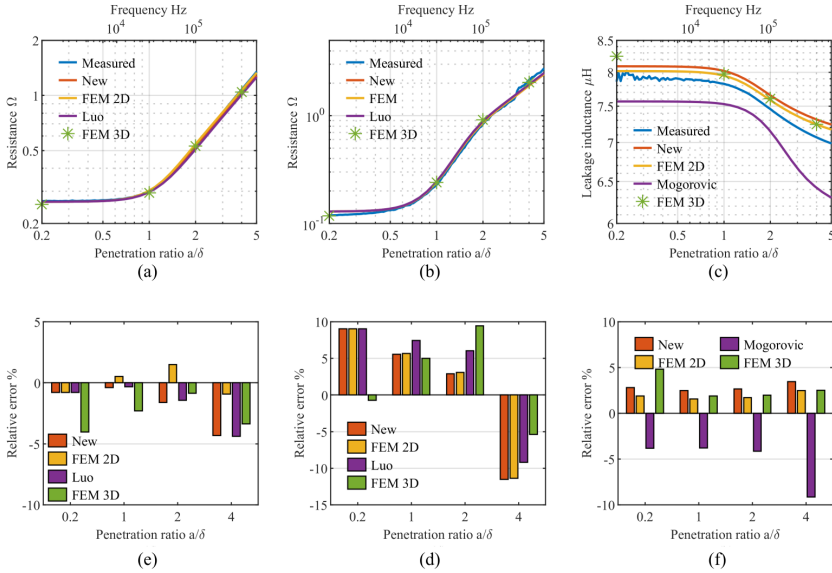
Figure 3.11: Scaled values and relative error for case (2), AC resistance in transformer mode (a),(d), AC resistance in inductor mode, (b), (e), leakage inductance, (c), (f), respectively.

measurements. The maximal error is close to 20% in case (1) and approximates 10% in case (2). Several aspects contribute to the difference between measurement and

estimation. The first one is the resonant compensation. When the testing frequency is near the resonant frequency, the impedance is very sensitive to the frequency. For this case, the accuracy of the circuit and resonant frequency are important. For case (1), the measured resonant frequency is at 493.8kHz, and the point $a/\delta = 4$ is at 270kHz, which is close to the resonant frequency. The second aspect is the inequality between the 3D and double 2D methods. The difference between the 3D FEM and scaled results implies that some error comes from this inequality. Next is the core loss prediction. When the core losses are comparable to winding losses, the error in the core loss estimation can lead to considerable differences in winding resistance. Besides, factors like imperfect geometric parameters and impedance phase measurement errors can also lead to winding resistance errors. For the leakage inductance, the relative differences between measurements and estimations stay below 10% for both cases. The scaled estimations from 2D FEM are more close to the results from 3D FEM than to the measurements.

- Computational speed

In addition to accuracy, computation time is another important feature. Table 3.5 compares computation time and degree of freedom (DoF) for three cases with 41 frequency points from FEM and the proposed method. The computation is done on a computer with Intel i7-10750H CPU 6 Cores @ 2.60GHz and 16GB RAM. For all situations, the proposed method is more than 50 times faster than FEM.

Item		Case1	Case2	Case3
	2D FEM Time	135s	64s	73s
	DoF	122353	72847	118930
Inside core window	Proposed method Time	2.09s	0.35s	1.47s
	DoF	450	180	375
	2D FEM Time	123s	63s	75s
	DoF	122844	73345	117299
Outside core window	Proposed method Time	1.12s	0.16s	0.78s
	DoF	450	180	375

Table 3.5: Computation time and degree of freedom of three cases with 41 frequency Points

Given the ability to handle various winding configurations and its comparable accuracy and rapid computational speed compared to 2D FEM, the proposed BEM & analytical coupled method is employed for calculating the AC resistance and leakage inductance in MF transformer design.

3.7.2. STATIC ELECTRIC FIELD
In a static electric field, electric potential Φ obeys Poisson's equation in the form (3.54).

$$\nabla^2 \Phi = -\frac{q}{\epsilon} \tag{3.54}$$

Through comparing (3.54) and (3.1), the relations between factors of circle elements and physical parameters as shown in (3.55). The physical properties q is the electric charge, ϵ is the permittivity, Q_c is the total electric charge inside and on a circle element, q_b is the surface charge density.

$$f_d = -\frac{q}{\epsilon} \qquad\qquad \delta = \epsilon$$

$$D_e = -\frac{Q_c}{2\pi\epsilon_e} \quad f_{b\_Neumann} = \sigma_b = -\frac{q_b}{\epsilon}$$

(3.55)

If domains inside circle elements are conductors, the f_d is 0, and there is no electric field in the domains. There are only surface charges on circle elements, and it leads to the relations in (3.56). Φ_c is the potential of the conductor, E_r is the radial direction electric field.

$$\Phi_c = C + D_e \ln(a)$$

$$\mathbf{E}_r(a,\varphi) = -\frac{D_e}{a} - \sum_{n=1}^{+\infty} 2na^{n-1}(A'_{en}\cos n\varphi + B'_{en}\sin n\varphi) = \frac{q_b(\varphi)}{\epsilon_e}$$

(3.56)

Sometimes, there is another concentric round insulation surrounding the conductor. It is assumed there is no surface charge on the interface between the background dielectric and the insulation, which is generally true in the AC situation. The relations between physical variables and circle elements' parameters become (3.57) and (3.58).

$$\Phi_c = C_e + D_e\left(\ln(b) + \frac{\epsilon_e}{\epsilon_i}\ln(a/b)\right)$$

$$-\mathbf{E}_r(a,\varphi) = \frac{\epsilon_e D_e}{\epsilon_i a} + \sum_{n=1}^{+\infty} \frac{2na^{n-1}}{T_{in}}(A'_{en}\cos n\varphi + B'_{en}\sin n\varphi)$$

(3.57)

$$T_{in} = \frac{\epsilon_i + \epsilon_e}{2\epsilon_e} + \frac{(\epsilon_i - \epsilon_e)a^{2n}}{2\epsilon_e b^{2n}}$$

$$-\mathbf{E}_r(b,\varphi) = \frac{D_e}{b} + \sum_{n=1}^{+\infty} nb^{n-1}(1+S_{in})(A'_{en}\cos(n\varphi) + B'_{en}\sin(n\varphi))$$

$$-\mathbf{E}_\varphi(b,\varphi) = \sum_{n=1}^{+\infty} nb^{n-1}(1-S_{in})(-A'_{en}\sin(n\varphi) + B'_{en}\cos(n\varphi))$$

(3.58)

$$S_{in} = \frac{((\epsilon_i - \epsilon_e)b^{2n} + (\epsilon_i + \epsilon_e)a^{2n})}{((\epsilon_i + \epsilon_e)b^{2n} + (\epsilon_i - \epsilon_e)a^{2n})}$$

When domains inside circle elements are dielectrics, it is assumed that there is no charge inside and on the circle elements. The voltage distribution inside the circle element is described by the element parameters in (3.59).

$$\Phi(r,\varphi) = C_e + \sum_{n=1}^{+\infty} \frac{2\epsilon_e r^n}{\epsilon_e + \epsilon_r}(A'_{en}\cos(n\varphi) + B'_{en}\sin(n\varphi))$$

$$-\mathbf{E}_r(r,\varphi) = \sum_{n=1}^{+\infty} \frac{2n\epsilon_e r^{n-1}}{\epsilon_e + \epsilon_r}(A'_{en}\cos(n\varphi) + B'_{en}\sin(n\varphi))$$

(3.59)

$$-\mathbf{E}_\varphi(r,\varphi) = \sum_{n=1}^{+\infty} \frac{2n\epsilon_e r^{n-1}}{\epsilon_e + \epsilon_r}(-A'_{en}\sin(n\varphi) + B'_{en}\cos(n\varphi))$$

Using the Fourier series to describe the charge on the surface has already been used in BEM [109], [125], which is also known as MoM. Compared to this, the proposed BEM can consider the insulation layer without adding polarization charges to the surface of the insulation layer. It reduces the final matrix size and can have a shorter computation time compared to normal line element BEM.

• Settings of the method

Similar to the quasi-static magnetic field, the truncated order N needs to be chosen before calculation. Besides, when there are boundaries other than circle elements, it is necessary to use the method of images or line elements. Therefore, the number of mirror actions N_r also needs to be selected. Two simple geometries, shown in Figure 3.12 (d), are used. Figure 3.12 (a) and (b) show the relative error compared to 2D FEM for two parallel wires without and with insulation layer, respectively. With increasing N, the relative error decreases. For two bare wires, the error can be reduced to below 1% when $N = 2$ and $d/2a > 1.25$. The same accuracy can be achieved when $N = 6$ and $d/2a > 1.05$. For wires with insulation wires, the error increases with decreasing $d/2b$ and b/a. If the $b/a = 1.1$, the error can be below 1%, when $N = 2$ and $d/2b > 1.2$, or when $N = 6$ and $d/2b > 1.02$.
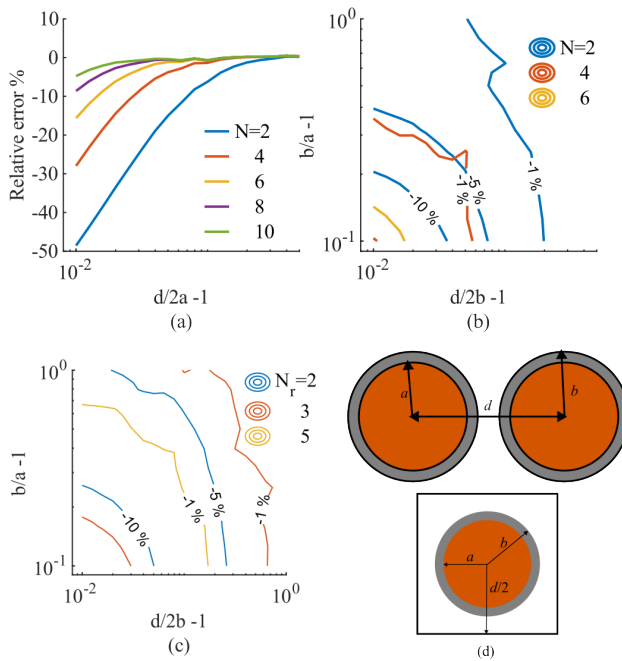
Figure 3.12: Relative error of capacitance between two parallel wires with different N compared to 2D FEM, wires without insulation layer (a); wires with insulation layer (b); relative error of capacitance between coaxial square and a wire with insulation layer and tunnel with different N_r (c); geometries used in configuration comparison. The number on the contour is the relative error in (b) and (c).

Figure 3.12 (c) shows the relative error of capacitance between a coaxial square and a

wire with an insulation layer. The calculation is performed by varying N_r while keeping $N = 6$. With higher N_r, the results have less error, and the error does not exceed 5% in the calculated range when N_r is 3. With higher N_r, the accuracy can be better, but it uses a longer computation time.

After the comparison for a simple case, the configuration $N = 6$ and $N_r = 3$ is chosen to ensure accuracy while maintaining a reasonable computational time for the case study.

- Approximate analytical equation

The proposed method can help to obtain approximate analytical capacitance equations. Two capacitance equations for two parallel wires without and with an insulation layer are provided as examples.

Firstly, the capacitance between two parallel wires without insulation layer is given by (3.60), where R_{da} is the ratio of distance d to radius a. When setting $N = 2$, the proposed BEM can provide the approximate equation (3.61). The relative error compared to 2D FEM is shown in Figure 3.13 (a). The (3.61) is closer to (3.60) with increasing R_{da}, and the error is less than 1% when $d/2a > 1.25$. It is obvious that the approximate equation cannot compete with the classic equation.

$$C = \frac{\epsilon_0 \pi}{\text{arcosh}(R_{da}/2)} \tag{3.60}$$

$$C = \frac{\epsilon_0 \pi}{\dfrac{3 - R_{da}^2 - 2R_{da}^4}{2 - 6R_{da}^2 - 2R_{da}^4 + 2R_{da}^6} + \ln(R_{da})} \tag{3.61}$$
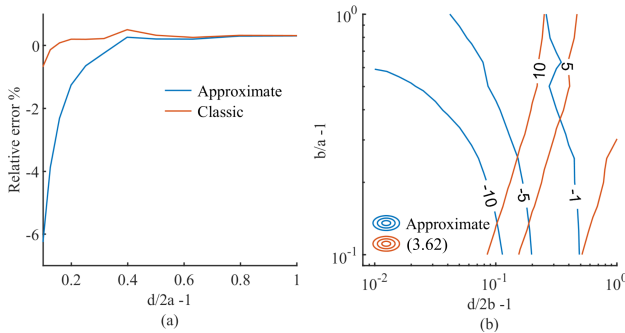
Figure 3.13: Relative error of two capacitance equations compared to 2D FEM, wires without insulation layer (a), wires with insulation layer (b).

There is not an analytical solution for parallel wires with an insulation layer. The equation, given by (3.62) [8], is derived from capacitor network, as introduced in Section 2.3. The R_{db} is the ratio of the distance d to the outer radius b, and R_{ba} is the ratio of the outer radius b to the inner radius a. When set $N = 1$, the proposed method can yield the approximate equation (3.63). Figure 3.13 (b) shows the relative error contour

compared to FEM. Equation (3.62) overestimates the capacitance, and the absolute value of error is higher than (3.63) in most cases. Equation (3.62) is obtained from a network of capacitances with assumed electric flux lines, and the error is caused by the unsatisfied assumption. These two examples show the proposed method can obtain approximate capacitance equations. With higher N, approximate equations can be more accurate, but the equations also become more complex.

3

$$C = \frac{\pi \epsilon_0}{\ln \left\{ R_{ba}^{\epsilon_0/\epsilon_{\text{ins}}} \left[R_{db}/2 + \sqrt{(R_{db}/2)^2 - 1} \right] \right\}} \tag{3.62}$$

$$C = \pi \epsilon_{\text{ins}} \epsilon_0 / \left\{ \epsilon_{\text{ins}} \ln (R_{db}) + \epsilon_0 \ln (R_{ba}) \right.$$

$$\left. + \frac{((1 + R_{ba}^2) \epsilon_{\text{ins}} + (1 - R_{ba}^2) \epsilon_0) \epsilon_{\text{ins}}}{((1 + R_{ba}^2)(1 - R_{db}^2) \epsilon_{\text{ins}} + (1 - R_{ba}^2)(1 + R_{db}^2) \epsilon_0)} \right\} \tag{3.63}$$

- Validation with simulation and measurement

The capacitance C obtained from the proposed method, FEM, Line element BEM and measurements are compared. The FEM and line element BEM simulations use different physics interfaces of COMSOL software. Five cases are simulated and measured with 1m long wires with an insulation layer to validate the proposed method. The capacitance per unit length calculated from different methods is scaled by 1m. The insulation layer is made of PVC. The measurements were done with the vector network analyzer Bode 100. The vector network analyzer used the series-thru configuration because of the high impedance of the samples. The capacitances were measured between 1kHz to 1MHz. Because the permittivity of the PVC can vary with frequencies, the relative permittivity is measured. The relative permittivity in the frequency range of measurement is fitted by the formula (3.64).

$$\epsilon_r = 4.484 - 0.2477 \log_{10} f \tag{3.64}$$

The geometries of sample cases are shown in Figure 3.14, and details are provided in Table 3.6. In cases 1 to 3, the wires are placed on the grounded plane. In cases 4 and 5, the wires are put into a grounded tunnel and are positioned along the middle line of the bottom. All cases consist of three wires, and the capacitance matrix C has the form given in (3.65). C_{aa}, C_{bb} and C_{cc} are the self-capacitance of each wire, which includes the capacitance between the wire and ground and the mutual capacitance between wires. The accuracy of simulations is verified by measuring the self-capacitance values. The capacitance is measured between one wire and the ground when two other wires are grounded. By applying the same process on three wires sequentially, three self-capacitances are obtained. Because the geometries are symmetric, all capacitances related to the side wires should be the same, for example, $C_{aa} = C_{cc}$.

$$C = \begin{bmatrix} C_{aa} & -C_{ab} & -C_{ac} \\ -C_{ab} & C_{bb} & -C_{bc} \\ -C_{ac} & -C_{bc} & C_{cc} \end{bmatrix} \tag{3.65}$$
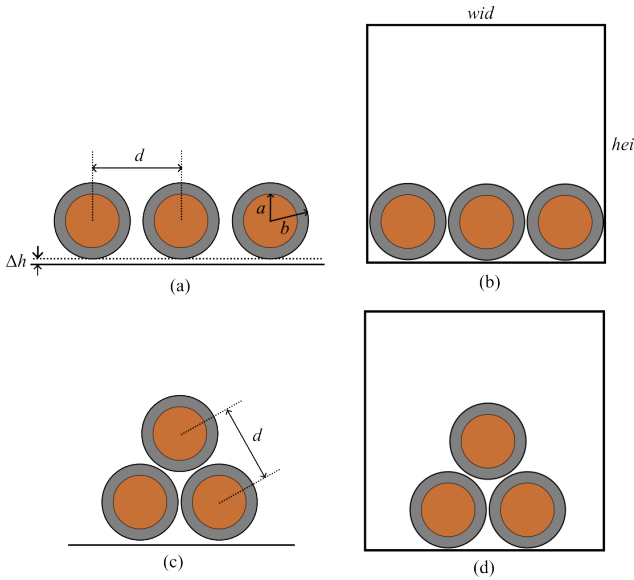
Figure 3.14: Four geometries for sample cases used in the simulations and measurements

Table 3.6: Details of geometries of 5 cases

No.	case 1	case 2	case 3	case 4	case 5
Type	(a)	(a)	(b)	(c)	(d)
d [mm]	8.5	20	8.5	8.5	8.5
b [mm]			4.25		
a [mm]			2.65		
Δh [μm]			85		
wid [mm]		Not Applied		30	
hei [mm]		Not Applied		30	

Figure 3.15 compares the capacitance of five cases from the measurement, the proposed method and 2D FEM. The results from the proposed method and 2D FEM overlap in all five cases. This implies that the proposed method can correctly calculate the capacitance of the geometries considered. In the frequency range of the measurement, the changes in measured capacitance follow the trend of the fitted relative permittivity curve. For case (1), as shown in Figure 3.15 (a), the measured C_{aa} is roughly higher than calculated results by 2 to 4%, the measured C_{bb} is lower than calculated results by up to 3%. The difference between the C_{aa} and C_{bb} is about 30pF, which is less than the capacitance between two wires with the same d, which is 50pF. It indicates that the summation of capacitance can lead to more than 10% error in compact wire arrangements. For the other two cases with one plane ground, the error compared to measurement is up to about 2%. Cases (4) and (5) have the same wire arrangements as cases (1) and (3), respectively. The C_{bb} only has a slight increase in
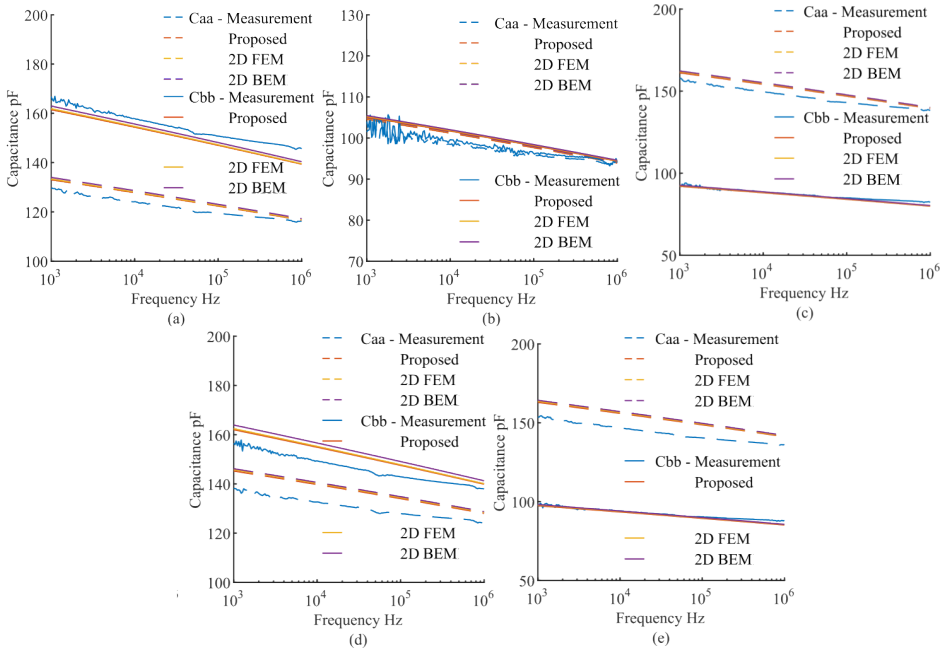
Figure 3.15: Capacitance of 1m wires from measurement, the proposed method, 2D FEM and 2D BEM with line element. (a)-(e) for case (1)-(5), respectively.

both cases because the upper boundary of the tunnel is a bit away from the middle wire and does not impact the capacitance much. The C_{aa} in cases (4) and (5) are around 10pF higher than the value in cases (1) and (3) because the tunnel is close to the wire and has stronger impact. In cases (4) and (5), shown in Figure 3.15 (d) and (e), the error remains up to 7%, which is higher than the cases with one ground plane. It may be caused by the imperfect matching between the real geometries in tunnels and the geometries in the calculation.

Based on the comparison between results from measurements, 2D FEM and the proposed method, the validation of the proposed method is proven. Besides, the proposed method also shows faster computational speed. 2D FEM and BEM, which are done with COMSOL, use 2min 57s and 2min 17s, respectively. The proposed method only uses 1.40s.

3.7.3. STATIONARY THERMAL CONDUCTION

Thermal conduction is described by PDE in (3.66), where T is temperature, t is time, Q_h is the heat generated per second in the circle elements, α is thermal diffusivity, k_c is thermal conductivity, c_p is specific heat capacity, ρ is density.

$$\frac{\partial T}{\partial t} = \alpha \nabla^2 T + \frac{Q_h}{c_p \rho}, \ \alpha = \frac{k_c}{c_p \rho} \tag{3.66}$$

In a stationary situation, the PDE becomes (3.67), and the relations between factors

of elements and physical parameters are shown in (3.68).

$$\nabla^2 T = -\frac{Q_h}{k_c} \tag{3.67}$$

$$f_d = -\frac{Q_h}{k_c} \qquad\qquad \delta = k_c$$

$$D_e = -\frac{Q_h}{2\pi k_{ce}} \qquad f_{b\_\text{Neumann}} = \sigma_b = -\frac{Q_{hb}}{k_{ce}} \tag{3.68}$$

When Q_h is a constant, the average $\bar{T}$ over the domain in the circle element is given by (3.69). It is also possible that the domain inside the circle element is composed of two concentric media with different thermal conductivity.

$$\bar{T} = C_e + D_e \left(\ln(a) + \frac{k_{ce}}{4k_{cr}} \right)$$

$$\bar{T} = C_e + D_e \left(\ln(b) + \frac{k_{ce}}{k_{cr2}} \ln\frac{a}{b} + \frac{k_{ce}}{4k_{cr}} \right) \tag{3.69}$$

As introduced in Section 2.4, a lumped thermal circuit is preferred due to its simplicity. If the node is chosen reasonably, the estimated temperature rise has an acceptable result compared with the result from CFD. However, there is still one problem that needs to be solved, which is the thermal resistance of windings. The windings are composed of conductors and insulation, which have a rather complex structure than the core. At the same time, hot spots are often present in the windings. Thus, it is necessary to obtain an accurate thermal resistance. In general, an equivalent thermal conductivity is extracted firstly [44], [129]–[131]. Because the winding is impregnated by the insulation material, there is no heat transfer mechanism other than thermal conduction. Therefore, the windings material can be approximated by a linear property, and the proposed method can used to calculate equivalent thermal conductivity.

- Settings of the method

Because the heat flux of interest is the outer boundary, the line element is used. The truncated order N and the length of the line element need to be set before calculation.
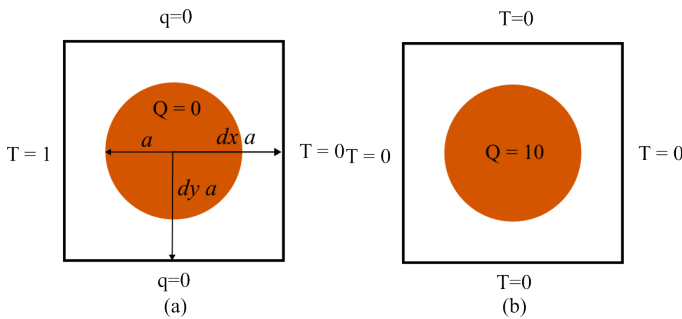
Figure 3.16: Illustration of geometry used for deciding settings of the method.

A simple geometry with two situations is used to have a basic understanding of their impact on the accuracy. As given in Figure 3.16, the first situation is that there is no heat generated in the conductor, and a temperature difference exists. The second is that all boundaries have the same temperature, and some heat is generated inside the conductor. The round conductor is assumed to be copper with 400 W/(m·K), and the insulation is assumed to have 0.5 W/(m·K).

The results are compared in Figure 3.17, (a) and (b) compared the error of flow-in heat flux with different line element lengths under various widths and heights. The truncated order is set as 4. The length uses the radius of a conductor as the unit length. It is obvious the error is larger when the length is the same as the radius. When the length reduces to half of the radius, the accuracy is effectively improved. With further reduction in length, the improvement is not considerable. Besides, the smaller the geometry, the smaller the length is needed. Therefore, the length choice varies with different winding packing.
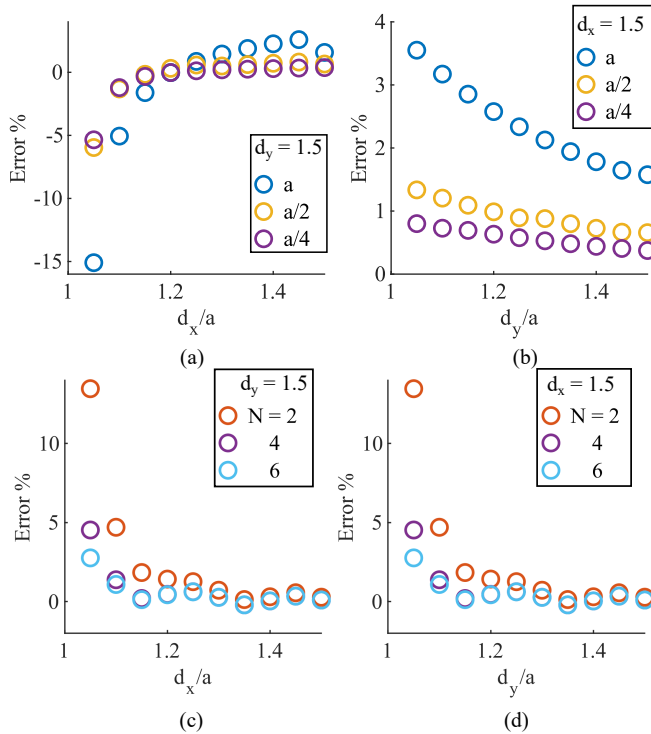
Figure 3.17: Relative error of flow-in heat flux with different line element lengths (a), (b), and relative error of temperature rising with different truncated order (c), (d), compared to 2D FEM.

Figures (c) and (d) show the impact of truncated order on the temperature-rising estimation. The length of the line element is set as $a/2$. With increasing order N, the accuracy is better, and the difference between order 4 and 6 is not obvious. Also, geometry influences the order choice. Therefore, considering the accuracy and

computational speed, the order N is set as 4, and the length of the line element is set as $a/2$ when $d_x/a \le 1.1$, otherwise, they are set as 2 and a, respectively.

- FEM validation

In order to validate the accuracy of the proposed method in calculating equivalent thermal conductivity. The equivalent thermal conductivity of the windings used in AC resistance estimation is calculated. The winding is assumed to be impregnated in the epoxy with $0.6\,\mathrm{W/(m \cdot K)}$. The case (2) has a PVC insulation around the conductor, whose thermal conductivity is set as $0.2\,\mathrm{W/(m \cdot K)}$. The loss in each conductor uses the case when the net MMF is zero, and the frequency is 5kHz and is set as the corresponding heat source. The windings can be regarded as an anisotropic medium in general; each direction needs to be calculated separately.

Figure 3.18 shows the temperature distribution of two winding cases when both left and right side boundaries are set as the reference temperature. Table 3.7 shows the results that come from the 2D FEM and the proposed method. For case (1), the heat flux on the two boundaries is almost the same from the two methods. The highest temperature rising is about 10% higher than FEM. For case (2), the temperature and flux from the two methods have a trivial difference. The FEM validate the effectiveness of the proposed method in calculating the equivalent of the thermal resistance of windings.
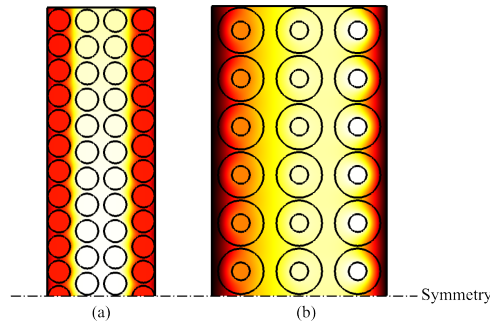
Figure 3.18: Temperature distribution from 2D FEM with internal heat generation.

3.8. CONCLUSION

THIS chapter presents a 2D circle boundary element & analytical coupled method, including mathematical part and applications in three different physical situations, i.e., quasi-static magnetic field, static electric field and stationary thermal conduction. The method was developed for several reasons. One is the trade-off between accuracy and the requirement of computational resources. The second reason is the small element number of boundary element method. The third reason is the match between the circle element and the conductor shape, which further reduces the element number. In the applications, the proposed method is used to calculate AC resistance,

	FEM		Proposed	
	Case (1)	Case(2)	Case(1)	Case(2)
ΔT_{max} K	0.024	0.243	0.026	0.243
Flux W/m	1.125	0.804	1.121	0.807
	1.124	1.604	1.120	1.611
Thermal Resistance	0.021	0.302	0.023	0.301
W/(m·K)	0.021	0.152	0.023	0.151

Table 3.7: The equivalent thermal resistance obtained from FEM and proposed method.

3

leakage inductance, stray capacitance and equivalent thermal resistance. The calculation is validated by FEM simulations and measurements. In all sample cases, the proposed method shows good accuracy compared to FEM, with less than 10% errors compared to measurements. Additionally, the computational time is an order of magnitude shorter than that of 2D FEM.

4

LITZ WIRE MODEL

Simple can be harder than complex.

Steve Jobs

This chapter focuses on analyzing Litz wires, which are commonly used for suppressing eddy currents. The primary focus is on losses, particularly those resulting from imperfect twisting. Two Litz wire models are proposed for modelling imperfect twisting Litz wires. One is based on the 2.5D approximation and round boundary element analysis. Another is a 3D model with cylindrical elements, which extends from 2D analysis to 3D. Both models are validated by 3D FEM and demonstrate good accuracy and fast computational speed. Additionally, the chapter explores the method to incorporate the Litz wire model into the winding model. The key idea of homogenization is adopted, which is validated through measurements.

4.1. INTRODUCTION

WINDING losses calculation is a basic step in the transformer or inductor design. In medium-frequency applications, eddy current cannot be neglected as in low frequency. To achieve high efficiencies, Litz wires are widely used to suppress eddy currents. Litz wires consist of dozens or hundreds of strands; each strand is electrically isolated from the others. Then, the strands are twisted together in single or multiple stages. A complex structure is built, as shown in Figure 4.1. Through twisting, Litz wires can dramatically reduce the proximity effect losses caused by the external magnetic field and average the current distribution in strands.

$\qquad$ (a) $\qquad$ (b) $\qquad$ (c)
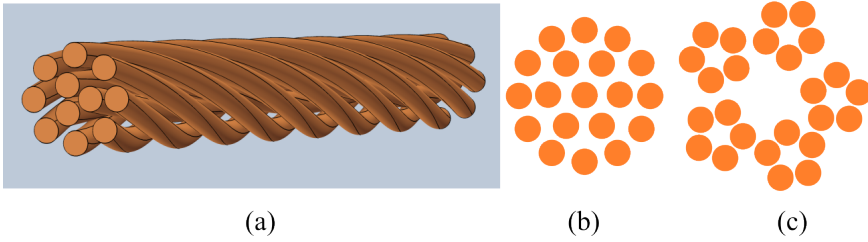
Figure 4.1: Illustration of Litz wire structure, 3D view (a), cross-section of single stage twisting (b), and cross-section of multi stage twisting (c).

In order to select suitable Litz wires, an accurate model is necessary, especially the AC resistance model. Because of complex structure of Litz wires, assumptions are used to facilitate the modelling. One popular assumption is that the twist is perfect and each strand has the same current and proximity losses due to external magnetic field [32], [132]–[134]. However, the practical twisting cannot achieve the perfect performance, and Litz wire models need to consider the twist effect [135], [136]. 3D FEM generally can provide accurate results [137], but it requires high computation resources and long computational time. In order to accelerate the computational speed, methods like partial element equivalent circuit (PEEC) [33], [138], [139], homogenisation [134], 2.5D approximation [140] and thin wire approximation [141] are developed.

In this chapter, the basic Litz wire model based on the perfect twisting assumption is briefly introduced. Then, a 2.5D approximation model is presented, which is based on the 2D BEM & analytical coupled method in Chapter 3. Next, a 3D model based on cylindrical elements is introduced, which extends the relation obtained from 2D to 3D situations. Finally, the homogenization technique is used to couple the Litz wire model with the whole winding model.

4.2. PERFECT TWISTING LITZ WIRE MODEL

THE eddy currents in Litz wires can be categorised into skin and proximity effects, and each effect can happen at bundle and strand levels [133], [135]. Strand level effects only relate to eddy current in single strand, whereas bundle level effects relate to eddy current circulating in multi strands, as shown in Figure 4.2. The perfect twisting assumption leads to the disappearance of the bundle-level eddy currents, which dramatically reduces the complexity of modelling.
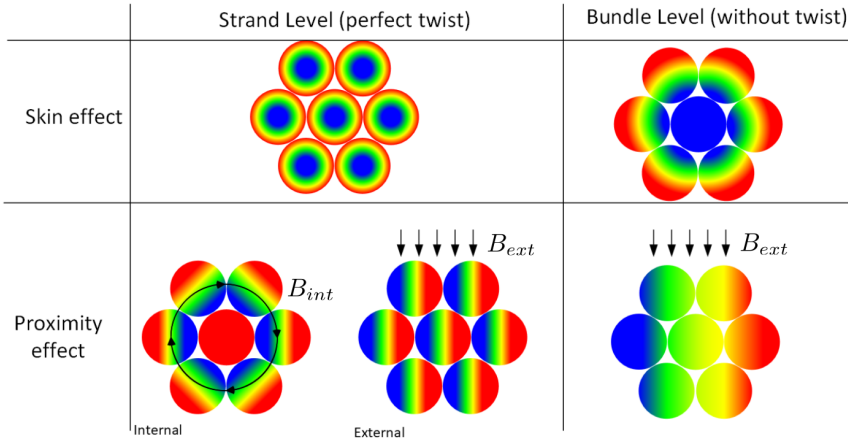
Figure 4.2: Conceptual illustration of the types of eddy currents in Litz wires.

The composition of strand level eddy current has skin effect, internal proximity effect and external proximity effect (4.1). The internal proximity effect is caused by the magnetic field induced by other turns in the same Litz wire, and the external proximity effect is incurred by the magnetic field from other wires. The different induced voltage among strands causes the bundle level eddy currents. Figure 4.2 shows the situation without twisting is similar to a single conductor.

$$P_{stand} = P_s + P_{int} + P_{ext} \tag{4.1}$$

1. Skin effect

Skin effect is the result of the self-induced magnetic field, which is only related to the cross-section geometry. With the perfect twisting assumption, all strands have the same skin effect. The losses can be estimated based on skin effect of a single strand. For round cross-section strands, the skin effect losses can be calculated by Ferreira's formula (4.2), where I_s is the peak current value flowing in a strand, a is the radius of a strand, n is number of strands, κ equal to $\sqrt{-j\omega\sigma_c\mu}$.

$$P_s = \frac{nI_s^2}{\pi a^2 \sigma} \Re\left(\frac{J_0(\kappa a)}{J_0(\kappa a) + J_2(\kappa a)} \right) \tag{4.2}$$

2. Proximity effect

Two magnetic field components, i.e., external applied field, H_{ext} and internal collective field of the strands, H_{int}, cause the proximity effect. The square of the magnetic field is given by (4.3).

$$H^2 = H_{ext}^2 + H_{int}^2 + 2H_e H_{int} \tag{4.3}$$

Because H_{int} is an rotational symmetry function across the cross-sections of round conductors and H_{ext} is assumed to be constant across the bundles, the average contribution of the third term in the above equation is zero over the cross-section of the Litz bundle [132]. Thus, two magnetic field components can be analysed separately.

If Litz wires have round cross-section and are composed of round wires, the proximity effect can be calculated by (4.4) and (4.5).

- Internal proximity effect

$$H_{int}(r) = \frac{\pi r^2 I}{\pi r_0^2} \frac{1}{2\pi r} = \frac{Ir}{2\pi r_0}$$
$$G_p = -2\pi\mu a^2\omega\Im\left(\frac{J_2(\kappa a)}{J_0(\kappa a)}\right) \qquad (4.4)$$
$$P_{int} = \int_0^{r0} \frac{2n\pi r}{\pi r_0^2} G_p H_{int}^2 \mathrm{d}r = \frac{nG_p I^2}{8\pi^2 r_0^2}$$

- External proximity effect

$$P_{ext} = nG_p H_{ext}^2 \qquad (4.5)$$

4.3. Imperfect twisting Litz wire model

PERFECT twisting asks each strand should be averagely located in both radial and azimuthal scale along the whole wire. It is hard to achieve, and imperfect twisting is more likely to happen in the Litz wire. The result of imperfect twisting is an unbalanced current distribution in each strand and a non-uniform magnetic field applied to each strand.

From the circuit point of view, the current distribution is directly determined by the impedance matrix. As Figure 4.3 shows, each strand current is decided by DC resistance R_{dc}, resistance due to skin effect R_{skin}, self-inductance L_s, and induced voltage due to proximity effect γi_{proxi} and induced voltage due to mutual inductance V_{mutual}. Among these elements, R_{dc}, R_{skin} and L_s are decided by the strands themselves, which are the elements on the main diagonal of the impedance matrix. Mutual inductance contributes to the non-diagonal elements. The γi_{proxi} depends on the current i_{proxi} in the second circuit. The magnetic field induces potential difference, which leads to the proximity effect. The dependent voltage sources βi represent the magnetic fields caused by currents i in strands. It can contribute to all terms in the impedance matrix.

The external magnetic field is also related to the impedance matrix. For simplicity, the external field is assumed to be uniform and should be the same for each strand. However, the uniform field results in different magnetic vector potentials on strands, which can lead to circular current between strands. Besides, the magnetic field generated by the eddy current can change the field on each strand. These impacts should also be shown in the impedance matrix. Therefore, there are several more dimensions representing the external fields in the impedance matrix.
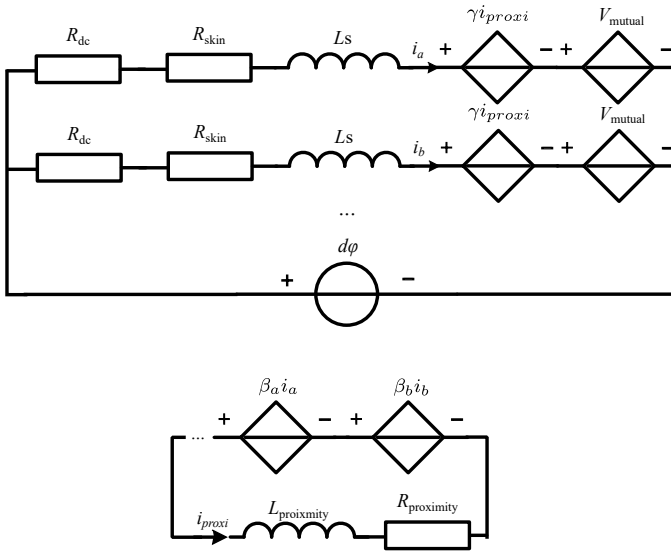
Figure 4.3: Equivalent circuit of Litz wire

Therefore, to model the unbalanced current distribution and non-uniform magnetic field, the impedance matrix is needed. To obtain the matrix, more details about the structure of Litz wires are needed.

4.3.1. LITZ WIRE STRUCTURE CONSTRUCTION

Structure information is important for building imperfect twisting Litz wire models. A recursive multilevel bundle structure [142] is adopted in the thesis. The inputs include the number of twisting stages, the number of strands or sub-level bundles in each stage, the construction of each basic level bundle, strand radius, insulation thickness and pitch. The structure is built with the recursive method. In general, each level trajectories are decided by the previous level trajectory and the radius of this level bundle position, as shown by Figure 4.4. This relation can be described by (4.6).

$$t_n(x, y, z) = t_{n-1}(x, y, z) + R_{n,pos} \cos(\lambda_n \varphi) \cdot \overrightarrow{n_{n-1}} + R_{n,pos} \sin(\lambda_n \varphi) \cdot \overrightarrow{b_{n-1}} \qquad (4.6)$$

The $t_n(x, y, z)$ is the trajectory of nth level bundle, φ is the global curve parameter in the range of 0 to 2π, $R_{n,pos}$ is the nth level bundle relative position to the trajectory of $n-1^{\text{th}}$ level bundle, λ_n is the ratio of the nth level bundle pitch to the global wire pitch, and $\overrightarrow{n_{n-1}}$ and $\overrightarrow{b_{n-1}}$ are two normalised vectors in Frenet–Serret frame, which is perpendicular to the $n-1^{\text{th}}$ level bundle curve. Several conditions from [33], [137] are used to avoid the overlapping of trajectories.
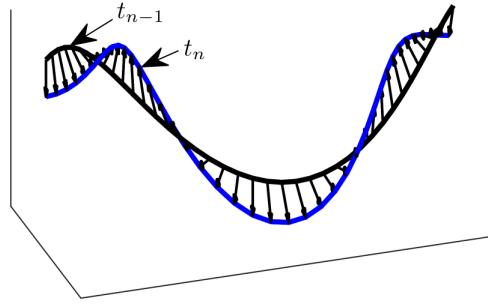
Figure 4.4: Illustration of the relation between two level's tracks

4

4.3.2. Litz wire model with 2.5D approximation

The 2.5D approximation uses several 2D cases to approximate the 3D situation [140]. The 2.5D method assumes the twisting far from the targeted section does not cause much deviation from the 2D situation, and the longitudinal current plays the dominant role, i.e., the currents flowing in azimuthal and radial directions are neglected. Litz wire strands mainly extend in longitudinal direction, which complies with the assumptions. The proposed 2.5D model uses the BEM & analytical coupled method in Chapter 3, which does not need discretization procedures for round conductors. The method guarantees accuracy and fast computational speed compared with 2D FEM.

After constructing the Litz wire, the construction is sliced into several sections, and each section is represented by a cross-section of Litz wires, as shown in Figure 4.5. Then, the 3D Litz wire model becomes several 2D models.
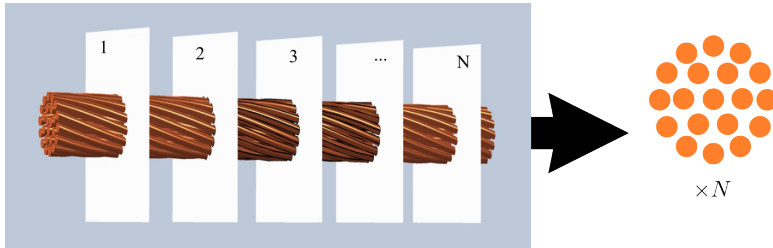
Figure 4.5: Illustration of slicing the Litz wire into sections

To calculate the Litz wire loss with 2.5D approximation, the procedure shown in Figure 4.6 is followed. External magnetic field and strand current distribution are the key information to determine the loss. The static magnetic field is considered for the external magnetic field. In other words, the change of the external magnetic field due to eddy current is neglected. The field strength can be calculated with various methods like FEM, Biot-Sarvat law, and its results differ from case to case.

The external magnetic field is the flux term and can be added to the BEM matrix as part of the flux contribution. The relation between the magnetic field and the constant
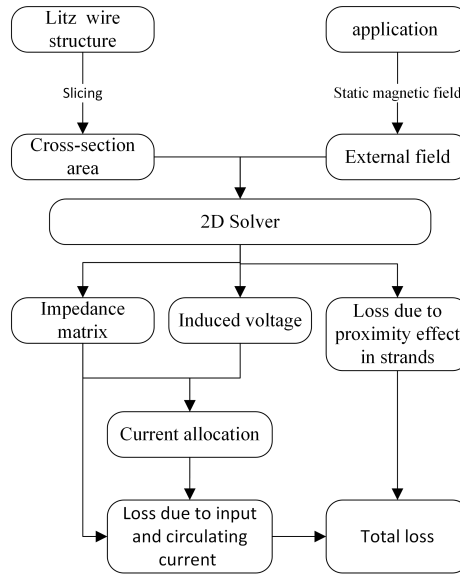
Figure 4.6: The flow chart for 2.5D approximation method.

and harmonic terms is given in (4.7). (x, y) is the vector point to the conductor from the centre of the cross-section of Litz wire. It is used to consider the difference existing in induced magnetic vector potential.

$$
\begin{array}{ll}
1 & \mu_0(H_x y - H_y x) \\
\cos\varphi & -\mu_0 H_y \\
\sin\varphi & \mu_0 H_x
\end{array}
\tag{4.7}
$$

As described at the beginning of the section, the allocation of strand currents is solved by computing the impedance matrix between the strands. The impedance matrix of the entire Litz wire is obtained by summing the impedance matrices of each cross-section, weighted by their respective lengths (4.8). The c represents the difference sections.

$$
Z_{Litz} = \sum_c Z_{ac}(c) \times l(c)
\tag{4.8}
$$

The impedance matrix of each cross-section is obtained by sweeping each strand with setting one strand current as 1A and others as 0A. The value is calculated based on (4.9). The induced voltage due to the external magnetic field can also be calculated in the same way. The induced voltage of one cross-section area is solved by setting all strands' current as 0A. When calculating the induced voltage, the proximity effect loss in strands is also obtained by the Poynting factor in Chapter 3. Then, the current distribution can be

obtained by equating the voltage drop on each strand. Finally, the loss can be calculated using the current impedance matrix and the proximity effect loss in strands.

$$-\nabla\phi = R_{dc} I + \frac{1}{S_c} \oiint j\omega A \, ds \tag{4.9}$$

4.3.3. Cylindrical element based 3D Litz wire model

PEEC is a promising numerical method which approximates the field problem with an electrical equivalent circuit [138], [139]. In [139], formulas from [132] are used to reduce discretization effort, which assumes a uniform magnetic field across the cross-section of strands and neglects the impact of eddy current on magnetic field at the same time. However, it has already been proven that the eddy current impacts the field distribution, especially when the conductor is compactly arranged and $a/\delta \geq 1$. Based on the order comparison in the preceding section, the order does not show a significant impact on the results. Besides, the current except longitudinal direction is ignored based on the assumption. Therefore, a cylindrical element-based Litz wire model is proposed, extending from 2D analysis with 1st order Fourier series to 3D. The discretization is shown in Figure 4.7. The cylindrical element leads to a small number of elements. The analytical analysis guarantees that it does not sacrifice accuracy.
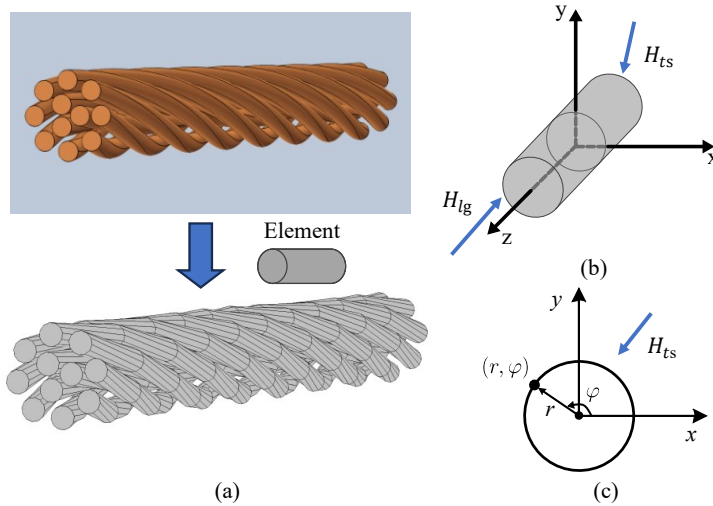
Figure 4.7: Illustration of Litz wire discretization with cylindrical elements (a), illustration of transverse and longitudinal magnetic fields on an element in 3D Cartesian coordinates (b), illustration of the transverse field in polar and 2D Cartesian coordinates.

As described in the circuit analysis, the impedance matrix plays a key role in determining the performance of Litz wires. Therefore, the primary problem is analysing strands' interactions and representing these interactions in the impedance matrix Z, which is composed of DC resistance R_{dc}, impedance from transverse field Z_{ts} and longitudinal field Z_{lg}. Two assumptions are made for this analysis. The first one is that the current flows along the paths of strands. The next one is the independence between

eddy currents caused by transverse and longitudinal magnetic fields.

$$Z = R_{dc} + Z_{ts} + Z_{lg} \tag{4.10}$$

1. Transverse magnetic field

Transverse magnetic field H_{ts} is the main factor causing eddy current in Litz wires. In Chapter 3, the 2D analysis for a round conductor gives a general solution of magnetic vector potential A, as shown in (4.11), when only considering 1st order Fourier series term [143]. The coefficient C is the vector potential contributed by other currents, D relates to the current I the conductor carrying, coefficients A'_1, A''_1, B'_1 and B''_1 relate to the 1st order Fourier series term.

$$A(r,\varphi) = C + D\ln(r) + \left(r A'_1 + \frac{A''_1}{r}\right)\cos(\varphi) + \left(r B'_1 + \frac{B''_1}{r}\right)\sin(\varphi) \tag{4.11}$$

If there are only round conductors, after converting coordinates to Cartesian coordinates, the relation like (4.12) is built for 2D situations.

$$
\begin{aligned}
C_i \quad & + \sum_{j\neq i} A''_{j1} \frac{x_{ji}}{x_{ji}^2 + y_{ji}^2} \quad + \sum_{j\neq i} B''_{j1} \frac{y_{ji}}{x_{ji}^2 + y_{ji}^2} \quad = \quad \sum_{j\neq i} \frac{D_j}{2}\ln(x_{ji}^2 + y_{ji}^2) \\
A'_{i1} \quad & + \sum_{j\neq i} A''_{j1} \frac{x_{ji}^2 - y_{ji}^2}{(x_{ji}^2 + y_{ji}^2)^2} \quad + \sum_{j\neq i} B''_{j1} \frac{2x_{ji}y_{ji}}{(x_{ji}^2 + y_{ji}^2)^2} \quad = \quad \sum_{j\neq i} D_j \frac{x_{ji}}{x_{ji}^2 + y_{ji}^2} \\
B'_{i1} \quad & + \sum_{j\neq i} A''_{j1} \frac{2x_{ji}y_{ji}}{(x_{ji}^2 + y_{ji}^2)^2} \quad - \sum_{j\neq i} B''_{j1} \frac{x_{ji}^2 - y_{ji}^2}{(x_{ji}^2 + y_{ji}^2)^2} \quad = \quad \sum_{j\neq i} D_j \frac{y_{ji}}{x_{ji}^2 + y_{ji}^2}
\end{aligned} \tag{4.12}
$$

The relations between some coefficients are listed in (4.13), J_n is the first kind of Bessel function, the subscript n is the order.

$$D = -\frac{\mu_0 I}{2\pi} \quad A''_1 | B''_1 = \frac{a^2 J_2(\kappa a)}{J_0(\kappa a)} A'_1 | B'_1$$
$$\kappa^2 = -j\omega\sigma\mu \tag{4.13}$$

Based on the relation between D and current I, it is found that the right side of equations in (4.12) are the vector potential A, the flux density $-B_y$, B_x caused by the current in conductor j in 2D. Besides, the first row of the left-hand side of the equal has the same geometric part. Therefore, these three geometric parts in the matrix can be replaced by the one in Biot-Sarvart law in 3D situations (4.14).

$$
\begin{aligned}
B_x &= -\frac{\mu_0 I}{2\pi} \frac{y}{2(x^2 + y^2 + z^2)^{3/2}} \\
B_y &= \frac{\mu_0 I}{2\pi} \frac{x}{2(x^2 + y^2 + z^2)^{3/2}}
\end{aligned} \tag{4.14}
$$

Then, there are two left geometric parts in the second and third rows. Through analogy, the equation in (4.15) is the 3D version of the two left geometric parts. All terms in the 3D version of (4.12) are known.

$$G_x = \frac{3xy}{2(x^2 + y^2 + z^2)^{5/2}} \qquad \int_{-\infty}^{\infty} G_x dz = \frac{2xy}{(x^2 + y^2)^2}$$

$$G_y = \frac{3(x^2 - y^2)}{4(x^2 + y^2 + z^2)^{5/2}} \qquad \int_{-\infty}^{\infty} G_y dz = \frac{x^2 - y^2}{(x^2 + y^2)^2}$$

(4.15)

Therefore, a matrix describing the relationships about the transverse field between cylindrical elements can be formed. It is also known that the skin effect is independent of the proximity effect in 2D and only related to radius a. So, the skin effect in Z_{ts} is calculated independently. After solving the matrix, each element's magnetic vector potential A's composition is obtained. Combining with the skin effect part, the Z_{ts} is obtained.

If only accounting for a uniform transverse external field, the portion of the proximity effect can be obtained by (4.16). H_{ik} and H_{jk} are the transverse field applied on element k from strand i and j, respectively. Element k can denote all elements. Subsequently, an approximate Z_{ts} for low frequencies is obtained.

$$Z_{ts\_pij} = -\frac{2\pi\kappa a J_1(\kappa a)}{\sigma J_0(\kappa a)} \sum_k H_{ik} H_{jk}$$

(4.16)

2. Longitudinal magnetic field

In general, the longitudinal magnetic field H_{lg} is neglected because of trivial longitudinal magnetic fields when the strands have a relatively long pitch. Here, the term associated with the longitudinal magnetic field is added to double-check the assumption. By solving a round conductor subjected to a uniform longitudinal field in 2D, the equation (4.17) is obtained by integrating the Poynting vector over the perimeter. The real part of S is the loss, and the imaginary part is the reactive power. If H_{lg-ik} and H_{lg-jk} are longitudinal fields applied to k caused by a unit current in i and j element, the impedance Z_{lg_ij} is calculated with (4.18). The impact of the generated eddy current is neglected.

$$S = -\frac{2\pi\kappa a J_1(\kappa a)}{\sigma J_0(\kappa a)} H_{lg}^2$$

(4.17)

$$Z_{lg\_ij} = -\frac{2\pi\kappa a J_1(\kappa a)}{\sigma J_0(\kappa a)} \sum_k H_{lg\_ik} \cdot H_{lg\_jk}$$

(4.18)

3. Litz wire's impedance matrix

The impedance matrices can be generalized into (4.19), $\mathbf{Z}_{ss}$ is the impedance matrix among the strands, $\mathbf{Z}_{sw}$ characterizes the voltage induced by a unit external magnetic field, $\mathbf{Z}_{ww}$ characterizes the energy consumed in the Litz wire caused by a unit external magnetic field. $\mathbf{Z}_{ws}$ represents the impact of current in strands on the source of external magnetic fields.

$$\mathbf{Z}_{Litz} = \begin{pmatrix} \mathbf{Z}_{ss} & \mathbf{Z}_{sw} \\ \mathbf{Z}_{ws} & \mathbf{Z}_{ww} \end{pmatrix}$$

(4.19)

First, the $\mathbf{Z}_{ss}$ is analyzed, and the size of it is $n_s \times n_s$, where n_s is the number of strands. The n row m column element in $\mathbf{Z}_{ss}$ represents the relationship between strand n and m. As described at the beginning of this section, each strand circuit elements can be separated into two parts.

The first part is the elements decided by the strand itself, involving DC resistance R_{dc}, resistance due to skin effect R_{skin} and self-inductance L_{s}. From the cylindrical element point of view, it is represented by R_{dc} in (4.9) and D related terms in (4.13). Since the current is the same for all cylindrical elements in a strand, this part is the summation of the production of the impedance of unit length and l_k for the elements in a strand, as shown in (4.20), where l_k is the length of element k.

$$Z_{self-n} = \sum_{k \in n} \left(R_{\mathrm{dc}} - \frac{\mu_0}{2\pi} (\ln a - \frac{J_2(\kappa a)}{\kappa a J_1(\kappa a)}) \right) l_k \qquad (4.20)$$

The second part relates to the mutual effect between strands involving two dependent voltage sources. One voltage source V_{mutual} is induced by mutual inductance, and the other is $\gamma i_{\mathrm{proxi}}$, which is caused by the proximity effect. Mutual inductance contributes to the non-diagonal elements in $\mathbf{Z}_{ss}$. The right-hand side of the equation in the first row of (4.12) represents the magnetic vector voltage in element i caused by j and is denoted by $A_{mutL-ij}$ for simplicity. The impedance due to mutual inductance is given in (4.21).

$$Z_{mutL-nm} = \sum_{i \in n} \sum_{j \in m} j\omega \frac{A_{mutL-ij}}{I_m} \qquad (4.21)$$

The $\gamma i_{\mathrm{proxi}}$ depends on the current i_{proxi} in the second circuit. The magnetic field induces potential difference, which leads to the proximity effect. The dependent voltage sources βi represent the magnetic fields caused by currents i in strands. The impedance calculation, compared to the previous two parts, is more complex and requires to solve the matrix built in Section II-A and (4.17). Set the current in m as 1A and others as 0A. Then, a matrix can be formed ignoring the right-hand side of the equation in the first row of (4.12), which is already considered in (4.21). Through solving the matrix, the variable C of each element can be obtained. Sum the variable C belonging to n together, and the part of $\gamma i_{\mathrm{proxi}}$ in strand n is obtained, which is caused by 1A in m, and equal to the impedance caused by the transverse magnetic field. The longitudinal field's contribution is calculated through (4.18). The impedance due to proximity effect is given in (4.22). The $\mathbf{Z}_{ss}$ is the summation of Z_{self-n}, $Z_{mutL-nm}$ and $Z_{proxi-nm}$.

$$Z_{proxi-nm} = \sum_{i \in n} j\omega C_i + \sum_{i \in n} \sum_{j \in m} \sum_k Z_{\mathrm{lg}\_ij} \qquad (4.22)$$

Then, the matrix $\mathbf{Z}_{sw}$ and $\mathbf{Z}_{ww}$ are analyzed. These two submatrices are caused by external magnetic fields. The size of $\mathbf{Z}_{sw}$ is $n_s \times 3$, and the size of $\mathbf{Z}_{ww}$ is 3×3. Columns represent external fields along x, y and z directions. The $\mathbf{Z}_{sw}$ and $\mathbf{Z}_{ww}$ are also represented by the two dependent voltage sources V_{mutual} and $\gamma i_{\mathrm{proxi}}$ in the circuit. The value is also calculated with the same method for $Z_{mutL-nm}$ $Z_{proxi-nm}$. The currents in all strands are set to 0 A, and an additional element producing an external field of 1 A/m
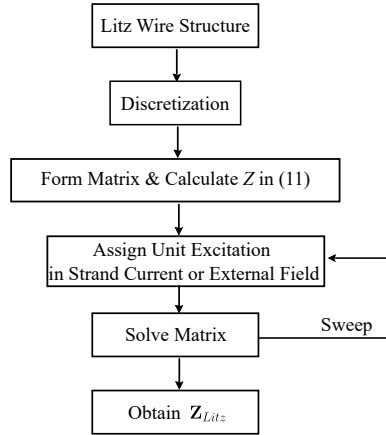
Figure 4.8: The flow chart for calculating the impedance matrix of Litz wires.

is introduced. The $\mathbf{Z}_{ws}$ is ignored since it can be replaced by $\mathbf{Z}_{sw}$ for another section of the coil.

Fig. 4.8 shows the flow chart for calculating the Litz wire impedance matrix. After building the matrix, the impedance matrix $\mathbf{Z}_{ss}$ can be calculated by sweeping the Litz wire strands with a unit current while others carry zero current. Then, $\mathbf{Z}_{sw}$ and $\mathbf{Z}_{ww}$ are obtained by sweeping the unit external fields in x, y and z dimensions and solving the matrix. To consider the impact of external fields, i.e., , are also swept to obtain three more dimensions in the impedance matrix.

4.3.4. VALIDATION AND COMPARISON

Two different cases are used to validate the methods. Figure 4.9 shows the structure of two cases. One is a two-level twisted wire, which is twisted in both radial and azimuthal directions. It has 3×3 strands, strand radius is 0.1mm, the insulation layer is 10μm, and the pitch is 10mm. Another is a one-level twisted wire, which is only twisted in the radial direction. It has 11 strands. The radius, insulation thickness and pitch are the same as in the first case. Both cases are calculated based on one pitch.
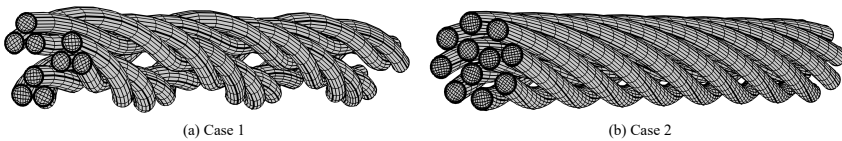
(a) Case 1   (b) Case 2

Figure 4.9: Litz wire structure and meshing in FEM, (a) Case 1 (b) Case 2

Results from 3D FEM are set as the reference, and 3D FEM is established and solved by COMSOL software. Loss due to excitation current is calculated by assigning 1A to litz wire. Loss due to external magnetic field is calculated based on 1 A/m external field. Besides the results from 3D FEM, a classic method [132] and a PEEC method [33] are

compared.

- Setting of 2.5D approximation

For 2.5D approximation, the first step is to choose the number of sections and the Fourier series order. Figure 4.10 shows the result of a pitch of case (1) with a different setting. From (a), it is known that the higher the number of sections is, the more accurate the results are. There is an interesting result that the error is significantly larger when $N_{section} = 5$ than when $N_{section} = 2$. It is attributed to that the induced voltage is uneven in each stand, and a large circulating current is generated when $N_{section} = 5$. Therefore, the $N_{section}$ needs to averagely capture the strands' radial and azimuthal locations, which requires a relatively high $N_{section}$. From (c) and (d), the different order choices do not impact the result significantly. Therefore, the $N_{section}$ is set as 10, and the Fourier series order is set as 1.
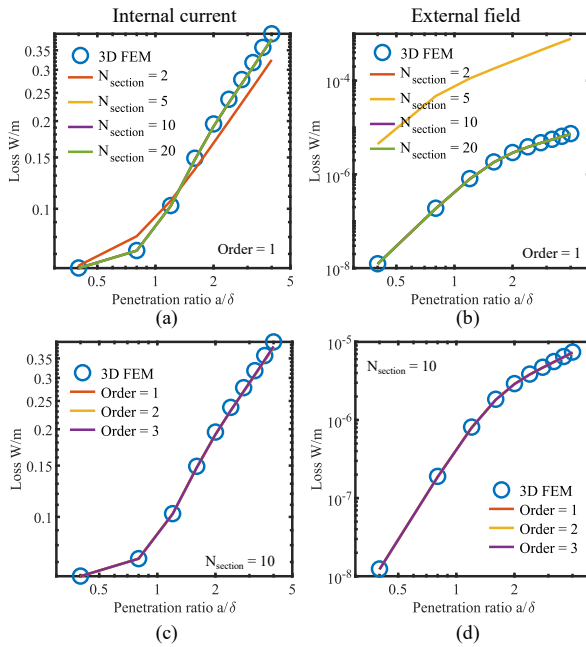
Figure 4.10: The impact of setting on the results of one pitch of case (1). (a) and (c) show the impacts of numbers of sections and Fourier series orders on the losses due to internal current, respectively; (b) and (d) show the impacts of numbers of sections and Fourier series orders on the losses due to external field, respectively.

- Setting of 3D cylindrical element

Because the number of elements in the 3D Litz wire model is significantly larger than the number in 2D, the iterative method is used to solve the matrix. There are two factors that can impact the results: one is the iteration number, and another is the element size. Figure 4.11 show the results of the case (1) with different element sizes

and iteration numbers. Figure 4.11 (a) and (b) show the results of the loss due to 1 A excitation current and 1 A/m external magnetic field with different iteration numbers. If only the initial value is used as the result, the result should be the same as the one obtained from [139]. With iteration, the results converge fast, and 5 iterations are used to calculate the results. The element size is represented by the number of elements in each strand. Its impact is not significant from Figure 4.11 (c) and (d). Because the cases' structure is not complicated, each strand is composed of 20 elements.
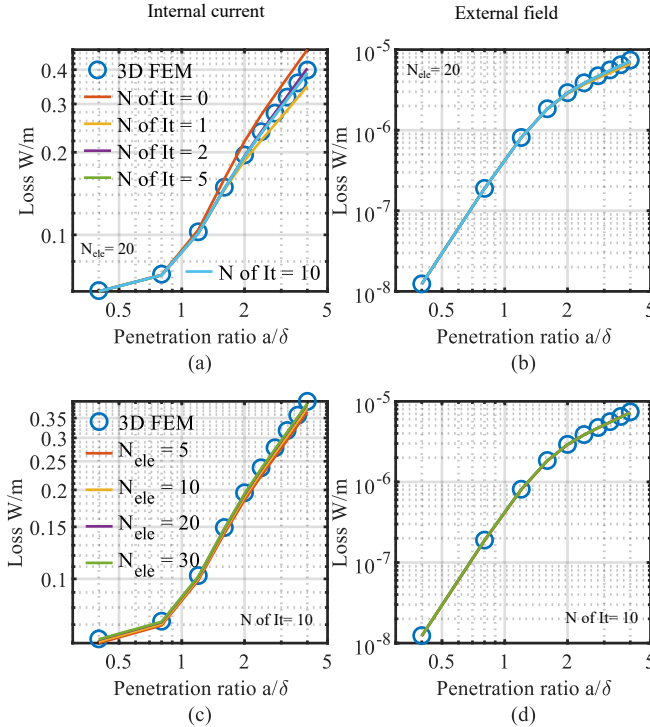
Figure 4.11: The impact of iteration and element size on the results of case (1). (a) and (c) show the impacts of numbers of iterations and elements on the losses due to internal current, respectively; (c) and (d) show the impacts of numbers of iterations and elements on the losses due to external field, respectively.

- Calculation results

The results for Case 1 are shown in Figure 4.12. Figure 4.12 (a) and (b) show the loss due to excitation current. All methods have good accuracy compared to 3D FEM when penetration ratio $a/\delta < 2$. Case 1 is twisted in both radial and azimuthal directions, which leads to roughly average current distribution in each strand. Therefore, there is no current distribution problem, which comply with the assumption of perfect twisting model. Figure 4.12 (c) and (d) show the loss due to the external magnetic field. The proposed and classic methods show good accuracy. Compared to these methods, the PEEC method underestimates the loss around 14% when a/δ is 1. It may be because of

the fineness of filament discretization, which leads to errors in the current distribution calculation.
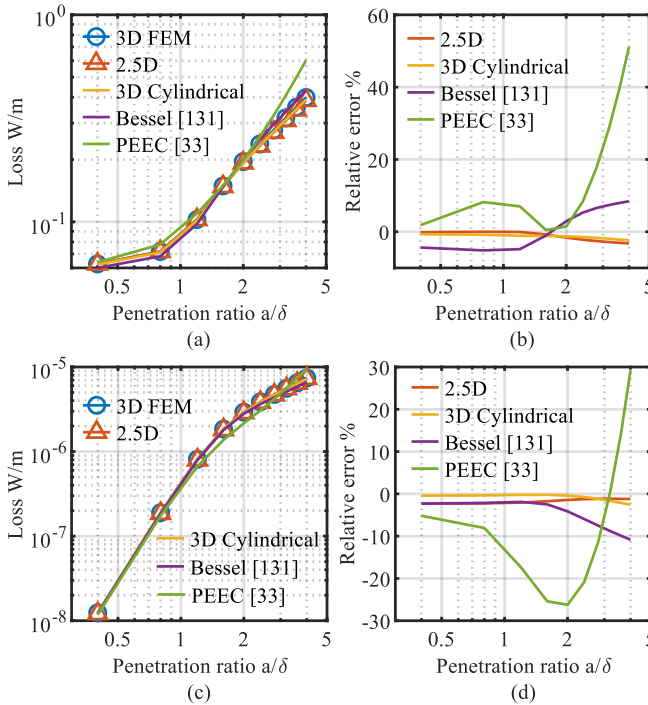
Figure 4.12: Case 1: loss per meter and relative error due to excitation current (a), (b), respectively; and loss per meter and relative error due to external magnetic field (c), (d), respectively.

For case 2, the results from different methods are shown in Figure 4.13. Case (2) is only twisted in the azimuthal direction and should have a current distribution problem. In Figure 4.13 (a) and (b), the loss due to excitation current is calculated with different methods. The classic method shows worse performance in Case 2. Because the wire is only twisted in the azimuthal direction, the strand current in the inner strands and outer strands is not the same, which makes the assumption in the classic method not valid. Figure 4.13 (c) and (d) show the loss due to the external magnetic field. Methods considering current distribution show a similar performance as the classic method because there is an integer pitch, and the induced voltage does not have much difference between strands.

In general, the 2.5D approximation method and 3D cylindrical element method provide good accuracy in a wider frequency range. PEEC provides accurate results when penetration ratio $a/\delta < 1$. Besides, the classic method also has good results in Case 1 because it complies with the equal current distribution assumption.

One important feature of Litz wire models is their computation speed. Table 4.1 shows the computational time of two cases, the model presented in this chapter are much faster than other two methods. The 3D cylindrical element is faster than the 2.5D
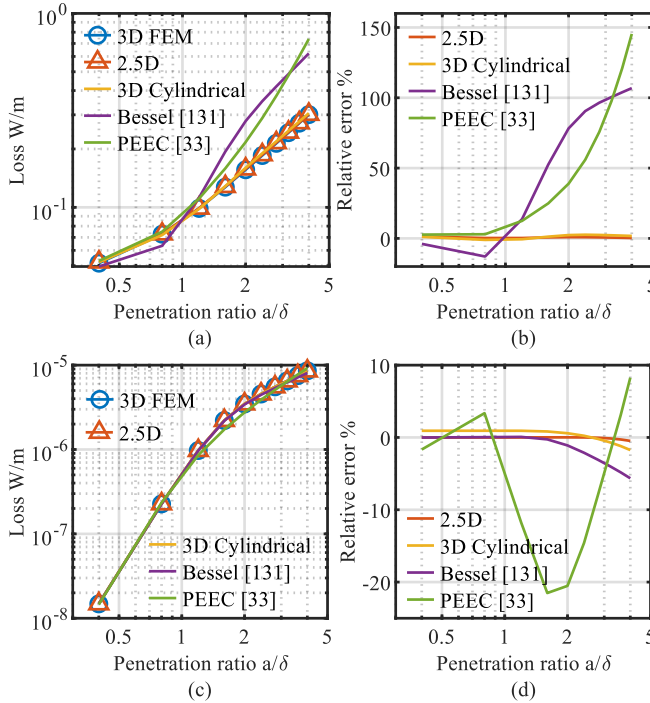
Figure 4.13: Case 2: loss per meter and relative error due to excitation current (a), (b), respectively; and loss per meter and relative error due to external magnetic field (c), (d), respectively.

approximation for the shown cases.

With 3D cylindrical element method, it is also possible to show the impact of the longitudinal field and induced eddy current. Figure 4.14 shows the results of the case (1). The uniform field represents the situations that do not consider the impact of eddy current. Figure 4.14 (a) and (c) show the loss due to 1A excitation current. The uniform field can have good accuracy in the low-frequency range. With the increasing frequency, the impact of eddy current can not be ignored and gradually has considerable error. The result considering the longitudinal field is slightly more accurate than the result that is not considered. Figure 4.14 (b) and (d) shows the loss due to external magnetic field and the error compared to 3D FEM. The uniform field has larger relative error at high frequency since it does not consider the impact of eddy current.

Figure 4.15 shows the results of case (2). As shown in Figure 4.15 (a) and (c), the result assuming a uniform field deviates from the results of 3D FEM at high frequency, which is similar to the case (1). The impact of the longitudinal field is trivial in case (2). The difference in the impact of the longitudinal field between case (1) and case (2) comes from the structure. The strands in case (1) are twisted to achieve evenly spatial distributed radially and azimuthally. The angle between the strand and the z-axis varies at different locations. Therefore, The strand in case (1) is more likely to form a large angle between itself and other strands and have a higher longitudinal field. Therefore,

Table 4.1: Computational speed and degree of freedom (DoF) of different methods

Items	Case 1	Case 2
3D FEM Time	6360s	8769s
3D FEM DoF	1234407	2170803
2.5D approximation Time	0.63s	0.77s
2.5D approximation DoF	10× 27	10 ×33
PEEC [33] Time	227.1s	220.5s
PEEC [33] DoF	14409	8811
3D cylindrical element Time	0.26s	0.32s
3D cylindrical element DoF	540	660
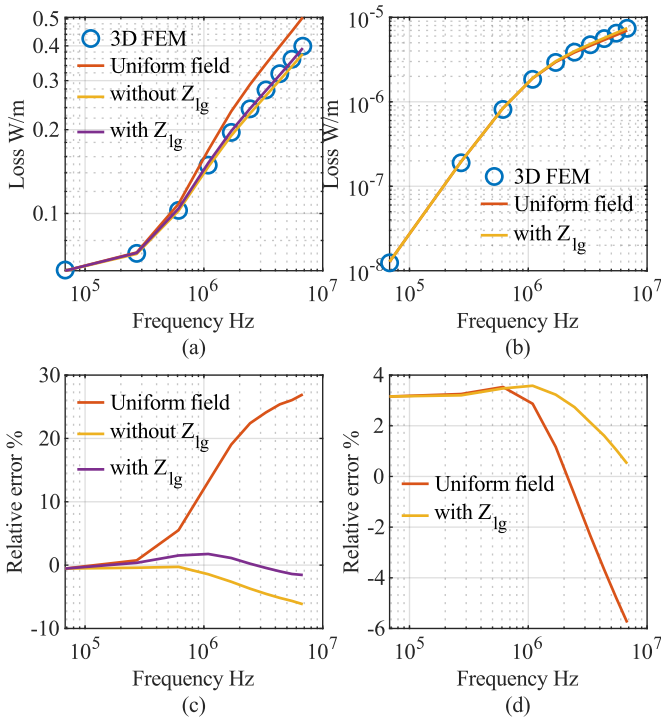
Figure 4.14: Case (1): loss per meter caused by 1A excitation current and relative error, (a) and (c), respectively; loss per meter 1A/m external magnetic field and relative error, (b) and (d), respectively.

the impact of the longitudinal field in case (1) is more obvious. Figure 4.15 (b) and (d) show the loss due to external magnetic field. The uniform field has larger relative error at high frequency, which is the same as case (1).
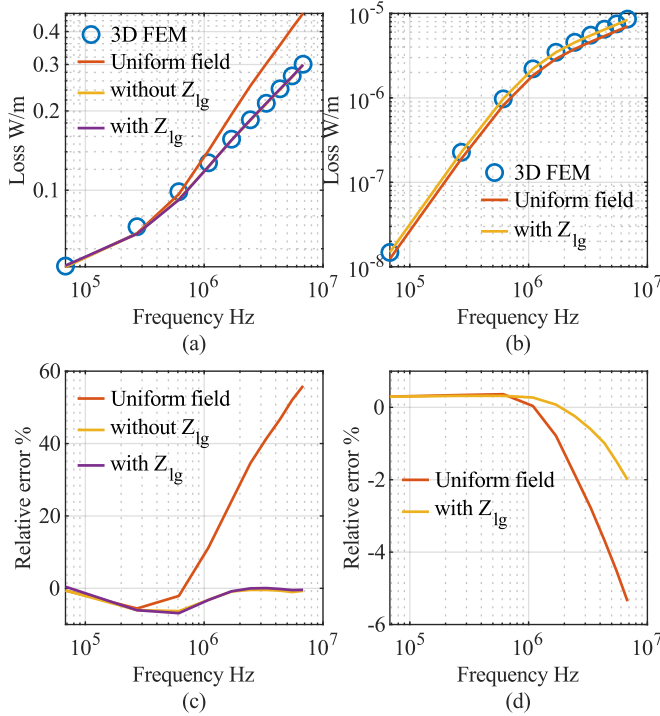
Figure 4.15: Case (2): loss per meter caused by 1A excitation current and relative error, (a) and (c), respectively; loss per meter 1A/m external magnetic field and relative error, (b) and (d), respectively.

4.4. COUPLING THE LITZ WIRE AND WINDING MODELS

IN the preceding section, Litz wire models are introduced. Although the proposed methods have much faster computational speed, it is still not practical to model the entire winding with each strand. Therefore, it is important to incorporate the Litz wire model into the whole winding model using a suitable method.

4.4.1. EQUIVALENT FACTORS FROM THE LITZ WIRE MODEL

One way is using complex permeability to approximate the proximity effect [144]–[146]. This technique is often used by combining homogenization to speed up the computation because it converts the problem from the frequency domain to a static field problem and reduces the element number. The complex permeability of an isolated round conductor is calculated under different frequencies. Based on the 2D analysis in Chapter 3, it is known that if a uniform field is applied to a conductor, the magnetic vector potential of the source needs to be (4.23). The vector potential with complex permeability under a static field is given in (4.24). Equating the vector potential in (4.23) and (4.24), the equivalent complex permeability μ_{rc}' is obtained, which is equal to the formula given in [145]. The value is valid when the field is nearly uniform because the complex permeability is derived based on the uniform external

field situation.

$$A = 2\pi\mu_0 a^2 \frac{(\mu_c - \mu_0)J_0(\kappa a) + (\mu_c + \mu_0)J_2(\kappa a)}{(\mu_c + \mu_0)J_0(\kappa a) + (\mu_c - \mu_0)J_2(\kappa a)} \frac{H^2}{I} \quad \text{time harmonic} \tag{4.23}$$

$$A = 2\pi\mu_0 a^2 \frac{\dot{\mu}_{rc} - 1}{\dot{\mu}_{rc} + 1} \frac{H^2}{I} \quad \text{static}$$

$$\dot{\mu}_{rc} = \mu_{rc} \frac{J_0(\kappa a) + J_2(\kappa a)}{J_0(\kappa a) - J_2(\kappa a)} \tag{4.24}$$

Then, the homogenized permeability of the magnetic composite can be evaluate using the Ollendorff formula (4.25), where the diamagnetic constant N is $1/2$ for round wires, η is the volume fraction. The complex permeability is used to replace the winding region and compute the magnetic energy under a static magnetic field. Then, the losses due to the proximity effect are approximated by the total magnetic energy times $j\omega$. The skin effect is calculated independently with AC resistance.

$$\langle \dot{\mu}_r \rangle = 1 + \frac{\eta(\dot{\mu}_{rc} - 1)}{1 + N(1 - \eta)\dot{\mu}_{rc}} \tag{4.25}$$

This technique is generally used in FEMs, which does not suit the winding model proposed in the previous chapter. Therefore, only the key idea is used, which is using a simplified domain with equivalent properties to replace the initial domain. The impedance matrix of a Litz wire can be obtained using the two proposed methods. Based on the impedance matrices (4.19), the parameters of the equivalent element can be obtained as follows steps. First, the equivalent impedance, which is only related to the Litz wire itself, is calculated by the total strand current under a unit voltage drop. Strand currents are obtained based on the $\mathbf{Z}_{ss}$, as given in (4.26), where U is a $n_s \times 1$ unit voltage vector. The equivalent impedance $\dot{Z}_s$ works as the Z_{self-n} in winding models.

$$\dot{Z}_s = 1 / \sum \mathbf{Z}_{ss}^{-1} U \tag{4.26}$$

The second part, $\mathbf{Z}_{sw}$, is used to calculate the impact of the potential circulating current. The difference in voltage drop V_{ind} on each strand is obtained by accumulating field-weighted induced voltage. The circulating current I_{ind} and its impedance Z_{ind} can be calculated, as shown in (4.27). The H_k is the magnetic field matrix on the kth equivalent element with $n_s \times 3$ size, which is caused by a unit current in the coil. The l_k is the length of the kth equivalent element. The impedance Z_{ind} is added to the total impedance of windings. The impact of the circulating current on magnetic field distribution is not considered.

$$V_{ind} = \mathbf{Z}_{sw} \sum_k H_k l_k$$

$$I_{ind} = (\mathbf{Z}_{ss} \sum_n l_n)^{-1} V_{ind} \tag{4.27}$$

$$Z_{ind} = -V_{ind} I_{ind}^* / (1\text{A})^2$$

The last part is about $\mathbf{Z}_{ww}$. It reflects the impact of external fields, which are given in (4.16) and (4.18). For equivalent cylindrical elements, the field is also divided into

transverse and longitudinal fields. For longitudinal fields, the value in $\mathbf{Z}_{ww}$ representing the impact of z direction field is used to replace the term before the summation symbol in (4.18). For transverse field analysis, the coefficient representing the relationship between $A''|B''$ and $A'|B'$ is important. The change of the energy due to a uniform external field is given in (4.28), and its real part is the proximity loss of a round conductor under a uniform external field. Combining (4.13) and (4.28), the coefficient Γ for the relationship between $A''|B''$ and $A'|B'$ of the equivalent element is given in (4.29).

$$UI = 2j\omega\pi\mu_0 \frac{A_1''}{A_1'}H^2 = 2j\omega\pi\mu_0 a^2 \frac{J_2(\kappa a)}{J_0(\kappa a)}H^2 \tag{4.28}$$

$$\Gamma = \frac{\dot{A}_1''}{\dot{A}_1'} \text{ or } \frac{\dot{B}_1''}{\dot{B}_1'} = \frac{\mathbf{Z}_{ww}}{2j\omega\pi\mu_0} \tag{4.29}$$

Among the three considered parts, $\dot{Z}_s$ and Γ are the properties for a single element. Z_{ind} is decided by the whole winding. After dealing with the impedance matrix obtained from the Litz wire model, the properties required for the winding model are obtained. Because the Litz wire model only considers the 1st order harmonic, the order of the winding model has to be set as 1. Besides, the extracted equivalent properties can also used in another 3D cylindrical element model.

4.4.2. VALIDATION WITH MEASURMENT

A planar coil is used to validate the coupling method. Its geometry is shown in Figure 4.16. The planar coil has 26 turns. Its inner radius is 25 mm, and the gap between turns is about 2.3 mm. The wire uses a one-level Litz wire, which has 24 strands with 0.3 mm diameter. The cross-section is shown in Figure 4.16 (b). The pitch of the wire is 25mm, and the outer radius a_o of the Litz wire is 0.95 mm.
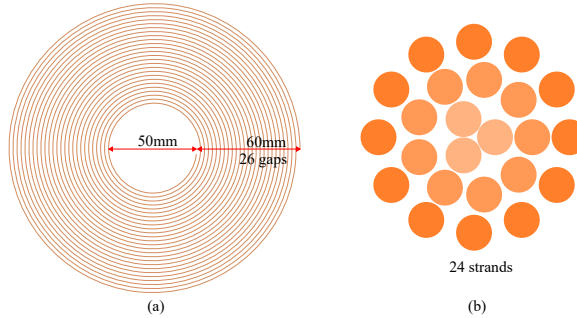
Figure 4.16: The geometry of the planar coil (a) and the Litz wire (b).

First, a pitch of Litz wire is modelled with the proposed 3D model. The model uses the same setting as the validation part in section 4.3.3, each strand is sectioned into 20 cylindrical elements, and the number of iteration is set as 5. The results are shown in Figure 4.17. Figure (a) and (b) show the results from 3D FEM and proposed method. It confirms the accuracy of the results from the proposed cylindrical element method.

Figure (c) is the factor Γ obtained from (4.29), and (d) is the complex permeability $\dot{\mu}_{rc}$ obtained from Γ.

$$\dot{\mu}_{rc} = \frac{1 + \Gamma/a_o^2}{1 - \Gamma/a_o^2} \tag{4.30}$$
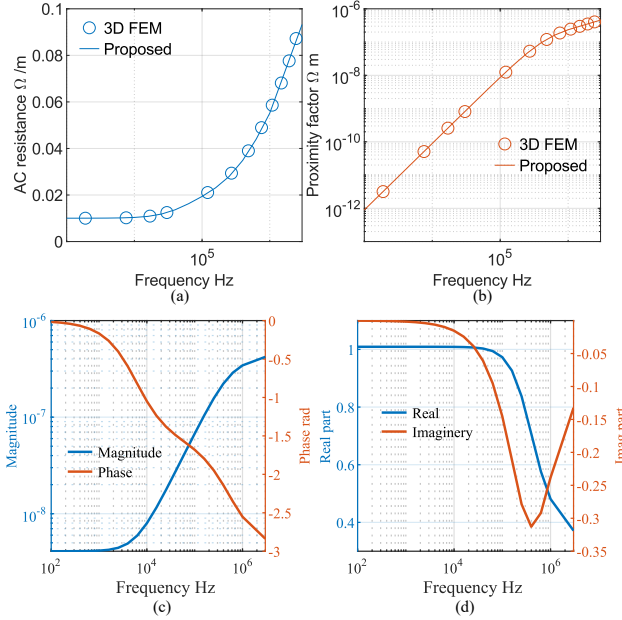
Figure 4.17: Equivalent properties of Litz wire, the AC resistance (a), the proximity effect factor (b), the ratio of $\dot{A}_1''$ to $\dot{A}_1'$ (c), complex permeability (d).

Then, the impedance of the coil is calculated by a 3D model with cylindrical elements and 2D axis-symmetry FEM with complex permeability. For the 3D model with cylindrical elements, each turn is sectioned into 36 elements. The FEMs are built with COMSOL, and two different settings are used. One is using complex permeability from (4.30) to replace the wire. Another is using homogenized complex permeability to replace the whole coil. Besides, a coil, shown in Figure 4.18 (a), is measured by impedance analyzer Bode 100 in the frequency range from 100 Hz to 3 MHz.

Figure 4.18 (b) shows the reactance of the coil obtained from different methods. The reactances obtained in three different calculations almost overlap with the measurements. Figure 4.18 (c) and (d) show the resistances obtained from different methods and their relative error compared to the measurement. The 3D model shows better performance than the results from 2D axis-symmetry FEM. It keeps the relative error within 10%, and the curve is relatively flat, which implies the 3D model properly captures the eddy current feature in the coil. When the frequency approaches 3MHz, the error has a fast change because it is close to the resonant point. For the results from the FEM, when the frequency is above 40 kHz, the resistance increases faster than the measurement. It leads to about 20% overestimation when the frequency is above 100

kHz. The FEM with homogenized complex permeability has similar results as the equivalent complex permeability, and it shows the validation of homogenization.
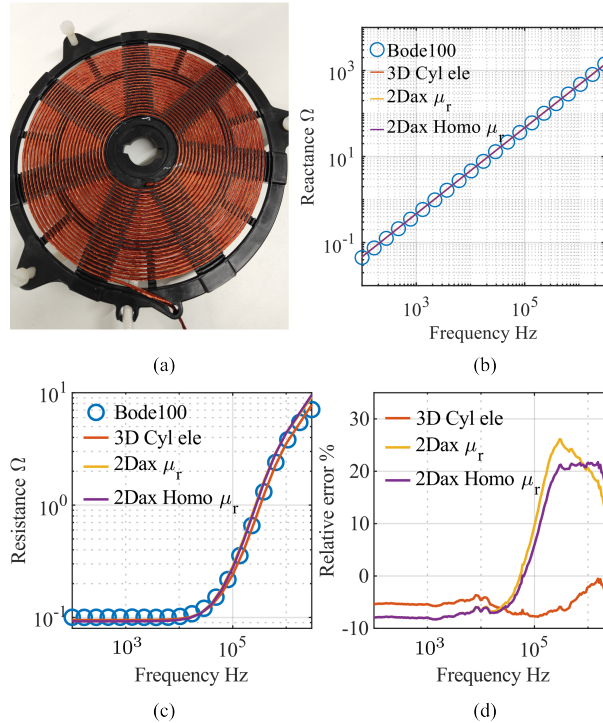
Figure 4.18: Photo of the coil (a) and comparison between measurement from Bode 100 and calculation results from different methods, reactance (b), resistance (c) and relative error of resistance (d).

4.5. CONCLUSION

THIS chapter investigates the impedance characteristics of Litz wires, which is a common choice for suppressing eddy currents. The focus of the analysis is on losses, especially those arising from imperfect twisting. Two Litz wire models are proposed to model imperfect twisting Litz wires. One is based on the 2.5D approximation and the round boundary element analysis. Another is a 3D model with cylindrical elements, which is based on the extension of 2D analysis to 3D. Both models are validated with 3D FEM, showing good accuracy with less than 5% error, and their computational speed can be several orders of magnitude faster than 3D FEM.

To incorporate the Litz wire model into the winding model, the key idea of homogenization is employed. Equivalent factors extracted from the Litz wire model are utilized in the winding model. This approach is validated through the measurement of a coil, which shows less than 10% error in the entire frequency range and better performance than FEM with homogenization.

5

Dry-type Insulation in MV MF Transformers

Security is not the absence of danger but the presence of measures to deal with it.

This chapter discusses insulation-related content. Firstly, the typical insulation failures in dry-type insulation are tested under various frequencies up to 5 kHz of sinusoidal waveform, including air spark, surface flashover and solid puncture. Then, the insulation requirements in relevant standards are summarized, and the insulation requirements for transformers are determined based on the application. Next, a compact insulation structure is presented, and the field strength selection method is proposed based on literature and standards.

5.1. Introduction

To ensure human safety and equipment operational reliability, the insulation of MV MF transformers must be properly considered. Compared to liquid insulation, dry-type insulation has several advantages, like eco-friendly, less required maintenance, ease of installation, etc. Therefore, dry-type insulation is chosen as the insulation in MV MF transformers. In dry-type insulation, the breakdown faults generally can be put in three catergories, i.e., puncture, sparkover and surface flashover.

With the development of wide-band-gap semiconductors, the stress applied to the MV MF transformer is often generated by SiC MOSFETs. It brings new challenges to the insulation design because the voltage is in the MF range, often not sinusoidal and has repeated high steep edges (up to 100 V/ns). Based on the literature, high frequency, rectangular waveform, and high steepness can degrade the behaviour of the insulation, like lower withstand voltage, lower partial discharge initial voltage (PDIV), etc. [41], [42], [147]–[149]. It requires thicker insulation, longer clearance and creepage distance. At the same time, compared to the widely studied insulation behaviour under power frequency stress, the quantitative behaviour of the insulation under stress generated by power electronics is not available. Therefore, the insulation design for MV MF transformers is more difficult.

In this chapter, the typical insulation failures in air-solid insulation are measured under various frequencies. Then, the insulation coordination requirements in related standards are summarized. The last section presents the designed insulation structure and the design field strength selection.

5.2. Insulation behavior test

In order to have some basic understanding of the insulation behaviour under medium frequency, the three common insulation breakdown types are tested under various frequency sinusoidal waveforms.

5.2.1. Test system

The test system used for breakdown voltage and PD are depicted in Figure 5.1 (a) and (b), respectively. For both applications, an HV amplifier Trek 30/20A is used to amplify the input signal to high voltage. A high-voltage probe, GE.3830, is used to measure the output voltage. The input signal is produced by a TENUMA 72-14111 function generator.
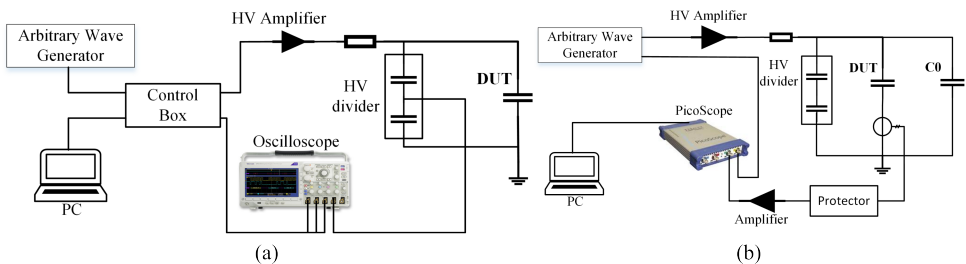
Figure 5.1: Experiment setup for (a) breakdown and (b) PD tests

For the breakdown voltage measurement, a ramping voltage is used, and the peak value of the sinusoidal wave rises at 1 kV/s. A DPO 3034 oscilloscope is used to monitor the breakdown voltage and waveform. Although the HV amplifier has internal short circuit protection, an additional short circuit current detector is used to minimise the potential damage of breakdown.

For PD measurements, a high-frequency current transformer (HFCT) is used, whose bandwidth is 34.4 kHz to 60 MHz and gain of 9.1 mV/mA. A signal from the HFCT passes through a protection circuit and an amplifier. The amplifier has a 22.2 dB gain and bandwidth of 25 kHz to 900 MHz. Due to the limitation of the power amplifier, a coupling capacitor with 50 pF is used, which can still guarantee a much larger capacitance than the device under test (DUT). PicoScope 6404C is used to collect PD signals. Its bandwidth is 500 MHz, and the maximal sampling rate is 2.5 Gs/s with two input channels. We acquired 1000 triggered pulses continuously, which are used to get phase resolved partial discharge pattern (PRPDP), and then data is transferred to a computer to process. PD flex [150] is used to analyse the obtained data.

5.2.2. AIR DISCHARGE UNDER VARIOUS FREQUENCIES

Air is the most natural insulation material and its electric properties are widely investigated. The homogeneous field air breakdown has been measured for a wide frequency range. Based on the results, there is a critical frequency where a reduction of the breakdown voltage begins to occur [151]. It is attributed to the fact that ions produced during an avalanche cannot sweep out of the gap within a half cycle. The ions stay in the gap, distort the electric field and eventually reduce the breakdown voltage. When the frequency is above MHz frequencies, the breakdown voltage reaches its minimum. It is because with further increasing frequency, the mobility of electrons also plays a role in the breakdown, and electrons stay in the gap [152], [153]. Therefore, the dielectric strength increases with increasing frequency after the point.

For inhomogeneous field air breakdown, the breakdown voltage is also measured by several research contributions. In [154], it is shown that the breakdown voltage drops about 50% at 75 kHz compared to at 50 Hz. Besides, Misere [155] measured the breakdown voltage at atmospheric pressure for 0.5 and 1.0 MHz for a gap greater than 1 cm. The results also showed that a significant breakdown voltage reduction occurs at higher frequencies. Seifert [156] measured the breakdown voltage from 50 Hz up to 30 kHz with the tip having different curvatures. They concluded that the accumulation of positive ions influences the field distribution in gaps, which causes the reduction of breakdown voltage at higher frequencies. Also, the partial discharge (PD) inception voltage for inhomogeneous fields also decreases under high frequency [157].

The air discharge performance is tested because there are relatively few data points about the air breakdown voltage for an inhomogeneous field under several kilohertz. The adjustable point-plate electrodes are used in the tests, as shown in Figure 5.2. The high-voltage electrode is a conical rod made of tungsten, and the ground electrode is made of brass. The support structure is made of plastic. The gap distance can be adjusted in a range. Breakdown voltage and PD measurements are performed from 50 Hz-5 kHz with different gap lengths g. Each situation was tested more than thirty times. The whole test was done in a laboratory environment. The temperature was controlled

at 20 ± 1 °C, and relative humidity was in the range of 20% to 30%.
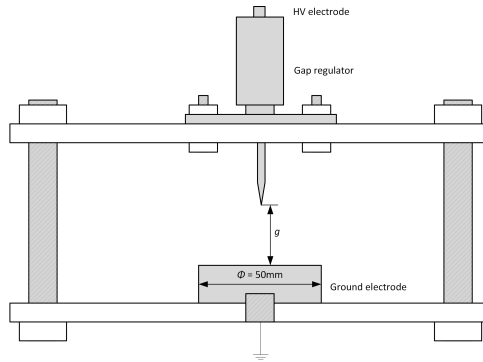
Figure 5.2: Schematic diagram of the electrode

• Breakdown voltage

Mean air breakdown voltages and 99 per cent confidence intervals for different combinations of gap and frequency are shown in Figure 5.3 (a). The results surprisingly contradict the trend mentioned in the introduction. In all four measured gaps, as frequency increases, the breakdown voltages rise to different degrees compared to the results at 50 Hz. The rising under 5 kHz is about 10%, 29%, 54% and 45% for 2.5 mm, 5 mm, 7.5 mm and 10 mm, respectively. The highest rising occurs at 7.5 mm, and the breakdown voltages of 2 kHz and 5 kHz are close to each other for the 10 mm gap, which suggests that there might be a critical frequency where the breakdown voltage starts to decrease for a certain gap.
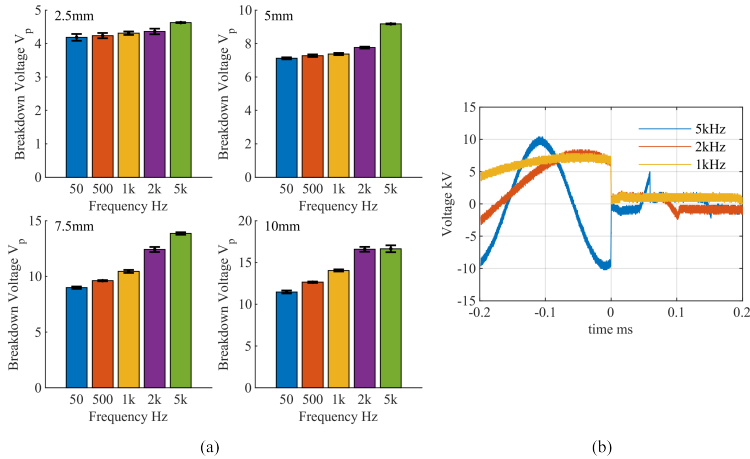
Figure 5.3: Mean air breakdown voltage at different frequencies with different gaps. Error bars show a 99% confidence interval (a), and breakdown voltage waveform with 5 mm gap for 1 kHz, 2 kHz and 5 kHz (b).

Of course, rising breakdown voltage relates to the ion movement in the inhomogeneous field. For the positive point-plane, the electrons produced by ionisation are rapidly absorbed by the anode. The positive space charges move further into the gap, causing field distortion. When the field strength at the tip of positive space charges is high enough, a streamer may be incepted and lead to a breakdown. Therefore, rising breakdown voltage for higher frequencies implies that higher voltage is needed to reach the streamer criterion. In the test range, the frequency might just rise to a high enough level to keep the ions staying in the gap. The negative ions produced during the negative half-cycle remain and move back during the positive half-cycle. They could recombine with the generated positive ions during moving and reduce the strength of positive ions. Therefore, a higher voltage is required to achieve the streamer criterion. It might explain why the breakdown voltage increases in the tests. Under higher frequency than used in this paper, due to short recombination time and travel distance, positive ions have higher density and are closer to the tip, which leads to breakdown voltage decrease under high frequency [156].

Furthermore, the polarity of breakdown was also observed. Figure 5.3 (b) shows the voltage waveforms under 1 kHz, 2 kHz and 5 kHz sinusoidal stress for a 5 mm gap. The breakdown happens roughly at the peak of the voltage. Unlike 1kHz and 2 kHz, the breakdown under 5 kHz happens in negative half-cycles. The probability of breakdown occurring at negative polarity is listed in Table 5.1. When the gap is 2.5 mm, the breakdown happens with both polarities for each frequency. This may be attributed to the fact that the breakdown voltage of both polarities is similar for small gaps. When the gap is 5 mm or 7.5 mm, the breakdown always happens during positive half-cycles except for 5 kHz. When the gap is 10 mm, the breakdown happens during positive polarity. According to classic inhomogeneous breakdown analysis, the positive point-plane breakdown voltage is lower than the negative point-plane. However, the increasing frequency might suppress the expansion of ionisation, leading to a higher voltage requirement. Once the voltage is enough to allow secondary emission at the cathode, a self-sustained discharge is achieved. However, the same voltage cannot have enough space charges to incept a streamer during the positive half-cycle. Then, the breakdown could happen during negative half-cycles.

Gap mm Frequency Hz	2.5	5	7.5	10
50	40%	0%	0%	0%
500	36.7%	0%	0%	0%
1k	30%	0%	0%	0%
2k	13.3%	0%	0%	0%
5k	90%	100%	83.3%	0%

Table 5.1: Probability of breakdown occurring at negative polarity

- Partial discharge

The partial discharge inception voltage (PDIV), PD repetition rate and PRPDP are measured under different frequencies and gaps. Based on the breakdown voltage measurement, the frequency might impact the positive corona. Therefore, the PDIV was measured based on polarities. The negative corona inception voltage is shown in Figure 5.4 (a). When the frequency increases from 50 Hz to 5 kHz, the inception voltage slightly reduces. The reduction of negative corona inception voltage is also observed in [158]. Compared to the negative corona inception voltage, the positive corona has significant changes. The results are listed in Figure 5.4 (b). In all gaps, the inception voltage at 5 kHz is at least double the value at 50 Hz. For the 10 mm and 7.5 mm gap, the inception voltage shows an obvious increase at 500 Hz, while it happened at 2 kHz for the 5 mm gap. It is obvious the higher frequency stress suppresses the inception of positive corona in the tested range. Figure 5.5 shows the test waveform with a 7.5 mm gap under 4.5 kV voltage (peak value) and the repetition rate with a 7.5 mm gap under 4.5 kV and 6 kV. It is shown that the repetition rates are closely proportional to the frequency in the test range.

In order to show the impact of frequency on the partial discharge more clearly, the PRPDPs are plotted. The brightness represents the density of discharge. The more bright, the higher the density is. First, the discharges are collected by PicoScope, with the window trigger having the same threshold for both polarities.

Figure 5.6 (a) shows the PRPDP with different voltages and gaps under 50Hz. PD mostly happened during the negative half-cycle. There are only several points located in the positive half-cycle among 1000 triggers. Compared to negative corona, the occurrence frequency of positive discharge is quite small. The charges per positive corona are larger than per negative corona. The charges per negative corona are quite constant and are insensitive to the voltage and gap. Figure 5.6 (b) and Figure 5.7 (a) show the PRPDPs under 500Hz and 5kHz. In the majority of situations, only negative corona discharges are captured.

Then, the discharges are collected with the normal trigger having a positive threshold, as shown in Figure 5.7 (b). The threshold was selected based on the observed minimum amplitude of the positive corona. Therefore, some negative coronas with high amplitude were also captured. The applied voltage is based on the inception voltage in Figure 5.4 (b). The charges per positive corona have a wider range of values compared to those per negative corona. For the situation with 50 Hz 4.5 kV, the charges vary between 7 pC to 30 pC. The charge value is quite different between frequencies. It means that with higher frequency, more energy is needed to cause a positive corona. The changes in positive corona can be explained by the ion movement. For higher frequencies, the positive ions move shorter distances, and there is less time for the occurrence of recombination. Therefore, positive ions have higher density and accumulate closer to the tip, which further decreases the field strength between space charges and the tip. Consequently, a higher voltage is needed to incept a positive corona discharge, and the charge per discharge also would be higher.

5.2.3. SURFACE DISCHARGE UNDER VARIOUS FREQUENCIES

Surface flashover is another insulation failure reason. Its performance is also heavily impacted by the stress frequency. In one of the earliest studies [159], the flashover

Freq Hz \ Gap mm	5	7.5	10
50	3kV	3.15kV	3.6kV
500	3kV	6kV	7.5kV
1k	3.3kV	7.5kV	11.1kV
2k	4.5kV	>8.4kV	>12kV
5k	>6kV	>8.4kV	>12kV
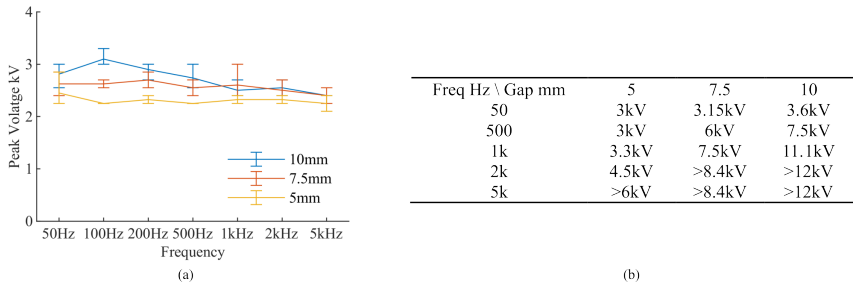
Figure 5.4: Mean PDIV at different frequencies with different gaps, error bars show results' range (a), and positive corona inception voltage under different situations, peak value (b).
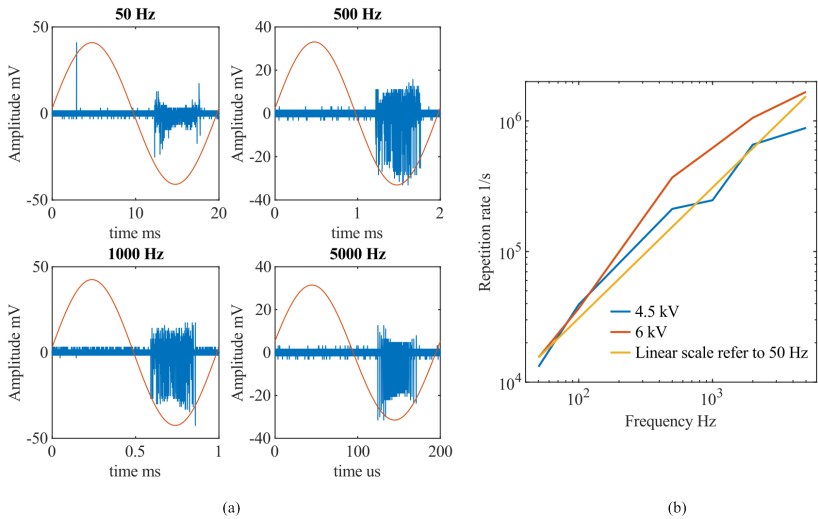
Figure 5.5: Test waveform with 7.5 mm 4.5 kV voltage (peak value) (a), repetition rates with 7.5 mm under 4.5 kV and 6 kV (b).

voltages of a 3/8 inch gap on several materials in the range of 60Hz to 100MHz are measured. It shows that the flashover strength decreases with increasing frequency. The reduction is also observed by [149]. Pfeiffer [154] attributed this reduction to the decreasing breakdown strength of air. In [160], tracking resistance was studied under 50-500 Hz stress according to IEC 587. Results show that higher frequency leads to a shorter time to tracking breakdown at the same voltage.

The partial discharge studies about surface discharge are relatively fewer in the medium frequency range. Zhao [149] showed the PDIV of surface discharge under square waveform does not vary much from 1 kHz to 20 kHz. Liu [161] studied the phase-resolved PD pattern (PRPDP) for surface discharge under 5-30 kHz sinusoidal voltage. Results show when the frequency is under 10 kHz, the average PD amplitude and total PD number per cycle will increase with frequency, and when it is above 10 kHz, the two parameters have opposite trends.
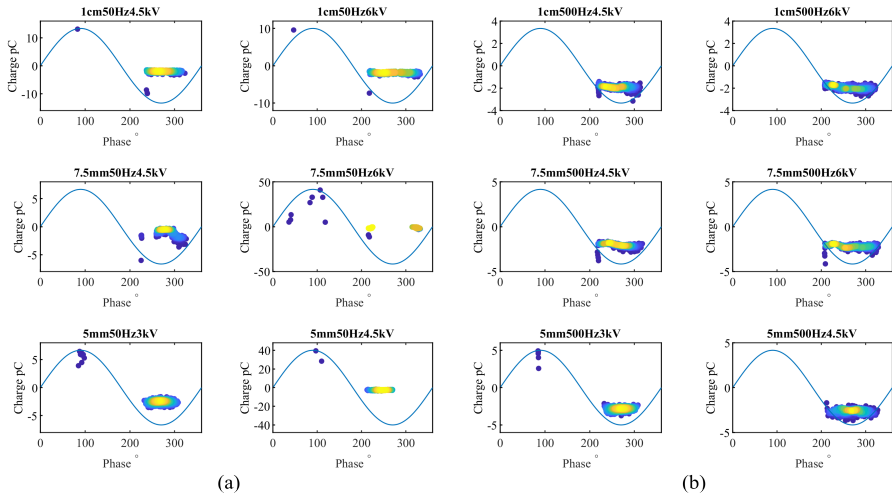
Figure 5.6: PRPDP with different voltage and gap under 50 Hz (a) and 500 Hz(b).

5
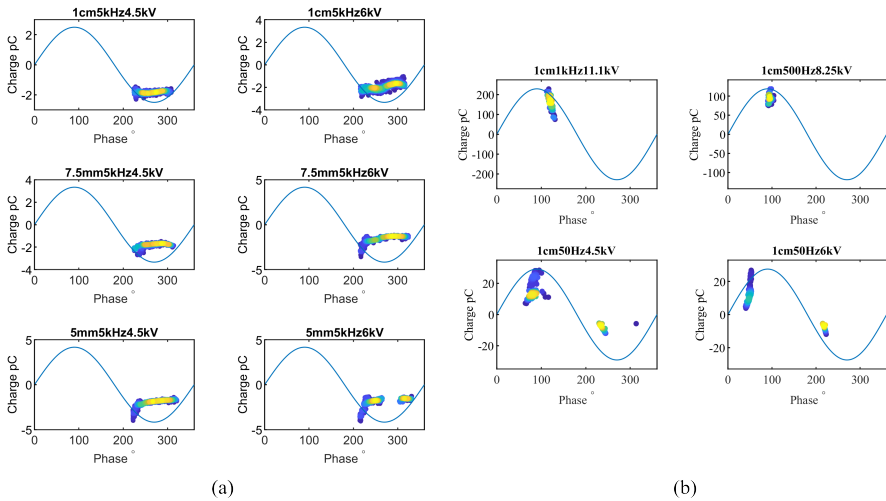
Figure 5.7: PRPDP with different voltage and gap under 5 kHz (a) and PRPDP collected triggered by positive threshold under 1cm gap different stress (b).

The adjustable point-plate electrodes are used in the tests, as shown in Figure 5.8. Flashover voltage is measured under 50 Hz, 500 Hz, 1 kHz, 2 kHz and 5 kHz with gap length d = 5 mm, 10 mm and 15 mm. Each case was tested more than ten times. PD is tested under the same frequency range with a 10 mm gap. All tests were done in a laboratory environment, where the temperature was controlled at 20 °C, and relative humidity was in the range from 50% to 60%. The electrodes were cleaned with wipe

paper every ten tests. Additionally, after completing a set of tests or if dark spots were observed on the electrodes, they were polished both by machine and by hand to maintain their surface condition.
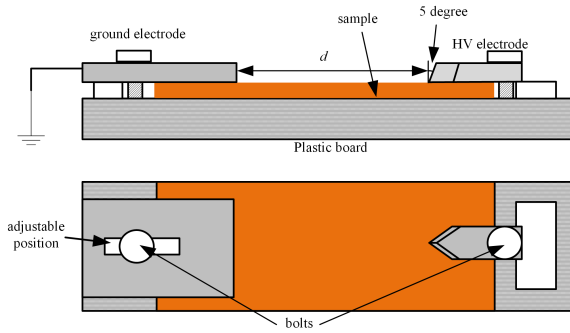
Figure 5.8: Schematic diagram of the electrode

The samples were prepared using bisphenol A epoxy resin (CY225) along with hardener (HY925) without filler, supplied by Huntsman. According to the datasheet, its comparative track- ing index (CTI) is above 600. The weight ratio of epoxy resin to hardener is 5:4. Initially, the epoxy resin and the hardener were both degassed at 60°C for one hour to remove air and moisture. Then, the hardener was added to the resin and mixed thoroughly. The mixture was evacuated to remove trapped air at 60°C for 1.5 hours. The samples were prepared using the hot press method. The mixture was cast in a mould at 60°C, which was composed of aluminium plates covered by silicon rubber and a paper spacer. The thickness of the samples was controlled by the spacer. Epoxy resin was cured at 120°C for 4 hours. Samples of around 150 μm thickness were used.

- Flashover voltage

For flashover voltage, a 2-parameter Weibull distribution as shown in (5.1) is used to analyse the flashover voltage.

$$F(E) = 1 - e^{-\left(\frac{E}{\eta w}\right)^{\beta}_w} \tag{5.1}$$

In (5.1), E is breakdown strength, $F(E)$ is the cumulative probability of breakdown, β_w is the shape parameter, which is the slope of the regression line in the probability plot, and η_w is the scale parameter. The probability of breakdown for the specimens is 63.2% at an electric field equal to η.

The Weibull plot of flashover tests for 10 mm is shown in Figure 5.9 (a). At 50 Hz, the flashover voltage is 12.63 kV, and it increases with rising frequency. At 1kHz, the voltage is 13.84 kV, which is nearly 10% higher than that of 50 Hz. And with further increasing frequency, it decreases. Case with 5 kHz has the lowest value, 12.14 kV. For part from 1 kHz to 5 kHz, the flashover voltage shows the same changes as [149] reported. However, for the whole range, the changes are not the same as what happened in solid and air, i.e., with higher frequency, the breakdown strength decreases in this frequency range.
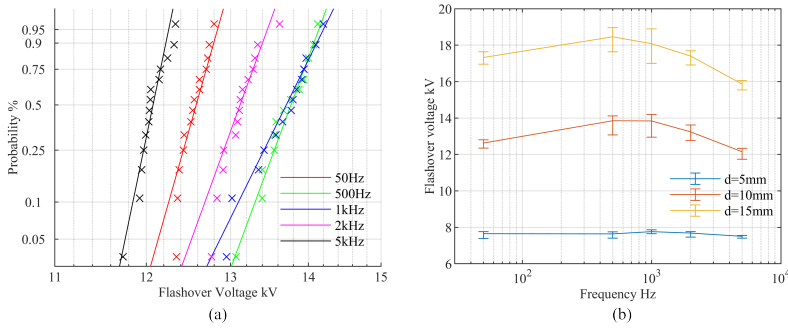
Figure 5.9: Flashover voltage (peak value) with d = 10 mm under different frequency (a), The effect of frequency on flashover voltage with different gap d (b)

The same trend also happens in the other two gaps, as shown in Figure 5.9 (b), which reflects the changes in flashover voltage with an error bar. Comparing to 15 and 10 mm, the trend in 5 mm is not obvious, when frequency is 1 kHz, flashover voltage only has slightly higher value, 7.76 kV compared to 7.65 kV at 50 Hz. Besides, with a bigger gap, the frequency of the highest value seems to move towards a lower frequency.

According to this tendency, this unusual trend could be attributed to the mobility of ions. With an inhomogeneous field, the electric field along the gap would be higher near the point and lower near the plate electrode. For the increasing trend of flashover voltage, although ions stay in the gap and distort the electric field, they could stay near the plate and lower the field near the plate while not contributing noticeably to the increase of the electric field near the point. For the decreasing trend of flashover voltage, it could be that the ions cannot move very far from the point during the negative half cycle, and hence, they enhanced the electric field near the point considerably during the positive half cycle while not decreasing the electric field in the rest of gap noticeably.

Figure 5.10 shows the relation between flashover voltage and gap length, which usually follows the power law [162], as (5.2).

$$V \propto d^{\alpha} \tag{5.2}$$

In (5.2), V is flashover voltage, d is gap length, and α is a coefficient, which is normally 0.5-1. With a smaller gap and rougher surface, α is closer to 1, and in the test, α is around 0.75, which is reasonable.

• Partial discharge

PDIV at different frequencies is measured on the same sample. the trigger is set according to the result of a 10 pC calibration pulse at 100 Hz. As shown in Table 5.2, PDIV seems to stay constant with increasing frequency, which is the same as the result from [149].

In order to get higher repetition frequency, PD pulses for phase-resolved surface discharge patterns are measured under 7.5 kV sine wave, peak value. The results are
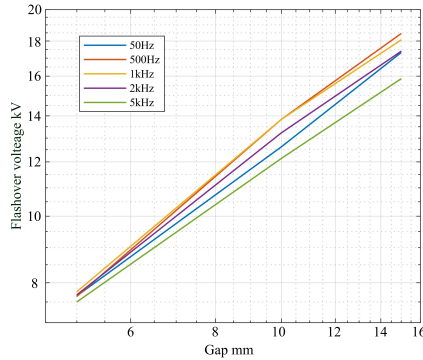
Figure 5.10: Relation between flashover voltage and gap length

Frequency Hz	50	500	1k	2k	5k
PDIV(peak) kV	4.2 ± 0.4	4.1 ± 0.3	4.1 ± 0.2	4.3 ± 0.2	4.3 ± 0.1

Table 5.2: PDIV of surface discharge at different frequencies

shown in Figure 5.11, in which different colour represents different pulse density. It is obvious that for all frequencies, most PD pulses congregate in 0-90 and 180-270 degrees, and positive pulses have higher maximal amplitude. Among all studied frequencies, 1kHz has the highest maximal value, which may relate to flashover voltage. There is a weak trend that PD has lower maximal amplitude at higher frequencies. Positive pulses distribute in a more narrow phase range and have a larger range of amplitude compared to negative pulses. Besides, pulse numbers in positive and negative polarity are roughly equal, whereas 50 Hz has more negative pulses.

5.2.4. EPOXY SOLID BREAKDOWN UNDER VARIOUS FREQUENCIES

Solid insulation generally has one order higher withstand field strength, but the solid breakdown leads to unrecoverable failure. Therefore, solid breakdown study is always an important topic in insulation. Numerous research has shown that higher frequency stress leads to lower breakdown strength [154], [163], [164] and lifetime [42], [165], [166]. The reduction of breakdown is attributed to enhanced dielectric loss or increased discharge repetition frequency. It is shown that the maximal magnitude decreases with frequency, while the partial discharge inception voltage (PDIV) increases with higher voltage frequency in [167]. Wang etc. [168] studied PD in rotation machines and found PD occurrence time decreases with increasing frequency and that the average magnitude is almost constant until 2 kHz.

The electrodes use sphere-sphere brass electrodes, and the diameter of the electrodes is 20 mm, as shown in Figure 5.12. The test samples are immersed in the transformer oil in case of PD occurrence in the air. Breakdown voltage is measured under 50, 500 and 5k Hz. The samples use the same epoxy in the surface discharge test,
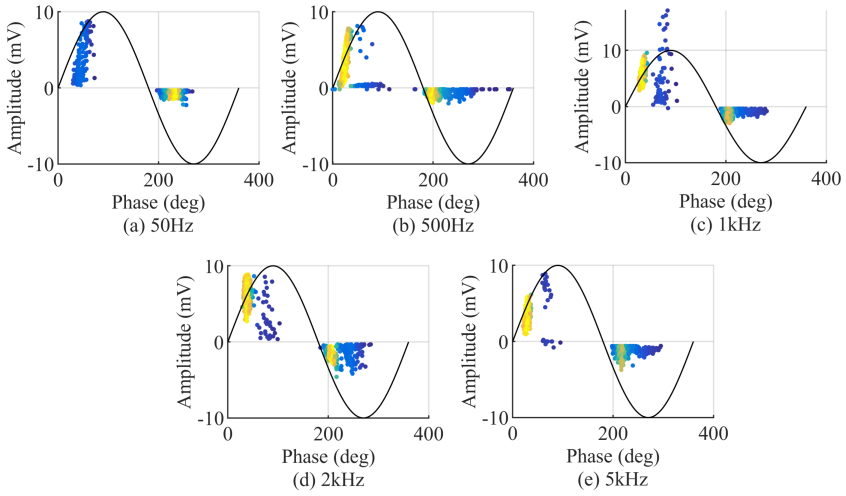
Figure 5.11: Phase resolved surface discharge pattern at various frequencies.

and the thickness is around 150 μm.
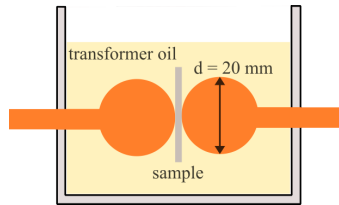
Figure 5.12: Schematic figure of the electrodes

Figure 5.13 shows the Weibull distributions of the breakdown field strength of epoxy under various frequencies and their parameters. It is obvious that the breakdown strength decreases considerably with increased frequency.

5.3. STANDARDS REQUIREMENTS

A set of standards has been established to define requirements and provide a pathway for insulation coordination design in various electrical instruments. In order to prevent sparkover, flashover and solid breakdown, standards set minimum clearance, creepage distance, and withstand voltage, respectively, for different applications and rated voltage. This section summarizes the standard requirements for MV MF transformers in these three aspects. According to the related standards, the insulation level is decided by following terms. Some values are listed in Table 5.3. For the **LI** column, the values are also the values for impulse voltage with overvoltage categories III and IV. The impulse voltage column shows the value with overvoltage
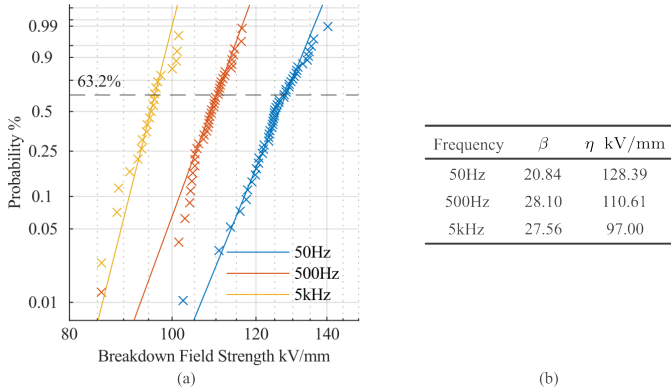
Figure 5.13: Weibull distribution of breakdown field strength (peak value) under various frequencies (a), and the parameters of Weibull distribution (b).

categories I and II. Besides, there is not **LI** requirement in IEC 60076-11, the value is obtained from IEC 61800-5-1.

- Highest voltage for equipment applicable to a transformer winding U_m [169].

  Highest RMS voltage for which a transformer winding is designed in respect of its insulation.

- Rated AC withstand voltage level to earth designed for the terminals of each winding **AC** [170].

- Rated lightning impulse withstand voltage level for the terminal of each individual winding **LI** [170].

  The choice between two values in Table 5.3 should be made considering the degree of exposure to overvoltages and the degree of protection used, etc.

- Working voltage (recurring peak voltage U_{rp}) [171].

  Maximum peak value of periodic excursions of the voltage waveform.

- Impulse voltage [171].

  Highest peak value of impulse voltage of specified form and polarity, which does not cause breakdown of insulation under specified conditions. Its value is determined by system voltage and Overvoltage Category. According to IEC 61800-5-1, the system voltage has the same value as U_m in IEC 60071.

- Temporary overvoltage [171].

  Overvoltage at power frequency of relatively long duration. Its value is decided by system voltage. According to IEC 61800-5-1 [172], its value equals the **AC** in IEC 60076.

- Maximum system voltage U_{sm} [173]

- Basic lightning impulse insulation level **BIL** [173]

IEC 60076-11 & 61800-5-1				IEEE C57.12.01		
U_m kV (RMS)	**AC** kV (RMS)	**LI** kV (peak)	Impulse voltage kV (peak)	U_{sm} kV (RMS)	Applied voltage test kV (RMS)	**BIL** kV (peak)
≤ 1.1	3	8	4	1.5	4	10
		12	6			20
3.6	10	20	9	3.5	10	20
		40	16			30
7.2	20	40	17.5	6.9	12	30
		60	29			45
12	28	60	29	11	20	45
		75	42.5			60
17.5	38	75	40	17	34	60
		95	55			95
24	50	95	52	26	50	110
		125	75			125

Table 5.3: Relation between different voltage terms in IEC and IEEE standards

5.3.1. Clearance

The clearance is the shortest distance in air between two conductive parts. In transformers, it refers to the distance between the live parts of the transformer and other conductive elements in the installation. In power transformers' standards, the minimum clearance value choice is decided by the impulse voltage and altitude. In IEC 60664-1 [171], the pollution degree, field distribution and frequency are also considered. Figure 5.14 (a) shows the withstand voltage (peak) under various field distributions and test waveforms at an altitude of 2000 m above sea level from [171]. Figure 5.14 (b) shows the required minimal clearance in the air with altitude up to 2000 m above sea level based on **LI** or **BIL**. It is shown that the required clearance for the power transformer is the continuance of the required clearance for the inhomogeneous field in [171].

The impact of the frequency (above 30 kHz) on the required clearance is set in IEC 60664-4 [151]. It is also set differently for homogeneous and inhomogeneous fields. For a homogeneous field, if no detailed evaluation is intended, the clearance shall be 125 % of the value obtained from Figure 5.14 (b).

$$f_{crit} = \frac{0.2}{d/mm} MHz \qquad (5.3)$$
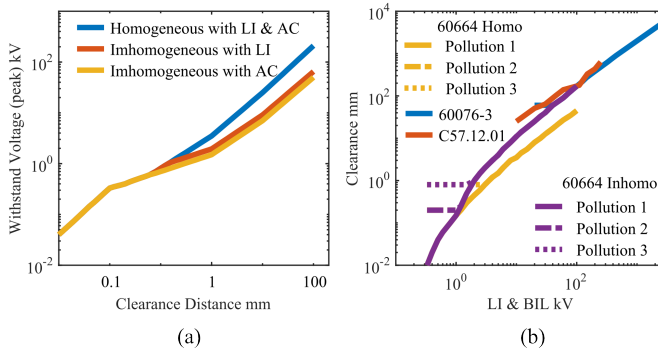
Figure 5.14: Withstand voltage of clearances in IEC 60664-1 for an altitude of 2000 m above sea level(a), and minimum clearance in the air up to 2000 m above sea level based on **LI** or **BIL** (b).

If a detailed evaluation is intended, the following applies:

- For frequencies below f_{crit} (5.3) the clearance shall be the same as Figure 5.14 (b).

- For frequencies above f_{min} (3 MHz) the clearance shall be 125 % of the required withstand voltage according to Figure 5.14 (b).

- For frequencies between f_{crit} and f_{min} the clearance shall be

$$100\% + \frac{f - f_{crit}}{f_{min} - f_{crit}} \times 25\%$$ (5.4)

of the required withstand voltage according to Figure 5.14 (b).

In order to obtain the critical frequency, firstly, the clearance is assumed for 100 % of the required withstand voltage according to Figure 5.14 (b). Then, the value is chosen depending on which condition is applicable. Since the evaluation can be influenced by the initial result, a second iteration may be necessary.

For inhomogeneous fields, if frequencies below f_{crit}, the clearance shall be designed for 100 % of the required withstand voltage according to Figure 5.14 (b). The value provided is shown in Figure 5.15 for frequencies equal to or greater than f_{crit}. The provided value for situations above 30 kHz is limited, and the value can be much larger than in normal situations.

5.3.2. CREEPAGE

Creepage distance is the shortest distance along the surface of a solid insulating material between two conductive parts. Creepage distances are generally determined by the long term RMS voltage stress across the considered insulation and the pollution degree. The pollution degree is characterized differently in IEC 60664 and IEC/TS 60815 [174]. The materials are categorized based on the comparative tracking index (CTI), and its group is also considered in creepage distance determination in IEC 60664.

The minimal creepage distances are given in Figure 5.16 (a). The dashed lines give the value based on extrapolation. For pollution degree 3, the extrapolated values are
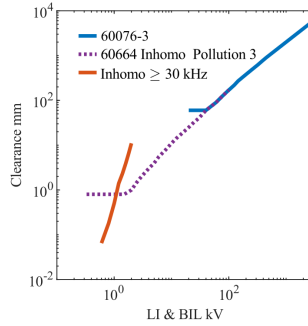
Figure 5.15: Minimum clearance in the air up to 2000 m above sea level based on **LI** or **BIL** for the inhomogeneous field.

not given in the standard. It is obvious that the minimum creepage distance is much longer when the pollution is characterized by site pollution severity (SPS). Besides, the value obtained based on SPS still needs to be corrected by altitude K_a, usually 1, and the insulator diameter K_{ad}. The K_{ad} is given in (5.5), where D_a is the average diameter.

$$K_{ad} = 1 \qquad D_a < 300\text{mm}$$
$$K_{ad} = 0.0005D_a + 0.85 \qquad D_a \geq 300 \tag{5.5}$$
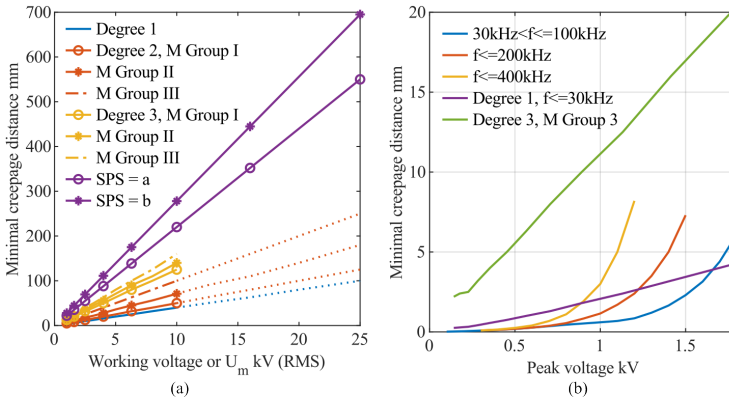
Figure 5.16: Required minimum creepage distance according to different situations (a), and the impact of frequency on required minimum creepage distance (b).

The impact of frequency on the minimal creepage distance is shown in Figure 5.16 (b). The characterizing voltage uses peak value. The values for the creepage distances apply for pollution degree 1. For pollution degree 2, a multiplication factor of 1.2 and for pollution degree 3, a multiplication factor of 1.4 shall be used. Similar to Figure 5.15, the data is only limited to a small range. Compared to the date under 30 kHz, the value

is nonlinear to the working voltage and the difference between material groups is not shown.

5.3.3. SOLID INSULATION

Solid insulation should be able to withstand long-term electrical stresses and environmental influences which can occur during the intended life of the equipment. The considered withstand the voltage stress involves three aspects.

- Transient overvoltages (**LI**).

- Temporary withstand overvoltages (**AC**).

- Working voltages (U_m or U_{rp})

Once the required withstand voltage is determined, the required insulation thickness can be calculated by the required withstand voltage and design field strength. Normally, a safety factor is applied to insulation thickness to ensure reliability and safety.

The design field strength is an essential factor, which is set based on the design requirements and insulation material properties. Electrical, thermal and mechanical properties all can impact the choice of material. After selecting the insulation material, the field strength can be set. In IEC 60664-4, a field strength (peak value) is given for solid insulation design for up to 10 MHz uniform stress, which is related to the thickness of the insulation. The value is listed below.

- $E_{peak} \leq 2$kV/mm, when $d_i \geq 0.75$mm.

- E_{peak} follow (5.6), when 30μm $< d_i < 0.75$mm

$$E = \frac{0.25}{d_i} + 1.667 kV/mm \tag{5.6}$$

- $E_{peak} \leq 10$kV/mm, when $d_i \leq 30\mu$m.

In AC situations, an inverse power law is generally used (5.7). There are two factors, E_0 and n, which depend on the insulation material. The E_0 is the dielectric strength of the insulation material for the reference thickness. The n is recommended to be 0.4 in [175] and is set as 0.57 for epoxy in [176]. Therefore, for specific materials, a set of data is needed to obtain the required properties.

$$E(d) = E_0 d^{-n} \tag{5.7}$$

5.4. INSULATION DESIGN

IN the preceding section, the requirements of standards are summarized. These requirements need to be fulfilled in the design and tests. In this section, the specific insulation design is introduced.

A transformer designed for isolated converters connecting the MV and LV buses is used as an example of insulation design. To handle the voltage at the MV side and high

current at the LV side, the input-series output-parallel (ISOP) modular converter is a preferred solution, as shown in Figure 5.17. The considered scenario is connecting a 10.5 kV bus to a 400 V bus with 3 sub-modules, and sub-modules use DAB topology. For each sub-module, the rated input voltage is 3.5 kV, and the rated output voltage is 400 V. However, due to the ISOP connection, the potential on the input of the transformer in sub-module 1 is 1.75 kV MF AC plus 8.75 kV DC, and the output voltage is 400 V. Therefore, the insulation level of the HV winding in sub-module 1 should follow the U_m at 12 kV. Because the MF transformers are inside the converter system and are not directly exposed to external overvoltages, the overvoltage category is set as III in IEC 60076-11 and the list 1 in IEC 60076-11. The value of **AC** and **LI** choose the higher voltage from the standards. The final design insulation level is set as **AC** 28 - **LI** 60/ **AC** 3 - **LI** 6.
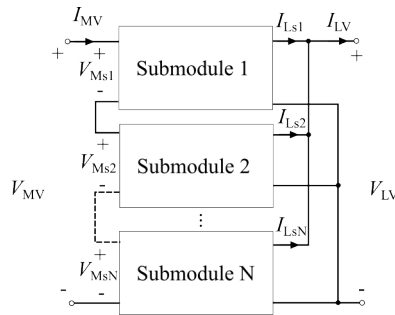
Figure 5.17: Structure of modular ISOP converters

5.4.1. INSULATION STRUCTURE

Compared to the shell type, the core type is easier to construct and has better heat dissipation due to more surface exposure to the external atmosphere. Therefore, core-type transformers are adopted in the MF transformer design in this thesis. The basic structure is shown in Figure 5.18. The core is grounded, and HV and LV windings are wound on each leg and surrounded by the selected insulation material. The insulation in the considered structure mainly includes 4 parts, which are introduced in sequence.

- Insulation between windings

The insulation between windings is firstly considered under simple configurations with multi-dielectrics, as shown in Figure 5.19. If the stress is alternative voltage, the field strength in each region is given in (5.8), which should be smaller than the design field strength. If there is a medium has both low permittivity and breakdown strength, like air, the field strength in the multi-dielectrics is limited to a small value because of the continuous displacement current.
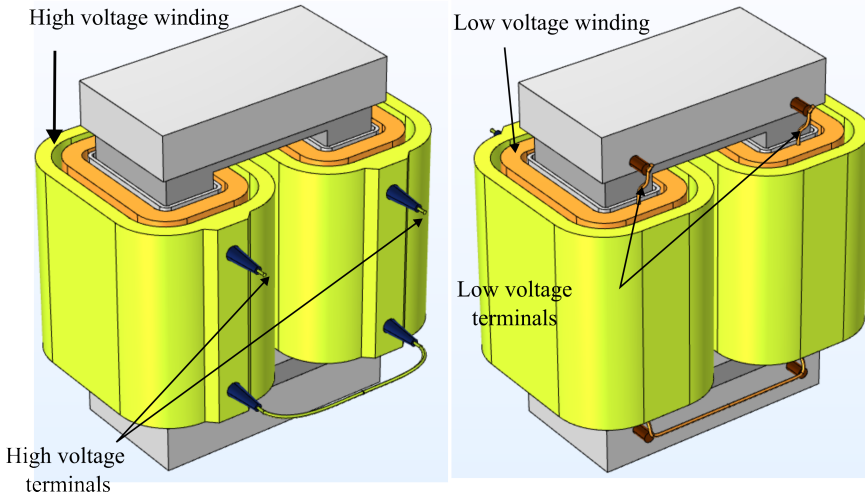
Figure 5.18: Illustration of the insulation structure of single phase core type transformers
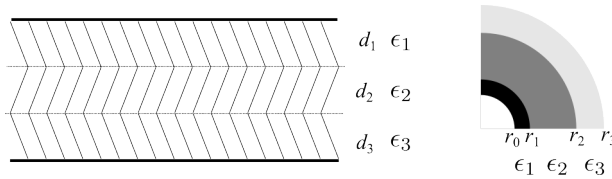
Figure 5.19: Considered simple configurations

$$E_i = \frac{V}{\epsilon_i \left(\dfrac{d_1}{\epsilon_1} + \dfrac{d_2}{\epsilon_2} + \dfrac{d_3}{\epsilon_3} \right)} \qquad i = 1,2,3$$

$$E_i = \frac{V}{r\epsilon_i \left(\dfrac{1}{\epsilon_1} \ln \dfrac{r_1}{r_0} + \dfrac{1}{\epsilon_2} \ln \dfrac{r_2}{r_1} + \dfrac{1}{\epsilon_3} \ln \dfrac{r_3}{r_2} \right)} \qquad i = 1,2,3$$

(5.8)

If the stress is DC, the low conductivity medium takes the most part of the stress because of the continuous current. It requires the insulation material with high breakdown strength to have corresponding low conductivity. If the multi-dielectrics do not have matched properties, it can result in a low window utilization factor. For example, a low conductivity media takes the most part of the voltage, but it has low breakdown strength resulting in thick insulation and low window utilization factor.

In the targeted superimposed stress, it is hard to achieve matched properties, especially since the electrical conductivity is sensitive to the temperature. Therefore, a single dielectric is preferred in the thesis. If the whole transformer is cast in solid insulation, heat dissipation is a challenge due to the poor heat conductivity of the organic insulation materials. Grounded shields are able to constrain the field within limited, simple domains. At the same time, it increases the winding-ground

capacitance. Considering the insulation requirements, the grounded shield is used for the HV winding.

- Insulation between winding and core

The insulation between the winding and core includes two parts. The first part is the insulation between the LV winding and the core. Because the cross-section of the cores can be rectangular, and the field stress at the corners is high. Therefore, a grounded electric shield with semiconductor material is used to prevent the high field stress at the core. The impact of the grounded electric shield is shown in Figure 5.20. The shield effectively eliminates the high-field spot at the corner. With the shield, the field can be calculated with (5.8).
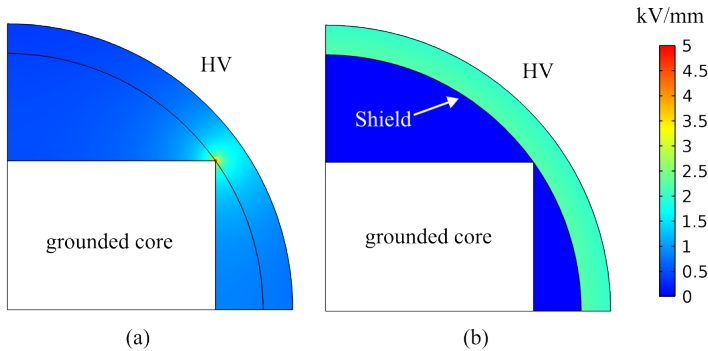
Figure 5.20: Impact of the grounded electric shield, without shield (a), with a shield with a conductivity of 1 S/m (b).

Another part is the insulation at the end of the windings. Figure 5.21 shows the field distribution at the end of the HV winding. The field in the air is high, and it requires a large distance to limit field strength when there is no ground shield. When the HV winding is covered by a grounded shield, the field is concentrated in the solid insulation and the field at the end is larger than at the middle part. Therefore, the thickness of the insulation is determined by the field at the end.

- Insulation between high voltage terminals and earthed parts

This part relates to the creepage distance and the clearance. For the clearance, the LV winding terminal must get out from the inner layer, and field distribution is complex. Therefore, the clearance under an inhomogeneous field is used. Besides, the pollution degree is not considered for clearance because the required LI is higher than the region where the pollution degree has an impact. For the creepage distance, the IEC/TS 60815 has different characteristics from the IEC 60664, and the difference is considerable. Because the converter systems are placed indoors, the situation in IEC 60664 is more suitable. Therefore, the pollution degree 2 is used, and the specific curve will be decided by the material group of the chosen insulation material.

Besides keeping the required creepage distance and clearance, the field around the terminal also needs to be careful due to the existence of multi-dielectrics. The solid
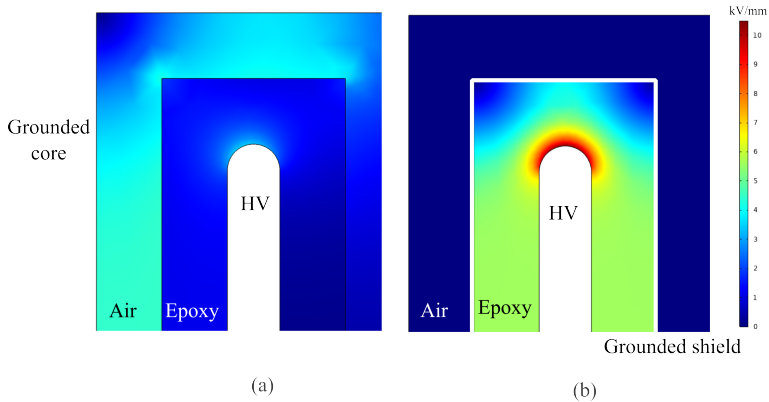
Figure 5.21: Impact of the grounded electric shield on the end of windings, without shield (a), with a grounded shield with a conductivity of 1 S/m (b).

insulation is thicker around the terminals, as drawn in Figure 5.18. The field at the HV terminal is simulated and is shown in Figure 5.22. When the grounded shield ends around the corner, the field in the air is higher than 3 kV/mm and triggers PD. Therefore, the grounded shield is prolonged and is covered by a semiconductor layer. Then, the maximal field is controlled to a safety range as shown in Figure 5.22 (b).
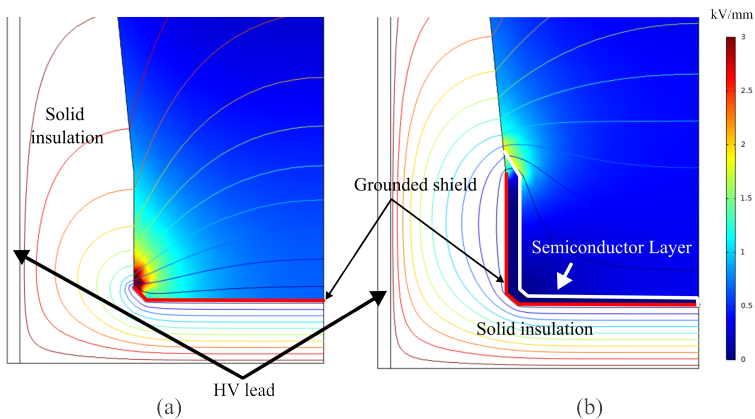
Figure 5.22: HV termination design. (a) High field spot at termination without stress-control layer. (b) High field spot at termination with semiconductor stress-control layer with a conductivity of 1 S/m

- Insulation between turns.

The insulation between conductors has to withstand continuous working voltage and impulse stresses. Firstly, the insulation requirement for withstanding working voltage is considered. It is assumed that the winding is composed of round wires, then the electric field between two turns is approximated by two round conductors, and the

impact of other turns is ignored. If the conductor can be regarded as a bare conductor with radius a, then the maximal field strength is given in (5.9). d is the distance between two centres of conductors, R_{da} is the ratio of the distance d to the radius a, V is the voltage difference between two conductors.

$$E_{max} = \frac{\sqrt{\dfrac{R_{da}^2}{4} - 1}}{a\left(\dfrac{R_{da}}{2} - 1\right)\text{acosh}\left(\dfrac{R_{da}}{2}\right)} \frac{V}{2} \tag{5.9}$$

If the wire has an additional insulation layer and the permittivity differs from the winding insulation material, an approximate maximal field between two round conductors can be obtained based on the method in section 3.7.

For the continuous working voltage stresses, the voltage difference V can be obtained by assuming the linear distribution of the voltage on windings. However, when facing impulse stresses, the voltage is not linearly distributed due to the capacitance. A well-known phenomenon is that the steep rise can cause an uneven voltage distribution along the winding. The initial voltage distributions and gradients can be described by (5.10), where c_g is winding to ground capacitance per length, c_s is inter-turn capacitance per length, l is length of winding. The initial voltage distribution is shown in Figure 5.23.

Grounded neutral   Isolated neutral

$$u = U_0 \frac{\sinh(kx)}{\sinh(kl)} \qquad u = U_0 \frac{\cosh(kx)}{\cosh(kl)}$$

$$\frac{du}{dx} = kU_0 \frac{\cosh(kx)}{\sinh(kl)} \qquad \frac{du}{dx} = kU_0 \frac{\sinh(kx)}{\cosh(kl)} \tag{5.10}$$

$$k = \sqrt{\frac{c_g}{c_s}}$$
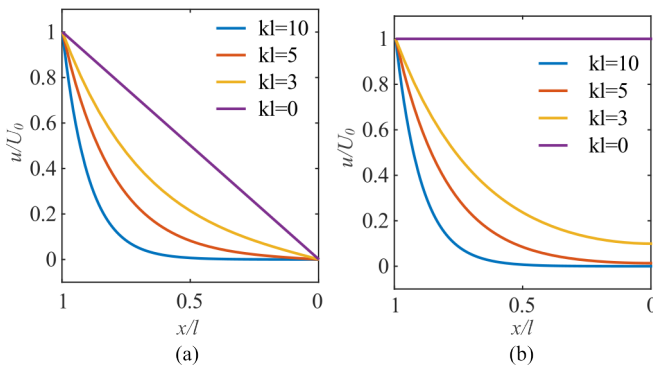
Figure 5.23: Initial voltage distribution, grounded neutral (a), isolated neutral (b)

If kl is larger than 3, the maximal gradients under two different neutrals can approximate the value kU_0. The distribution constant α is used to character the initial

voltage distribution and is calculated by (5.11), where V_{imp} is the voltage difference between the first two turn under impulse, V_{uni} is the voltage difference under uniform distribution, C_g is the winding- ground capacitance and C_s is the series capacitance.

$$V_{imp} = \alpha V_{uni} \quad \alpha = \sqrt{\frac{C_g}{C_s}} \tag{5.11}$$

5.4.2. DESIGN FIELD STRENGTH

In the preceding section, the insulation structure is introduced, and several field strength equations are given under different situations. Then, there is still one important issue that is determining the value of the design field strength. For the air gap, the field strength is decided by the air breakdown field, which is around 2.5–3 kV/mm in atmospheric air. For safety, a margin is considered, and the field strength in the air is limited to 1.5 kV/mm. Besides, according to standards, if the application is at high altitudes, the air breakdown value must be corrected.

For solid insulation, it is more complex. In IEC 60664-4, the field strength is given in (5.6), which is even lower than atmospheric air for insulation ≥ 0.75mm. Besides, the rated frequency would be lower than 30 kHz. Hence, the field strength would be determined based on existing data and the known relationship between lifetime and various factors.

In IEC 60505 [177], the ageing stresses for the insulation system have four categories, i.e., electrical, thermal, mechanical and environmental. Among these categories, the relation between electrical stress and the lifetime is the main focus. For electrical stress, an empirical relationship, the inverse power model (5.12), is often used to relate electrical stress with lifetime L_e under AC and DC situations. The exponent n_E is called the voltage endurance coefficient.

$$L_e = L_0 V^{-n_E} \tag{5.12}$$

However, the stress applied to the insulation is the superimposition of DC and MF bipolar square waves. The factors like frequency and waveform need to be considered. Compared to the RMS value of field strength, the peak-to-peak value is accepted as the major factor in electrical ageing [42], [178]. The relation between frequency and lifetime is normally modelled by (5.13) [42], where γ varies with materials and is often assumed to be 1 [178].

$$L_e = L_0 \left(\frac{f}{f_0}\right)^{-\gamma} \tag{5.13}$$

The peak-to-peak voltage is much more influential than the steepness. Therefore, the lifetime is estimated based on the combination of peak-to-peak strength (5.12), insulation thickness (5.7) and the frequency (5.14) with $\gamma = 1$. Although it strongly simplifies the ageing mechanism, it can give guidance for choosing the field strength.

$$L_e = L_0 \left(\frac{E_p}{E_0}\right)^{-n_E} \left(\frac{d_i}{d_0}\right)^{-n_d} \frac{f_0}{f} \tag{5.14}$$

Figure 5.24 is a lifetime curve from an epoxy datasheet, and the n_E can be obtained from the designed working temperature. For example, the n_E is around 11 when the temperature is 85 °C. Since two waveforms superimpose the stress, the lifetime is
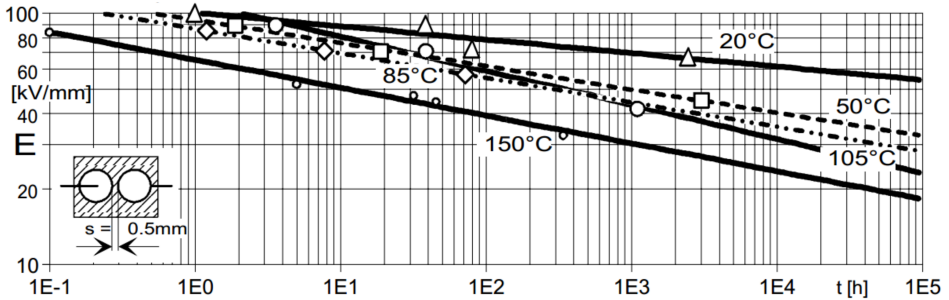
Figure 5.24: Lifetime curves of the electric field stress (E) at 20, 50, 85, 105 and 150 °C [179].

considered as a combination of lifetimes under two independent waveforms with Miner's rule [178]. For simplicity, DC ageing is considered equal to AC ageing, and all ageing factors remain the same. Then, the expected lifetime is (5.15). If n_E is a large value, the denominator might close to 1 in the ISOP connection because E_{p1}/E_{p2} is larger than 3 (2 sub-module). For example, in the considered scenario $E_{p1}/E_{p2} = 5$, if $f_2 = 5$ kHz, $n_E = 11$, the denominator is about 1, whose impact is trivial. Then, an iteration is used to correct the field strength, considering the impact of the thickness. If the n_d is set as 0.57, the field strength is 10.35 kV/mm. Using a safety factor of 1.2, the final design field strength is 8.5 kV/mm.

$$L_e = \frac{L_1 L_2}{L_1 + L_2} = L_0 \frac{\left(\dfrac{E_{p1}}{E_0}\right)^{-n_E} \dfrac{f_0}{f_1}}{\left(\dfrac{E_{p1}}{E_{p2}}\right)^{-n_E} \dfrac{f_2}{f_1} + 1} \left(\frac{d_i}{d_0}\right)^{-n_d} \tag{5.15}$$

For many materials, the lifetime curve is not available, and only breakdown strength is given based on IEC 60243-1. Therefore, the factors n_E and n_d can be set based on the values in the literature about similar materials. Besides, the breakdown strength is generally tested with 1 mm thickness according to IEC 60243-1 and IEC 60455-2, which should be set as d_0.

5.5. Conclusion

This chapter provides the insulation behaviours of the typical dry-type insulation failures under various frequency sinusoidal waveforms up to 5 kHz. The results show that the breakdown voltage of air does not show an obvious decrease in the test range. The surface flashover voltage decreases as the frequency is beyond a critical value, which is determined by the creepage distance. The breakdown strength of solids decreases considerably as the frequency increases. Then, the summarized relevant standards provide insulation requirements for the transformer. A 10kV ISOP modular

converter is used as an example of the insulation design procedure. An insulation structure is presented, which can address the possible high field in the air. A field strength selection method is provided, which considers the superimposing stress, impacts of frequency and dielectric thickness.

5

6

DESIGN OPTIMIZATION

You can't have the best of both worlds.

This chapter introduces the MF transformer design optimization process, including design variables, constraints, objective function, and optimization flow. Particle swarm optimization is used for optimization because of its advantages. The optimization process is done for both nanocrystalline and N87 magnetic cores. The final design is selected based on the efficiency, power density and safety margin for thermal stability. The design parameters based on the final design are given.

6.1. INTRODUCTION

DESIGN optimization is the approach towards the best design parameters that realize desired performance while satisfying various constraints. It generally involves four parts, i.e., objective function, design variables, constraints and optimization techniques [180]. The objective function describes the goal of the optimization, which maximizes or minimizes some attributes like efficiency and power density. However, the proper optimization function of the multi-variable optimization is not straightforward; any adjustment leads to a re-optimization. The general formats include linear, quadratic and non-linear. According to the author's limited knowledge, there is no standard function format which shows better performance and guarantees finding the global optimum. Optimization techniques are tools to find the best solution. Since magnetic component design is a non-linear and non-convex problem comprising continuous and discrete variables, it is almost impossible to guarantee its convergence and find the global optimum. There are many algorithms and methods used in the magnetic component design, like Monte Carlo method [181], [182], gradient-based methods [46], genetic algorithms [48], [183], particle swarm optimization (PSO) [47] and data-driven approaches [184].

In the thesis, PSO is selected as the optimization technique for several reasons. Firstly, PSO has fewer parameters and is relatively simple to implement compared to other optimization techniques. Then, it is efficient for searching the global space. The collective behaviour of particles can help to avoid local optima and reach the global optimum. The last reason is that PSO is very suitable for parallel computing, which can significantly reduce computation time. This chapter introduces an MF transformer design optimization process and its results. The second part introduces the details of the optimisation process, including design variables, constraints, objective function, and optimization flow. The third part shows the results of the optimization.

6.2. OPTIMIZATION ALGORITHM

THE starting point of the design of MF transformers is setting the specifications, variables and constraints. First, specifications of the MF transformers are needed, which are used in ISOP modular converter with DAB topology and SPS control. Since the thesis focuses on the electromagnetic and thermal field, only related specifications are considered and listed in Table 6.1.

Rated Power	105 kVA	Switching frequency	5 kHz
Primary winding voltage	3.5 kV	Secondary winding voltage	400 V
Primary winding current	30 A	Secondary winding voltage	262.5 A
Phase	Single	Ambient temperature	40 °C
Cooling type		Air Natural Convection	
Insulation Level (kV)		**AC** 28-**LI** 60 / **AC** 3-**LI** 6	

Table 6.1: Specifications of the design MF transformer.

In addition to the above specifications, there are some natural specifications. These specifications are from manufactory databases or standards, including core material properties, core dimensions, wire diameters, and insulation material properties. Some used properties are listed in 6.2.

VITROPERM 500F [185]								
B_{sat}	1.1 T	k	8.7E-3 W/m^3	α	1.747	β	2.19	k_t	[0.37,28,28] W/(m·K)

N87								
B_{sat}	0.39 T	k	14.15 W/m^3	α	1.265	β	2.697	k_t	4 W/(m·K)

Epoxy CY225-HY925 [179]								
ϵ_r	4.5	E_m	18 kV/mm	n_d	0.57	n_E	11	k_t	0.8 W/(m·K)

Table 6.2: Specifications of the materials.
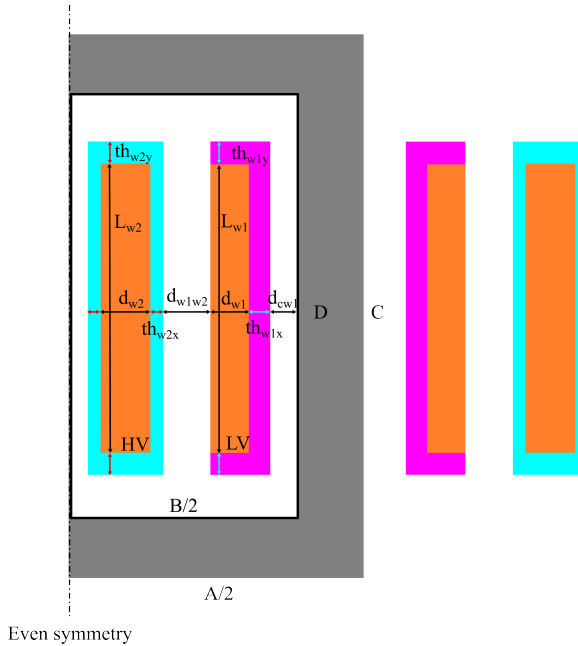
Figure 6.1: MF transformer geometry for design optimization

Besides the specifications, design variables build the global design space. The chosen variables relate to wire selection, core selection and core window arrangements. The 8 design variables are listed in Table 6.3. Variables a/δ and J are related to wire selection. Variables K_c and N_s relate to core selection. Variabls K_{w1} and K_{w2} relate to winding geometries and variables K_{w1w2} and K_{cw1} relate to dimensions between

Variables	Min	Max	Unit
Flux Density ratio $K_c = B_{max}/B_{sat}$	0.5	0.9	p.u.
Penetration ratio a/δ	0.5	1	-
Current density J	3	6	A/mm^2
Secondary winding number of turns N_s	2	10	-
HV-LV distance ratio $K_{w1w2} = d_{w1w2}/d_{free}$	0.1	0.5	p.u.
LV-C distance ratio $K_{cw1} = d_{cw1}/d_{free}$	0.1	0.5	p.u.
LV geometry ratio $K_{w1} = d_{w1}/L_{w1}$	0.02	1	p.u.
HV geometry ratio $K_{w2} = d_{w2}/L_{w2}$	0.02	1	p.u.

Table 6.3: Variables of the design MF transformer.

windings and the core. The geometric-related variables are defined based on the parameters described in Figure 6.1.

$$d_{free} = \frac{B}{2} - d_{w1} - d_{w2} - 2th_{w2x} - th_{w1x} - d_{clear} \tag{6.1}$$

The constraints focus on the maximum temperature and electrical field strength, which should not exceed the predefined limits.

- $T_{max} < T_{ins}°C$ in the windings, which is required by the properties of insulations.

- $T_{max} < T_{core}°C$ in the core, which is required by the properties of magnetic materials.

- $E_{max} < E_0$, and the design field E_0 strength is decided by the method introduced in Section 5.4.

After obtaining the inputs and constraints, the optimization follows the basic flowchart in Figure 6.2. The optimization tool uses MATLAB built-in PSO function [186]. Firstly, the specifications are imported, and the variables are generated based on uniform distribution in the predefined ranges. Then, the wire requirements are obtained through penetration ratio, current density and rated current. The properties of the wire are estimated by the 3D Litz wire model introduced in Chapter 4. A PSO is implemented to optimize the Litz wire properties. However, in order to achieve a relatively short computation time, the PSO only has a small swarm size and a small number of maximal iterations, and optimum design is not the target. A nested optimisation process is formed since there is another PSO for the Litz wire. To reduce the running time of PSO for Litz wire, the wire-related variables a/δ and J form the first level of optimization. The other variables are optimized in the second level, and the PSO for Litz wire only work once with one set of a/δ and J.

Next, the winding dimension is calculated based on the number of turns N_s, the winding geometry ratios K_{w1}, K_{w2} and dimensions of the wire and initial estimated

insulation thickness. The core dimension is chosen according to the required winding dimensions and the available core dimensions in the datasheets. The number of parallel cores is decided based on the number of turns, maximum flux density and winding voltage. This part of the process results in a basic geometry of the MF transformer.
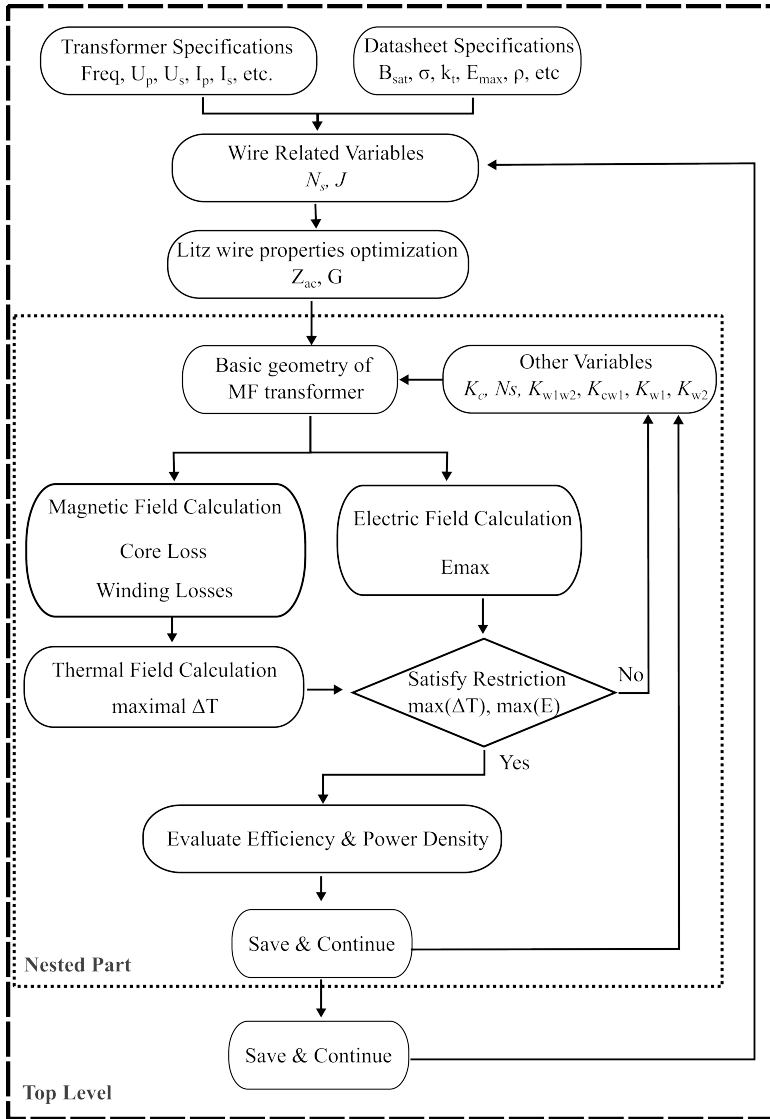
Figure 6.2: Flowchart of MF transformer design optimization

Next, the constraints-related parameters are estimated. Based on the analysis in previous chapters, the core loss is calculated by IGSE. The proposed analytical BEM

coupled method calculates winding loss, maximal electrical field strength, and equivalent winding thermal conductivity. The maximal temperature is obtained through a thermal resistance circuit. If the maximal temperature and electric field strength satisfy the constraints, properties like efficiency and volumetric and gravimetric power density are estimated.

As mentioned in the introduction, the objective function is not straightforward and may have various formats. The target of the thesis is designing high efficiency and high power density MF transformers. Therefore, the objective function aims to minimize the loss, $(1 - \eta)$, the volume V_{MFT} and the weight m_{MFT}, and a weighted linear function is used in PSO, and the w_1, w_2 and w_3 are the weighted factor, as shown in (6.2).

$$\text{Minimize} f(x) = w_1(1 - \eta) + w_2 V_{MFT} + w_3 m_{MFT} \tag{6.2}$$

6.3. OPTIMIZATION RESULT

The proposed optimization process is applied to both the Nanocrystalline VITROPERM 500F and N87. The geometries of magnetic cores use data from manufacturers [187], [188]. The maximum temperatures of the core and the windings are set to 120 °C and 100 °C, respectively. The PSO process is limited by predefined maximal iterations due to time consideration, and the maximum number of considered possibilities is 192000. After the process, there are 48124 and 36934 possible designs based on nanocrystalline and N87 materials, respectively. All obtained possible MF transformer designs are shown in Figure 6.3 and 6.4.
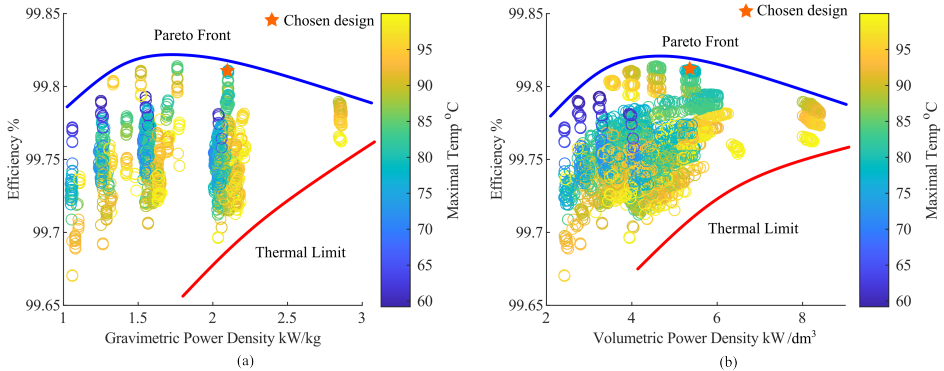
Figure 6.3: Possible MF transformer designs obtained by PSO process based on Nanocrystalline, (a) Efficiency vs gravimetric power density; (b) Efficiency vs volumetric power density. Colour corresponds to the highest temperature.

Figure 6.3 shows the relationship between efficiency and gravimetric power density (a) and volumetric power density (b) in the designs with nanocrystalline. Figure 6.4 shows the same relationship in the designs with N87. The colour represents the maximal temperature of the designs. The dispersive clusters of the designs are caused by the discrete core geometries, especially the number of parallel cores. The upper boundary of the possible design is the Pareto front, which is extrapolated based on the
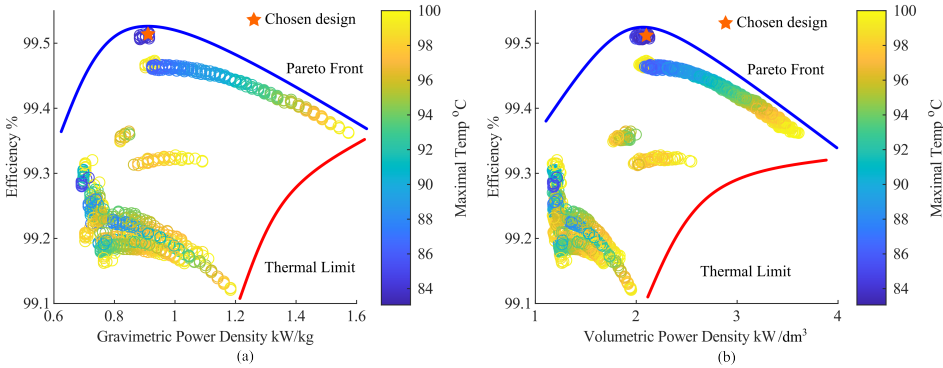
Figure 6.4: Possible MF tranformer designs obtained by PSO process based on N87, (a) Efficiency vs. gravimetric power density; (b) Efficiency vs. volumetric power density. Colour corresponds to the highest temperature.

known data points. The red boundary is the thermal limit, which is estimated based on the known points. This represents the trade-off between efficiency and power density. To achieve high power density, the magnetic flux in the core and current density in the windings also need to be high, which can lead to high loss and low efficiency. The lower boundary represents the thermal limit. The high power density also implicates poor available thermal convection area, therefore, only designs with higher efficiency are possible.

In Figure 6.3 and 6.4, one design is chosen in each figure. The chosen designs are decided by (6.2) and may not have the highest efficiency or power density. However, since the thermal model is based on empirical equations, especially for natural air convection, it is better to consider a safety margin for maximal temperature. In order to choose a thermally stable design, an additional requirement that the maximal temperature is smaller than $85\,^{\circ}C$ is added.

Comparing the selected designs based on nanocrystalline and N87, the designs with nanocrystalline achieve higher power density due to the higher saturation flux density. With the same number of turns, the N87 needs a more effective core cross-section area. The design with a nanocrystalline core also shows better efficiency because the more core cross-section area indicates a more parallel core and longer mean length of turns, which results in more loss in windings. Therefore, the final design with nanocrystalline is chosen.

In Table 6.4, specifications of the final selected design are given. The first row gives the values of the design variables. The second row gives the efficiency η, the gravimetric and volumetric power density, the maximal temperature, the core loss P_c, the winding loss P_w, the leakage inductance L_σ, the capacitance of primary winding to ground C_p. The capacitance is calculated by considering the DC voltage and voltage distribution in the winding. The third row gives the capacitance of secondary winding to ground C_s, radius of strands r_s, the number of strands in the Litz wire for the secondary winding ns_s and for the primary winding ns_p, creepage distance and clearance for the primary and

secondary windings. The higher value is for the primary winding.

K_c	a/δ	J	N_s	K_{w1w2}	K_{cw1}	K_{w1}	K_{w2}
0.865	0.5	3	2	0.5	0.1	1	0.02
η	kW/kg	kW/L	T_{max}	P_c	P_w	L_σ	C_p
99.81%	2.1	5.36	78.6°C	96.44 W	101.40 W	79.6 μH	1.49 nF
C_s	r_s	ns_s	ns_p	Creepage		Clearance	
1.40 nF	0.335 mm	249	29	134.4mm	5.12mm	90 mm	5.5mm

Table 6.4: Specifications of the final selected design

The parasitic parameters are checked with COMSOL 3D FEM. The results are shown in Figure 6.5 (c), which have less than 10% error compared to the estimated value in Table 6.4. It validates the effectiveness of the models used in the optimization process.

C_p	C_s	$L_{\sigma DC}$
1.51 nF	1.43 nF	81.94μH

(a)   (b)   (c)
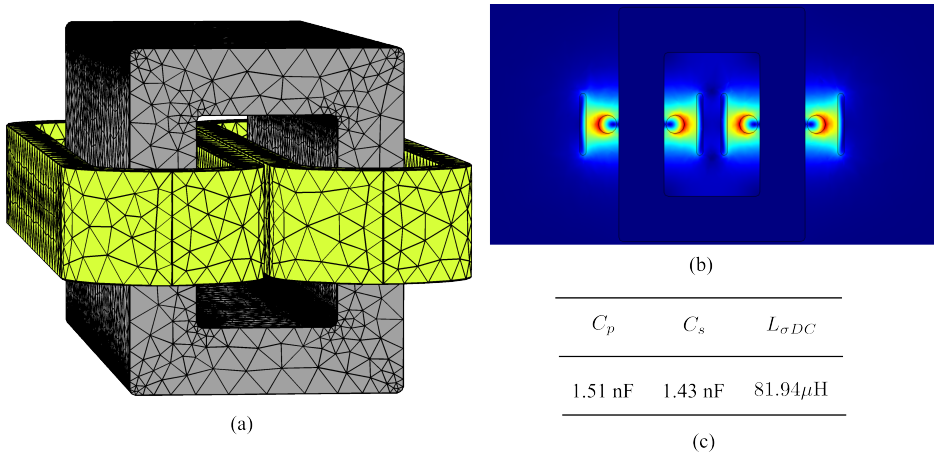
Figure 6.5: A 3D geometry of MF transformer design (heat sink is not shown) (a), magnetic field distribution (b), parasitic parameters (c).

6.4. CONCLUSION

To optimize MF transformer designs, this chapter provides a procedure for MF transformer design optimization. The global design space is built based on 8 design variables, which decide the wires, cores and winding arrangements. Particle swarm optimization is chosen as the optimization method. A nested optimization algorithm is built to reduce the computational cost since the performance of the Litz wire is also optimized during the algorithm. The optimization process is done for both nanocrystalline and N87 magnetic cores and results in 48124 and 36934 possible designs, respectively. A design is selected based on a weighted linear function, which depends on the efficiency and power densities. The design parameters are 99.81%

efficiency, 2.1 kW/kg gravimetric power density and 5.36 kW/dm^3 volumetric power density. The design parameters based on the final design are given and are less than 10% error compared to the results from 3D FEMs.

6

7

CONCLUSIONS AND FUTURE RECOMMENDATIONS

This chapter summarises the conclusions of each previous chapter and answers the research questions in Chapter 1. Based on the works of this thesis, several future research directions are recommended.

7.1. CONCLUSIONS

THIS thesis studies the modelling and optimization procedure of medium voltage high power medium frequency transformers, which are one of the most important parts of isolated power electronic converters. The study first summarizes the available sophisticated multi-physical models. Then, several methods are proposed for modelling, especially for eddy current and Litz wire issues. Next, the insulation behaviours are tested under sinusoidal stress with various frequencies, and an insulation design method is proposed. Finally, an optimization process involving a medium frequency transformer and Litz wire is developed based on particle swarm optimization. The modelling methods developed in this thesis show good accuracy and fast computation speed compared with a commercial FEM software and several several state of art methods. The final design parameters reach the same level as the works in 1.3. The following section outlines the conclusion of the thesis by addressing the research questions.

1. Which types of models are suitable for modelling MF transformers?

   The models for MF transformers involve multiple physics and are coupled together to different degrees. It is difficult and time-consuming to solve the full-coupled fields. In practice, decoupled models are generally used for different aspects of the MF transformers. In Chapter 2, several commonly used models are summarized, which focus on magnetic, electric and thermal fields. These models are mainly analytical and empirical models because of their short computation time. The models involve magnetizing inductance, core losses, winding loss, parasitic parameters and thermal conditions. Besides, eddy currents in round conductors are analyzed, and new winding loss models are proposed, which can take the interaction between eddy currents into account. In Chapter 3, a two-dimensional circle boundary element & analytical coupled method is developed for windings. The suitable shape of the boundary element and the analytical solution for the inside domain leads to significantly smaller element numbers and faster computational speed compared to 2D FEM. This model can be applied to the quasi-static magnetic, static electric field and heat conduction, which shows good potential for modelling the MF transformers. The following methods are selected to model MF transformers. Magnetization inductance is calculated by reluctance method with Patridge's equation. Core loss is estimated with IGSE. Winding loss, leakage inductance, stray capacitance and windings' equivalent heat resistances are calculated with the proposed boundary element & analytical method. The thermal distribution is calculated with thermal circuits.

2. How to model Litz wires and incorporate its results into the model for whole windings?

   In medium-frequency applications, eddy current is an important source of losses. Litz wires are widely used in kHz applications to reduce the impact of eddy currents. Through twisting, Litz wires can dramatically reduce the proximity effect losses caused by the external magnetic field and average the current distribution in strands. However, it also leads to complex structures, which are

difficult to model. In Chapter 4, the ideal Litz wires model is introduced. In order to consider the imperfect twisting impact, two Litz wire models are proposed. One is based on the 2.5D approximation and round boundary element analysis. Another is a 3D model with cylindrical elements, which analyses the transverse and longitudinal field individually. Both models are validated with two cases, which include perfect and imperfect twisting Litz wires. They demonstrate good accuracy and fast computational speed compared to 3D FEM. The 3D cylindrical element method is selected to model Litz wires since it can consider the longitudinal field and impact from elements that 2.5D cannot. The method incorporating the Litz wire model and the boundary element & analytical method is developed. The key idea of the homogenization technique is adopted, and the method is validated through measurements. The method is used in modelling windings with Litz wires.

3. What are the considerations when designing an air-solid insulation system for MV MF transformers?

With the development of wide-band-gap semiconductors, the stresses applied to the insulation are often in the kHz range, not sinusoidal and have repeated high steep edges (up to 100 V/ns), which can lead to poorer insulation behaviour compared to that under AC stress. At the same time, compared to the widely studied insulation behaviour under AC stress, the quantitative behaviour of the insulation under stress generated by power electronics is not available. Chapter 5 shows the tests of the insulation behaviours of air-solid insulation under various frequencies. Based on the relevant standards and literature, guidance for deciding the insulation level, clearance and creepage distance of MV MF transformers is provided. Single dielectric insulation is selected because of the superimposed stress in SSTs. The corresponding insulation structure is presented. A field strength selection method is provided, which considers the superimposing stress, impacts of frequency and dielectric thickness.

4. How to optimize the design of MV MF transformers?

Design optimization can help improve the performance of MF transformers in the required aspects. Transformer design is a non-linear and non-convex problem comprising of continuous and discrete variables. There are various optimization function formats and optimization techniques. However, there is no specific combination showing clearly superior performance in the literature. In Chapter 6, an optimization procedure combining particle swarm optimization with 8 variables and the linear objective function is proposed. A nested optimization algorithm is developed to save computational costs when optimizing the Litz wires within the algorithm. The optimization process is done for both nanocrystalline and N87 magnetic cores. The final design is selected based on the objective function. The design parameters are 99.81% efficiency, 2.1 kW/kg gravimetric power density and 5.36 kW/dm^3 volumetric power density. 3D FEM validates the accuracy of designed parasitic parameters. The proposed optimization procedure is suitable for optimizing MV MF transformers.

7.2. FUTURE WORK

BASED on the work in this thesis, there are recommendations for future research. The first recommendation is about modelling for windings. In the thesis, the windings are supposed to be composed of round conductors. Conductors like continuously transposed conductors (CTC) or foil are also commonly used conductors. Therefore, applying the developed method for CTC and foil can also be useful in applications.

The second recommendation is time domain models for magnetic components. The transient analysis needs time domain models, which often determine the worst working conditions. Since magnetic cores are non-linear media, a model that can simultaneously analyze core and winding in the time domain is important for transformer transient analysis.

The third recommendation is about insulation. Since the mechanism of insulation breakdown is complicated, the experiment is still the most reliable method to study the insulation. It is recommended to build a database saving insulation behaviours based on some test parameters like sample thickness, material, frequency, waveform, etc. The database is important and meaningful. Based on the database, a data-driven model can be developed, which can be helpful for the insulation design.

The fourth recommendation is the sensitivity analysis of the design optimization. The final design is chosen based on several parameters in the thesis, and the full-scale prototype is not built. Therefore, the tolerance during production and its impact are not clear. The sensitivity analysis helps understand the robustness and reliability of the design and provides insights into which variables are most influential in the optimization process. Then, build a full-scale prototype to validate the design.

7

BIBLIOGRAPHY

[1] S. Errede, *A Brief History of Electromagnetism*, 2007.

[2] F. Uppenborn, *History of the Transformer*. London ; New York: E. & F.N. Spon, 1889.

[3] E. T. Center. "The History of the Transformer". (2024), [Online]. Available: https://edisontechcenter.org/Transformers.html.

[4] Engineering and T. H. Wiki. "Milestones: Alternating Current Electrification, 1886". (2004), [Online]. Available: https://ethw.org/Milestones:Alternating_Current_Electrification,_1886.

[5] V. Smil, *Creating the Twentieth Century: Technical Innovations of 1867-1914 and Their Lasting Impact*. Oxford University Press, Jul. 2005.

[6] X. She, A. Q. Huang, and R. Burgos, "Review of Solid-State Transformer Technologies and Their Application in Power Distribution Systems", *IEEE Journal of Emerging and Selected Topics in Power Electronics*, vol. 1, pp. 186–198, 3 Sep. 2013.

[7] ABB, *Distribution Transformers*, ABB, 2001.

[8] M. Kazimierczuk, *High-Frequency Magnetic Components*. Wiley, Dec. 2013.

[9] M. Guarnieri, "Solidifying Power Electronics [Historical]", *IEEE Industrial Electronics Magazine*, vol. 12, no. 1, pp. 36–40, 2018.

[10] D. Prince, "The direct current transformer utilizing thyratron tubes", *General Electric Review*, vol. 31, no. 7, pp. 347–350, 1928.

[11] F. C. Schwarz and J. B. Klaassens, "A Controllable 45-kW Current Source for DC Machines", *IEEE Transactions on Industry Applications*, vol. IA-15, no. 4, pp. 437–444, 1979.

[12] M. Kheraluwala, R. W. Gascoigne, D. M. Divan, and E. D. Baumann, "Performance characterization of a high-power dual active bridge DC-to-DC converter", *IEEE Transactions on industry applications*, vol. 28, no. 6, pp. 1294–1301, 1992.

[13] S. Hazra, A. De, L. Cheng, *et al.*, "High switching performance of 1700-V, 50-A SiC power MOSFET over Si IGBT/BiMOSFET for advanced power conversion applications", *IEEE Transactions on Power Electronics*, vol. 31, no. 7, pp. 4742–4754, 2015.

[14] G. Wang, S. Baek, J. Elliott, *et al.*, "Design and hardware implementation of Gen-1 silicon based solid state transformer", in *2011 Twenty-Sixth Annual IEEE Applied Power Electronics Conference and Exposition (APEC)*, 2011, pp. 1344–1349.

[15] D. Wang, J. Tian, C. Mao, *et al.*, "A 10-kV/400-V 500-kVA electronic power transformer", *IEEE Transactions on Industrial Electronics*, vol. 63, no. 11, pp. 6653–6663, 2016.

[16] C. Zhao, D. Dujic, A. Mester, *et al.*, "Power Electronic Traction Transformer—Medium Voltage Prototype", *IEEE Transactions on Industrial Electronics*, vol. 61, no. 7, pp. 3257–3268, 2014.

[17] A. Q. Huang, "Medium-Voltage Solid-State Transformer: Technology for a Smarter and Resilient Grid", *IEEE Industrial Electronics Magazine*, vol. 10, pp. 29–42, 3 Sep. 2016.

[18] H. A. B. Siddique and R. W. De Doncker, "Evaluation of DC Collector-Grid Configurations for Large Photovoltaic Parks", *IEEE Transactions on Power Delivery*, vol. 33, no. 1, pp. 311–320, 2018.

[19] P. Lakshmanan, R. Sun, and J. Liang, "Electrical collection systems for offshore wind farms: A review", *CSEE Journal of Power and Energy Systems*, vol. 7, no. 5, pp. 1078–1092, 2021.

[20] I. E. Agency, *CO2 Emissions in 2022*, https://www.iea.org/reports/co2-emissions-in-2022, Accessed on March 15, 2024, 2023.

[21] E. Council, *European Council, 12-13/12/2019*, https://www.consilium.europa.eu/en/meetings/european-council/2019/12/12-13/, Accessed on March 15, 2024, 2019.

[22] P. Wheeler, T. S. Sirimanna, S. Bozhko, and K. S. Haran, "Electric/Hybrid-Electric Aircraft Propulsion Systems", *Proceedings of the IEEE*, vol. 109, pp. 1115–1127, 6 Jun. 2021.

[23] J. S. Chalfant and C. Chryssostomidis, "Analysis of various all-electric-ship electrical distribution system topologies", in *2011 IEEE Electric Ship Technologies Symposium*, 2011, pp. 72–77.

[24] P. Czyz, T. Guillod, D. Zhang, *et al.*, "Analysis of the Performance Limits of 166 kW/7 kV Air- and Magnetic-Core Medium-Voltage Medium-Frequency Transformers for 1:1-DCX Applications", *IEEE Journal of Emerging and Selected Topics in Power Electronics*, vol. 10, no. 3, pp. 2989–3012, 2022.

[25] T. Guillod, D. Rothmund, and J. W. Kolar, "Active Magnetizing Current Splitting ZVS Modulation of a 7 kV/400 V DC Transformer", *IEEE Transactions on Power Electronics*, vol. 35, no. 2, pp. 1293–1305, 2020.

[26] G. Ortiz, M. Leibl, J. W. Kolar, and O. Apeldoorn, "Medium frequency transformers for solid-state-transformer applications — Design and experimental verification", in *2013 IEEE 10th International Conference on Power Electronics and Drive Systems (PEDS)*, 2013, pp. 1285–1290.

[27] T. B. Gradinger, U. Drofenik, and S. Alvarez, "Novel insulation concept for an MV dry-cast medium-frequency transformer", in *2017 19th European Conference on Power Electronics and Applications (EPE'17 ECCE Europe)*, 2017, P.1–P.10.

[28] M. Mogorovic and D. Dujic, "100 kW, 10 kHz Medium-Frequency Transformer Design Optimization and Experimental Verification", *IEEE Transactions on Power Electronics*, vol. 34, no. 2, pp. 1696–1708, 2019.

[29] N. Djekanovic and D. Dujic, "Copper Pipes as Medium Frequency Transformer Windings", *IEEE Access*, vol. 10, pp. 109 431–109 445, 2022.

[30] P. Yao, X. Jiang, P. Xue, S. Li, S. Lu, and F. Wang, "Design optimization of medium-frequency transformer for DAB converters with DC bias capacity", *IEEE Journal of Emerging and Selected Topics in Power Electronics*, vol. 9, no. 4, pp. 5043–5054, 2020.

[31] X. Guo, Z. Zheng, and C. Li, "The Full-Analytical Model of AC Loss for Hollow Copper Winding in Medium Frequency Transformer", *IEEE Transactions on Power Electronics*, vol. 38, pp. 7471–7479, 6 Jun. 2023.

[32] T. Ewald and J. Biela, "Analytical winding loss and inductance models for gapped inductors with Litz or solid wires", *IEEE Transactions on Power Electronics*, pp. 1–13, 2022.

[33] R. Y. Zhang, J. K. White, J. G. Kassakian, and C. R. Sullivan, "Realistic litz wire characterization using fast numerical simulations", in *Conference Proceedings - IEEE Applied Power Electronics Conference and Exposition - APEC*, IEEE, Mar. 2014, pp. 738–745.

[34] C. R. Sullivan and R. Y. Zhang, "Simplified design method for litz wire", in *2014 IEEE Applied Power Electronics Conference and Exposition - APEC 2014*, IEEE, Mar. 2014, pp. 2667–2674.

[35] B. Zhao, Q. Song, W. Liu, and Y. Sun, "Overview of Dual-Active-Bridge Isolated Bidirectional DC–DC Converter for High-Frequency-Link Power-Conversion System", *IEEE Transactions on Power Electronics*, vol. 29, no. 8, pp. 4091–4106, 2014.

[36] R. L. Lin and L. H. Huang, "Efficiency Improvement on LLC Resonant Converter Using Integrated LCLC Resonant Transformer", vol. 54, no. 2, 2018.

[37] T. Guillod, D. Rothmund, and J. W. Kolar, "Active magnetizing current splitting ZVS modulation of a 7 kV/400 V DC transformer", *IEEE Transactions on Power Electronics*, vol. 35, no. 2, pp. 1293–1305, 2019.

[38] B. Yang, F. C. Lee, A. J. Zhang, and G. Huang, "LLC resonant converter for front end DC/DC conversion", in *APEC. Seventeenth Annual IEEE Applied Power Electronics Conference and Exposition (Cat. No. 02CH37335)*, IEEE, vol. 2, 2002, pp. 1108–1112.

[39] M. A. Saket, N. Shafiei, and M. Ordonez, "LLC Converters with Planar Transformers: Issues and Mitigation", *IEEE Transactions on Power Electronics*, vol. 32, no. 6, 2017.

[40] M. Popov, L. van der Sluis, R. P. P. Smeets, and J. Lopez Roldan, "Analysis of Very Fast Transients in Layer-Type Transformer Windings", *IEEE Transactions on Power Delivery*, vol. 22, no. 1, pp. 238–247, 2007.

[41] A. Cavallini, D. Fabiani, and G. Montanari, "Power electronics and electrical insulation systems - Part 1: Phenomenology overview", *IEEE Electrical Insulation Magazine*, vol. 26, no. 3, pp. 7–15, 2010.

[42] A. Cavallini, D. Fabiani, and G. Montanari, "Power electronics and electrical insulation systems - part 2: life modeling for insulation design", *IEEE Electrical Insulation Magazine*, vol. 26, no. 4, pp. 33–39, 2010.

[43] M. Mogorovic and D. Dujic, "Thermal modeling and experimental verification of an air cooled medium frequency transformer", *2017 19th European Conference on Power Electronics and Applications, EPE 2017 ECCE Europe*, vol. 2017-January, Nov. 2017.

[44] M. Jaritz, A. Hillers, and J. Biela, "General Analytical Model for the Thermal Resistance of Windings Made of Solid or Litz Wire", *IEEE Transactions on Power Electronics*, vol. 34, pp. 668–684, 1 Jan. 2019.

[45] A. Fouineau, M. Guillet, B. Lefebvre, M.-A. Raulet, and F. Sixdenier, "A Medium Frequency Transformer Design Tool with Methodologies Adapted to Various Structures", in *2020 Fifteenth International Conference on Ecological Vehicles and Renewable Energies (EVER)*, 2020, pp. 1–1.

[46] A. K. Das, Z. Wei, B. G. Fernandes, *et al.*, "Multi-variable optimization methodology for medium-frequency high-power transformer design employing steepest descent method", in *2018 IEEE Applied Power Electronics Conference and Exposition (APEC)*, IEEE, 2018, pp. 1786–1793.

[47] H. Qin, J. W. Kimball, and G. K. Venayagamoorthy, "Particle swarm optimization of high-frequency transformer", in *IECON 2010-36th Annual Conference on IEEE Industrial Electronics Society*, IEEE, 2010, pp. 2914–2919.

[48] A. Garcia-Bediaga, I. Villar, A. Rujas, L. Mir, and A. Rufer, "Multiobjective optimization of medium-frequency transformers for isolated soft-switching converters using a genetic algorithm", *IEEE Transactions on Power Electronics*, vol. 32, no. 4, pp. 2995–3006, 2016.

[49] D. Wilcox, M. Conlon, and W. Hurley, "Calculation of self and mutual impedances for coils on ferromagnetic cores", *IEE Proceedings A Physical Science, Measurement and Instrumentation, Management and Education, Reviews*, vol. 135, p. 470, 7 1988.

[50] C. W. T. McLyman, *Transformer and inductor design handbook*. CRC press, 2004.

[51] TDK, *Mn-Zn Large Size Ferrite Cores for High Power UU series*, Large size cores for transformers with large power outputs. Can also be used in reactors., 2021.

[52] G. Bertotti, "General properties of power losses in soft ferromagnetic materials", *IEEE Transactions on Magnetics*, vol. 24, pp. 621–630, 1 Jan. 1988.

[53] S. Hui, J. Zhu, and V. Ramsden, "A generalized dynamic circuit model of magnetic cores for low- and high-frequency applications. II. Circuit model formulation and implementation", *IEEE Transactions on Power Electronics*, vol. 11, pp. 251–259, 2 Mar. 1996.

[54] J. Zhu, S. Hui, and V. Ramsden, "A generalized dynamic circuit model of magnetic cores for low- and high-frequency applications. I. Theoretical calculation of the equivalent core loss resistance", *IEEE Transactions on Power Electronics*, vol. 11, pp. 246–250, 2 Mar. 1996.

[55] D. Lin, P. Zhou, W. Fu, Z. Badics, and Z. Cendes, "A Dynamic Core Loss Model for Soft Ferromagnetic and Power Ferrite Materials in Transient Finite Element Analysis", *IEEE Transactions on Magnetics*, vol. 40, pp. 1318–1321, 2 Mar. 2004.

[56] M. A. Bahmani, E. Agheb, T. Thiringer, H. K. Høidalen, and Y. Serdyuk, "Core loss behavior in high frequency high power transformers—I: Effect of core topology", *Journal of Renewable and Sustainable Energy*, vol. 4, p. 033 112, 3 May 2012.

[57] T. Matsuo, "Anisotropic Vector Hysteresis Model Using an Isotropic Vector Play Model", *IEEE Transactions on Magnetics*, vol. 46, pp. 3041–3044, 8 Aug. 2010.

[58] D. Jiles and D. Atherton, "Ferromagnetic hysteresis", *IEEE Transactions on Magnetics*, vol. 19, pp. 2183–2185, 5 Sep. 1983.

[59] D. Jiles and D. Atherton, "Theory of ferromagnetic hysteresis", *Journal of Magnetism and Magnetic Materials*, vol. 61, pp. 48–60, 1-2 Sep. 1986.

[60] I. Mayergoyz, "Mathematical models of hysteresis", *IEEE Transactions on Magnetics*, vol. 22, pp. 603–608, 5 Sep. 1986.

[61] I. Mayergoyz and C. Serpico, "Nonlinear diffusion of electromagnetic fields and excess eddy current losses", *Journal of applied physics*, vol. 85, no. 8, pp. 4910–4912, 1999.

[62] C. Steinmetz, "On the law of hysteresis", *Proceedings of the IEEE*, vol. 72, pp. 197–221, 2 1984.

[63] J. Reinert, A. Brockmeyer, and R. D. Doncker, "Calculation of losses in ferro- and ferrimagnetic materials based on the modified Steinmetz equation", *IEEE Transactions on Industry Applications*, vol. 37, pp. 1055–1061, 4 2001.

[64] J. Li, T. Abdallah, and C. Sullivan, "Improved calculation of core loss with nonsinusoidal waveforms", vol. 4, IEEE, 2001, pp. 2203–2210.

[65] K. Venkatachalam, C. Sullivan, T. Abdallah, and H. Tacca, "Accurate prediction of ferrite core loss with nonsinusoidal waveforms using only Steinmetz parameters", vol. 2002-Janua, IEEE, 2002, pp. 36–41.

[66] J. Muhlethaler, J. Biela, J. W. Kolar, and A. Ecklebe, "Improved Core-Loss Calculation for Magnetic Components Employed in Power Electronic Systems", *IEEE Transactions on Power Electronics*, vol. 27, pp. 964–973, 2 Feb. 2012.

[67] Y. LeCun, Y. Bengio, and G. Hinton, "Deep learning", *nature*, vol. 521, no. 7553, pp. 436–444, 2015.

[68] J. Schmidhuber, "Deep learning in neural networks: An overview", *Neural networks*, vol. 61, pp. 85–117, 2015.

[69] H. Li, D. Serrano, T. Guillod, *et al.*, "How MagNet: Machine Learning Framework for Modeling Power Magnetic Material Characteristics", *IEEE Transactions on Power Electronics*, vol. 38, no. 12, pp. 15 829–15 853, 2023.

[70] H. Li, D. Serrano, S. Wang, and M. Chen, "MagNet-AI: Neural Network as Datasheet for Magnetics Modeling and Material Recommendation", *IEEE Transactions on Power Electronics*, vol. 38, no. 12, pp. 15 854–15 869, 2023.

[71] D. Serrano, H. Li, S. Wang, *et al.*, "Why MagNet: Quantifying the Complexity of Modeling Power Magnetic Material Characteristics", *IEEE Transactions on Power Electronics*, vol. 38, no. 11, pp. 14 292–14 316, 2023.

[72] *Princeton MagNet-AI Platform*, https://mag-net.princeton.edu.

[73] M. Pavlovsky, S. de Haan, and J. Ferreira, "Partial Interleaving: A Method to Reduce High Frequency Losses and to Tune the Leakage Inductance in High Current, High Frequency Transformer Foil Windings", vol. 2005, IEEE, 2005, pp. 1540–1547.

[74] S. Vaisambhayana, C. Dincan, C. Shuyu, A. Tripathi, T. Haonan, and B. R. Karthikeya, "State of art survey for design of medium frequency high power transformer", *2016 Asian Conference on Energy, Power and Transportation Electrification, ACEPT 2016*, pp. 1–9, Oct. 2017.

[75] L. Taylor, X. Margueron, Y. L. Menach, and P. L. Moigne, "Numerical modelling of PCB planar inductors: impact of 3D modelling on high-frequency copper loss evaluation", *IET Power Electronics*, vol. 10, pp. 1966–1974, 14 Nov. 2017.

[76] P. Dowell, "Effects of eddy currents in transformer windings", *Proceedings of the Institution of Electrical Engineers*, vol. 113, p. 1387, 8 1966.

[77] J. Ferreira, "Improved analytical modeling of conductive losses in magnetic components", *IEEE Transactions on Power Electronics*, vol. 9, pp. 127–131, 1 Jan. 1994.

[78] J. Mühlethaler, J. W. Kolar, and A. Ecklebe, "Loss modeling of inductive components employed in power electronic systems", IEEE, May 2011, pp. 945–952.

[79] M. Bartoli, N. Noferi, A. Reatti, and M. K. Kazimierczuk, "Modelling winding losses in high-frequency power inductors", *Journal of Circuits, Systems, and Computers*, vol. 5, no. 04, pp. 607–626, 1995.

[80] X. Nan and C. R. Sullivan, "An improved calculation of proximity-effect loss in high-frequency windings of round conductors", vol. 2, IEEE, 2003, pp. 853–860.

[81] X. Nan and C. R. Sullivan, "Simplified high-accuracy calculation of eddy-current loss in round-wire windings", vol. 2, IEEE, 2004, pp. 873–879.

[82] G. Dimitrakakis, E. Tatakis, and E. Rikos, "A Semiempirical Model to Determine HF Copper Losses in Magnetic Components With Nonlayered Coils", *IEEE Transactions on Power Electronics*, vol. 23, pp. 2719–2728, 6 Nov. 2008.

[83] M. A. Bahmani, T. Thiringer, and H. Ortega, "An Accurate Pseudoempirical Model of Winding Loss Calculation in HF Foil and Round Conductors in Switchmode Magnetics", *IEEE Transactions on Power Electronics*, vol. 29, pp. 4231–4246, 8 Aug. 2014.

[84]   D. Ahmed, L. Wang, M. Wu, L. Mao, and X. Wang, "Two-Dimensional Winding Loss Analytical Model for High-Frequency Multilayer Air-Core Planar Inductor", *IEEE Transactions on Industrial Electronics*, vol. 69, pp. 6794–6804, 7 2022.

[85]   J. Lammeraner and M. Štafl, *Eddy currents*. CRC Press, 1966.

[86]   M. Albach and H. Roßmanith, "The influence of air gap size and winding position on the proximity losses in high frequency transformers", vol. 3, IEEE, 2001, pp. 1485–1490.

[87]   P. Wallmeier, "Improved analytical modeling of conductive losses in gapped high-frequency inductors", *IEEE Transactions on Industry Applications*, vol. 37, pp. 1045–1054, 4 Jul. 2001.

[88]   W. Roshen, "Fringing Field Formulas and Winding Loss Due to an Air Gap", *IEEE Transactions on Magnetics*, vol. 43, pp. 3387–3394, 8 Aug. 2007.

[89]   V. C. Valchev and A. Van den Bossche, *Inductors and transformers for power electronics*. CRC press, 2018.

[90]   R. Prieto, J. Cobos, O. Garcia, P. Alou, and J. Uceda, "Study of 3-D magnetic components by means of "double 2-D" methodology", *IEEE Transactions on Industrial Electronics*, vol. 50, pp. 183–192, 1 Feb. 2003, Double 2D concept.

[91]   H. Choi, "Analysis and design of LLC resonant converter with integrated transformer", in *Conference Proceedings - IEEE Applied Power Electronics Conference and Exposition - APEC*, 2007.

[92]   M. Luo, D. Dujic, and J. Allmeling, "Leakage flux modeling of multiwinding transformers for system-level simulations", *IEEE Transactions on Power electronics*, vol. 33, no. 3, pp. 2471–2483, 2017.

[93]   Z. Ouyang, J. Zhang, and W. G. Hurley, "Calculation of Leakage Inductance for High-Frequency Transformers", *IEEE Transactions on Power Electronics*, vol. 30, no. 10, pp. 5769–5775, Oct. 2015.

[94]   X. Margueron, J. P. Keradec, and D. Magot, "Analytical calculation of static leakage inductances of HF transformers using PEEC formulas", *IEEE Transactions on Industry Applications*, vol. 43, no. 4, pp. 884–892, Jul. 2007.

[95]   X. Margueron, A. Besri, P. O. Jeannin, J. P. Keradec, and G. Parent, "Complete analytical calculation of static leakage parameters: A step toward hf transformer optimization", in *IEEE Transactions on Industry Applications*, vol. 46, May 2010, pp. 1055–1063.

[96]   S. Kulkarni and S. Khaparde, *Transformer Engineering*. Boca Raton: CRC Press, May 2004.

[97]   A. Boyajian, "Leakage Reactance of Irregular Distributions of Transformer Windings by the Method of Double Fourier Series [includes discussion]", *Transactions of the American Institute of Electrical Engineers. Part III: Power Apparatus and Systems*, vol. 73, no. 2, pp. 1078–1086, Jan. 1954.

[98]   W. Hurley and D. Wilcox, "Calculation of leakage inductance in transformer windings", *IEEE Transactions on Power Electronics*, vol. 9, no. 1, pp. 121–126, Jan. 1994.

[99]   M. Mogorovic and D. Dujic, "Medium frequency transformer leakage inductance modeling and experimental verification", in *2017 IEEE Energy Conversion Congress and Exposition (ECCE)*, vol. 2017-Janua, IEEE, Oct. 2017, pp. 419–424.

[100]   R. Schlesinger and J. Biela, "Comparison of Analytical Models of Transformer Leakage Inductance: Accuracy Versus Computational Effort", *IEEE Transactions on Power Electronics*, vol. 36, no. 1, pp. 146–156, Jan. 2021.

[101]   M. Popov, L. van der Sluis, R. P. P. Smeets, and J. Lopez Roldan, "Analysis of Very Fast Transients in Layer-Type Transformer Windings", *IEEE Transactions on Power Delivery*, vol. 22, no. 1, pp. 238–247, Jan. 2007.

[102]   H. Zhao, S. Luan, Z. Shen, *et al.*, "Rethinking Basic Assumptions for Modeling Parasitic Capacitance in Inductors", *IEEE Transactions on Power Electronics*, vol. 37, no. 7, pp. 8281–8289, 2022.

[103]   A. Massarini and M. Kazimierczuk, "Self-capacitance of inductors", *IEEE Transactions on Power Electronics*, vol. 12, no. 4, pp. 671–676, Jul. 1997.

[104]   L. Dalessandro, F. da Silveira Cavalcante, and J. W. Kolar, "Self-Capacitance of High-Voltage Transformers", *IEEE Transactions on Power Electronics*, vol. 22, no. 5, pp. 2081–2092, Sep. 2007.

[105]   H. Zhao, D. N. Dalal, A. Bjorn Jorgensen, *et al.*, "Physics-Based Modeling of Parasitic Capacitance in Medium-Voltage Filter Inductors", *IEEE Transactions on Power Electronics*, vol. 36, no. 1, pp. 829–843, Jan. 2021.

[106]   Z. Shen, H. Wang, Y. Shen, Z. Qin, and F. Blaabjerg, "An improved stray capacitance model for inductors", *IEEE Transactions on Power Electronics*, vol. 34, no. 11, pp. 11 153–11 170, Nov. 2019.

[107]   J. Biela and J. W. Kolar, "Using transformer parasitics for resonant converters - A review of the calculation of the stray capacitance of transformers", in *Conference Record - IAS Annual Meeting (IEEE Industry Applications Society)*, vol. 3, IEEE, 2005, pp. 1868–1875.

[108]   Qin Yu and T. Holmes, "A study on stray capacitance modeling of inductors by using the finite element method", *IEEE Transactions on Electromagnetic Compatibility*, vol. 43, no. 1, pp. 88–93, 2001.

[109]   Y. Tanaka and Y. Baba, "Development of a Method for Calculating the Capacitance of Cables Installed in a Rectangular Tunnel Taking Account of the Permittivity of the Outer Sheath", *IEEE Transactions on Electromagnetic Compatibility*, pp. 1–10, 2023.

[110]   H. Nishiyama and M. Nakamura, "Form and capacitance of parallel-plate capacitors", *IEEE Transactions on Components, Packaging, and Manufacturing Technology: Part A*, vol. 17, no. 3, pp. 477–484, 1994.

[111]   N. Malik, "A review of the charge simulation method and its applications", *IEEE Transactions on Electrical Insulation*, vol. 24, no. 1, pp. 3–20, 1989.

[112] M. Naghed and I. Wolff, "Equivalent capacitances of coplanar waveguide discontinuities and interdigitated capacitors using a three-dimensional finite difference method", *IEEE Transactions on Microwave Theory and Techniques*, vol. 38, no. 12, pp. 1808–1815, 1990.

[113] J. Savage and W. Smith, "Capacitance calculations for cable harnesses using the method of moments", *IEEE Transactions on Electromagnetic Compatibility*, vol. 37, no. 1, pp. 131–137, 1995.

[114] J. H. Lienhard IV and J. H. Lienhard V, *A Heat Transfer Textbook*, 5th. Mineola, NY: Dover Publications, Dec. 2019, 784 pp.

[115] K. Stephan and A. Laesecke, "The thermal conductivity of fluid air", *Journal of physical and chemical reference data*, vol. 14, no. 1, pp. 227–234, 1985.

[116] A. Dumas and M. Trancossi, "Design of exchangers based on heat pipes for hot exhaust thermal flux, with the capability of thermal shocks absorption and low level energy recovery", SAE Technical Paper, Tech. Rep., 2009.

[117] G. F. Naterer, *Advanced heat transfer*. CRc Press, 2021.

[118] W. M. Rohsenow, J. P. Hartnett, Y. I. Cho, *et al.*, *Handbook of heat transfer*. Mcgraw-hill New York, 1998, vol. 3.

[119] L. Gaul, M. Kögl, and M. Wagner, *Boundary element methods for engineers and scientists: an introductory course with advanced topics*. Springer Science & Business Media, 2013.

[120] K.-J. Bathe, *Finite element procedures*. Klaus-Jurgen Bathe, 2006.

[121] W. Rucker and K. Richter, "Calculation of two-dimensional eddy current problems with the boundary element method", *IEEE Transactions on Magnetics*, vol. 19, no. 6, pp. 2429–2432, Nov. 1983.

[122] Y. Luo, T. Theodoulidis, X. Zhou, and A. Kyrgiazoglou, "Calculation of AC resistance of single-layer coils using boundary-element method", *IET Electric Power Applications*, vol. 15, no. 1, pp. 1–12, 2021.

[123] S. Yin, L. D. Rienzo, X. Ma, and Y. Huangfu, "Efficient BEM Computation of the Impedance of Axisymmetric Air-Core Inductors", *IEEE Transactions on Electromagnetic Compatibility*, vol. 64, no. 2, pp. 585–589, 2022.

[124] J. Savage and W. Smith, "Capacitance calculations for cable harnesses using the method of moments", *IEEE Transactions on Electromagnetic Compatibility*, vol. 37, no. 1, pp. 131–137, 1995.

[125] J. Clements, C. Paul, and A. Adams, "Computation of the Capacitance Matrix for Systems of Dielectric-Coated Cylindrical Conductors", *IEEE Transactions on Electromagnetic Compatibility*, vol. EMC-17, no. 4, pp. 238–248, Nov. 1975.

[126] P. Silvester, "TEM wave properties of microstrip transmission lines", *Proceedings of the Institution of Electrical Engineers*, vol. 115, p. 43, 1 1968.

[127] T. Luo, M. G. Niasar, and P. Vaessen, "Two-Dimensional Frequency-Dependent Resistance and Inductance Calculation Method for Magnetic Components With Round Conductors", *IEEE Transactions on Magnetics*, vol. 60, no. 1, pp. 1–11, Jan. 2024.

[128] K. Niyomsatian, J. J. Gyselinck, and R. V. Sabariego, "Experimental Extraction of Winding Resistance in Litz-Wire Transformers - Influence of Winding Mutual Resistance", *IEEE Transactions on Power Electronics*, vol. 34, no. 7, pp. 6736–6746, Jul. 2019.

[129] N. Simpson, R. Wrobel, and P. H. Mellor, "Estimation of equivalent thermal parameters of impregnated electrical windings", *IEEE Transactions on Industry Applications*, vol. 49, pp. 2505–2515, 6 Nov. 2013.

[130] A. Boglietti, E. Carpaneto, M. Cossale, S. Vaschetto, M. Popescu, and D. A. Staton, "Stator winding thermal conductivity evaluation: An industrial production assessment", *IEEE Transactions on Industry Applications*, vol. 52, pp. 3893–3900, 5 Sep. 2016.

[131] R. Wrobel and P. H. Mellor, "A general cuboidal element for three-dimensional thermal modelling", *IEEE Transactions on Magnetics*, vol. 46, pp. 3197–3200, 8 2010.

[132] J. Ferreira, "Analytical computation of AC resistance of round and rectangular litz wire windings", *IEE Proceedings B Electric Power Applications*, vol. 139, no. 1, p. 21, 1992.

[133] C. C. R. Sullivan, "Optimal choice for number of strands in a litz-wire transformer winding", *IEEE Transactions on Power Electronics*, vol. 14, no. 2, pp. 283–291, Mar. 1999.

[134] K. Niyomsatian, J. Gyselinck, and R. V. Sabariego, "Closed-form complex permeability expression for proximity-effect homogenisation of litz-wire windings", *IET Science, Measurement and Technology*, vol. 14, no. 3, pp. 287–291, May 2020.

[135] C. R. Sullivan and R. Y. Zhang, "Analytical model for effects of twisting on litz-wire losses", in *2014 IEEE 15th Workshop on Control and Modeling for Power Electronics (COMPEL)*, IEEE, Jun. 2014, pp. 1–10.

[136] H. Rossmanith, M. Doebroenti, M. Albach, and D. Exner, "Measurement and Characterization of High Frequency Losses in Nonideal Litz Wires", *IEEE Transactions on Power Electronics*, vol. 26, no. 11, pp. 3386–3394, Nov. 2011.

[137] E. Plumed, J. Acero, I. Lope, and C. Carretero, "3D finite element simulation of litz wires with multilevel bundle structure", in *Proceedings: IECON 2018 - 44th Annual Conference of the IEEE Industrial Electronics Society*, IEEE, Oct. 2018, pp. 3479–3484.

[138] J. Lyu, H. C. Chen, Y. Zhang, Y. Du, and Q. S. Cheng, "Litz Wire and Uninsulated Twisted Wire Assessment Using a Multilevel PEEC Method", *IEEE Transactions on Power Electronics*, vol. 37, no. 2, pp. 2372–2381, Feb. 2022.

[139] S. Ehrlich, H. Rossmanith, M. Sauer, C. Joffe, and M. Marz, "Fast Numerical Power Loss Calculation for High-Frequency Litz Wires", *IEEE Transactions on Power Electronics*, vol. 36, no. 2, pp. 2018–2032, Feb. 2021.

[140] T. Guillod, J. Huber, F. Krismer, and J. W. Kolar, "Litz wire losses: Effects of twisting imperfections", in *2017 IEEE 18th Workshop on Control and Modeling for Power Electronics, COMPEL 2017*, IEEE, Jul. 2017, pp. 1–8.

[141] G. Cerri, S. A. Kovyryalov, and V. M. Primiani, "Modelling of a Litz-wire planar winding geometry for an accurate reactance evaluation", *IET Science, Measurement and Technology*, vol. 4, no. 4, pp. 214–219, Jul. 2010.

[142] E. Plumed, I. Lope, C. Carretero, and J. Acero, "A recursive methodology for modelling multi-stranded wires with multilevel helix structure", *Applied Mathematical Modelling*, vol. 83, pp. 76–89, Jul. 2020.

[143] T. Luo, M. G. Niasar, and P. Vaessen, "Two-Dimensional Frequency-Dependent Resistance and Inductance Calculation Method for Magnetic Components With Round Conductors", *IEEE Transactions on Magnetics*, vol. 60, no. 1, pp. 1–11, Jan. 2024.

[144] J. Gyselinck and P. Dular, "Frequency-domain homogenization of bundles of wires in 2-D magnetodynamic FE calculations", *IEEE Transactions on Magnetics*, vol. 41, no. 5, pp. 1416–1419, 2005.

[145] H. Igarashi, "Semi-analytical approach for finite-element analysis of multi-turn coil considering skin and proximity effects", *IEEE Transactions on Magnetics*, vol. 53, no. 1, pp. 1–7, Jan. 2017.

[146] K. Niyomsatian, J. Gyselinck, and R. V. Sabariego, "Closed-form complex permeability expression for proximity-effect homogenisation of litz-wire windings", *IET Science, Measurement & Technology*, vol. 14, no. 3, pp. 287–291, May 2020.

[147] P. Wang, A. Cavallini, G. Montanari, and G. Wu, "Effect of rise time on PD pulse features under repetitive square wave voltages", *IEEE Transactions on Dielectrics and Electrical Insulation*, vol. 20, pp. 245–254, 1 Feb. 2013.

[148] Z. Guo, A. Q. Huang, R. E. Hebner, G. C. Montanari, and X. Feng, "Characterization of Partial Discharges in High-Frequency Transformer Under PWM Pulses", *IEEE Transactions on Power Electronics*, vol. 37, pp. 11 199–11 208, 9 Sep. 2022.

[149] Y. Zhao, G. Zhang, D. Han, K. Li, Z. Qiu, and F. Yang, "Experimental study on the insulation properties of epoxy casting resins under high-frequency square waveform", *CSEE Journal of Power and Energy Systems*, vol. PP, pp. 1–10, 99 2020.

[150] A. R. Mor, L. C. Heredia, D. Harmsen, and F. Muñoz, "A new design of a test platform for testing multiple partial discharge sources", *International Journal of Electrical Power & Energy Systems*, vol. 94, pp. 374–384, Jan. 2018.

[151] International Electrotechnical Commission (IEC), "IEC 60664-4: Insulation coordination for equipment within low-voltage systems – Part 4: Consideration of high-frequency voltage stress", IEC Central Office, International Standard 60664-4, 2005.

[152] J. C. Biswas and V. Mitra, "High-frequency breakdown and paschen law", *Applied Physics*, vol. 19, pp. 377–381, 4 Aug. 1979.

[153] I. A. Aponte, B. Esser, Z. C. Shaw, J. C. Dickens, J. J. Mankowski, and A. A. Neuber, "Fundamental study of DC and RF breakdown of atmospheric air", *Physics of Plasmas*, vol. 26, p. 123 512, 12 Dec. 2019.

[154] W. Pfeiffer, "High-frequency Voltage Stress of Insulation: Methods of Testing", *IEEE Transactions on Electrical Insulation*, vol. 26, pp. 239–246, 2 Apr. 1991.

[155] W. Dunbar, D. Schweickart, J. Horwath, and L. Walko, "High frequency breakdown characteristics of various electrode geometries in air", IEEE, 1998, pp. 221–224.

[156] F. Seifert, S. Jugelt, and C. Leu, "Measurement and Numerical Simulation of Discharge Characteristics in Air at Medium Frequency Voltages", *IEEE Transactions on Dielectrics and Electrical Insulation*, vol. 28, pp. 1506–1513, 5 Oct. 2021.

[157] R. Plessow and W. Pfeiffer, "Influence of the frequency on the partial discharge inception voltage", *Conference on Electrical Insulation and Dielectric Phenomena (CEIDP), Annual Report*, pp. 97–102, 1994.

[158] A. N. Esfahani, S. Shahabi, G. Stone, and B. Kordi, "Investigation of Corona Partial Discharge Characteristics under Variable Frequency and Air Pressure", IEEE, Jun. 2018, pp. 31–34.

[159] L. J. Frisco and J. J. Chapman, "The Flashover Strength of Solid Dielectric", *Transactions of the American Institute of Electrical Engineers. Part III: Power Apparatus and Systems*, vol. 75, pp. 77–83, 3 Jan. 1956.

[160] T. Kamosawa, N. Yoshimura, M. Nishida, and F. Noto, "Tracking Breakdown of Organic Insulating Materials under High Frequency Voltage Application—by means of IEC Publication 587", *IEEJ Transactions on Fundamentals and Materials*, vol. 107, pp. 17–24, 1 1987.

[161] T. Liu, Y. Xiao, Y. Lu, X. Huang, Q. Li, and Z. Wang, "Effect of voltage frequency on surface discharge characteristics and aging process", *2017 IEEE Electrical Insulation Conference, EIC 2017*, pp. 463–466, June 2017.

[162] H. C. Miller, "Flashover of insulators in vacuum: the last twenty years", *IEEE Transactions on Dielectrics and Electrical Insulation*, vol. 22, pp. 3641–3657, 6 Dec. 2015.

[163] J. Mason, "Effects of frequency on the electric strength of polymers", *IEEE Transactions on Electrical Insulation*, vol. 27, pp. 1213–1216, 6 1992.

[164] W. Yin, "Failure mechanism of winding insulations in inverter-fed motors", *IEEE Electrical Insulation Magazine*, vol. 13, pp. 18–23, 6 Nov. 1997.

[165] D. Fabiani, G. C. Montanari, and A. Contin, "Aging acceleration of insulating materials for electrical machine windings supplied by PWM in the presence and in the absence of partial discharges", IEEE, 2001, pp. 283–286.

[166] M. S. Moonesan, S. H. Jayaram, and E. A. Cherney, "Time to failure of medium-voltage form-wound machine turn insulation stressed by unipolar square waves", *IEEE Transactions on Dielectrics and Electrical Insulation*, vol. 22, pp. 3118–3125, 6 Dec. 2015.

[167] A. Cavallini, "Effect of supply voltage frequency on testing of insulation system", *IEEE Transactions on Dielectrics and Electrical Insulation*, vol. 13, pp. 111–121, 1 Feb. 2006.

[168] P. Wang, G. C. Montanari, and A. Cavallini, "Partial Discharge Phenomenology and Induced Aging Behavior in Rotating Machines Controlled by Power Electronics", *IEEE Transactions on Industrial Electronics*, vol. 61, pp. 7105–7112, 12 Dec. 2014.

[169] International Electrotechnical Commission (IEC), "IEC 60076-1: Power transformers – Part 1: General", IEC Central Office, International Standard 60076-1, 2011.

[170] International Electrotechnical Commission (IEC), "IEC 60076-3: Power transformers – Part 3: Insulation levels, dielectric tests and external clearances in air", IEC Central Office, International Standard 60076-3, 2018.

[171] International Electrotechnical Commission (IEC), "IEC 60664-1: Insulation coordination for equipment within low-voltage systems – Part 1: Principles, requirements and tests", IEC Central Office, International Standard 60664-1, 2020.

[172] International Electrotechnical Commission (IEC), "IEC 61800-5-1: Adjustable speed electrical power drive systems – Part 5-1: Safety requirements – Electrical, thermal and energy", IEC Central Office, International Standard 61800-5-1, 2017.

[173] IEEE Standards Association, "IEEE C57.12.00: Standard for General Requirements for Liquid-Immersed Distribution, Power, and Regulating Transformers", IEEE Standards Association, IEEE Standard C57.12.00, 2010.

[174] International Electrotechnical Commission (IEC), "IEC/TS 60815: Guide for the selection and dimensioning of high-voltage insulators intended for use in polluted conditions", IEC Central Office, Technical Specification, 2008.

[175] M. Chanda and S. K. Roy, *Plastics Technology Handbook*, 4th. Boca Raton, FL: CRC Press, 2006.

[176] W. Wang, Y. Liu, J. He, *et al.*, "An Improved Design Procedure for a 10 kHz, 10 kW Medium-Frequency Transformer Considering Insulation Breakdown Strength and Structure Optimization", *IEEE Journal of Emerging and Selected Topics in Power Electronics*, vol. 10, no. 4, pp. 3525–3540, Aug. 2022.

[177]   International Electrotechnical Commission, "IEC 60505:2011 - Evaluation and qualification of electrical insulation systems", International Electrotechnical Commission, Geneva, Switzerland, Standard, 2011.

[178]   G. Carlo Montanari, P. Morshuis, P. Seri, and R. Ghosh, "Ageing and reliability of electrical insulation: the risk of hybrid AC/DC grids", *High Voltage*, vol. 5, no. 5, pp. 620–627, Oct. 2020.

[179]   Vantico Ltd., *Araldite Casting Resin System-CY225-HY925*, Huntsman, 2000.

[180]   A. Antoniou and W.-S. Lu, *Practical optimization: algorithms and engineering applications*. Springer, 2007, vol. 19.

[181]   M. A. Bahmani, T. Thiringer, and M. Kharezy, "Design Methodology and Optimization of a Medium-Frequency Transformer for High-Power DC–DC Applications", *IEEE Transactions on Industry Applications*, vol. 52, pp. 4225–4233, 5 Sep. 2016.

[182]   M. Mogorovic and D. Dujic, "100 kW, 10 kHz Medium-Frequency Transformer Design Optimization and Experimental Verification", *IEEE Transactions on Power Electronics*, vol. 34, pp. 1696–1708, 2 Feb. 2019.

[183]   P. Shuai and J. J. Biela, "Design and optimization of medium frequency, medium voltage transformers", *2013 15th European Conference on Power Electronics and Applications, EPE 2013*, pp. 1–10, Mv Sep. 2013.

[184]   T. Guillod, P. Papamanolis, and J. W. Kolar, "Artificial Neural Network (ANN) Based Fast and Accurate Inductor Modeling and Design", *IEEE Open Journal of Power Electronics*, vol. 1, pp. 284–299, July 2020.

[185]   D. Aguglia and M. Neuhaus, "Laminated magnetic materials losses analysis under non-sinusoidal flux waveforms in power electronics systems", in *2013 15th European Conference on Power Electronics and Applications (EPE)*, IEEE, 2013, pp. 1–8.

[186]   I. The MathWorks, *particleswarm*, Accessed: 2024-06-20, 2024.

[187]   P. India, *AMCC Cut Core Catalogue*, Accessed: 2024-06-23, 2024.

[188]   T. E. AG, *U/I Cores Product Catalog*, Accessed: 2024-06-23, 2024.

ACKNOWLEDGEMENTS

Completing a PhD is a challenging journey, and I feel deeply fortunate to have reached its final stage. During the last several years, I experienced happiness, excitation, nostalgia, depression, etc. I would like to express my gratitude to everyone who has supported and accompanied me on this long journey.

I would like to express my gratitude to my promoter Prof. Peter Vaessen. I really appreciate your valuable advice on my research and life. Your feedback is always constructive and timely. Also, thank you very much for providing me with many opportunities to participate in activities in academia and industry. I also want to express my gratitude to my other promoter, Prof. Pavol Bauer, for providing me with the opportunity to pursue my PhD degree and for all the support during my research. Many thanks to my daily supervisor, Dr. Mohamad Ghaffarian Niasar. Thank you for your patient guiding and inspiring discussion during the long-term research. Your positive comments give me the confidence to continue. You have an impressive passion for research and education, which always encourages me to explore and learn new things.

Research is not only one person's contribution. Thanks to our experienced technicians, whose support was fundamental to the experiments conducted in this thesis. Luis, I appreciate your support on my measurements, which is very helpful. Wim, thank you for the support in developing test setups. Gert, thank you for your help in insulation testing. Imke, thank you for your support in the HV lab. Besides, I want to express my gratitude to the staff within the HVT and DCE&S group. Sharmila and Marieke, thank you for your help in many practical aspects of my PhD. Jianning, thank you for sharing your knowledge in magnetics. Fabio and Guillermo, thank you for your welcome when I joined the group.

I feel fortunate to have so many wonderful fellow PhD candidates. Christian, Dhanashree, and Weichuan, it is a great experience to share the office with you, which forms a comfortable environment. Christian, your expertise in PD analysis is invaluable. You are a good tennis player, playing together is always delighting. There are many unforgettable memories, especially during ISH2023. Thank you for guiding me back to the hotel in Glasgow. Weichuan, it is my pleasure to collaborate with you on insulation experiments. Dhanashree, thank you for sharing before PhD milestones. Yun, there were many delightful discussions and experiences in both research and life. Reza, it is very nice to have someone working on a similar topic. Discussion with you always lets me think about problems in different aspects. Sohrab, thank you for bringing so much delight to the group, and the HVT logo is very cool. Guangyao, your meticulous attitude is very impressive. I obtain knowledge and fun from the discussion with you. I will always remember the time we spent cycling. Lu, talking with you is very interesting. You always have good stories. Yunhe, I appreciate you inviting me to celebrate the Chinese New Year when I just arrived in the Netherlands. Lyu, you are a good tennis partner, and thank you for your help from the circuit perspective. Yang,

CURRICULUM VITAE

Tianming Luo

17-10-1993   Born in Jinan, China.

EDUCATION

2020-2024   Ph.D. candidate
Delft University of Technology, the Netherlands

2015–2018   MSc in Electrical Engineering
China Electric Power Research Institute, China

2011–2015   BSc in Electrical Engineering
Chongqing University, China

AWARDS

2024   Best Student Presentation Awards - IEEE CEFC 2024

2024   IEEE International Challenge in Design Methods for Power Electronics, Excellent Innovation Award, 2nd Place

LIST OF PUBLICATIONS

Journal Paper:

1. T. Luo, M. G. Niasar and P. Vaessen, "Improved Winding Losses Calculation Based on Bessel Functions," in IEEE Transactions on Magnetics, vol. 59, no. 6, pp. 1-10, June 2023.

2. T. Luo, M. G. Niasar and P. Vaessen, "2-D Winding Losses Calculation for Round Conductor Coil," in IEEE Transactions on Power Electronics, vol. 38, no. 4, pp. 5107-5117, April 2023.

3. T. Luo, M. G. Niasar and P. Vaessen, "Fast 2.5-D Loss Calculation for Round Litz Wires," in IEEE Transactions on Magnetics, vol. 60, no. 3, pp. 1-4, March 2024.

4. T. Luo, M. G. Niasar and P. Vaessen, "Two-Dimensional Frequency-Dependent Resistance and Inductance Calculation Method for Magnetic Components With Round Conductors," in IEEE Transactions on Magnetics, vol. 60, no. 1, pp. 1-11, Jan. 2024.

5. T. Luo, M. G. Niasar and P. Vaessen, "A Fast 3D Numerical Impedance Calculation for Litz Wire and Air-Core Coils," in IEEE Transactions on Power Electronics. (Early access)

6. T. Luo, M. G. Niasar and P. Vaessen, "An Improved 2D Method of Moments for the Capacitance Calculation of Round Conductors with Insulation Layers." (Submitted)

As co-author:

7. C. Mier, A. R. Mor, T. Luo, P. Vaessen, "Partial discharge and interference discrimination in gas-insulated systems using electric and magnetic sensors," in International Journal of Electrical Power & Energy Systems, vol. 158, July. 2024.

8. Z. Li et al., "A Data-Driven Model for Power Loss Estimation of Magnetic Materials Based on Multi-Objective Optimization and Transfer Learning," in IEEE Open Journal of Power Electronics, vol. 5, pp. 605-617, 2024.

9. M. Chen et al., "MagNet Challenge for Data-Driven Power Magnetics Modeling," in IEEE Open Journal of Power Electronics. (Early access)

Conference Paper:

1. T. Luo, W. Zhao and M. G. Niasar, "Experimental study of epoxy surface discharge under different frequencies," 2021 IEEE Conference on Electrical Insulation and Dielectric Phenomena (CEIDP), Vancouver, BC, Canada, 2021, pp. 574-577.

2. T. Luo, M. G. Niasar and P. Vaessen, "Experimental study of air discharge under various frequency stress with inhomogeneous field," 23rd International Symposium on High Voltage Engineering (ISH 2023), Glasgow, UK, pp. 1162-1166.

3. T. Luo, M. G. Niasar and P. Vaessen, "PEEC Based Fast 3D Litz Wire Model," IEEE 21st Biennial Conference on Electromagnetic Field Computation (CEFC2024), Jeju, Korea, Republic of, 2024, pp. 1-2.

 As co-author:

4. W. Zhao, T. Luo and M. G. Niasar, "Ramp sinusoidal breakdown of epoxy resin under high voltage waveforms at different frequencies," 22nd International Symposium on High Voltage Engineering (ISH 2021), Hybrid Conference, Xi'an, China, 2021, pp. 2083-2088,